Exploring Small Molecule Reactivity with Low-Valent Nickel and Cobalt Complexes Supported by Lewis Acidic Metalloligands

A DISSERTATION

SUBMITTED TO THE FACULTY OF THE

UNIVERSITY OF MINNESOTA

BY

Matthew V. Vollmer

IN PARTIAL FULFILLMENT OF THE REQUIREMENTS

FOR THE DEGREE OF

DOCTOR OF PHILOSOPHY

Connie C. Lu, advisor

May 2019

Acknowledgments

I would like to thank everyone that helped me reach, and to complete, my graduate studies. No one has ever said that completing a Ph.D. is easy, and I can attest that the road to finishing is paved with hard miles. That being said, my time in graduate school has certainly been a great adventure and I have learned as much about the chemistry detailed in this body of work as I have about myself.

I am thankful to all the members of the Lu lab that I have had the pleasure to interact closely with over the years. I learned innumerable lessons from both Reed Eisenhart and Laura Clouston about the chemistry in our lab, but more importantly how to succeed in graduate school. Throughout my time in the group, I worked closely with Ryan Cammarota. I am grateful to Ryan not only for his invaluable scientific input, but also, his timely reminders not to take life too seriously (but maybe not the 2 a.m. VT sessions!). Ryan, Jingyun Ye, Jing Xie, and I have had a great collaboration over the years which serves as a firm reminder that success is better with good friends. Towards the end of graduate school, I helped Brendan Graziano to acclimate to the lab. While doing so, I not only found a good friend, but I also learned invaluable lessons about myself while acting as a mentor. I have also worked alongside Sai Desai, JT Moore, and Bianca Ramirez and I thank you for our numerous scientific and personal conversations over the years. I was fortunate to study at PNNL during my last summer, and I am also thankful to John Linehan, Eric Wiedner, Peter Dunn, Andrew Preston, and Joe Laureanti for making it such a fantastic and unique experience.

I would also like to thank Connie Lu and Justin Walensky for their incredible support over the years. To Justin, I am grateful that you took a chance on an undergraduate that wanted to, "just make some cool stuff." I would have never thought working in your lab would have taken me to where I am now. To Connie, the support and academic freedom you have given me over the years has allowed me to thrive during graduate school. In retrospect, I appreciate that you left me to my own devices. In doing so you helped me to learn things for myself and taught me that carving my own path requires a strong internal drive. I could not have asked for better advisors during my secondary education. I suspect that the academic rigor, attitudes of curiosity, and the demands for high-quality work will

serve me long after my studies are complete. Finishing my thesis feels like a massive accomplishment, and it suffices to say that it would not have been possible without your support.

I am also extremely grateful for the support of my own parents, Cheri and James, as well as my wife's parents, Barb and Joe, throughout the past five years. It cannot be understated how important having such a great emotional support system was for my own sanity during graduate school. Simply being able to have a conversation with you all really did make all the difference. I also would like to thank Ashley, Kevin, and Penelope, for reminding me of everything that life after graduate school may hold.

Lastly, and most importantly, I would like to thank my wife Lindsey and our dog Aurora. After grueling days in the lab or office, you truly are the best thing in the world that I could ever imagine coming home too. Moreover, I struggle to find the words to say how valuable Lindsey's support truly is to me. Without her, it is highly likely that I would have never finished my studies at all. I might not ever be able to accurately express how thankful I am, but I will continue to try. The three of us have been on a wild journey that is finally coming to a close. If our present is any indication, the future holds even more adventure, and I am thrilled to see where our next chapter takes us.

Table of Contents

List of Figures

List of Tables

List of abbreviations

σ	sigma type interaction
ω	Larmor frequency
ν	NMR spectrometer frequency
$(1,5\text{-COD})_2Cu^+$	copper bis(1,5-cyclooctadiene) cation
τ_c	rotational correlation time
(g)	gas phase
γ_H	^1H gyromagnetic ratio
τ_{H2}	rotational correlation time for H_2 ligand
τ_{mol}	molecular rotational correlation time
$[CO_2\bullet]-$	radical anion of carbon dioxide
$[N_2\bullet]^-$	radical anion of dinitrogen
$\{MM\}^n$	Eltham–Enemark Notation to describe ambiguous bonding scenarios
°	degree
°C	degrees Celsius
ΔG°	standard state change in free energy kcal/mol
$\Delta G^\circ_{H_2}$	free energy of dihydrogen binding
$\Delta G^\circ_{H^-}$	hydride donor strength, hydricity, kcal/mol
$\Delta H^\circ f_{298}$	standard heat of formation, kcal/mol
ΔH°	standard reaction enthalpy, kcal/mol
ΔS°	standard reaction entropy kcal $mol^- K^-$
1,5-COD	1,5-cyclooctadiene, C_8H_{12}
222-crypt	4,7,13,16,21,24-Hexaoxa-1,10-diazabicyclo[8.8.8]hexacosane
A	hyperfine coupling, EPR, mT
Å	Ångström = $1x10^{-10}$ m
a(Å)	crystallographic unit cell a-axis, Å
ADF	Amsterdam Density Functional
ADP	adenosine diphosphate
A_{iso}	isotropic hyperfine coupling, EPR, mT
Al	aluminum
$AlCl_3$	aluminum trichloride
ArH	generic aromatic proton
atm	atmospheric pressure, equivlant to 760mmHg
ATP	adenosine triphosphate
b(Å)	crystallographic unit cell b-axis, Å
$BArF_{24}$	tetrakis(bis(3,5-trifluoromethylphenyl))borate anion, $B(C_8H_3F_6)_4^-$
$baseH^+$	generic protonated base
BDFE	bond dissociation free energy, kcal/mol
BFI^-	N,N'-bis(tris(pentafluorophenyl)–borane)imidazolate anion
Bi	bismuth
BnMgBr	benzyl magnesium bromide Grignard reagent
Bu_4N^+	tetra-butylammonium cation

c(Å)	crystallographic unit cell c-axis, Å
C_2H_4	ethylene
C_3	trigonal symmetry
C_6D_6	deuterated benzene
C_6H_6	benzene
C_9H_{12}	mesitylene, 1,3,5-trimethyl-benzene
Ca	calcium
CASSCF	complete active space self-consistent field calculations
CDT	all–*trans*–1,5,9–cyclododecatriene
CH_4	methane
CN^-	cyanide anion
C_nH_{2n+2}	generic saturated linear hydrocarbon
CO	carbon monoxide
Co	cobalt
$Co(P_4N_2)H$	1,5-diphenyl-3,7-bis(diphenylphosphino)propyl-1,5-diaza-3,7-diphosphacyclooctane cobalt hydide
CO_2H^-	formate
CO_3^{2-}	carbonate
$CoCl_2$	cobalt dichloride
Cp*	1,2,3,4,5-pentamethylcyclopentadienide, $C_{10}H_{15}^-$
Cp_2ZrMe_2	bis(cyclopentadienyl)-dimethyl-zirconocene
Cryst syst	crystallographic system
Cu	copper
CV	cyclic voltammogram
Cy_3P	tri-cyclohexyl-phosphine
D	deuterium nuclear isotope
d	doublet
D_2	deuterium diatomic gas
D_2O	deuterium oxide, heavy water
DBU	1,8-Diazabicyclo[5.4.0]undec-7-ene
DBU–H^+	protonated 1,8-Diazabicyclo[5.4.0]undec-7-ene
D_{calcd}	crystallographically calculated crystal density (g cm^{-3})
depe	bis(diethylphosphino)ethane
DFT	density functional theory
d_{HH}	interatomic H-H distance, Å
DME	1,2-dimethoxyethane, $C_4H_{10}O_2$
DMF	dimethylformamide
dmpe	1,2–bis(dimethylphosphino)ethane
d^n	number of d orbital electrons
DPB^{Mes}	di(o-diisopropyl-phosphinophenyl)-mesitylborane
e^-	electron
E°	standard reduction potential, V
$E_{1/2}$	reversible electrochemical reduction potential, V
E_4	Janus state, nitrogenase enzyme

EPR	electron paramagnetic resonance
Et_2O	diethyl ether, C_4H_8O
Fc/Fc^+	ferrocene/Ferrocenium electrochemical redox couple, V
Fe	iron
FeMo	iron-molybdenum nitrogenase
FLP	frustrated Lewis pair
Fw	formula weight
g	gram
g	g-value
Ga	gallium
GC-FID	gas chromatography flame ionization detector
GGA	generalized gradient approximation
Gt	gigaton, 10^9 tons
h	heptet
H-CCAr	acetylide
H-SR	thiol
H^-	hydride anion
$H(OEt_2)_2^+$	protonated diethyl ether cation complex
H•	hydrogen atom
H^+	proton
H^+/e^-	proton/electron equivalent
H_2	hydrogen diatom
H_2:CO_2	1:1 mixture of hydrogen and carbon dioxide
H_2O	water
H_3L	protonated ligand precursor, $N(o\text{-}(NHCH_2PiPr_2)C_6H_4)_3$
H_3PO_4	phosphoric acid
$HBEt_3^-$	triethylborohyride anioni
HBPin	4,4,5,5–Tetramethyl–1,3,2–dioxaborolane
HC(O)OEt	ethyl formate
HD	deuterium hydride
HDO	deuterium hydrogen oxide
He_2^+	helium radical cation
^HL	$MeC(CH_2NHPh\text{-}o\text{-}NH_2)_3$
HOMO	highest occupied molecular orbital
HOMO-*n*	n^{th} highest occupied molecular orbital
Hz	hertz, s^{-1}
hν	light or wavelength
I	nuclear spin
In	indium
iPr	isopropyl group
IR	Infrared spectroscopy
J	Generic, coupling constant
K	Kelvin

KBr	Potassium bromide
K_c	comproportionation constants
kcal	kilocalorie
K_{eq}	equilibrium constant
L	liter
Li	lithium
$LiAlH_4$	lithium aluminum hydride
LPMO	lytic polysaccharide monooxygenase
L^{tBu}	*ß*-diketiminate ligand, $[HC(C(t\text{Bu})NC_6H_3(i\text{Pr})_2)_2]^-$
LUMO	lowest occupied molecular orbital
M	molar, mol/L
$M–N_3$	crystallographically defined tri-nitrogen plane of L to M
Me_2-cAAC	cyclic alkyl amino carbene
MeBPin	4,4,5,5–Tetramethyl–1,3,2–dioxa-methyl-borolane
MeCN or CH_3CN	acetonitrile
MeLi	methyl lithium
MeMgBr	methyl magnesium bromide
MeMgCl	methyl magnesium chloride
mg	milligram, 10^{-3} g
MHz	megahertz, 10^6 Hz
mM	millimolar, 10^{-3} M
Mn	manganese
M^n	metal center in its n^{th} oxidation state
M^{n+2}	oxidized metal center in its $n^{th}+2$ oxidation state
mol	mole
mol^- or /mol	per mole
ms	millisecond, 10^{-3} s
Mt	megaton, 10^6 ton
mV	millivolt, 10^{-3} volts
N_2	dinitrogen
N_2H_2	diazene
N_2H_4	hydrazine
Na	sodium
NaHg	sodium amalgam
NaK	sodium potassium eutectic
^{n}BuLi	n-butyl lithium
NDI	naphthyridine−diimine
NH_3	ammonia
Ni	nickel
NMR	nuclear magnetic resonance
NO_2^-	nitrate anion
O_2	oxygen
OEC	oxygen-evolving complex

OTf or $CF_3SO_3^-$	trifluoromethanesulfonate anion
p	quintet
P_3	crystallographically defined tri-phosphine plane of L
$P_4{}^tBu$	1-*tert*-Butyl-4,4,4-tris(dimethylamino)-2,2-bis[tris(dimethylamino)-phosphoranylidenamino]-2λ^5,4λ^5-catenadi(phosphazene)
PBD	Protein Data Bank
PBE	Perdew-Burke-Ernzerhof exchange correlation functional
pCO_2	partial pressure of carbon dioxide
PEEK	polyether ether ketone polymer
PF_6^-	hexafluorophosphate anion
Ph	phenyl group, C_6H_5
pH_2	partial pressure of hydrogen
$PhCO_2H$	benzoic Acid
PhMgBr	phenyl magnesium bromide
$PhSiH_3$	phenyl silane, C_6H_8Si
pK_a	the logarithm of the acidity dissociation constant
Pm	10^{-9} meters
PMDTA	N,N,N',N'',N''–pentamethyl–diethylenetriamine
PNNL	Pacific Northwest National Laboratory
ppm	parts per million
PPN^+	bis(triphenylphosphine)iminium cation, $C_{36}H_{30}NP_2^+$
PR_3	generic, organophosphine
PSII	photosystem II
P^tBu_3	tri-tertbutyl-phosphine
PTFE	polytetrafluoroethylene
q	quartet
r	interatomic distance
r	formal shortness ratio
R_1	rate of magnetic relaxation
R_{1min}	minimum longitudinal relaxation rate
R_2N^-	imido ligand
R_{Co}	relaxation enhancement due to cobalt, Hz
Reflns	reflections
Rh	rhodium
R_L	relaxation enhancement due to ligand protons, Hz
s	singlet
S	sulfur
S	spin state
Sb	antimony
SHE	standard hydrogen electrode
SOMO	singly occupied molecular orbitals
Sr	strontium
T	tesla
t	triplet

T.S.	transition state
T_1	longitudinal relaxation time
T_{1min}	minimum longitudinal relaxation time
T_{1min_calc}	corrected T_{1min} value
TBA or Bu_4N	tetra(n-butyl)ammonium
^tBu	tert-butyl group
$^tBuCH_2Li$	neopentyl lithium
$^{tBu}N(NHC)$ or $^{tBu}N(^{iPr}NHC^{Me})$	*N*-(*tert*-butyl)-1,3-diisopropyl-4,5-dimethyl-1,3-dihydro-2*H*-imidazol2-imine
^tBuNXyl	N-3,5-dimethyl-phenyl-tertbutyl-amine
^tBuTMG	tert-Butyl-tetramethylguanidine, Barton's base
$^tBuTMG–H^+$	protonated tert-Butyl-tetramethylguanidine, protonated Barton's base
TD-DFT	Time-dependent density function theory
terpy	*m*-terpyridine
tetraphos	generic tethered tetraphosphine ligand
THF	tetrahydrofuran, C_4H_8O
THF-d_8	deuterated tetrahydrofuran, C_4D_8O
$TMSCH_2Li$	(trimethylsilyl)methyl-lithium
TOF	turnover frequency
toluene-d_8	deuterated toluene, C_7D_8
TON	turnover number
TPB	tris(phosphino)borane
UMN	University of Minnesota – Twin Cities
UV-vis	ultraviolet visible spectroscopy
V	volt
V ($Å^3$)	crystallographic unit cell volume
Vkd or ^{iPr}Vkd	Verkade base, 2,8,9-triisopropyl-2,5,8,9-tetraaza-1-phosphabicyclo[3,3,3]undecane
$VkdH^+$ or $^{iPr}VkdH^+$	Protonated Verkade's base
VT	Variable temperature
x,y,z	cartesian coordinates
XRD	x-ray diffraction
Z	number of molecules in asymmetric unit
Zn	zinc
ZORA	zeroth-order regular approximation
α (deg)	crystallographic unit cell angle
β (deg)	crystallographic unit cell angle
γ (deg)	crystallographic unit cell angle
δ	chemical shift
η	hapticity
μ_n	bridging ligand spanning *n* centers
$\nu(N_2)$	dinitrogen stretching frequency, cm^{-1}
π	electrons residing in an orbital of pi symmetry
χ	Pauling electronegativity

cm^{-1}	wavenumber
3d/4d/5d	first, second, and third row d-orbital manifold
^{1}H	Hydrogen-1 nuclear isotope
$^{1}J_{HD}$	single bond deuterium/hydrogen coupling, Hz
cm^{-1}	wavenumber
$[M(CO)_n]^{2-}$	carbonyl metallate dianion
$SiMetBu_2^-$	(ditert-butyl)methylsilane anion
$[MeB(C_6F_5)_3]^-$	tris(pentafluorophenyl)methyl borate anion
$[Ni(CO)_3]^-$	tricarbonyl nickel radical anion
$B(C_6F_5)_3$	tris(pentafluorophenyl)borane
$BR_3\bullet^-$	borane radical anion
$Me_2CP(dma)_3$	tris(dimethylamido)(propan-2-ylidene)phosphorane
$N(SiMe_3)_3$	tris(trimethylsilyl)amine
$^{n}BuNP_1(tmg)_3$	(tert-butylimino)tris(tetramethylguanidine)phosphorane
$B(C_6F_5)_4$ or $BArF_{20}$	tetralos(pentafluorophenyl)borate anion
KC_8	potassium graphite
^{13}C	carbon-13 nuclear isotope
12-crown-4	1,4,7,10-tetraoxacyclododecane, $C_8H_{16}O_4$
^{19}F	fluorine-19 nuclear isotope
18-crown-6	1,4,7,10,13,16-hexaoxacyclooctadecane, $C_{12}H_{24}O_6$
^{31}P	phosphorous-31 nuclear isotope
$^{1}H\{^{31}P\}$	^{1}H NMR spectrum, ^{31}P decoupled

Chapter 1

Introduction

1.1 Small molecule reactivity and its relation to energy-rich molecules

A longstanding scientific challenge is the catalytic transformation of underutilized and abundant small molecules into useful and energy-rich feedstocks.[1-4] The impetus for this challenge stems directly from our societies ever-increasing demand for value-added energy-rich chemicals such as ammonia[5-6] (NH_3), hydrocarbon fuels[7-8] (C_nH_{2n+x}), and methanol[9-10] (CH_3OH). The importance of such chemicals is easily recognized when simply considering the scale in which they are produced annually as shown in Table 1.1

Table 1.1: Annual production of commodity chemical feedstocks

Process	Chemical Reaction(s)	Approx. production Mt/year(10^6 tons)
Fischer–Tropsch	$CH_4 + H_2O \rightarrow CO + 3H_2$ $(2n+1)H_2 + CO \rightarrow C_nH_{2n+2} + H_2O$	15*
Steam Reforming	$CH_4 + H_2O \rightarrow CO + 3H_2$ $CO + 2\ H_2 \rightarrow CH_3OH$	92
Haber–Bosch	$3H_2 + N_2 \rightarrow 2NH_3$	175

*Annual crude oil production exceeded 4.4 Gt in 2018 (10^9 tons)[7]

Future demand for these vital feedstocks is only anticipated to rise alongside exponential population growth and decreasing anthropogenic fuel availability.[11] Furthermore, our society's historical reliance on fossil fuels is strongly tied to the increasing levels of atmospheric CO_2, oceanic acidity, and rising average temperatures.[12] This environmental concern alone provides an urgent and timely basis for developing new catalysts to generate these energy-rich feedstocks from renewable energy sources (H_2O, $h\nu$, N_2, O_2, etc.).[13] Despite the abundance of precious metals for performing these processes, their long-term use is not sustainable due to a combination of low natural abundance and prohibitive cost. To supplant existing technologies, new catalysts must be

designed with earth abundant base metals (e.g., Ti, Fe, Co, Cu, Ni, etc.) for both sustainability and widespread proliferation.[14-15]

Understanding the intrinsic thermodynamics of reduction of these common feedstocks is vital for effective catalyst design. From this perspective, the transfer of multiple proton and electron equivalents (H^+/e^-) to small molecules such as N_2 and CO_2 is critical to lowering the energetic cost of their transformations. This is conveniently observed when comparing the change in standard electrochemical reduction potential (ΔE°) as a function of the number of proton/electron equivalents (H^+/e^-) added (Fig. 1.1). Carbon dioxide is quite difficult to reduce by direct electron transfer (E° = -1.9 V vs. SHE pH = 7).[16] Moreover, CO_2 also exhibits negligible acid/base behavior as evidenced by the highly unfavorable proton transfer to form the conjugate acid, CO_2H^+ (ΔG°_{H+} = 127 kcal/mol).[17] However, the simultaneous addition of H^+/e^- equivalents greatly reduces the energetic cost of the transformation, being nearly 1.5 V more favorable for the reduction of carbon dioxide to formic acid (HCO_2H). Further addition of multiple H^+/e^- equivalents makes subsequent transformations progressively more favorable for both methanol (ΔE° = 1.7 V) and methane (ΔE°= 1.9 V).[16] A similar trend is observable for the reduction of dinitrogen. The radical anion, $[N_2\bullet]^-$, is only reluctantly generated (est. E° = -4.2 V vs SHE pH = 7)[18], and the formation of the conjugate acid by proton transfer, N_2H^+, is likewise unfavorable (ΔG°_{H+} = 118 kcal/mol).[17] The addition of H^+/e^- equivalents greatly increase the ease of this reductive even as well, even when forming metastable molecules such as diazene (N_2H_2, $\Delta E^\circ \sim 2.5$ V) and hydrazine (N_2H_4, $\Delta E^\circ \sim 3.4$ V).[18]

Concerted transfer of multiple H^+/e^- equivalents to both CO_2 and N_2 decrease the unfavorable nature of their chemical reduction. This observation suggests that efficient

catalysts for conversions of these small molecules should take advantage of this principle. In practice, the development of such catalysts is by no means an easy task, especially considering the propensity of base metals to frequently engage in single electron transfer (e.g. $Co^{II/III}$, $Fe^{II/III}$).[19-20] Conversely, the widespread use of precious metals in catalytic transformations takes advantage of the more desirable two electron processes these metals frequently cycle between.[21]

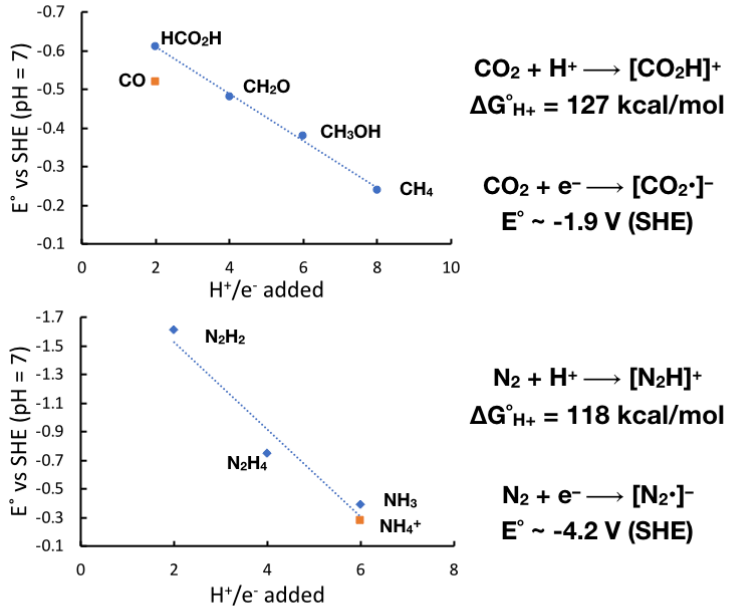

Figure 1.1: Plots showing the energetic bias developed from concerted H^+/e^- transfer to CO_2 (top) and N_2 (bottom) along with the product formed in each reaction. For comparison the estimated single electron transfer and proton transfer reactions are shown as well.

The development of catalytic processes that employ base metals to transform small molecules inherently involves the binding and activation of these ligands. Accordingly, the binding and activation of small molecules (such as H_2, N_2, and CO_2) at base metal centers remains a prominent field of challenging chemical research.[3, 22-33] While great strides have been made in past decades, large barriers remain. In particular, base metals typically exhibit weaker bonds to their ligands when compared to their 4d and 5d counterparts.[34] This

observation is a direct consequence of the nature of the 3d orbitals when compared to the diffuse 4d/5d orbitals.[35] Furthermore, the binding and activation of small molecules strongly relies on stabilization from π–backbonding interactions, which is also weaker for 3d metals for similar reasons. While the identity of the metal atom is certainly important, it is appreciated that supporting ligands play a large, perhaps even equal, role in promoting small molecule activation.[36] Over the years synthetic chemists have devised a number of clever methodologies to promote and participate in the activation of small molecules. Many of these strategies take inspiration or strongly parallel biological systems, whose enzymatic active sites frequently feature only base metals, and mediate a wide variety of difficult chemical transformations with high efficiency.

1.2 Biological design features for small molecule conversions

Despite the challenges inherent to transforming small molecules into useful feedstocks, nature has developed numerous mechanisms by which these processes may occur under ambient conditions with exquisite performance. Even more impressive is the abundance of base-metals in the active sites of these complex catalysts; which stems from their natural abundance and biological availability (e.g. Mn, Fe, Co, Ni, Cu).[14-15, 37-38] While nature has established a high benchmark for catalytic proficiency, it has also provided a detailed blueprint for how to design new catalysts for small molecule transformations. To elaborate on this notion, descriptions of the enzymatic systems of nitrogenase, photosystem II, and hydrogenase will be discussed in detail to draw attention to various design features synthetic chemists implement in the catalytic transformation of small molecules.

1.2.1 Nitrogenase: steric protection and multimetallic cooperativity

Amongst the most daunting chemical transformations is the conversion of dinitrogen to produce ammonia.[39-41] While thermodynamically reasonable, this reaction is kinetically difficult as a result of the highly inert character of the N–N triple bond ($\Delta H f_{298}$ = 225 kcal/mol).[42] Despite this challenge, ammonia is formed via the energy-intensive Haber-Bosch process which utilizes approximately 3% of annual global energy demands.[6, 41, 43] Conversely, nitrogenase enzymes are capable of performing this challenging transformation under ambient conditions (298K, 1 atm N_2) according to the general equation listed shown in Figure 1.2.[44] The active site of the most well-studied member of this remarkable enzyme family, iron-molybdenum nitrogenase, is composed of a unique Fe_8S_9 sulfur cluster containing an interstitial carbide and a capping molybdenum center (the FeMo cofactor).[44-45] It should be noted that despite the rarity of molybdenum in biological systems, it is not vital to the function of the FeMo nitrogenase enzyme. For example, all-iron (FeFe) and iron-vanadium (FeV) nitrogenase enzymes also exist naturally and mediate the reduction of N_2 to NH_3 as well. This observation suggests iron is the only metal needed to reduce N_2 to NH_3.[46-49]

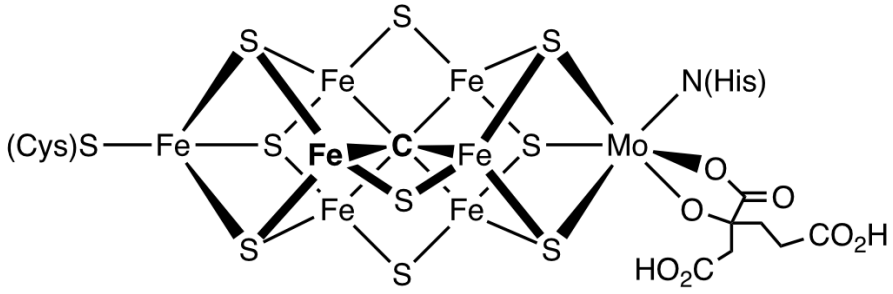

$$N_2 + 8H^+ + 8e^- + 16\ MgATP \longrightarrow 2NH_3 + H_2 + 16\ MgADP + 16P_i$$

Figure 1.2: The iron-molybdenum cofactor of nitrogenase, and the chemical reaction it mediates.

Utilizing the FeMo cofactor as the active site, the nitrogenase enzyme leverages the $8H^+/8e^-$ reduction of N_2 to produce NH_3 and H_2 with high efficiency from MgATP and H^+ (ATP = adenosine triphosphate, ADP = adenosine diphosphate). The architecture of the FeMo cofactor is vital to its efficiency and is showcased in the dinitrogen binding event. Current mechanistic studies support the notion that the FeMo cofactor undergoes four sequential H^+/e^- additions to generate the E_4 state, which has been termed the "Janus intermediate."[44, 46, 49] In the Janus intermediate proposal, the four H^+/e^- equivalents are stored in the form of two bridging hydride moieties (Fe(μ–H)Fe), and two protonated sulfide residues (Fe(μ-SH)$^+$Fe). When exposed to N_2 this state rapidly evolves H_2 with concomitant N_2 activation.[50] It is proposed that the N_2 unit is activated and then and protonated to give a diazene ligand which remains coordinated to the face of the cofactor for further reduction.[44, 51] The ability to store multiple H^+/e^- equivalents is a critical design principle that can be drawn from nitrogenase, and stems from the number of metal atoms in close proximity.[52] The large number of iron atoms in close proximity facilitates the distribution of electron density throughout the active-site (via covalent Fe-S linkages) to

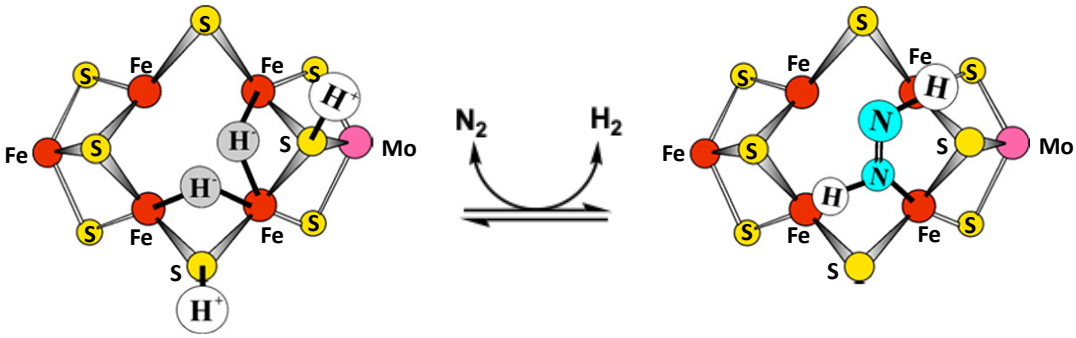

Figure 1.3: Elementary N_2 binding reaction of the FeMo cofactor via the Janus state. There are a variety of conformers possible for the E_4 states, not shown. Figure adapted from Reference 44. Only the Fe_4 belt is shown to emphasizes that the chemistry occurring on the face of the cluster.

create a network of structural and magnetic communication. Notably, the storage of the four H^+/e^- equivalents exceeds the limitations of mononuclear complexes, highlighting the importance of the multiplicity of metals atoms for this cooperativity to function.

Furthermore, the nitrogenase enzyme utilizes an elaborate protein architecture to protect the FeMo cofactor from external influence during this difficult transformation. Indeed it is common to observe enzymatic active sites buried deep within the tertiary structure of an enzyme, albeit there are many examples to the contrary as well (for example in lytic polysaccharide monooxygenase, LPMO).[53-55] While synthetic chemists typically utilize simple organic ligands containing bulky functionalities (^{t}Bu, ^{i}Pr, etc.) to protect metal centers, enzymatic systems protect their active sites with their tertiary protein structure. This concept is conveniently showcased by the residence of the FeMo cofactor within the nitrogenase enzyme, which is buried in a hydrophobic pocket approximately 10-20 Å from the surface of the FeMo subunit.[56]

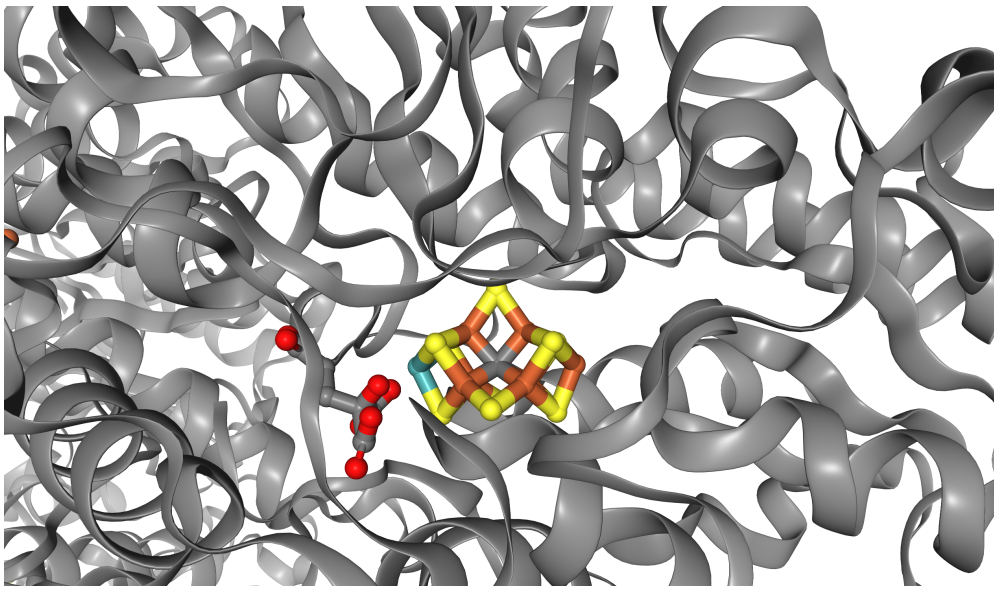

Figure 1.4: The tertiary protein architecture of nitrogenase protects the FeMo cofactor from foreign ligation. Image generated utilizing PBD structure viewer (Dataset: 4WES 1.06 Å resolution).

1.2.2 Photosystem II: multimetallic and metal-Lewis acid cooperativity

A similarly complex enzymatic system is found in the oxygen-evolving complex (OEC) of photosystem II (PSII).[57] The OEC active site is directly responsible for the oxidation of water to generate oxygen, protons, and electrons (Fig 1.5). Similar to the FeMo cofactor, the active site of OEC contains multiple metal centers working in close proximity to facilitate electron transfer. However, OEC is an oxidase and thus the Mn centers must undergo sequential oxidations (generating electron holes) rather than multiple reductions via electron transfer. The OEC is believed to mediate water oxidation by first undergoing four sequential single-electron oxidations to generate a highly oxidized $[Mn_4O_5Ca]^{n+4}$ cluster containing only high-valent manganese (e.g Mn^{IV}).[58-60] This oxidized cluster then binds and activates H_2O, to produce $2H^+$ and O_2. The ability of the $[Mn_4O_5Ca]$ cluster to stabilize the sequentially more oxidized states is believed to be a key design feature that is engendered by the presence of the Lewis-acidic Ca^{2+} moiety. For example, if the Ca^{2+} atom

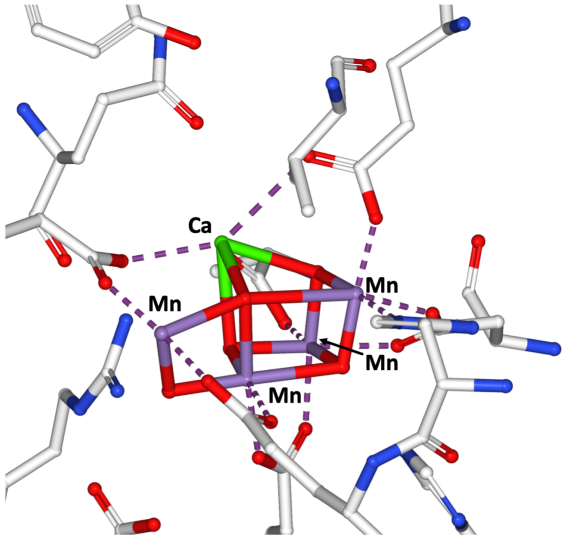

Figure 1.5: Active site of the OEC in PSII. Image generated utilizing PDB structure viewer (Dataset 3WU2 resolution = 1.9Å).

is replaced by any other atom, the catalytic performance decreases dramatically (M= Sr^{2+}) or ceases altogether (any other M ion). Thus, a reasonable design feature that one might infer is that redox-inactive metals (e.g. Ca^{2+}, Sr^{2+}) can be utilized cooperatively to electronically tune metal centers and clusters for desired reactivity.[61-64] Recent model complexes have shed further light on the specific role of these Lewis-acidic heteroatoms in multinuclear clusters (*vide infra*).[65-67]

1.2.3 Hydrogenase: metal-ligand and metal-Lewis acid cooperativity

Cooperative effects are also key to the chemistry of hydrogenase enzymes, which are responsible for the reversible reduction of H^+ to form H_2.[53] Hydrogenase enzymes have attracted a great deal of research interests as they produce H_2 with ease (a potential ecologically friendly fuel) and almost exclusively utilize base metals in their active sites.[68-71] Amongst hydrogenase enzymes, the mechanism of action for nickel-iron (NiFe) and diiron (FeFe) hydrogenases are amongst the most well studied. The active site of NiFe-hydrogenase contains nickel and iron in close proximity supported by cysteine (Ni) and CN/CO ligands (Fe). The mechanism of NiFe-hydrogenase directly highlights a number of small molecule reaction motifs such as bimetallic cooperativity and metal-ligand cooperativity (Fig 1.6).

It is believed that the activation of dihydrogen occurs in the reduced Ni-SI_a state via a non-classical nickel dihydrogen complex (T.S. in Fig. 1.6). Noteworthy, is the presence of a short Ni•••Fe interaction (ca. 2.5 Å) which may play a role in H_2 activation and/or coordinative stabilization.[52, 72] After coordinating to nickel, the H_2 ligand is cooperatively cleaved by the Lewis-acidic Fe^{II} center and Brønsted basic Ni–cysteine residue.[68, 73-75] The proton and hydride fragments of this formal heterolysis reaction are

respectively stabilized as thiolate (SH^+) or bridging hydride fragments (Ni(μ-H)Fe) in the reduced Ni-R state. This role of the coordinated base (Ni-SCys) has been recognized as a strong motif for direct metal-ligand cooperativity and has found use in homogeneous systems.[76-84] Furthermore, the proximal Lewis-acidic iron stabilizes both the putative Ni(η^2–H_2) species and the subsequently generated H^- ligand, providing a unique snapshot of bimetallic cooperativity.[75] The Ni-R state undergoes oxidation to generate the oxidized Ni^{III}(μ–H)Fe^{II} state (Ni–C) which is also cooperatively stabilized by the presence of the Lewis-acidic iron center. Further oxidation of Ni-C results in the reformation of Ni-SI_a and evolution of H^+. It should be noted that throughout the entire catalytic cycle the iron center remains divalent, acting as a redox innocent Lewis-acid to support the Ni-mediated transformations both electrostatically (e.g Ni•••Fe proximity in SI_a) and through direct cooperation (via Ni(H_2)•••Fe).[53]

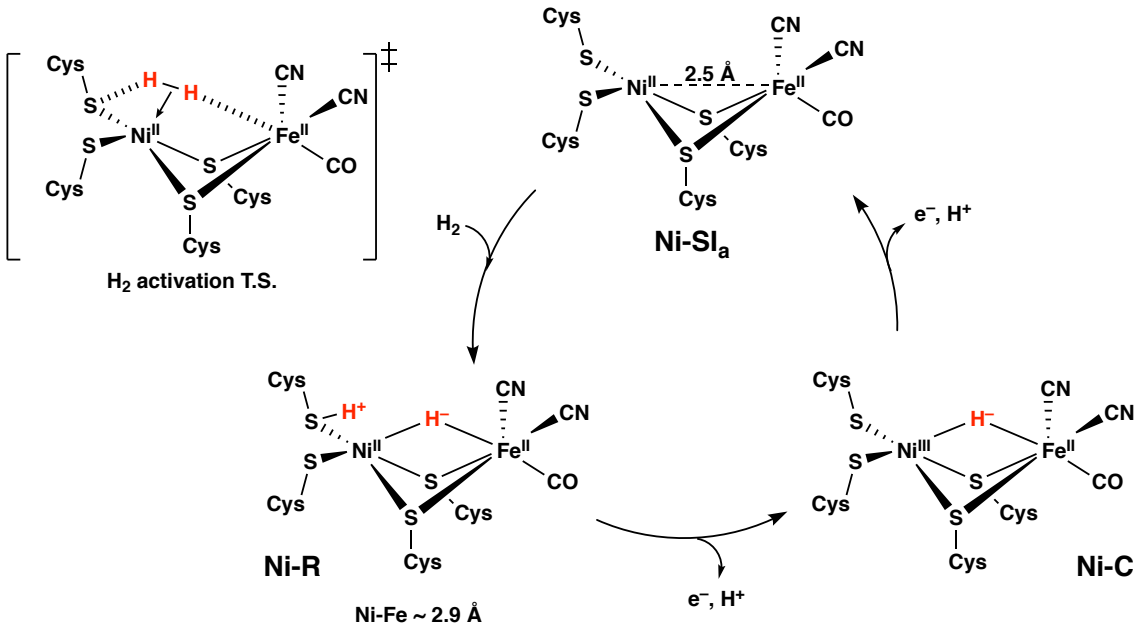

Figure 1.6: Proposed mechanism of H_2 oxidation mediated by NiFe-hydrogenase.

Hydrogenase enzymes also utilize their secondary coordination spheres to mediate difficult transformations as well.[54, 85-86] This is showcased in the H_2 cleavage mediated by FeFe-hydrogenase which likewise catalyzes the reduction of H_2 to protons and electrons. An important difference between these two enzymes is the composition of their active sites which differ by the presence of a second iron atom (rather than Ni) and a bridging dithio-amino group (Fig. 1.7). It is believed that the presence of a basic amino group in the secondary coordination sphere of FeFe-hydrogenase facilitates the deprotonation of H_2 by acting as a kinetically accessible and strong base.[87] Similar to NiFe-hydrogenase, an interaction between the two metal centers (here $Fe^{II}Fe^{I}$) is believed to be important in stabilizing the reduced states within the catalytic cycle.[52-53]

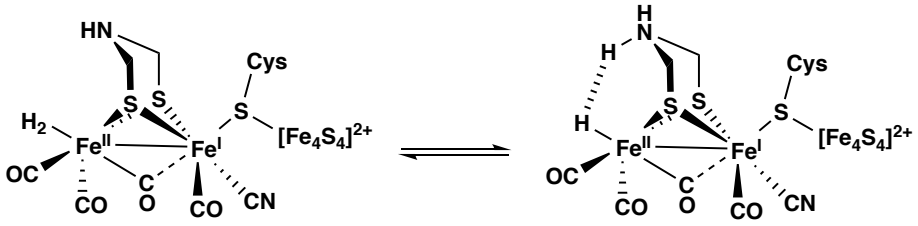

Figure 1.7: Active site of FeFe-hydrogenase reversible activates H_2 via a secondary coordination sphere interaction cooperativity.

1.3 Parallel designs in enzymatic and homogeneous systems

Synthetic chemists have long sought to capture the design implements of biological systems in hopes of emulating their catalytic performance. Many of these strategies can be generally grouped into those that promote coordinative unsaturation, metal-ligand cooperativity, and multimetallic cooperativity (including Lewis acids). To a large extent, the principle interactions present in many biological systems have been implemented into synthetic mimics. The following sections detail select examples that aim to draw parallels

between observations made in biological and those implemented within homogeneous systems.

1.3.1 Steric protection and coordinative unsaturation

The strategy of steric protection takes advantage of the inherent size of small molecules to generate selectivity in their reactions with coordinatively unsaturated centers. Unsaturated metal centers frequently bind small molecules due to the energetic stabilization that is gained from the formation of a new, frequently noble, electron configuration (e.g. 18/16e$^-$).[88-89] In biological systems, this protection is achieved with ornate tertiary structure, but synthetic chemists are often limited to the installation of large bulky groups to promote unsaturation (examples include 2,6-di-isopropyl-phenyl, ^{t}Bu, Cy, etc.).

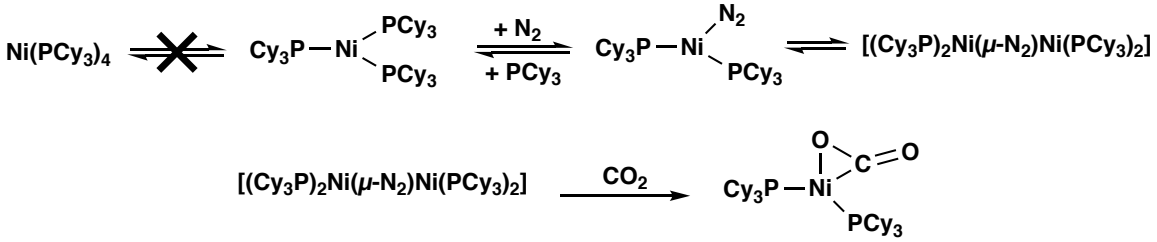

Figure 1.8: Synthesis of bridging nickel dinitrogen complex, $[(Cy_3P)_2Ni(\mu\text{-}N_2)Ni(PCy_3)_2]$ which permits for the isolation of the first η^2–CO_2 complex.

The power of coordinative unsaturation is conveniently demonstrated by the isolation of the first side-on carbon dioxide complex, $(Cy_3P)_2Ni(\eta^2\text{-}CO_2)$, as reported by Aresta *et al.*[90-91] Preceding the isolation of $(Cy_3P)_2Ni(\eta^2\text{-}CO_2)$, came the observation that the large steric bulk of the tri-cyclohexyl-phosphine (PCy_3) ligand inhibits the formation of the 18e$^-$ complex, $(Cy_3P)_4Ni$. Rather, the bulk of PCy_3 leads to the formation of its 16e$^-$ analog, $(Cy_3P)_3Ni$.[92] The trigonal species $(Cy_3P)_3Ni$ is itself a reactive molecule and can bind N_2 (identified by IR).[92] Ultimately, a PCy_3 ligand is dissociated and trapped in the

form an N_2 sandwich complex, $[(Cy_3P)_2Ni(\mu\text{-}N_2)Ni(PCy_3)_2]$.[92] The unsaturation engendered by the bulky PCy_3 ligand leads to preferential displacement for the small N_2 molecule. The coordinated N_2 ligand is quite labile and is readily displaced by CO_2 to generate Aresta's complex. This species, $(Cy_3P)_2Ni(\eta^2\text{-}CO_2)$, was the first crystallographically characterized example of CO_2 bound side on (η^2) to a metal center.

The use of steric protection to engender small molecule reactivity is also apparent in the cleavage of N_2 by a molybdenum-tris(amido) complex reported by Cummins *et al.*[93-94] In this example, the use of an exceedingly bulky amido ligand (^{t}BuNXyl, Xyl = 3,5-dimethyl-phenyl) allowed for the isolation of the three-coordinate species, $Mo(N^tBuXyl)_3$ (notably isolobal to atomic N). After $Mo(N^tBuXyl)_3$ binds N_2, it dimerizes to form a sandwich complex, and ultimately extrudes two equivalents of $N{\equiv}Mo(N^tBuXyl)_3$ forming a molybdenum-nitrogen triple bond (Fig. 1.19). This remarkable reaction was the first where a molecular species mediates the concerted cleavage of the N_2 triple bond. These examples highlight the utility and simplicity of steric protection in generating coordinatively unsaturated metal centers that promote small molecule binding.

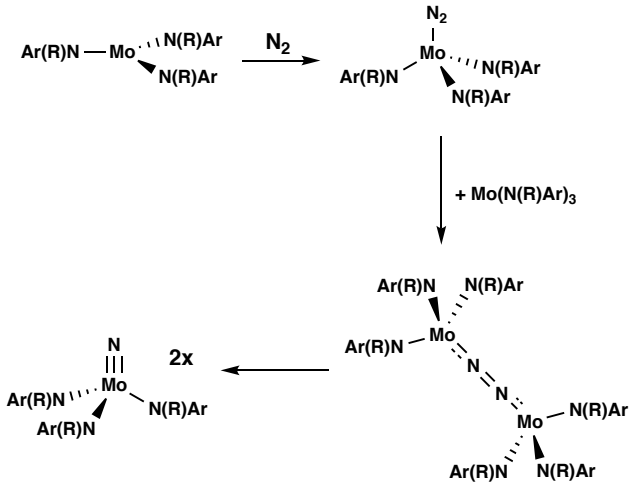

Figure 1.9: Chemical splitting of N_2 mediated by $Mo(N(R)Ar)_3$ (R = ^{t}Bu and Ar = 3,5-dimethylphenyl).

1.3.2 Metal-ligand cooperativity in primary coordination spheres

Metal-ligand bonds can also directly participate in the activation of small molecules. This strategy draws parallels to our understanding of ligand non-innocence in biological systems, such as those observed in hydrogenase enzymes. Worth noting is that ligands may also facilitate reactivity via redox activity in their π manifolds, though this concept is beyond the scope of this work and has been comprehensively reviewed.[95]

The strategy of incorporating a strong Brønsted base in the primary coordination sphere has been widely employed to activate small molecules, especially those that are modestly acidic or polarized. For example, the seminal contribution from Caulton *et al.* reported the reaction of an unsaturated Ni^{II} cation supported by a PNP pincer ligand with a strongly basic amido ligand (R_2N^-).[96] This complexes quickly binds and splits H_2 to yield a terminal hydride with concomitant protonation of the amido group. This strategy is also effective in promoting the activation of other organic functionalizes including acetylides (H-CCAr) and thiols (H-SR) as demonstrated by Ozerov.[97]

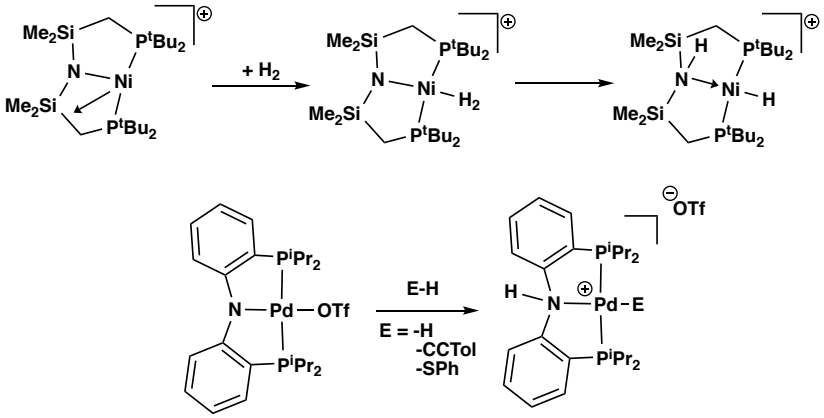

Figure 1.10: Select examples of coordinate bases working cooperatively in molecular scaffolds.

The notion a proximal base can facilitate small molecule transformations has wide-reaching catalytical ramifications. In one example, Schneider has examined the acceptor-less dehydrogenation of alcohols to ketone catalyzed by an iron pincer complex.[98] In this example, a basic iron-amido unit is involved in the reversible activation of H_2 to form an iron-amino complex. Furthermore, the five-coordinate iron-amido species is believed to cooperatively activate alcohols via a concerted transition state in which partial N-H and Fe-H bonds have formed (DFT calculated TS, Fig. 1.11). This type of concerted bond activation occurring through a coordinating ligand in the primary coordination sphere is broadly applicable, as recently reviewed by Milstein.[76]

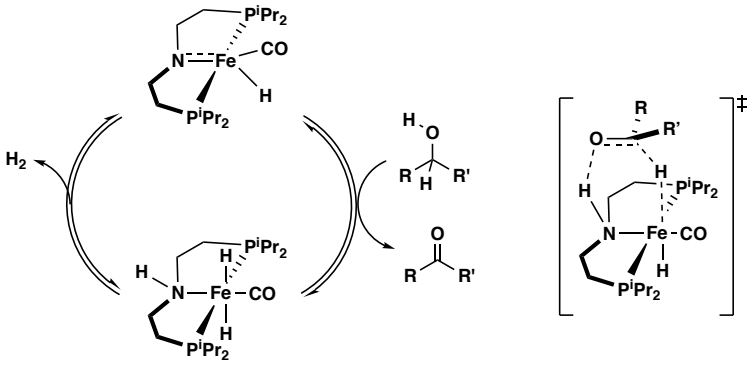

Figure 1.11: Iron mediated acceptor-less dehydrogenation of alcohols to ketones. Left, proposed mechanism. Right, proposed concerted substrate activation.

1.3.3 Metal-ligand cooperativity in secondary coordination spheres

Ligands can also be installed in the secondary coordination sphere of a metal complex to facilitate the activation of small molecules. This strategy has strong biological parallels. For example, FeFe-hydrogenase utilizes a tertiary amine as an external base to deprotonate the H_2 moiety.

Similar strategies have been incorporated into homogeneous systems and are exemplified by the pioneering work of Bullock and Dubois in synthetic hydrogenase mimics.[73, 81, 99-100] Taking direct inspiration from nature, new electrocatalysts were developed with pendant amines to act as proton shuttles in the electrochemical reduction of H^+ to H_2. In a feat of impressive ligand design and reaction engineering, the current state-of-the-art catalysts for the hydrogen evolution reaction, $[Ni(P^{Ph}_2N^{Ph})_2]^{2+}$, (see Fig. 1.12, left) exhibits a turnover frequency (TOF) exceeding 100,000 s^{-1} under ambient conditions.[101] The impressive TOFs of these synthetic hydrogenases even exceeds those observed for some hydrogenase enzymes (TOF ~ 9000 s^{-1}). Though for fair comparison the TOF of these synthetic hydrogenases should be examined with some scrutiny. The overpotential needed for synthetic mimics to operate is quite large (ca. 300-600 mV) when compared to enzymatic systems (<100mv).

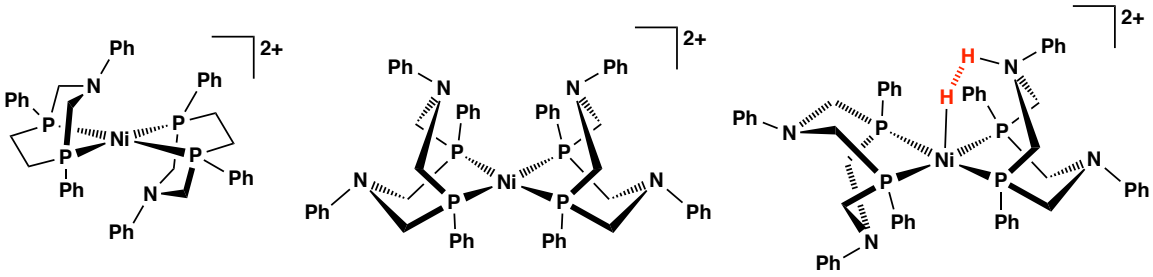

Figure 1.12: Left and center, catalysts for the electrochemical reduction of H^+. Right transition state that is believed to lead to H_2 evolution facilitated by pendant amines.

1.3.4 Multimetallic cooperativity

Another pervasive theme that synthetic chemists have attempted to incorporate into homogeneous systems is multimetallic cooperativity in hopes of achieving multiple-electron transfer reactivity. Importantly, the presence of multiple metal atoms in close proximity, either directly bonded or in a cluster, permits electronic communication that

frequently facilitates redox chemistry.[52, 102] These motifs are reminiscent of the active sites of PSII and FeMo nitrogenase.

Despite the prevalence of multimetallic clusters in biological systems, only two centers are needed to exhibit cooperative chemistry. This concept is elegantly showcased in recent reports from Uyeda *et al.*, where a dinickel species, (NDI)Ni_2, has been shown to traverse multiple electron transformations.[103] The multiple electron chemistry of (NDI)Ni_2 is attributed to the presence of the Ni-Ni bond and supporting ligand framework. Notably, the number of electrochemical transitions observed for (NDI)Ni_2 exceeds the number typically observed for mononuclear nickel species in similar scaffolds (Fig 1.13). Furthermore, the ability of this Ni_2 core to mediate multiple electron transformations is key in stabilizing binuclear oxidative addition products, where a C-X bond can be added across the Ni-Ni unit. This oxidative reactivity is vital to mediate the difficult [4+1] cycloaddition of a dienophile and carbene source.[104] Remarkably, $(NDI)_2Ni$ is capable of mediating the

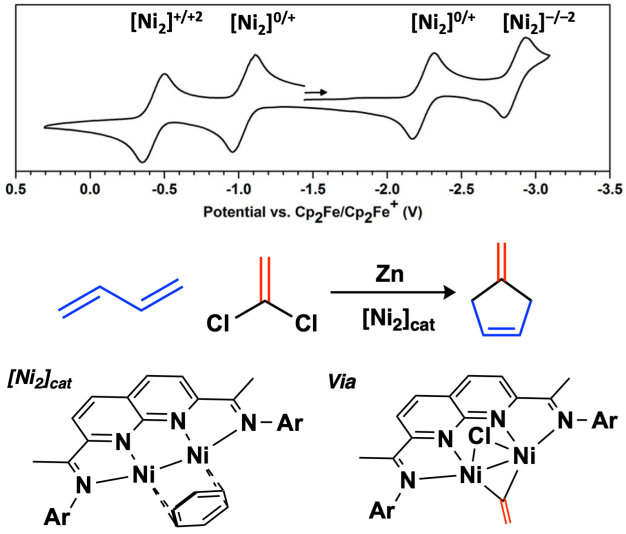

Figure 1.13: Left, $(NDI)_2NI$ mediates the reduction [4+1] cycloaddition of a dichloroalkene and dienophile. Right, cyclic voltammogram of $(NDI)_2NI$. Adapted from reference 103.

[4+1] addition of carbene sources with a wide variety of dienophiles, offering an improved route to substituted methylenecyclopentenes.

Another example of cooperativity between two transition metal centers comes from Thomas *et al.* who have described the addition of CO_2 to a CoZr bimetallic complex. In this near idyllic example, the carbon-oxygen bond in CO_2 in cleaved by electron transfer from a formal ZrCo triple bond, generating a Zr(μ-O)Co(CO) species (Fig. 1.14).[105] The ability of this early/late heterobimetallic species to elegantly traverse the two-electron reduction of CO_2 is attributed to the reduced $Zr^{IV}Co^{-I}$ redox state, the flexibility of the supporting amido/phosphine ligands, and the oxophilic nature of Zr.[106-107] Noteworthy is that these two metal centers work in concert to directly stabilize the Zr(μ–O)Co motif, which itself can be further functionalized. For example, the Zr(μ–O)Co species can be further reduced and reacted with CO_2 to generate a CoZr(CO_3^{2-}) complex. Further studies on this ZrCo species, and others, have provided a wealth of unique reactivity originating from a bimetallic core.[107-109]

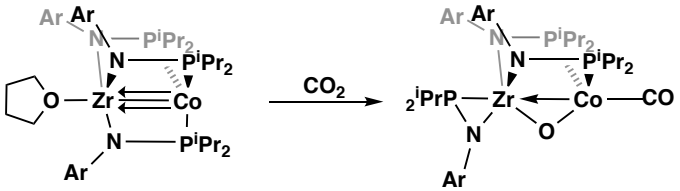

Figure 1.14: Cooperative CO_2 cleavage by a bimetallic ZrCo complex.

Despite their synthetic complexity, multimetallic synthetic clusters also facilitate multiple electron transfer and reactivity. For example, Betley *et al.* have reported that the presence of multiple iron-iron interactions in synthetic clusters, $Fe_6(L)_6(^{H}L)_2$, leads to rich electrochemistry and small molecule reactivity (where $^{H}L = MeC(CH_2NHPh\text{-}o\text{-}NH_2)_3$).[110] When ligated by cyanide ($L = CN^-$) or solvated by DMF (L = DMF) these clusters reveal that multiple metal centers facilitate both electronic communications and rich redox

activity (Fig. 1.15).[111] In particular, the observation of a simple doublet in the ^{57}Fe Mössbauer spectra of these clusters, independent of ligation or charge, indicates that the rate of electronic delocalization of the Fe_6 cluster occurs at rates exceeding the nuclear relaxation of ^{57}Fe nucleus (ca. 10^{-7} s^{-1}). Furthermore, these clusters exhibit large comproportionation constants, K_c, with values spanning from 10^3 (L = DMF) to 10^{21} (L = CN^-) that indicate a strongly coupled and delocalized Fe_6 octahedron.[111] Even more remarkable is that this scaffold can support the reduction of six equivalents of nitrate (NO_2^-) to nitric oxide (NO) utilizing only a weak acid (benzoic acid, $PhCO_2H$).[112] Related are trinuclear systems in a similar ligand framework that exhibit multicentered small molecule reactivity.[113-114]

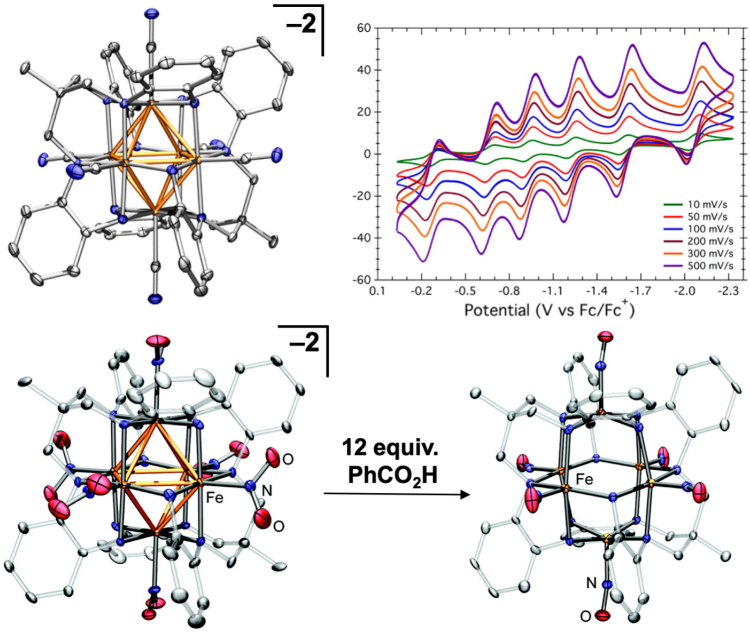

Figure 1.15: Top left, molecular structure of $[Bu_4N]_2[Fe_6(CN)_6(^HL)_2]$. Top right, variable scan rate cyclic voltammetry studies. Bottom, reduction of NO_2^- to NO mediated by the Fe_6 cluster. Figures adapted from references 111 and 112.

Multiple metal centers can also be utilized to achieve coordination environments not feasible in mononuclear systems. For example, Murray *et al.* have reported that a tris(ß-

diketiminate)cyclophane ligand is capable of supporting trinuclear complexes of a variety of base-metal complexes.[115-116] A particularly unique example is the use of this ligand to support a trinuclear copper complex which reversibly binds dinitrogen.[117] Notably, only one other example of a well-characterized Cu(N_2) complex exists. Moreover, the only additional evidence for the existence of such species has comes from cryogenic gas matrix studies.[118] Related iron and cobalt complexes have also revealed rich coordination chemistry involving small molecules such as N_2, CO_2, and olefins.[119]

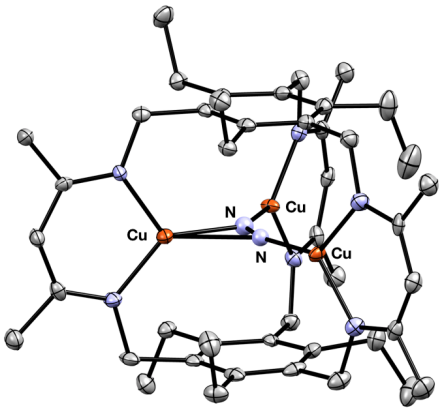

Figure 1.16: Trinuclear $Cu_3(\mu\text{-}\eta^1\text{:}\mu\text{-}\eta^2)$ species reported by Murray *et al.* Structure rendered at 50% thermal ellipsoid probability with hydrogen atoms and solvent molecules omitted for clarity. Due to disorder of the N_2 ligand, anisotropic displacement factors were not utilized.

1.3.5 Cooperativity from indirect Lewis acidic interactions

The use of Lewis acids to promote small molecule reactivity, or to activate substrates for further activation, is a strategy that has gained significant research interest in recent years. Lewis acids frequently alter the mechanisms of chemical reactions and are typically observed to do so via induction and/or direct participation.[120-123] As previously discussed, this is a strategy noted in enzymatic systems such as PSII and NiFe-hydrogenase.

Synthetic systems have made significant strides in incorporating Lewis acids to electronically tune metal centers. A preeminent example comes from Agapie *et al.* where a series of heterometallic Lewis acid/manganese clusters, $[Mn_3O_4M]^{n+}$, were synthesized and mimic the core structure of PSII (Fig. 1.17, M = Na^+, Sr^{2+}, Ca^{2+}, Zn^{2+}, Y^{3+}).[66] Varying the identity of the redox-inactive Lewis acid modulates the electrochemical reduction potential ($E_{1/2}$) over a range exceeding 1V (vs. Fc/Fc^+ Fig. 1.17). Furthermore, the reduction potentials of these synthetic clusters correlate well with the pK_a of the M-H_2O complex, which is a common proxy for the Lewis acidity of a metal atom in aqueous media.[124] Collectively these results suggest that appropriate Lewis acidity of the heteroatom of the $[Mn_4O_5M]$ cluster of PSII is key to electronically modify and stabilize the highly oxidized intermediates. As discussed previously, the identity of Ca^{2+} in PSII has been shown to be key to its reactivity.[63-64, 125] The studies reported by Agapie indicate that the large, and electropositive, calcium ion modulates the electrochemical nature of the cluster by virtue of its Lewis acidity via the Ca(μ-O)Mn linkages of the cluster.

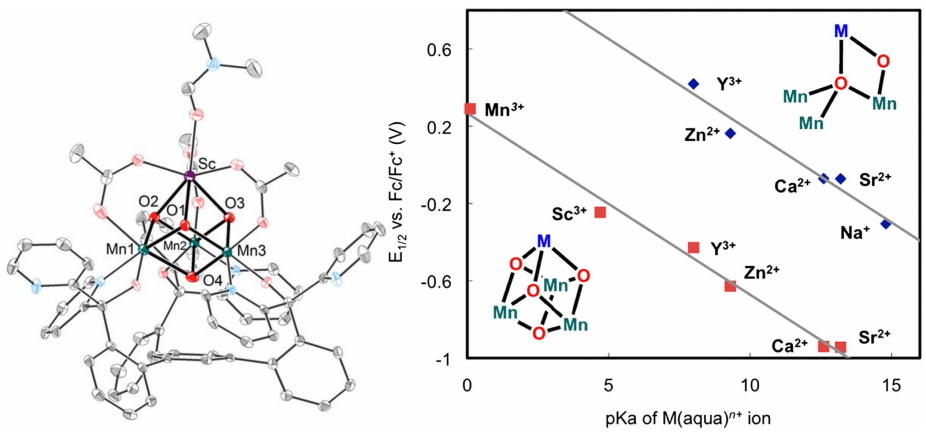

Figure 1.17: Left, molecular structure of OEC mimic, $[Mn_3O_4Sc]$. Right, correlation between the metal-aquo pK_a of Lewis-acidic heteroatom in $[Mn_3O_4M]^{n+}$ and the electrochemical reduction potential of the cluster. Figure adapted from references 65 and 66.

1.3.6 Cooperativity from direct Lewis acid interactions

Lewis acids also play an important role in promoting reactions via direct interactions.[30, 120-121, 123] Examples of these motifs span all areas of chemistry from simple reactions such as the Friedel-Craft alkylation[126] ($AlCl_3$) to biomimetic iron oxidase model complexes ($Fe(O_2)$•••Sc^{3+}).[127] Sophisticated Lewis acids have emerged in recent years and have been shown to cooperatively promote the cleavage and activation of small molecules and even metal-ligand bonds. Despite not featuring a transition metal, the chemistry of tris(pentafluorophenyl)borane is demonstrative of these concepts in the context of both polymerization and frustrated Lewis-pair chemistries.[128-130]

The Lewis acidic properties of tris(pentafluorophenyl)borane were first realized as a promoter in the polymerization of olefins mediated by Ziegler-Natta catalysts (e.g. Cp_2ZrX^+). Polymerization reaction promoted with tris(pentafluorophenyl)borane were shown to produce long-lived catalysts with increased catalytic activity.[131-132] Later studies would reveal tris(pentafluorophenyl)borane can abstract a methyl ligand from Cp_2ZrMe_2 to produce catalytically robust $[Cp_2ZrMe][MeB(C_6F_5)_3]$.[133] The Lewis acidity of tris(pentafluorophenyl)borane was later utilized in the cleavage of H_2 by its "frustrated," Lewis pair with tri-tertbutyl-phosphine (e.g. FLP).[134-136] Here the steric bulk of a large

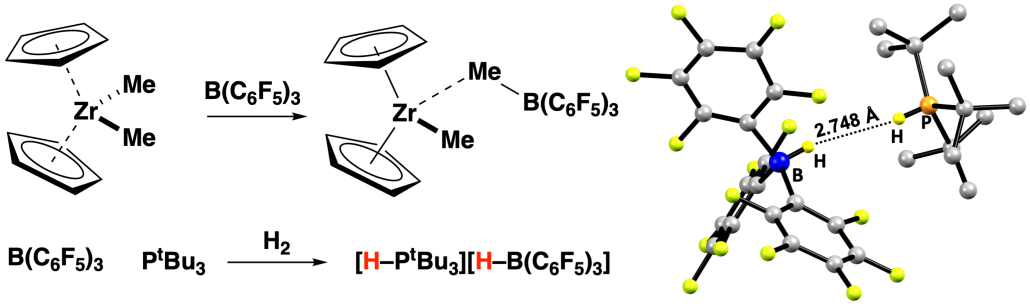

Figure 1.18: Left, cooperative activation utilizing $B(C_6F_5)_3$. Right, molecular structure (Ball and stick model) of the H_2 cleavage product $[HP^tBu_3][HB(C_6F_5)]$.

phosphine and the potent Lewis acidity of tris(pentafluorophenyl)borane work in concert to reversibly cleave the strong bond of H_2 without utilizing a transition metal (Fig 1.18). The Lewis acidity of tris(pentafluorophenyl)borane is attributed to its electron deficient boron center and strongly electron withdrawing pentafluorophenyl groups.[129]

The principles of frustrated Lewis pair chemistry have enjoyed success for small molecule activation when incorporated into synthetic systems that feature low-valent transition metals.[120] These systems typically contain a transition metal directly bonded to an electron deficient main group atom such as those encountered in group 13 and occasionally the heavier group 15 elements (Sb and Bi).[137-146] In contrast to traditional dative bonds (e.g. L→M), the polarity of the metal–ligand bond in these complexes is inverted (M→L) and hence they are named Z-type ligands.

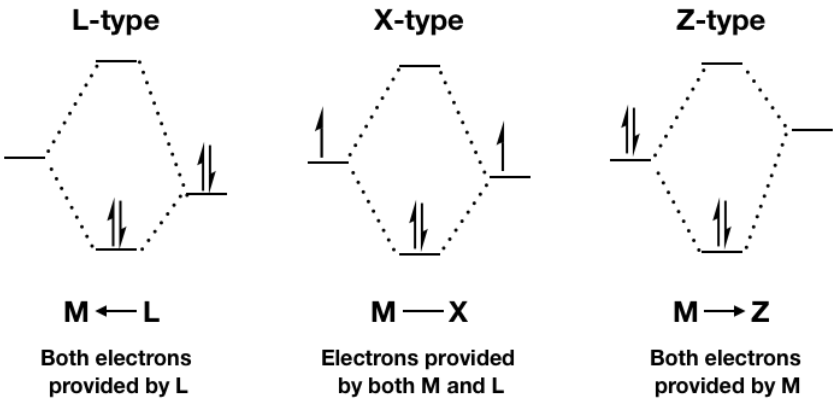

Figure 1.19: Bonding motifs for L, X, and Z-type ligands.

Importantly, the bonding electrons must arise from the transition metal center, and thus Z-type ligands make metal centers more electron poor and enhance their electrophilic character. This bonding scenario is graphically displayed in the Fig 1.19.[147] Many have recognized that Z-type ligands engender a continuum of oxidative character, and thus one can envision two bonding extremes where the metal center is oxidized by two full electrons

(e.g. M^{n+2}) or where the dative bond only induces charge delocalization (e.g. M^{n}).[141] Realistically most M→Z bonds are intermediate within these extremes. Indirect metal-Lewis acid interactions have proven to be a strong tool to modulate the electronic structure of PSII and corresponding model complexes. One might suspect that direct Lewis acid-metal interactions may be a similarly powerful tool for the synthetic chemist to electronically tune transition metal centers for optimal reactivity.

Regardless of their bonding formalisms, Z-type ligands have emerged as strong promoters of small molecule reactivity. A demonstrative example is the oxidative addition of H_2 across the Ni→B bond of (^{iPr}DPB^{Mes})Ni.[140, 148] This example showcases the prominence of boron in Z-type bonding, the enhanced electrophilicity that the Z-type bonding interaction confers, and their potential catalytic use. The species (^{iPr}DPB^{Mes})Ni is formed by the reduction of divalent nickel precursors in the presence of the preformed amphiphilic ligand ^{iPr}DPB^{Mes} (di(o-diisopropyl-phosphinophenyl)-mesitylborane). This ligand allows for the isolation of a coordinatively unsaturated Ni^0 complex supported by the two phosphine ligands as well as a persistent Ni→Arene interaction. When exposed to H_2, (^{iPr}DBP^{Mes})Ni rapidly forms a rare nickel-dihydrogen complex, (^{iPr}DBP^{Mes})Ni(η^2-H_2), which slowly undergoes oxidative addition to generate a Ni^{II} supported borohydride. In a

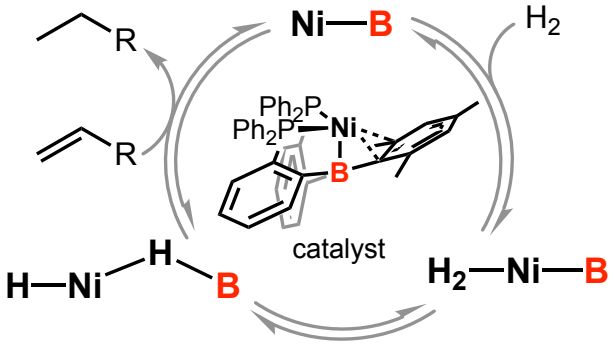

Figure 1.20: H_2 addition across a Ni→B bond allows for hydrogenation of olefins.

ligand variant where the supporting phosphine ligands contain phenyl groups, the resultant oxidative product HNi(μ-H)B, is intercepted by olefins to regenerate the pre-catalyst.

Intriguingly, (^{iPr}TPB^{Mes})Ni is an archetype for direct Lewis acid-metal species as a whole. The overwhelming majority of complexes that feature a M→Z interaction utilize boron, a consequence of the difficulty in synthesizing heavier group 13 analogs. Indeed, many M→B bonds are also formed via B-H activation process of borates and low-valent metal centers.[121] Furthermore, a large section of this class of complexes utilize pre-formed amphiphilic ligands that feature a Lewis acid acceptor (Z-type) alongside other supporting ligands (X or L).[149] The lack of diversity in this class is inherently tied to the weaker bonds in the main group elements, which decreases moving down each respective group.[150] Despite these challenges, many groups have utilized Z-type ligands to stoichiometrically and catalytically activate a variety of small molecules. Interest in M→Z interactions in both catalysis and stoichiometric activity has increased dramatically in recent history[77, 151-173], and reviews detailing the unique chemistry of these complex have also emerged. [120, 149, 166]

1.4 Relating metal-metal bonds and Lewis-acidic metalloligands

Enzymatic active sites utilize a large suite of strategies to promote the binding and activation of small molecules. Among others, one observation that appears fairly widespread throughout biology is the use of multiple metal centers to promote the transfer of multiple H^+/e^- equivalents simultaneously (see FeMo cofactor or OEC). Synthetic analogs of these systems remain very difficult to study, no doubt due to their inherent complexity, which evolves over millennia in biological systems. To better understand how two metal centers may act in concert to promote the binding of small molecules, the Lu

group has developed a number of ligand scaffolds that promote the formation of metal-metal bonds.[174] In particular, we have sought to systematically examine how two or more metal centers may act cooperatively to effect the transformations of small molecules.[102, 175]

Early studies in metal-metal bonding focused on the attractive goal of utilizing multiple metal-metal bonds as electron reservoirs for small molecule reactivity. The attractiveness of this scenario is evident when considering a hypothetical reaction between a generic MM triple bond and N_2 to generate a metal-nitride (eg. M≡M + ½ N_2 → MM≡N). To this end, our lab has used a tris(amido)phosphine ligand (H_3L) for the stepwise and rational synthesis of bimetallic complexes that feature unprecedented metal-metal bonding configurations in homo and heterobimetallic species. Notably, this framework is highly flexible and supports a variety of heterometallic complexes with intermetallic distances that span 1 Å (100 pm).[174, 176-177]

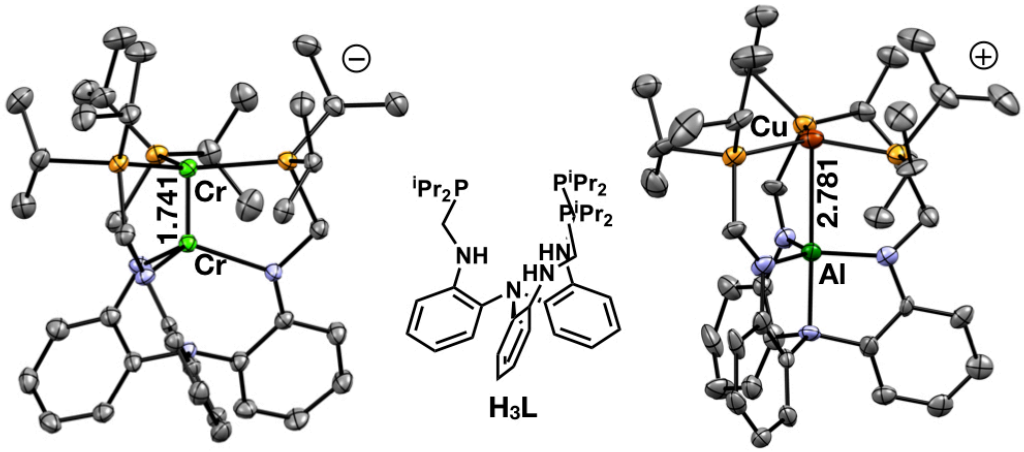

Figure 1.21: Figure showing the large degree of flexibility in the H_3L ligand framework. On the left, $[CrCrL]^-$ and on the right $[CuAlL]^+$. Both structures are rendered at 50% thermal ellipsoid probability and hydrogen atoms, counter ions, and solvent molecules are omitted for clarity.

Studies regarding metal-metal multiple bonds in the H_3L framework rapidly uncovered a large stabilization inherent to multiple order metal-metal bonds. The only first-

row heterobimetallic complexes supported by the H_3L^{iPr} ligand framework that engage in small molecule reactivity are those in which a low-valent cobalt center is supported by vanadium (CoVL), chromium (CoCrL), or an additional cobalt atom (Co_2L).[178-179] Notably, CoCrL and CoVL both exhibit polarized metal-metal bonds that enable the formation of a d^{10} Co^{-I} state. The π-basicity of this highly reduced state is key in the formation of end-on dinitrogen complexes, $[(N_2)CoML]^-$.[180] The dicobalt analog, Co_2L, features an energetically matched Co–Co single bond and behaves similarly due to its overall electron count. When reduced, Co_2L forms an analogous dinitrogen complex $[(N_2)Co_2L]^-$, but the phosphine supported cobalt center retains a formal Co^0 oxidation state as a consequence of a high-spin supporting Co^{II} center. The flexibility of the Co-Co bond and a propensity to bind N_2 when reduced are believed to be key features in the catalytic reduction of N_2 to $N(SiMe_3)_3$.[179]

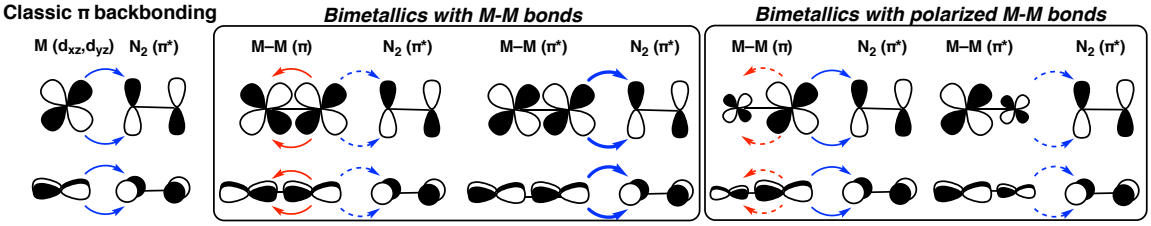

Figure 1.22: Molecular orbital depiction of how the identity of a supporting metal modulates the electronic structure and N_2 activation of the M-M(N_2) motif.

Comprehensive electronic structure studies on the $[(N_2)MML]^-$ complexes allowed for detailed investigations on how the MM pair modulates N_2 activation.[175, 180] Surprisingly, the use of a second transition metal is counterproductive to small molecule activation. This is most clearly illustrated when examining the π-bonding interaction between N_2 and the $[MML]^-$ fragments. Here, the presence of a supporting transition metal competes with N_2 for electron density and disturbs the traditional π-backbonding

interactions frequently encountered in mononuclear complexes.[22] Based on these observations, one hypothesis is that small molecule binding could be promoted if the supporting metal site did not utilize the d-orbital manifold to form intermetallic interactions.

Furthermore, if the supporting metal atom could also confer electrophilicity to the active metal site, it may lead to small molecule reactivity extending beyond N_2. Examining how Lewis acids can modulate structure and activity relationships in enzymatic and synthetic systems, the electron deficient Lewis acids of group 13 (e.g. B, Al, Ga, and In) are prime candidates to support this hypothesis. Shortly before our group began to investigate such complexes, the importance of M→B interactions to mediate catalytic and stoichiometric transformations was coming into focus. For example, the Peters' lab had highlighted the ability of iron-borane complex (TPB)Fe(N_2) to mediate the catalytic reduction of N_2 to NH_3 and to stabilize both low-valent and high-valent iron complexes.[141, 181] These complexes, and some of their derivatives, revealed a rich chemistry with dihydrogen and silanes as well.[138, 182]

Inspired by these reports, our group then began to investigate the ability of Lewis acids to support low-valent first-row metal fragments with the end goal of small molecule reactivity. In initial studies performed by Dr. P. Alex Rudd, the notion that a metal support without d-orbitals promotes small molecule reactivity in the H_3L framework held true. Utilizing a Lewis-acidic aluminum metalloligand allowed for isolation of a family of rare zero-valent metal-aluminum complexes including: FeAlL, CoAlL, and NiAlL.[183] Due to the π-basicity of the Fe^0 and Co^0 centers, both FeAlL and CoAlL were found to bind dinitrogen at room temperature giving rise to the sandwich complex LAlFe(μ-N_2)FeAlL,

and end-on dinitrogen complex (N_2)CoAlL. It would later be discovered that even NiAlL binds N_2 to a small extent despite the poor ability of Ni to activate N_2 in general.[22, 184] The ability of aluminum to confer Lewis acidity to these low-valent metal centers supports the hypothesis that Z-type ligands promote small molecule binding by enhancing the metal center's electrophilicity through an inverse-dative interaction. Moreover, this strategy

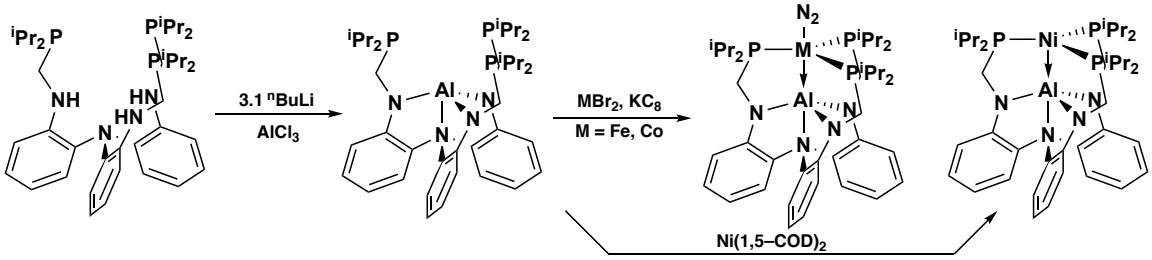

Figure 1.23: Synthesis and characterization of the MAlL family of complexes.

proved successful to further activate the N_2 ligand.[185] For example, (N_2)FeAlL was found to undergo reduction to the reduced Fe^{-I} state and could be further functionalized with silyl electrophiles. Similar redox processes were noted for (N_2)CoAlL, which can be reduced to its Co^{-I} analog, $[(N_2)CoAlL]^-$ under mild conditions.[186]

With the ability to stabilize base metal complexes supported by an aluminum metalloligand, our group then began to explore the extent to which this metal→Lewis acid interaction could be used to modify the electronic environments of transition metal centers. Looking closely at PSII and the model systems developed by Agapie, it was speculated that the identity of the Lewis acid might confer differential reactivity to the supported metal site by electronic tuning. To this end, Dr. Ryan Cammarota developed the chemistry of the remainder of the group 13 triad (Ga and In) specifically towards their hydrogenation chemistry with nickel.[187] The use of the heavier group 13 congeners allowed for the characterization of two addition bimetallic complexes, NiGaL and NiInL. Moreover, these

species exhibited rich coordination chemistry with H_2 and N_2 allowing for the characterization of rare H_2 and N_2 adducts (η^2-H_2)NiInL and (N_2)NiInL. To date, only a handful of isolable dihydrogen complexes for first-row transition metal complexes have been spectroscopically observed, let alone crystallographically characterized. Moreover, the use of M = Ga allowed for spectroscopic characterization of (η^2-H_2)NiGaL, which is a reactive intermediate in the hydrogenation of terminal olefins to alkanes. Furthermore, the identity of the Lewis acid is vital to tuning the nickel center for optical catalytic performance, a concept which strongly parallels some of the enzymatic system discussed

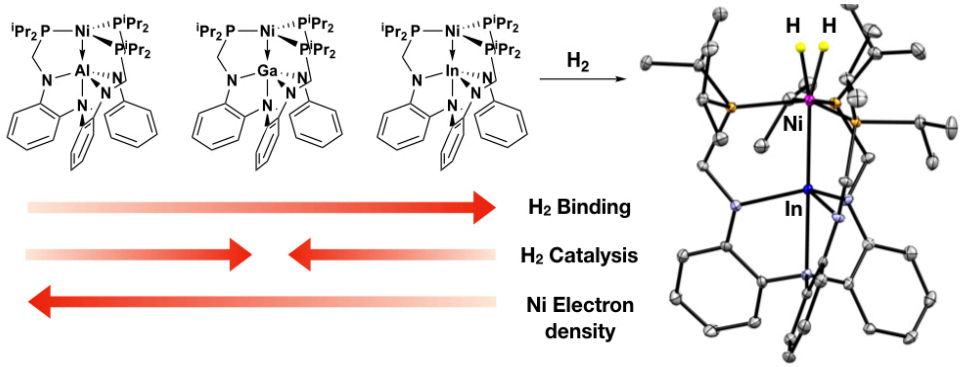

Figure 1.24: Left, effect of varying Lewis acids on hydrogenation activity and dihydrogen binding by NiML complexes. Right, molecular structure of (η^2–H_2)NiInL rendered at 50% thermal ellipsoid probability.

here (*vide supra*). Even though NiGaL only modestly binds H_2 (ΔG°= 0.5 kcal/mol at 1 atm), it is the best catalysts of the triad as it balances the steps required for hydrogenation to occur. The ability of NiGaL to bind H_2 proved key in developing a catalytic cycle for CO_2 hydrogenation to produce formate.[184, 188]

1.5 Scope of this work

This thesis aims to further develop and extend the ability of Lewis-acidic metalloligands to promote small molecule reactivity at first-row transition metal centers. The findings reported in the following chapters explore our efforts to harness Z-type ligands to promote small molecule reactivity and develop new catalytic applications. Furthermore, the chemistry developed in the following chapter extends beyond d^{10} nickel centers suggesting a more general applicability.

The first chapter of this thesis details the ability of Lewis-acidic metalloligands to promote the binding of H_2 in a series of d^{10} Co^{-I} complexes supported by the tris(phosphinoamido)amine ligand framework $[(\eta^2\text{–}H_2)CoML]^-$ (M=Al, Ga, or In). The ability to examine three isostructural complexes in close detail by X-ray crystallography and NMR spectroscopy reveals that Z-type metalloligands reinforce the activation of H_2 ligand through a symbiotic relationship. This observation is contrary to the expectation of a normal *trans*-influencing ligand, and thus an *inverse-trans* influence is proposed.

Building on these studies, Chapter 3 examines the abilities of the Co^{-I} complexes to promote the catalytic hydrogenation of CO_2 into formate salts (CO_2H^-). These results build on our initial findings that the isoelectronic nickel complexes are competent catalysts for the same transformation. Mechanistic and kinetic studies of this catalytic reaction are examined in detail by the use of stoichiometric experiments, isotopic labeling, and in-operando high-pressure NMR spectroscopy. Important findings include a unique $Co^{-I/I}$ redox mechanism that operates with weak organic bases through two rare dihydrogen complexes.

Chapter 4 builds upon the electronic origins of the *inverse-trans* influence that is exhibited in the $[(H_2)CoML]^-$ complexes by studying the electronic structure of similarly reduced nickel analogs, $[NiML]^-$. With an S= ½ spin state, these nickel complexes offer a unique opportunity to examine the electronic structure that is conferred by the Lewis-acidic metalloligands. This is most evident by a detailed EPR and computational investigation that reveals an important role of the nickel $4p_z$ orbitals in the ground state electronic structures of the d^{10} $[CoML]^-$ and NiML complexes. The highly reducing nature of these formally Ni^{-I} complexes is utilized to stoichiometrically disproportionate CO_2 into CO_3^{2-} and CO. Preliminary results extending this strategy to isoelectronic copper analogs are also presented.

The final chapter of this thesis describes the use of Lewis-acidic metalloligands to support a family of anionic Ni^0 organometallic complexes. We find that the NiML scaffold is capable of supporting various anionic complexes, $[XNiML]^-$, due to the Lewis acidity conferred by the supporting atom. In the case of the unique d^{10} hydride complexes, $[HNiML]^-$, a comprehensive thermodynamic landscape of the Ni–H bond is developed from experimentally determined acidity and hydricity measurements.

Chapter 2

Synthesis, characterization, and reactivity of an isostructural series of subvalent cobalt dihydrogen complexes

In part from:

Vollmer, M. V.; Xie, J.; Lu, C. C. "Stable Dihydrogen Complexes of Cobalt(−I) Suggest an Inverse *trans*-Influence of Lewis Acidic Group 13 Metalloligands" J. Am. Chem. Soc. **2017**, *139* (19), 6570-6573

Vollmer, M.V.; Ye, J.; Xie, J.; Preston, A.; Linehan, J. C.; Wiedner, E.; Appel, A.; Gagliardi, L.; Lu, C. C. CO_2 hydrogenation via a $Co^{-I/I}$ cycle featuring two stable dihydrogen complexes. *Manuscript in preparation.*

2.1 Overview

A triad of d^{10} cobalt dihydrogen complexes were synthesized by utilizing Lewis acidic group 13 metalloligands, M[N((*o*-C_6H_4)$NCH_2P^iPr_2)_3$], where M = Al, Ga, and In. These complexes have formal Co^{-I} oxidation states, representing the only coordination complexes in which dihydrogen is bound to a subvalent transition metal center. Single-crystal X-ray diffraction and NMR studies support the assignment of these complexes as non-classical dihydrogen adducts of Co^{-I} by comparison with a previously reported dinitrogen analog. Further validation of this assignment is garnered from density functional theory.

The series of complexes is rigorously examined by ^1H NMR studies including isotopic labeling and relaxation measurements. An examination of the theory that is relevant to the relaxation measurements of M(η^2-H_2) complexes is presented. Conclusively, the degree of H_2 activation increases in the order of Al < Ga < In. Similarly, single crystal X-ray diffraction supports the notion that the strength of the Lewis-acid metal interaction increases in the same order.

The reactions of these new species with simple donor ligands such as N_2 and $PhSiH_3$ are explored in detail. In the case of N_2, simple dissociation of the H_2 ligand to generate anionic Co^{-I} dinitrogen complexes are observed. In these new species, the N_2 unit undergoes modest activation by the π-basic Co^{-I} center. In the case of $PhSiH_3$, formal activation of the Si-H bond is observed to generate a Co^{I} silyl hydride species.

2.2 Introduction

Non-classical dihydrogen adducts of transition metals, M(η^2-H_2), are ubiquitous intermediates in the transfer of H_2 to a variety of substrates.[1-3] Isolable M(η^2-H_2) species are most commonly observed with 4*d* and 5*d* transition metal centers, which are recognized to form stronger metal–ligand bonds and are generally more proficient at π–backbonding than 3*d* metals.[4-6] Despite recent progress in their isolation, well characterized H_2 adducts of first-row transition metals remain rare.[4, 7-10] The study of such intermediates represents a fundamental step in utilizing base metals for H_2 transfer reactions.[11-14]

In particular, examples of non-classical cobalt dihydrogen complexes are limited to only a small family of compounds (Fig. 2.1). Following the detection of transient Co(η^2-H_2) species in inert-gas matrices[15-16], the characterization of $[(tetraphos)Co(H)_2]^+$ and $[Cp^*Co(\eta^2–H_2)H(PR_3)]^+$ were complicated by facile H_2 activation and H_2/hydride exchange, respectively[17-20]. Heinekey described a remarkable study of a bonafide Co(η^2-H_2) species in a phosphinite pincer system which was investigated by low-temperature and high-pressure NMR methods.[21] The tris(phosphino)-silyl and borane ligand platforms reported by Peters *et al.* have allowed for the isolation of thermally stable Co(η^2–H_2) complexes and elucidation of their solid-state structures.[22-23] More recently, a phosphine supported Co(η^2–H_2) bis(carbene) pincer complex reported by Fout *et al.* was shown to catalyze olefin hydrogenation and *E*-selective alkyne semi-hydrogenation.[24-25]

Currently, the majority of well-defined H_2 adducts of d^{10} centers are isolated to a handful of Ni(0) complexes that feature either Z-type[26] group 13 metalloligands or a silyl ligand (Fig. 2.1b).[27-30] The $Ni^0(\eta^2–H_2)$ bis(phosphino)borane complex (Peters *et al.*) was observed as a transient intermediate prior to H_2 addition across the Ni→B bond.[8-9] Using

Z-type ligands of the heavier group 13 congeners, two additional $Ni^0(\eta^2–H_2)$ adducts were characterized, including an X-ray structure of $Ni^0(\eta^2–H_2)InL$, where L is $[N((o–C_6H_4)NCH_2P^iPr_2)_3]^{3–}$.[31] The rarity of d^{10} $M(\eta^2–H_2)$ complexes can be understood by considering a simple bonding rationale: d^{10} metals lack an empty d-orbital that is needed to accept electron density from the $\sigma–H_2$ bond.[32] Inspired by the Ni precedents, we targeted the isoelectronic d^{10} $Co^{–I}(\eta^2–H_2)$ species using the group 13 metalloligands, ML, where M = Al, Ga, and In.[33-34] Importantly, the LUMO of the unsaturated nickel complexes features a low lying $Ni(4p_z)$ orbital, which we have found critical to support σ-adduct formation. The triad of $Co^{–I}(\eta^2–H_2)$ complexes were investigated by NMR methods, single-crystal X-ray diffraction, and density functional theory (DFT). Overall, the data is consistent with the formulation of these species as H_2 adducts of subvalent $Co^{–I}$. Moreover, the choice of the group 13 ion fine tunes H_2 activation at Co. We propose an inverse *trans*-influence exerted by the group 13 supports to explain the stability of the $Co^{–I}(\eta^2–H_2)$ complexes.

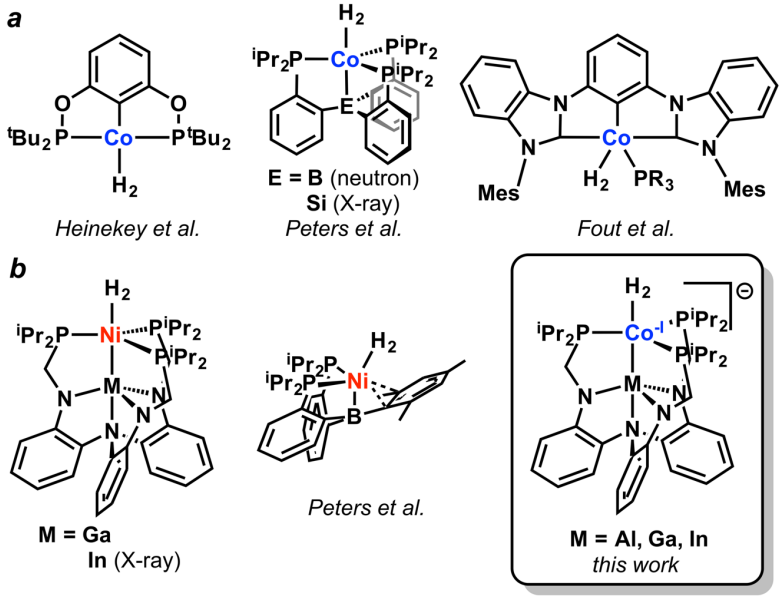

Figure 2.1: Selected cobalt H_2 complexes and rare H_2 adducts of d^{10} transition metals.

2.3 Results and Discussion

2.3.1 Synthesis of Co^{-I} dihydrogen complexes

The triad of cobaltate complexes, $[Co(\eta^2–H_2)ML]^-$ (**[1(H₂)]⁻** to **[3(H₂)]⁻** ,1 = Al, 2 = Ga, 3 = In) were synthesized by adding 3.1 equiv. $Li[HBEt_3]$ to a cooled mixture of the corresponding group 13 metalloligand, ML, and $CoBr_2$ in THF under argon at -78˚C (Fig 2.2). Effervescence, presumably due to H_2 release, was observed, and diamagnetic products **[1(H₂)]⁻** to **[3(H₂)]⁻**were cleanly generated (*vide infra*). The diamagnetism of **[1(H₂)]⁻** to **[3(H₂)]⁻** are consistent with a d^{10} count of the subvalent $Co^{–I}$ oxidation state, and add to a growing number of well-defined $Co^{–I}$ coordination complexes.[35-41]. Complexes **[1(H₂)]⁻** to **[3(H₂)]⁻** are exceedingly air sensitive, as is typically observed for $Co^{–I}$ compounds supported by phosphine donors.[35] Of note, the dinitrogen analog of **[1(H₂)]⁻**, **[1(N₂)]⁻** has been reported in the literature and is fully consistent with the invoked d^{10} $Co^{–I}$ oxidation state. As might be expected for a d^{10} metal center, complexes **[1(H₂)]⁻** to **[3(H₂)]⁻** are void of any visible absorptions leading to their pale-yellow appearance in both solution and the solid state. The ground state electronic structure is analogous to species such as $[(1,5\text{-}COD)_2Co]^-$ or $Ni(COD)_2$ which are also pale yellow and diamagnetic on the basis of their electronic saturation and lack of accessible d-d or d-p transitions.[40, 42] The synthetic strategy to generate the $Co^{–I}$ source is not limited to Li^+ salts, indeed the use of $KHBEt_3$ or $NaHBEt_3$ generates the $K^+(THF)_n$ and $Na^+(THF)_n$ salts respectively, which can be further encapsulated with 222-crypt, 18-crown-6, or 12-crown-4. However, only the $Li(THF)_4^+$ salts proved amenable to the growth of suitable X-ray crystals for a structural determination.

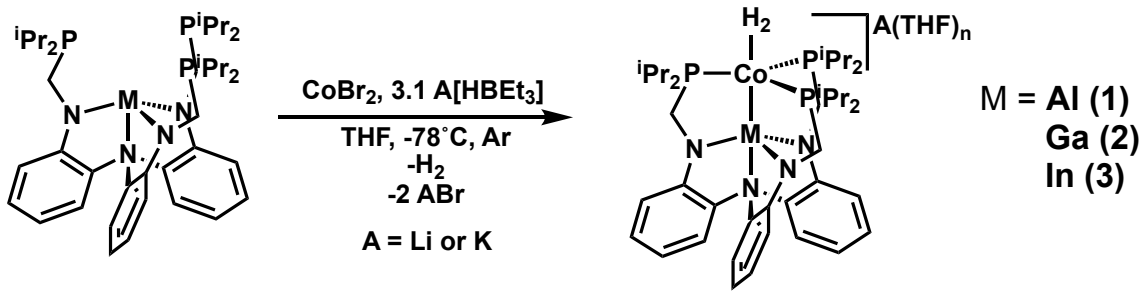

Figure 2.2: Synthesis of anionic Co(η^2–H_2)ML complexes **[1(H₂)]**$^-$ to **[3(H₂)]**$^-$

2.3.2 Nuclear Magnetic Resonance Studies of Co(η^2–H_2) complexes

Initial inspection of the ^{31}P NMR spectra of **[1(H₂)]**$^-$ to **[3(H₂)]**$^-$ reveals that each species exhibits a single ^{31}P resonance that is diagnostic of a C_3 symmetric molecule (Fig 2.3). The isostructural series of complexes appear to be susceptible to subtle electronic modulations as evidenced by the large changes in the ^{31}P chemical shifts by nearly 20 ppm downfield as the supporting metal is varied from Al (73.2 ppm), to Ga (84.5 ppm), and finally In (91.9 ppm). This trend qualitatively follows that reported for the analogous NiML series of complexes, for which a strong electronic modulation of the Ni coordination environment has been invoked and spans a similar chemical shift range.[43] The application of ^{1}H coupling did not lead to observable coupling, a consequence of the 100% abundant *I* = 7/2 cobalt nuclei. Under the limiting assumption that the H_2 ligand is intact, the rapid processional motion (*vide infra*) of the H_2 ligand likely inhibits the observation of any ^{31}P-^{1}H coupling.

The ^{1}H NMR spectra of **[1(H₂)]**$^-$ to **[3(H₂)]**$^-$ in THF-d_8 each contain a broad resonance (2H) in the upfield region at –7.0, –7.7, and –7.8 ppm, respectively, suggestive of M-H character (Fig. 2.4). Neither the application of heat or vacuum solicits any change to this resonance, indicating that the M-H_2 moiety is non-labile. The series of complexes each contain the appropriate number of ^{1}H resonances for the 12 aromatic (ArH), six

methylene (N*CH*$_2$P), six methine (PC*H*Me$_2$), and 36 methyl (PCH*Me*$_2$) proton environments. At room temperature, the fluxionality of each species with respect to CH_2 inversion modifies the appearance of each resonance such that the CH_2 resonance may appear as a coalesced singlet (if fluxional) or an AB quartet (if diastereotopic). It is well appreciated that when the L^{3-} framework has become stereochemically rigid (either as a function of temperature control or ligand substitution) both methylene and methine chemical environments become magnetically inequivalent by ^{1}H NMR.[44,45] In the case of the methylene (N*CH*$_2$P) resonance an AB quartet is observed after decoalescence of the averaged signal.

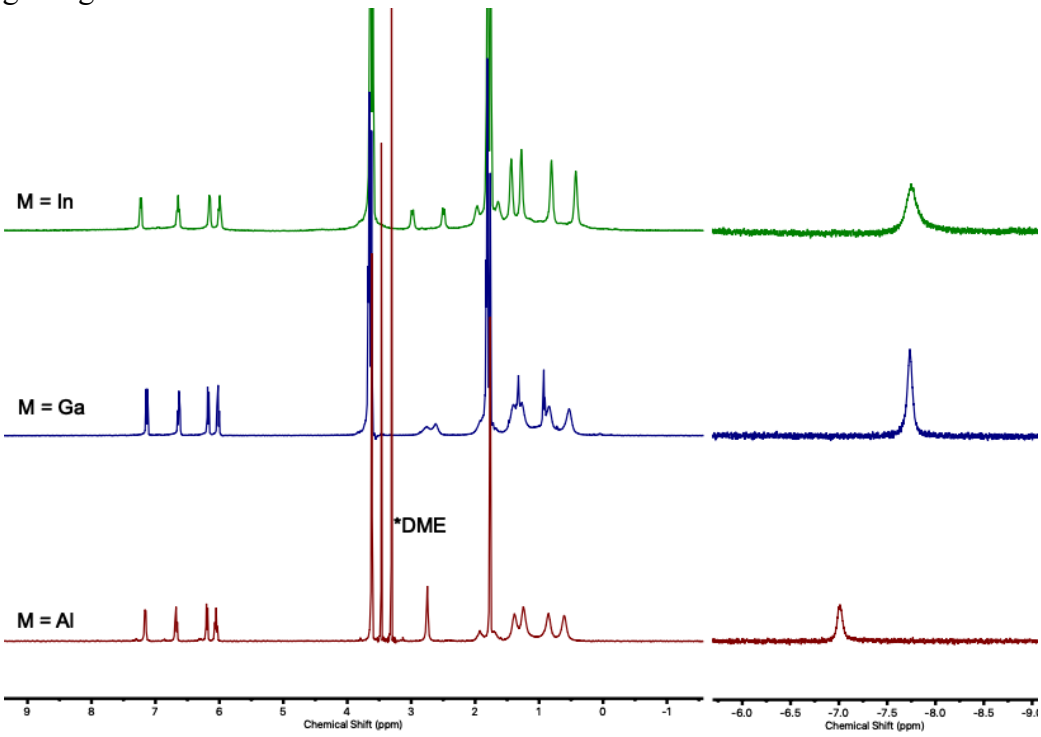

Figure 2.3: Overlay of ^{1}H NMR spectra of **[1(H$_2$)]**$^-$ to **[3(H$_2$)]**$^-$ (400 MHz, THF–d$_8$). The asterisk denotes DME from the recrystallization of Li(DME)$_3$LAlCo(H$_2$)

Given that the ^{1}H NMR of complexes **[1(H$_2$)]**$^-$ to **[3(H$_2$)]**$^-$ appear to be rigorously C_3-symmetric (indeed, even at low temperature no changes in the ^{31}P/^{1}H NMR are noticeable), one might suspect that the NMR data simply support a non-classical M(η^2–H$_2$)

formulation. However, it is appreciated that *cis*-MH_2 complexes can lead to deceptively symmetric NMR spectra due to rapid H-H interchange.[46] Thus, to discern between these bonding extremes (MH_2 vs $M(\eta^2–H_2)$), we rigorously studied these complexes with the established "T_1 criterion," and J_{HD} measurements that have been widely established for differentiating classical and non-classical dihydrogen complexes.

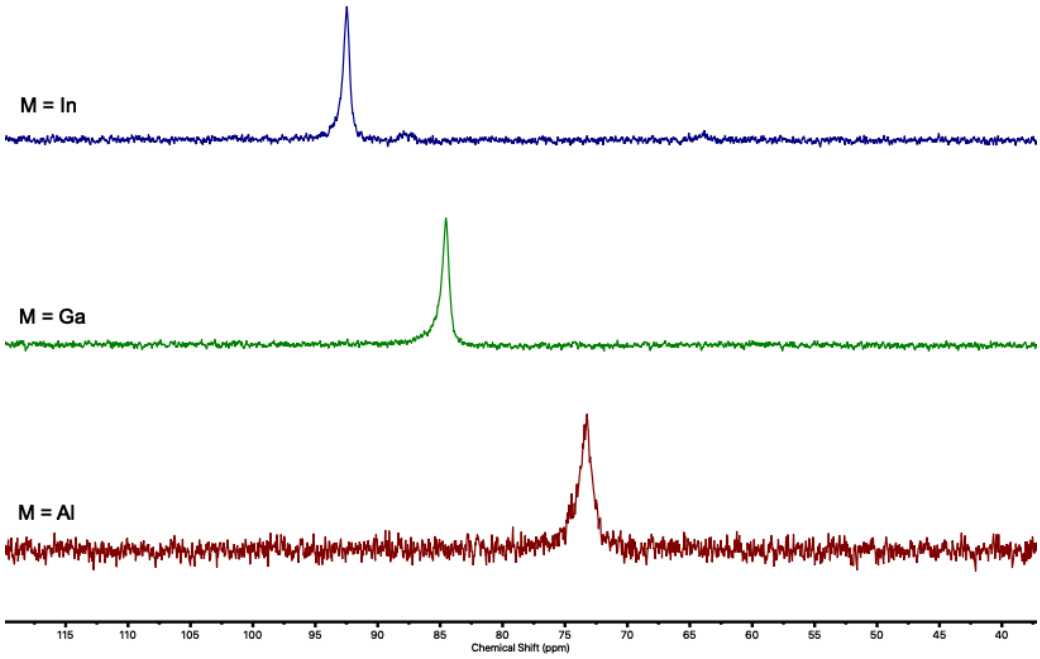

Figure 2.4: Overlay of ^{31}P NMR spectra of **[1(H₂)]⁻** to **[3(H₂)]⁻** (400 MHz, THF-d_8)

The "T_1 criterion," is a ^1H NMR method by which the longitudinal relaxation time (T_1) of a coordinated M-H fragment is measured as a function of temperature in order to minimize the contribution of processional motion of H_2 along the M-H_2 vector (T_{1min}).[4, 47-50] This method relies on the large homonuclear dipolar coupling that is present in $M(H_2)$ complexes, which is often the largest contributor to magnetic relaxation in a coordinated dihydrogen ligand. In order to accurately explain the ramifications of the T_1 measurements performed on complexes **[1(H₂)]⁻** to **[3(H₂)]⁻**, a short derivation is presented below that

relates the *rate* of magnetic relaxation (the inverse of time $R_1 = 1/T_1$) to a simple model of the described cobalt dihydrogen complexes. As previously shown and illustrated below, there are non-negligible contributions from the protons residing in the ligand framework and the cobalt atom. The major contributors to this magnetic relaxation are shown below in Figure 2.5

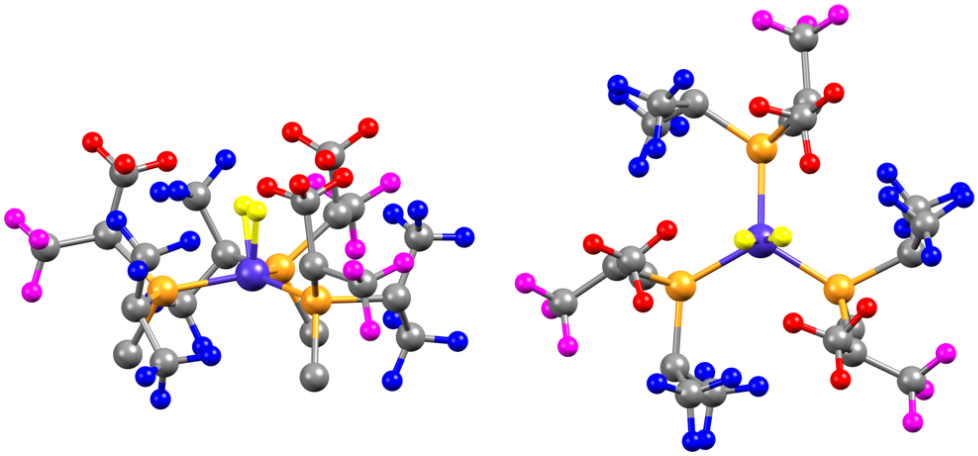

Figure 2.5: Molecular view of the local coordination environment of **[1(H₂)]⁻** to **[3(H₂)]⁻** for which we will describe the effect of dipolar coupling on the intermolecular H-H distance of coordinated H_2.

For a ^{1}H nucleus that resides in a magnetic field of arbitrary strength, the relaxation rate (inverse of relaxation *time*) due to homonuclear (e.g. H-H) dipolar coupling, R_{HH}, is generally given by Eq. 1 as shown by Halpern *et al.*[47]

$$R_{HH} = \frac{3\gamma_H^4\hbar^2}{10r^6}\left\{\frac{\tau_c}{1+\tau_c^2\omega^2} + \frac{4\tau_c}{1+4\tau_c^2\omega^2}\right\} \qquad \text{Eq. 1}$$

In Eq. 1, γ_H is the gyromagnetic ratio of the proton, ω is the Larmor frequency, *r* is distance (in Å) between the corresponding dipoles (e.g. d_{HH}) , and τ_c is the rotational correlation time. The rotational correlation time, τ_c, is related to the rate of molecular tumbling in solution, and thus as temperature increases its value decreases (and vice versa). As one may infer from Eq. 1, the relaxation time for a coordinated H_2 ligand is expected to

be remarkably rapid (T_1 <100 ms), on account of the H-H distance which typically falls between 0.74–1.0Å. In other terms, the R_{HH} is expected to be on the order of 5-50 Hz.

In the limiting case where the motion of molecular tumbling is rapid with respect to relaxation (the fast motion regime $\omega^2\tau_c^2 << 1$) it can be shown that the Eq. 1 simplifies to:

$$R_{HH} = \frac{3\gamma_H^4\hbar^2}{10r^6}\{5\tau_c\} \qquad \text{Eq. 2}$$

$$R_{HH} = \frac{3\gamma_H^4\hbar^2}{10r^6}\left\{\frac{2}{\omega^2\tau_c}\right\} \text{ where } \omega = \frac{2\mu_e B}{\hbar} \qquad \text{Eq. 3}$$

On the other extreme (the slow-motion regime, $\omega^2\tau_c^2 >> 1$), molecular tumbling is slow with respect to magnetic relaxation and Eq. 1 simplifies to give Eq. 3, where the rate of relaxation is now dependent on both the correlation time in solution *and* the Larmor frequency of the ^{1}H nuclei. An important experimental ramification of this approximation is that due to the dependence of ω on magnetic field strength the rate of relaxation is now an inherent function of the spectrometer frequency (ν) employed. Halpern suggested that separately, Eq. 2 and 3, do not satisfy the behavior of magnetic relaxation as a function of temperature and field strength, as τ_c lies between these two extremes. Equations 2 and 3 do approximate the parabolic shape that is observed for variable temperature T_1 studies if it is assumed that slow motion is observed at low-temperature and fast motion is observed near ambient temperatures.

From the experimental point of view, the temperature at which a minimum relaxation rate is reached can inferred by solving the derivative of Eq. 1 with respect to τ_c such that $\partial R_{HH}/\partial\tau_c = 0$, as shown below:

$$\frac{\partial R_{HH}}{\partial\tau_c} = 0 = \frac{3\gamma_H^4\hbar^2}{10r^6}\left\{\frac{1 - \tau_c^2\omega^2}{(1 + \tau_c^2\omega^2)^2} + \frac{4(1 - \tau_c^2\omega^2)}{(1 + 4\tau_c^2\omega^2)^2}\right\} \qquad \text{Eq. 4}$$

Solving for the minimum at zero gives rise to the informative polynomial:

$$\frac{\partial R_{HH}}{\partial \tau_c} = 0 = 32\tau_c^6\omega^6 + 20\tau_c^4\omega^4 + \tau_c^2\omega^2 - 5 \text{ (where } \tau_c \propto T^{-1} \text{ and } \omega \propto B) \qquad \text{Eq. 5}$$

Thus, one can reasonably deduce via a few algebraic manipulations that the minimum rate of relaxation of a given M-H_2 resonance will not only change as a function of magnetic field, but also that the temperature at which this minimum will be reached is a function of the same field. In this vein, higher field instruments can be used to find T_{1min} values at less dramatic temperatures.

In a typical T_1 experiment, the observer would use a high field NMR instrument to measure the relaxation time of a given chemical resonance, typically 400-500 MHz. As an example, at 500 MHz the magnetic field strength is 11.7 T and the inherent Larmor frequency of the ^{1}H nucleus is 3.142 x 10^9 s^{-1}, which leads to a correlation time of $\tau_{c(min)}$ = 1.96 x 10^{-10} s at T_{1min} (by solving Eq. 5 for ω = 3.142 x 10^9 s^{-1}). Re-solving Eq. 1 with this $\tau_{c(min)}$ allows one to greatly simplify Eq. 1 to give the powerful relationship:

$$R_{HH} = \frac{3\gamma_H^4\hbar^2}{10r^6}\left\{\frac{2}{\omega^2\tau_c}\right\} = \frac{77.51 \text{ Å}^6 \text{ s}^{-1}}{r^6} \qquad \text{Eq. 6}$$

Based on a series of simple relaxation measurements, one can quantitatively predict the bond distance of a M(H_2) complex with a fair degree of accuracy. The power of the relationship is apparent when comparing two model compounds with d_{HH} 0.74 and 1.6 Å, which are extremes of the M-H_2 bonding motif. For the former, a typical M(η^2–H_2) complex, a T_{1min} is predicted to be ca. 2 ms, whereas the former (a dihydride) results in a T_{1min} = 147 ms.

The power of this approach is further extended in accuracy by using the same strategy described above to compensate for the dipolar relaxation enhancement induced by other nuclei. Doing a similar analysis for Co (R_{Co}) allows one to derive similar conclusions

provided a fair approximation of the M-H bond distance can be obtained by computational methodologies.[48] The magnitude of this relaxation enhancement is particularly large for ^{57}Co, which is 100% abundant with a high nuclear spin (I = 7/2). In Eq. 7, γ_{Co} is the gyromagnetic ratio of the cobalt, ω_+ and ω_- are the respective sum/differences of the two opposing Larmor frequencies, and S is the nuclear spin of the metal atom. This can be evaluated for $\tau_{c(min)}$ = 1.96 x 10^{-10} s and any metal-hydrogen pairings to give the simple inverse relationship shown below. Equation 7 also highlights the large relaxation enhancement of high nuclear spin atoms on nearby hydrogen atoms.

$$R_{Co} = \frac{2\gamma_H^2\gamma_{Co}^2\hbar^2}{15r^6}S(S+1)\left\{\frac{\tau_c}{1+\tau_c^2\omega_-^2}+\frac{3\tau_c}{1+\tau_c^2\omega_H^2}+\frac{6\tau_c}{1+\tau_c^2\omega_+^2}\right\} = \frac{K_x}{d_{MH}^6} \qquad \text{Eq. 7}$$

$$\frac{1}{T_{1M}} = R_M = \frac{K_x}{d_{MH}^6} \;\; ; \quad R_{Co} = \frac{88.80\ \text{Å}^6\text{s}^{-1}}{d_{MH}^6} \qquad \text{Eq. 8}$$

One can then approximate the relaxation enchantment of adjacent ligand ^{1}H nuclei to the rate of relaxation of the M(η^2–H_2) unit. This is done by compiling the sum of all of the interactions between the H_2 unit and the ligand in a given organic structure (Eq. 9). The major contributors in the species at hand, **[1(H₂)]**$^-$ to **[3(H₂)]**$^-$ are highlighted in Fig. 2.5.

$$\frac{1}{T_{1L}} = R_L = \frac{K_x}{d_{HH}^6} = \sum_{all\ H}\frac{77.51\ \text{Å}^6 s^{-1}}{d_{HH}^6} \qquad \text{Eq. 9}$$

Taken together, one can then adjust an experimental relaxation measurement such that an accurate representation of the relaxation rate due solely to dipolar H-H coupling can be obtained, as shown in Eq. 10 to yield T_{1min_calc}.

$$\frac{1}{T_{1\text{min }\_calc}} = \frac{1}{T_{1min}} - \frac{1}{T_{1L}} - \frac{1}{T_{1M}} \; or \; R_{calc} = R_{obs} - R_L - R_M \qquad \text{Eq.10}$$

To finally extract an accurate value of d_{HH}, one more limiting assumption must be made and concerns the rate of H_2 rotation with respect to the frequency of the NMR spectrometer. To meaningfully interpret this assumption, we must consider both the rotation of the H_2 within the molecule (τ_{H2}) relative to the rate of molecular tumbling in solution (τ_{mol}) in addition to their additive sum (τ_c). The inclusion of this additional degree of freedom complicates Eq. 1 and gives rise to Eq. 12 and 13, whose origins are beyond the scope of this discussion.

$$\frac{1}{\tau_c} = \frac{1}{\tau_{H2}} + \frac{1}{\tau_{mol}} \qquad \text{Eq. 11}$$

$$J(\omega) = \left\{\frac{0.25\,\tau_{mol}}{1+\tau_{mol}^2\omega^2} + \frac{0.75\,\tau_c}{1+\tau_c^2\omega^2}\right\} and\ J(2\omega) = \left\{\frac{0.25\,\tau_{mol}}{1+4\tau_{mol}^2\omega^2} + \frac{0.75\,\tau_c}{1+4\tau_c^2\omega^2}\right\} \qquad \text{Eq. 12}$$

$$R_{HH} = \frac{3\gamma_H^4\hbar^2}{10r^6}\left\{\frac{J(\omega) + 4J(2\omega)}{1 + \tau_c^2\omega^2}\right\} \qquad \text{Eq. 13}$$

One may envision two extremes wherein the H_2 ligand is rotating rapidly with respect to molecular tumbling ($1/\tau_{H2} >> 1/\tau_{mol}$) as well as the converse ($1/\tau_{H2} << 1/\tau_{mol}$). The latter, termed the slow-motion regime, simplifies Eq. 11 and 12 as we must now only consider the molecular tumbling correlation time, τ_c, as $1/\tau_c \simeq 1/\tau_{mol}$. Equation 11 can then be simplified, and ultimately gives rise to Eq. 3. Solving for *r* with respect to the spectrometer frequency gives rise to Eq. 16.

$when\ 1/\tau_{H2} << 1/\tau_{mol}$ $$R_{HH} = \frac{3\gamma_H^4\hbar^2}{10r^6}\left\{\frac{\tau_c}{1 + \tau_c^2\omega^2} + \frac{4\tau_c}{1 + 4\tau_c^2\omega^2}\right\} \qquad \text{Eq. 14}$$

$when\ 1/\tau_{H2} >> 1/\tau_{mol}$ $$R_{HH} = \frac{3\gamma_H^4\hbar^2}{10r^6}\left\{\frac{\left\{\frac{\mathbf{0.25}\,\tau_c}{1 + \tau_c^2\omega^2} + \frac{\mathbf{0.25}\,\tau_c}{1 + 4\tau_c^2\omega^2}\right\}}{1 + \tau_c^2\omega^2}\right\} \qquad \text{Eq. 15}$$

In the fast-motion regime, where $1/\tau_{H2} > 1/\tau_{mol}$, $1/\tau_c \simeq 1/\tau_{H2}$ and thus Eq. 11 again is used to simplify the expression. As the second bracketed component of Eq. 12 has now become negligible, we can again simplify to give rise to Eq. 15. Solving again for the interatomic distance, *r* or d_{HH}, carries an addition constant ($\sqrt[6]{0.25}$) through the derivation which brings us finally to Eq. 17 with respect to the spectrometer frequency, in which we observe that an H_2 ligand rotating rapidly with respect to molecular tumbling has a four-fold relaxation enhancement when compared to its slow-rotation alternative.[4]

$$d_{HH}^{slow} = 5.81 \sqrt[6]{\frac{T_{1HH}}{\nu}} \qquad \text{Eq. 16}$$

$$d_{HH}^{fast} = 5.81 \sqrt[6]{\frac{T_{1HH}}{\mathbf{4}\nu}} \qquad \text{Eq. 17}$$

The majority of $M(H_2)$ complexes have rates of H_2 rotation that greatly exceed that of the NMR timescale.[4] The notable exceptions typically have ligand frameworks/geometries in which a preferential orientation of the H_2 ligand can be realized.[48] In the case of **[1(H₂)]⁻** to **[3(H₂)]⁻**, the fast rotation regime is a more accurate descriptor, and is the most pertinent.

Table 2.1: Manipulations to experimental relaxation data for the estimation of d_{HH}

	T_{1min} 400MHz (ms)	T_{1min}, 500MHz (ms)	DFT Co–H (Å)		DFT Avg. Co–H (Å)	R_{Co} s^{-1}	R_L s^{-1}	T_{1min_calc} (ms)
[1(H₂)]⁻	25.8(1)	32.3	1.60	1.59	1.60	5.4	2.70	43.6
[2(H₂)]⁻	26.5(1)	33.1	1.59	1.59	1.59	5.5	2.66	45.4
[3(H₂)]⁻	29.0(1)	36.3	1.59	1.58	1.58	5.6	2.65	51.8

Experimentally **[1(H₂)]⁻** to **[3(H₂)]⁻** exhibit T_{1min} relaxation times of 25.8(1), 26.5(1), and 29.0(1) ms at temperatures near –20˚C (THF–*d*₈, 400 MHz, Fig 2.6). The gradual increase in the magnitude of T_{1min} suggests the identity of the Lewis acid support

has a measurable effect on the activation of the H_2 ligand. In conjunction with chemical theory (*vide infra*) and Eq. 1-17, we can deconstruct the experimental rates of relaxation. First, we must account for the use of a 400 MHz spectrometer rather than 500 MHz, which is done by simply multiplying the observed T_{1min} by a factor of 5/4. Alongside the contributions from cobalt (R_{Co}) and the ligand proton contributions (R_L), we can correct the experimental T_{1min} measurement for **[1(H₂)]⁻** to **[3(H₂)]⁻** to yield the corrected T_{1min_calc}

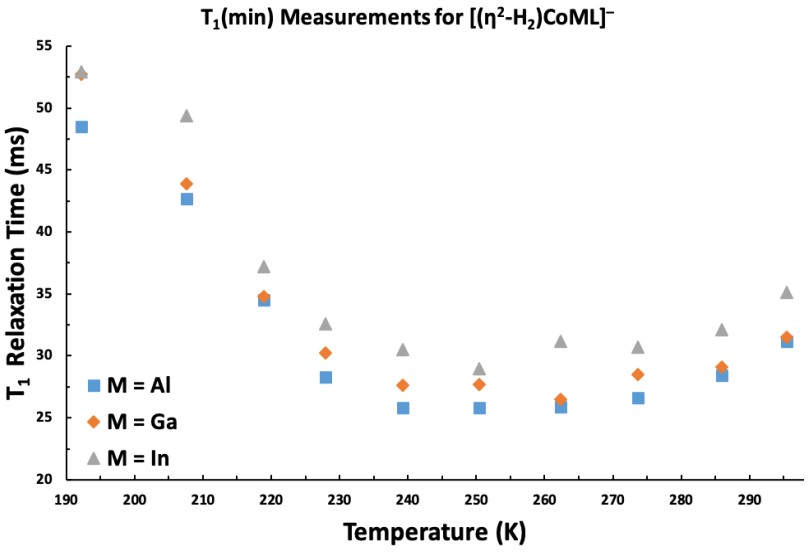

Figure 2.6: Profile of relaxation times (T_1) for the M(η^2–H_2) resonance in **[1(H₂)]⁻** to **[3(H₂)]⁻**as a function of temperature.

values of 43.6, 45.4 and 51.6 ms respectively. Working under the fast H_2-rotation approximation (Eq. 17) this leads to the conclusion that the H-H bond in complexes **[1(H₂)]⁻** to **[3(H₂)]⁻** are 0.97(1), 0.98(1), and 1.00(1) Å, respectively. The slow-rotation approximation leads to much longer bond distances upwards of 1.2 Å, which disagree with the values obtained from HD labeling studies.

In order to verify this exciting result, isotopic labeling experiments were then conducted by preparing the HD isotopomers of **[1(H₂)]⁻** to **[3(H₂)]⁻**. The addition of HD gas (or 1:1 H_2/D_2) conveniently leads to the observation **[1(HD)]⁻** to **[3(HD)]⁻** by ^{1}H NMR

spectroscopy due to isotopic scrambling at ambient temperature. An example ^{1}H NMR spectrum for **[2(HD)]**$^-$ shown in Fig 2.7. One might reason that as the interatomic H-D distance elongates the magnitude of the J_{HD} coupling constant should decrease. Indeed, this is observed experimentally as well; free HD gas gives rise to a 1:1:1 triplet with J_{HD} = 43.5 Hz, and metal dihydrogen complexes typically exhibit J_{HD} values in the range of 25-40 Hz.

The value of this coupling constant, J_{HD}, was measured with values of 28.5(3), 27.7(9), and 26.3(8) Hz for complexes [**1(HD)]**$^-$ to **[3(HD)]**$^-$ respectively. As a result of the pioneering work of Heinekey, Morris, and Crabtree J_{HD} can be directly related to d_{HH}.[4, 51-52] Morris and Heinekey independently discovered the empirical relationship between J_{HD} and d_{HH} by correlating the values obtained from NMR analysis with known structural data obtained from single crystal neutron diffraction (in which H-H distances can be accurately measured):

$$d_{HH} = 1.42 - 0.0167(J_{HD}) \quad \text{(Morris)} \qquad d_{HH} = 1.44 - 0.0168(J_{HD}) \quad \text{(Heinekey)} \qquad \text{Eq. 18}$$

Using the equations shown above and the measured J_{HD} values we can then calculate the interatomic d_{HH}, which for complexes **[1(H$_2$)]**$^-$ to **[3(H$_2$)]**$^-$ corresponds to

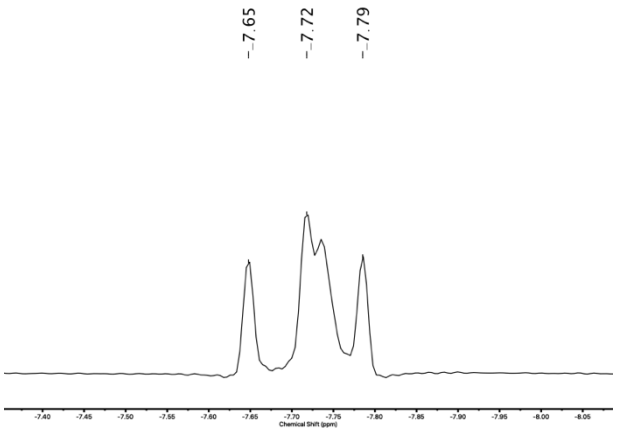

Figure 2.7: ^{1}H NMR showing Co(HD) coupling for **[2(HD)]**$^-$ The center resonance (at ca. -7.74 ppm) arises from the parent H_2 complex.

0.96(1), 0.98(2), and 1.00(1) Å, respectively. On examining the limited literature precedent for stable cobalt dihydrogen complexes, it is immediately apparent that complexes **[1(H₂)]⁻** to **[3(H₂)]⁻** activate the H_2 ligand more any other well-characterized species. For example, Peters and coworkers have prepared a thermally stable Co(η^2–H_2) complex supported by a tris(phosphino)silyl ligand that exhibited a J_{HD} value = 30 Hz (d_{HH} = 0.94 Å).[23] Heinekey *et al.* has described the characterization of thermally unstable complexes supported by a pincer framework having J_{HD} = 29 Hz (d_{HH} of 0.95 Å).[21] Fout *et al.* has prepared related pincer Co^{I} dihydrogen complexes with J_{HD} values of 32-33 Hz (d_{HH} = 0.87-0.89 Å).[25]

There is excellent agreement between the values of d_{HH} obtained from both J_{HD} and T_{1min_calc}, under the assumption that H_2 rotation is fast with respect to molecular tumbling in solution. The d_{HH} values for **[1(H₂)]⁻** to **[3(H₂)]⁻** lie in between the values of Kubas-type complexes (0.77–1.0 Å) and stretched dihydrogen complexes (1.0–1.2 Å).[4, 19] The H_2 ligand in complexes **[1(H₂)]⁻** to **[3(H₂)]⁻** are substantially more activated than their isoelectronic Ni(η^2–H_2)GaL and Ni(η^2–H_2)InL counterparts (0.87 and 0.91 Å, respectively), which do not scramble H_2/D_2.[53] Consistent with this increased extent of activation, the H_2 ligands in **[1(H₂)]⁻** to **[3(H₂)]⁻** are not labile to vacuum/heat. Though Ni(η^2–H_2)InL shows similar stability, Ni(η^2–H_2)GaL is stable only under an H_2 atmosphere. These collective observations are consistent with the greater π-basicity of Co relative to Ni and the negative charge of the Co fragment relative to the neutral Ni analogues.

2.3.3 Crystallographic Studies of Co(η^2–H_2) complexes

Bright-yellow single crystals of the Li(solvent) salt of **[1(H₂)]⁻** to **[3(H₂)]⁻** were obtained by recrystallization from DME/hexane (**[1(H₂)]⁻**) or from THF/pentane solutions

($[2(H_2)]^-$ and $[3(H_2)]^-$). The molecular structures of the Li(solvent)$_n$ salts of $[1(H_2)]^-$ to $[3(H_2)]^-$ are shown in Fig. 2.8, and relevant geometrical parameters are provided in Table 2.2. Due to the inherent asymmetry of the Li(solv)$_n$ cation (omitted in Fig. 2.8) each of the

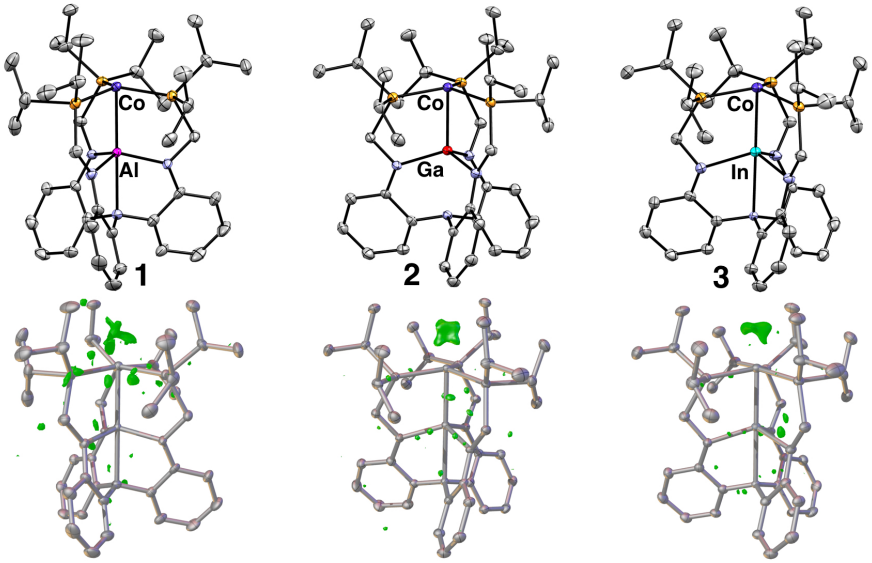

Figure 2.8: Top, Molecular structures of the anionic fragment of Li^+ salts $[1(H_2)]^-$ to $[3(H_2)]^-$ drawn with thermal ellipsoids at 50% probability. The cationic fragment, residual solvents, and hydrogen atoms are omitted for clarity. Bottom: Residual electron density in the difference Fourier map, rendered at 0.1 Å resolution and at 0.2, 0.6, and 0.6 e/Å^3 for $[1(H_2)]^-$ to $[3(H_2)]^-$, respectively

species crystallize in relatively low symmetry space groups: P_n ($[1(H_2)]^-$,) and P-1 ($[2/3(H_2)]^-$,). For complexes $[1(H_2)]^-$ and $[2(H_2)]^-$, there are two distinct residues per unit cell (Z'=2). While the possibility of a pseudo-symmetric solution was pursued, ultimately the lower symmetry solutions were the most accurate descriptor of the crystalline specimens.

All three structures are close to ideal C_3 symmetry as indicated by the sum of the P–Co–P valence angles, which approaches 360˚. The average Co−P bond lengths elongate modestly moving down group 13, ranging from 2.14 to 2.20 Å for $[1(H_2)]^-$ to $[3(H_2)]^-$, respectively. This trend is consistent with decreased Co→P π-back bonding moving down

group 13, as suggested by the increasingly downfield ^{31}P NMR shifts (Fig. 2.3). The Co−P bond lengths in **[1(H$_2$)]$^-$** (avg. 2.144(2) Å) compare well to those for the cobaltate end-on N_2 species, [Li(crypt-222)][(N_2)CoAlL] (**[1(N$_2$)]$^-$** avg. 2.177(1) Å), which also contains Co^{-I} bonded to the AlL metalloligand.[34] By contrast, the neutral (N_2)CoAlL complex with a formal Co^0 center features longer Co−P bond length (Avg = 2.241(1) Å).[33] The Co−Al bond distances in **[1(H$_2$)]$^-$** and **[1(N$_2$)]$^-$** are similar at 2.471(2) and 2.507(2) Å, respectively.

Table 2.2: Selected structure metrics and NMR Data for **[1(H$_2$)]$^-$** to **[3(H$_2$)]$^-$**

Metric	**[1(H$_2$)]$^-$** [a]	**[2(H$_2$)]$^-$** [a]	**[3(H$_2$)]$^-$**
Co–M (Å)	2.471(2)	2.383(5)	2.465(1)
r[b]	1.00	0.96	0.92
M–P (Å)	2.144(2)	2.157(9)	2.201(9)
M–N_{ax} (Å)	2.331(4)	2.454(2)	2.472(2)
M–N_{eq} (Å)	1.908(4)	1.965(2)	2.131(9)
ΣP–Co–P (deg)	356.0(6)	354.4(3)	354.3(4)
ΣN_{eq}–M–N_{eq} (deg)	344.84(2)	337.03(1)	337.2(9)
M–N_3 plane (Å)	0.436	0.555	0.599
Co–P_3 plane (Å)	0.249	0.294	0.306
J_{HD} (Hz)	28.5	27.6	26.3
T_{1min_obs} (ms)[c]	26	27	29
T_{1min_calc} (ms)[d]	44	45	52
d_{HH} (Å)	0.96(1)[e] 0.97(1)[f]	0.98(2)[e] 0.98(1)[f]	1.00(1)[e] 1.00(1)[f]

[a] All values are averaged, Z'=2. [b] Ratio of the Co–M bond length to the sum of respective covalent radii.[54-55] [c] Observed at 400 Mhz. [d] Scaled and corrected as discussed in the text. [e] Value obtained from J_{HD}. [f] Value obtained from T_{1min_calc}

To compare Co−M interactions in **[1(H$_2$)]$^-$** to **[3(H$_2$)]$^-$**, a particularly useful parameter is the covalent ratio (*r*) of the Co−M bond distance to the sum of the metals' tabulated covalent radii.[54-55] The *r* values of **[1(H$_2$)]$^-$** to **[3(H$_2$)]$^-$** decrease significantly from 1.00 to 0.92, and suggest a strengthening of the Co→M interaction for M = Al < Ga < In.

Because X-ray crystallography cannot accurately resolve positions of hydrogen atoms, the H_2 ligand cannot be accurately located. However, the presence of the H_2 ligand is structurally inferred from the difference Fourier maps which show a relatively concentrated volume of excess electron density in the apical cobalt binding site (bottom, Fig 2.8). Moreover, the nearly ideal trigonal structure of **[1(H₂)]⁻** to **[3(H₂)]⁻** is inconsistent with a H−Co(μ−H)M structure, which would be anticipated to widen one P–Co–P angle to accommodate a hydride ligand.[7]

2.3.4 Computational Studies of Co(η^2–H_2) complexes

To further probe the nature of the Co−H_2 bonding, density functional theory (DFT) calculations were performed (M06−L, full ligand, Fig 2.9, see experimental for full details) on complexes **[1(H₂)]⁻** to **[3(H₂)]⁻**. Three structural isomers were investigated: a non-classical dihydrogen adduct Co(η^2−H_2)ML, a terminal dihydride Co(H)$_2$ML, and finally a

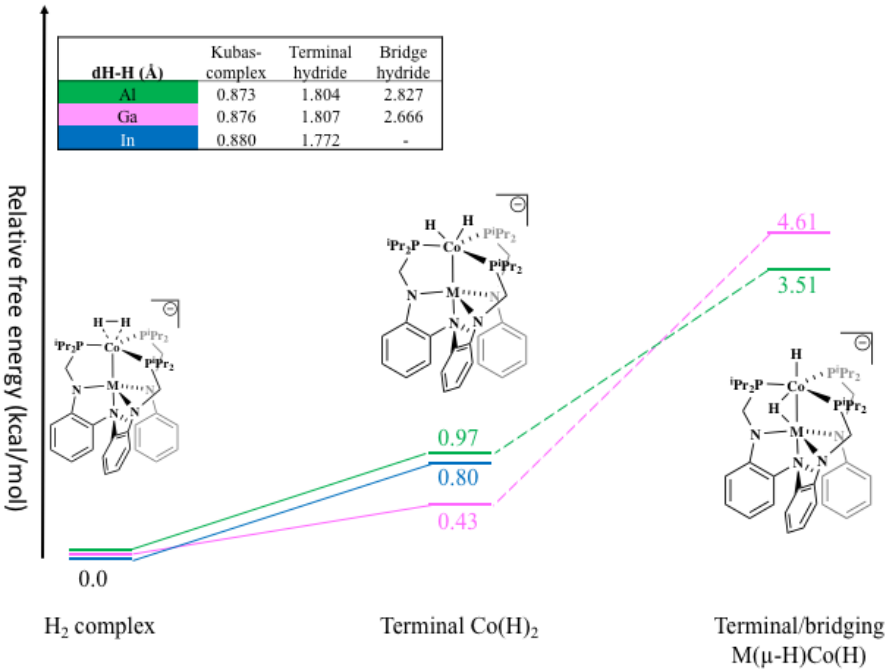

Figure 2.9: Calculated energy profile of structural isomers of **[1(H₂)]⁻** to **[3(H₂)]⁻** with M06-L along with the interatomic distances H-H distances in each type of structure. Values shown are in kcal/mol with respect to the H_2 complex.

bridging/terminal dihydride H−Co(μ−H)ML. Of note, all three isomers were optimized for M = Al and Ga. A stable structure of the bridging isomer, H−Co(μ−H)In, for M = In could not be found, suggestive of instability. Across the Co−M series, the non-classical dihydrogen adduct (d_{HH} ~ 0.87 to 0.88 Å) was energetically lower than both the terminal dihydride (ΔG° = 0.4 to 1.0 kcal/mol, d_{HH} ~ 1.8 Å), and the bridging/terminal dihydride structural isomers (ΔG° = 3.5 to 4.6 kcal/mol, d_{HH} > 2.6 Å). The small energy difference between the H_2 adduct and terminal dihydride species is within the error of the theory employed and are predicted to be isoenergetic. Furthermore, the small energy difference may suggest facile H_2 activation at Co^{-I}, which is consistent with the H/D scrambling observed for **[1(H₂)]**$^-$ to **[3(H₂)]**$^-$. Of interest is the overall energy for which H_2 may undergo oxidative addition. The oxidation to yield a terminal dihydride with no bridging Lewis-acidic interaction is nearly thermoneutral and suggests that complexes **[1(H₂)]**$^-$ to **[3(H₂)]**$^-$ may exhibit reactivity characteristic of metal hydrides. Furthermore, there is a minimal energetic consequence to reorganize this terminal Co(H_2) motif to a bridging M(μ–H)CoH motif.

2.4 Reactivity studies of Co(η^2–H_2) complexes

2.4.1 Reactivity studies with dinitrogen

A hallmark of many dihydrogen complexes is that they oftentimes undergo exchange reactions with a variety of other small molecules.[4, 6, 56] From a thermodynamic standpoint, the substitution of H_2 for other small molecules is entropically favored in light of the high absolute entropy of H_2 and its ease of extrusion in the form of a gas.

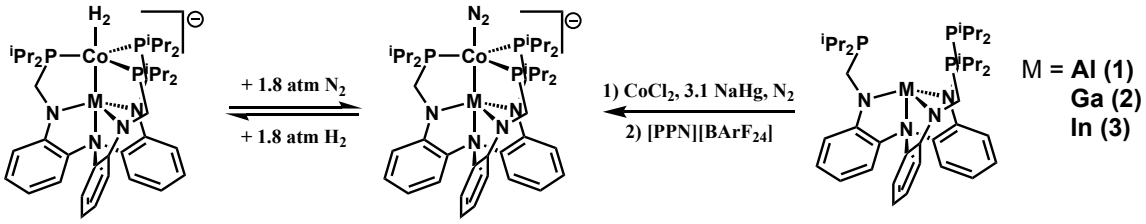

Figure 2.10: Reactivity of **[1(H₂)]**$^-$ to **[3(H₂)]**$^-$ with N_2 and independent synthesis of **[1(N₂)]**$^-$ to **[3(N₂)]**$^-$ as PPN^+ salts.

We first examined the reaction of complexes **[1(H₂)]**$^-$ to **[3(H₂)]**$^-$ with N_2. This reaction proceeds rapidly to generate diamagnetic d^{10} dinitrogen complexes, **[1(N₂)]**$^-$ to **[3(N₂)]**$^-$, by comparison of ^{31}P NMR signatures to isolated **[1(N₂)]**$^-$ and independent synthesis.[34] In **[1(N₂)]**$^-$ to **[3(N₂)]**$^-$ the N_2 is coordinated terminally to the cobalt center with modest activation (Fig. 10, *vide infra*). The ^{31}P NMR of this reaction is in agreement with the of the addition of π-base such as N_2, which is expected to withdraw electronic density from metal centers via π-backbonding.[53] In this respect, there is an upfield shift of ca. 16-18 ppm between the ^{31}P shift of the corresponding H_2 and N_2 fragments for each supporting metal atom (Fig. 2.11). The ^{1}H NMR spectra of **[1(N₂)]**$^-$ to **[3(N₂)]**$^-$ are similar to that recorded for the dihydrogen complexes with the exception of the Co(η^2–H_2) resonance.

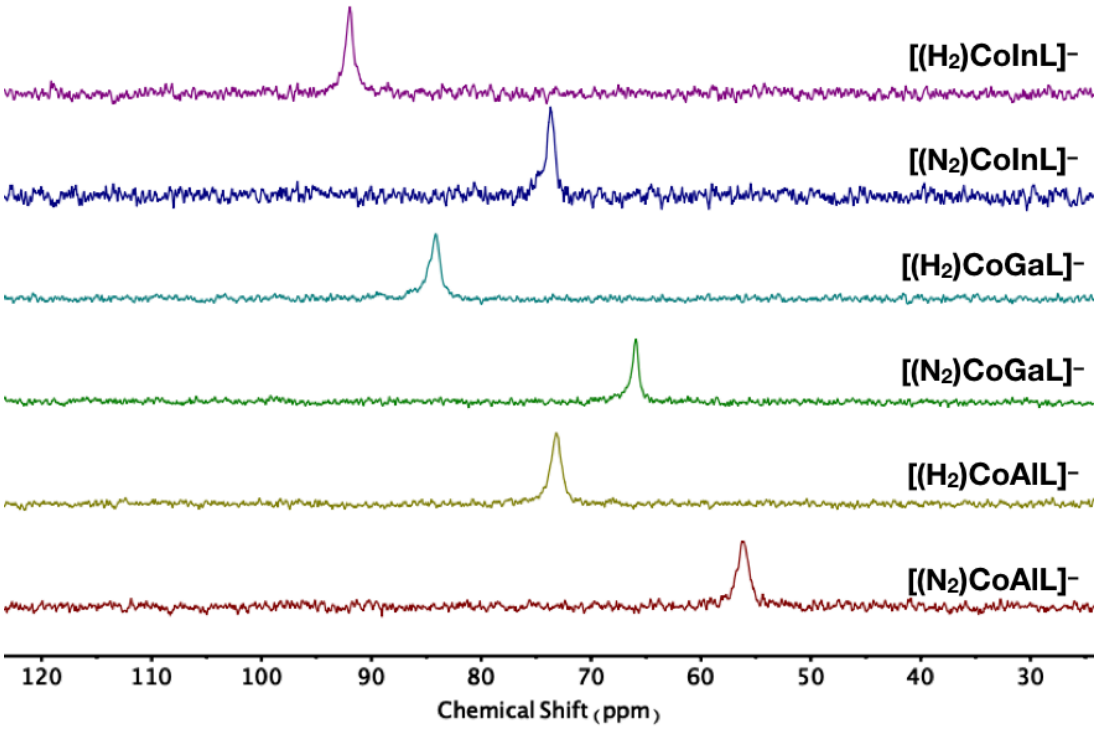

Figure 2.11: Overlaid ^{31}P NMR (THF-d_8) spectra of **[1(H$_2$)]$^-$** to **[3(H$_2$)]$^-$** and their N_2 analogs, showing the changes in the chemical shift before and after exposure to N_2.

Further validation of the product of theses reactions comes from their independent synthesis. The dinitrogen complexes **[1(N$_2$)]$^-$** to **[3(N$_2$)]$^-$** are easily synthesized as bright yellow crystalline solids by the NaHg reduction of LM and $CoCl_2$ mixture under 1 atm of N_2. As had been noted for **[1(N$_2$)]$^-$,** these conditions produce the solvated alkali salts of the N_2 species.[34] For the sake of isolation, the convenient metathesis reagent [PPN][BArF$_{24}$], allows for the exchange of the sodium cation for weakly-coordinating PPN$^+$ cation (BArF$_{24}$ = tetrakis(3,5-bis(trifluoromethyl)phenyl)borate).[41] While PPN$^+$ salts of **[1(N$_2$)]$^-$** to **[3(N$_2$)]$^-$** are substantially less soluble than their analogous K$^+$ or Na$^+$ analogs, they can be isolated on 0.5-0.75g scales in a highly pure and easily recrystallizable form. Furthermore, the PPN$^+$ salts have the added benefit that the cation is free of solvent molecules, which

permits accurate stoichiometric control. The lack of solvent molecules permits accurate elemental analysis to be obtained (short of the N content, which is often problematic for N_2 complexes). The presence of the N_2 ligand is unequivocally evidenced by IR spectroscopy (KBr) in which the terminal N_2 stretches at 1981, 1995, and 2021 cm^{-1} are observed for the PPN^+ salts of **[1(N₂)]⁻** to **[3(N₂)]⁻** respectively. Worth noting is that the addition of H_2 to solutions of **[1(N₂)]⁻** to **[3(N₂)]⁻** at pressures as low as 1.8 atm rapidly leads to **[1(H₂)]⁻** to **[3(H₂)]⁻**, a reaction that will be further developed in the following chapter due to its synthetic utility.

2.4.2 Crystallographic studies of terminal Co(N₂) complexes

Given the relatively small, but growing, number of cobalt dinitrogen complexes in the literature, single crystal studies of complexes **[2(N₂)]⁻** and **[3(N₂)]⁻** were performed to further validate their composition. The formation of these species was identified by former student Dr. P. Alex Rudd, who was able to structurally characterize the aluminum complex as a lithium salt, [Li(crypt-222)][(N_2)CoAlL], and strongly evidenced the identity of the M = Ga, In analogs by NMR and IR spectroscopies.[57]

When isolated as PPN^+ salts, complexes of **[1(N₂)]⁻** to **[3(N₂)]⁻** are highly crystalline, and single crystals are easily obtained from layered THF/Et_2O or DME/Et_2O mixtures. Akin to their H_2 analogs, crystalline species are pale-yellow due to their d^{10} formulation. Due to the inherent asymmetry of the PPN^+ residue, crystalline specimens typically have diffraction patterns that are consistent with primitive monoclinic or triclinic unit cells. This is noteworthy, as salts of 18-crown-6 and crypt-222 typically lead to poor

crystals belonging to rhombohedral or orthorhombic settings when paired with an anion in the H_3L^{iPr} framework.

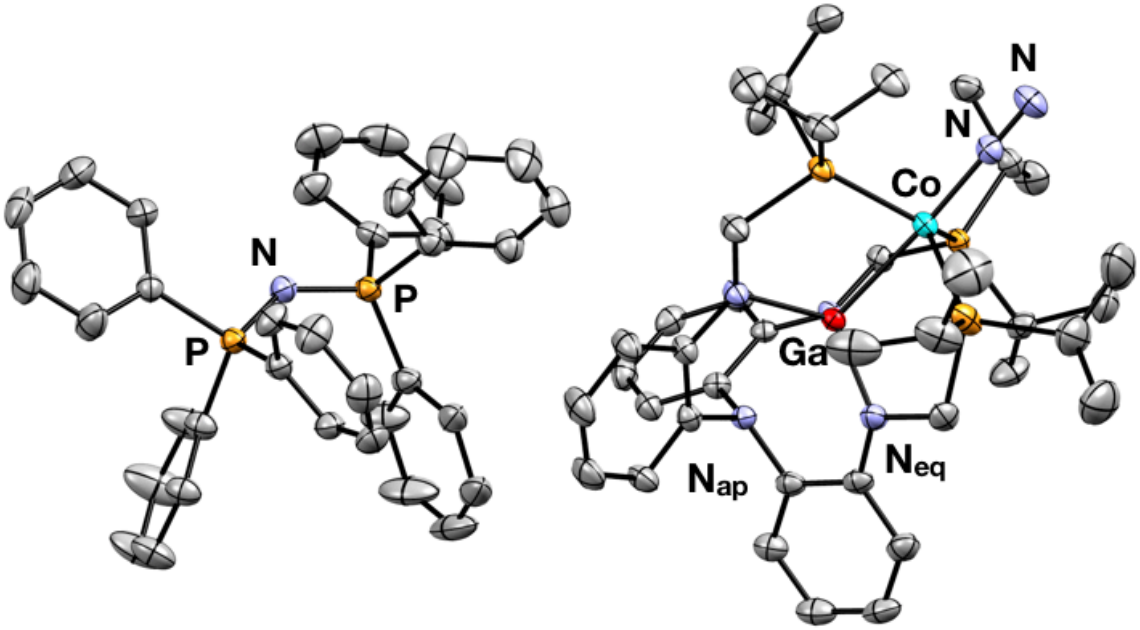

Figure 2.12: Molecular structure of [PPN]**[2(N₂)]**, rendered at 50% thermal ellipsoid probability, showing both cation and anion. Hydrogen atoms and crystallization solvents are omitted for clarity.

Complex **[2(N₂)]**$^-$ crystallizes in the monoclinic space group P-1 with one molecule per asymmetric unit and three molecules of ordered THF (Fig 2.12). As an example of the utility of the PPN^+ cation the ion pair is shown in Fig 2.12. The bond distances are comparable to other PPN^+ moieties, possessing C_1 symmetry due to the asymmetric nature of the P–N–P linkage. There are important π-π stacking interactions between the PPN^+ residue and the aryl rings of the ligand, which are believed to facilitate the growth of high-quality single crystals. The presence of a terminal N_2 ligand is directly observed in the connectivity of **[2(N₂)]**$^-$. There is a noticeable pyramidalization of the Ga atom in the tris(amide) pocket to accommodate the addition of the N_2 ligand. The structure of **[3(N₂)]**$^-$

is isomorphous (P-1) to **[2(N₂)]**⁻ with the exception of the In atom (Fig 2.13) and likewise contains three THF molecules in the unit cell.

The geometries of the cobalt center in **[2(N₂)]**⁻ and **[3(N₂)]**⁻ are similar to that reported for its aluminum congener, [Li(crypt-222)]**[1(N₂)]**, with a few subtle differences. The respective Co–Ga and Co–In distances, 2.439(1) and 2.506(1) Å respectively, are both shorter than the aluminum congener when examined as their normalized formal shortness ratio, *r*. There is a noticeable pyramidalization of the Lewis acid from its respective N_3 plane when comparing **[1(N₂)]**⁻ to **[2(N₂)]**⁻ or **[3(N₂)]**⁻. Taken together, the shortening of the Lewis acid-cobalt bond and the pyramidalization of the supporting metal suggest a formal strengthening of the interaction. This is further supported by the continual decrease of *r* as a function of the Lewis acid, in the order Al > Ga > In. One might expect this trend based on hard-soft acid-base theory as the more diffuse 4p/5p orbitals of Ga and In engender better-matched interactions with "soft," Co than the "hard," 3p orbitals of Al.[58]

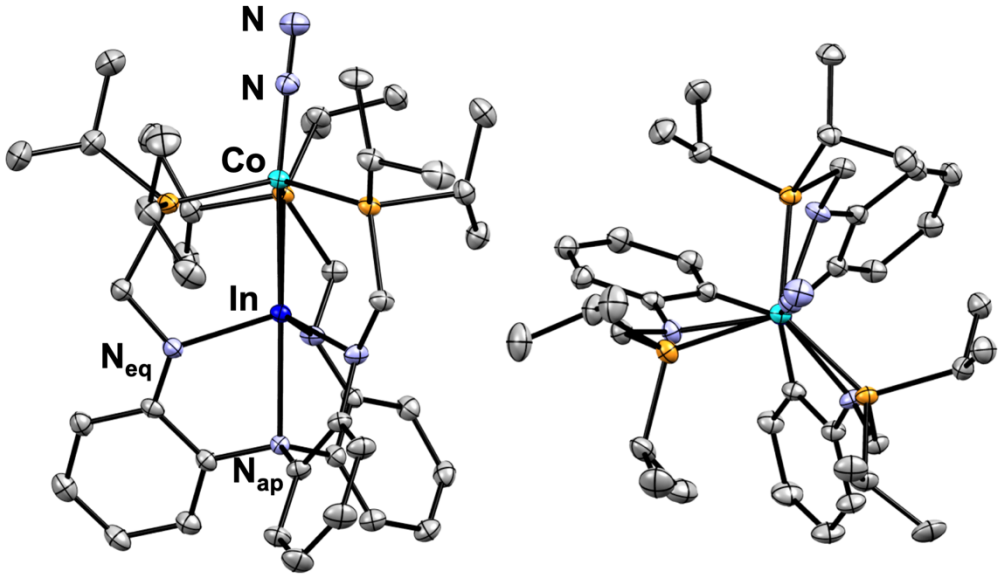

Figure 2.13: Molecular structure of **[3(N₂)]**⁻ rendered at 50% thermal ellipsoid probability both perpendicular (left) and coincident (right) to the In–Co axis. Hydrogen atoms, PPN^+ cation, and solvent molecules omitted for clarity

This effect manifests itself in the N_2 ligand for which stretching frequencies reflect increasingly worse π-backbonding. It should be noted however, that this may be an oversimplification. While the N_2 stretching frequency does become less activated with stronger Lewis acid-cobalt interaction (from 1981 to 2021 cm^{-1} for **[1(N₂)]⁻** to **[3(N₂)]⁻**), the N–N bond distance elongates slightly from 1.110(8) to 1.125(4) Å across the series, which is contrary to the expectation (albeit statistically insignificant).[59] Nevertheless, the metrics of **[1(N₂)]⁻** to **[3(N₂)]⁻** support the notion that as the size of the metal increases, the strength of the Lewis acid-cobalt interaction increases as well.

Table 2.3: Selected metrics for of **[1(H₂)]⁻** to **[3(H₂)]⁻**

parameter	**[1(N₂)]⁻**	**[2(N₂)]⁻**	**[3(N₂)]⁻**
Co–M (Å)	2.507(2)	2.439(1)	2.506(1)
r [a]	1.02	0.99	0.94
M–P (Å)	2.177(1)	2.206(1)	2.251(1)
$M–N_{apical}$ (Å)	2.324(6)	2.473(1)	2.460(2)
$M–N_{eq}$ (Å)	1.898(3)	1.963(3)	2.135(2)
ΣP–Co–P (deg)	351.29(2)	352.16(1)	350.13
ΣN_{eq}–M–N_{eq} (deg)	345.34(7)	336.5(1)	336.12
$M–N_3$ plane (Å)	0.428	0.581	0.615
$Co–P_3$ plane (Å)	0.385	0.358	0.411
$Co–N_2$ (Å)	1.789(3)	1.783(3)	1.776(3)
N–N (Å)	1.110(8)	1.122(5)	1.125(4)
ν(N_2) (cm^{-1})[b]	1981	1995	2021

[a] Ratio of the Co–M length to the sum of respective covalent radii.[54-55] [b] Recorded as KBr pellet

It is interesting to note that the trend of N_2 activation in of **[1(N₂)]⁻** to **[3(N₂)]⁻**, is inverse to that observed for **[1(H₂)]⁻** to **[3(H₂)]⁻** (*vide supra*). Namely, complexes **[1(H₂)]⁻** to **[3(H₂)]⁻** activate the H_2 ligand in the order Al < Ga < In, whereas **[1(N₂)]⁻** to **[3(N₂)]⁻** activate N_2 in the opposite order, In < Ga < Al. This might reflect the nature of the Lewis-

acidic metalloligand acting as a σ-acceptor, however we have not developed a detailed reasoning for these opposing trends.

2.4.3 Oxidative addition of $PhSiH_3$

Given that the $[CoML]^-$ fragment is capable of activating both H_2 and N_2 ligands, we sought to examine if direct cleavage of E–H bonds weaker than H_2 was feasible. To this end we examined the reaction of $PhSiH_3$ with the hope that the π-basic metal center would be capable of direct oxidative addition of the Si-H bond.[60-61] This strategy is often realized for metal complexes that are strong activators of H_2 and N_2 and frequently leads to interesting poly-hydride or metal silyl compounds.[62-63]

The addition of an excess of $PhSiH_3$ to **[1(H₂)]⁻** or **[2(H₂)]⁻** results in the formation of a new C_3 symmetric species as indicated by both ^1H and ^{31}P NMR that is assigned as the hydrido-silyl complexes **[1-H(PhSiH₂)]⁻** or **[2-H(PhSiH₂)]⁻**. With **[3(H₂)]⁻** sluggish reactivity and eventual decomposition to an intractable mixture was observed. As the NMR spectra of **[1-H(PhSiH₂)]⁻** and **[2-H(PhSiH₂)]⁻** are nearly identical, only the details pertaining to **[1-H(PhSiH₂)]⁻** will be discussed in detail here (see experimental for details pertaining to **[2-H(PhSiH₂)]⁻**). Both species were obtained as potassium salts for single crystal and NMR studies.

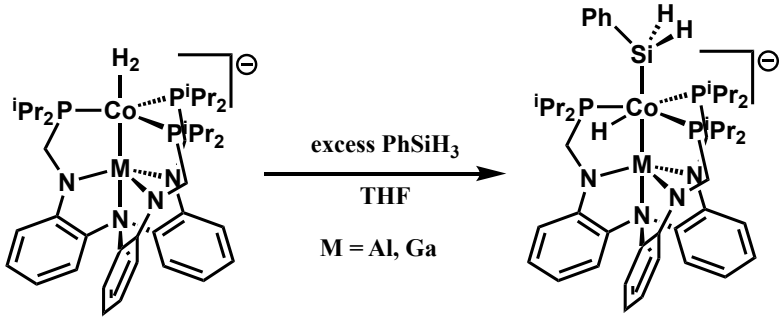

Figure 2.14: Synthesis of **[1/2-H(PhSiH₂)]⁻** as potassium salts.

In addition to the expected signals for the ligand framework, the ^{1}H NMR of **[1-H(PhSiH$_2$)]$^-$** reveals a resonance at ca. -14.2 ppm that is indicative of a Co-H rather than an agostic σ-PhSiH$_3$ adduct (typically near –1 to –3 ppm, see Fig 2.15). This hydride resonance shows signs of small coupling to ^{31}P nuclei and the ^{1}H nuclei attached to the PhSiH$_2$ fragment and appears as a quintet in the ^{1}H NMR spectrum. The coupling to the PhSiH$_2$ protons to the ^{31}P nuclei is evidenced by the collapse of the observed quintet into a doublet ($^{2}J_{PH}$ = 7.7 Hz) after ^{31}P decoupling. The residual coupling is also observed in the ^{1}H NMR region from 5.5-4.5 ppm for which there are two distinct ^{1}H resonances (a doublet and doublet of quartets) that each integrate to one proton with respect to the ligand framework. Based on the chemical shift of free PhSiH$_3$ (4.3 ppm in CDCl$_3$), these resonances are assigned as the two SiH protons. One of SiH resonances (5.3 ppm) appears as a quartet with J = 8.7 Hz, and after ^{31}P decoupling, this signal collapses into a singlet. The other SiH signal (5.0 ppm), gives rise to a more complicated splitting pattern that is best described as a doublet of quartets. The smaller coupling is due to the presence of the CoH, which is likewise a doublet with J = 7.7 Hz when the ^{31}P nuclei are decoupled. Akin to the other SiH resonance, the quartet arises from ^{31}P-H coupling with a value of 14.5 Hz. The complicated pattern observed arises due to the approximately scalar relationship between the two coupling constants (14.5 Hz /7.7 Hz ~ 2). In line with the observation that each ^{31}P nuclei couples equivalently to the corresponding Si-H resonances, the ^{31}P NMR spectrum (and ^{31}P{^{1}H}) reveals a sharp singlet at 58.7 ppm for M = Al and at 67.5 ppm for M = Ga. It is interesting that the room temperature ^{31}P NMR shows a sharp resonance in light of the asymmetry that is apparent in the ligation of the PhSiH$_2$ ligand. It is possible that on lowering the temperature that each ^{31}P environment may become inequivalent.

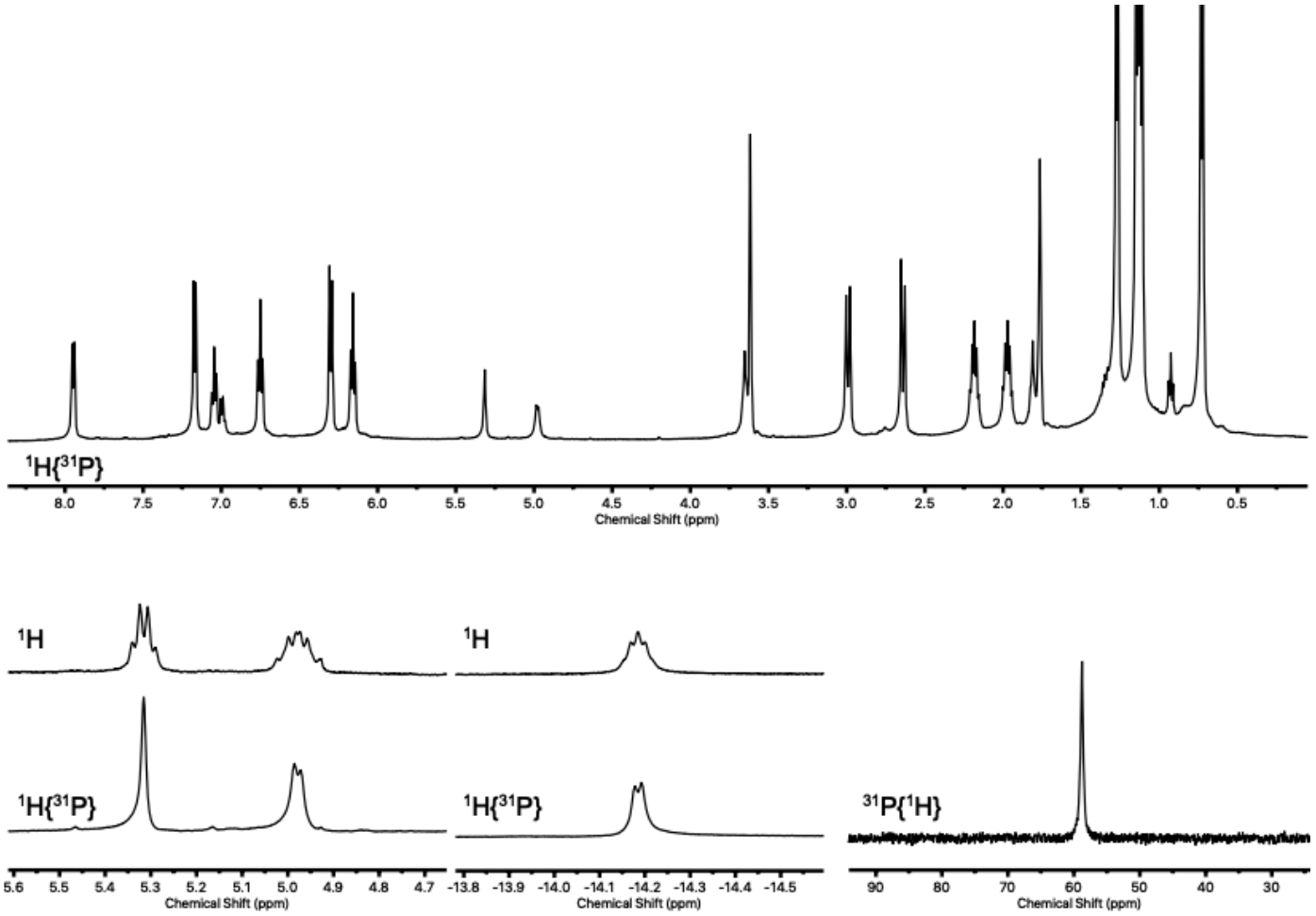

Figure 2.15: Overlaid NMR spectra for $[K(THF)_4]$**[1-H(PhSiH$_2$)]** recorded in THF-d_8. Top, $^{1}H\{^{31}P\}$ NMR spectra. Bottom-left, ^{1}H NMR (5.5-4.7ppm) showing the SiH resonances. Bottom–middle, expanded ^{1}H NMR region showing the Co-H signals. Bottom–right, ^{31}P NMR.

2.4.4 Crystallographic studies of hydride-silyl cobalt complexes

Crystalline specimens of **[1-H(PhSiH$_2$)]$^-$** and **[2-H(PhSiH$_2$)]$^-$** were both isolated as K^+ salts. For M = Al, **[1-H(PhSiH$_2$)]$^-$** crystallizes as large blocks from cold DME/hexane mixtures in the orthorhombic space group *Pca2$_1$* with Z' = 2 (Fig. 2.16). The K^+ ion is not encapsulated and is coordinated by four DME molecules giving rise to $K^+(C_4H_{10}O_2)_4$. The quality of the structure is sufficient to preliminarily locate the Co-H, which lies mainly in the coordination sphere of the cobalt atom, but with a noticeable influence from the $PhSiH_2$ moiety. It is well appreciated that metal silyl complexes engage in a similar bonding continuum to dihydrogen complexes.[61]

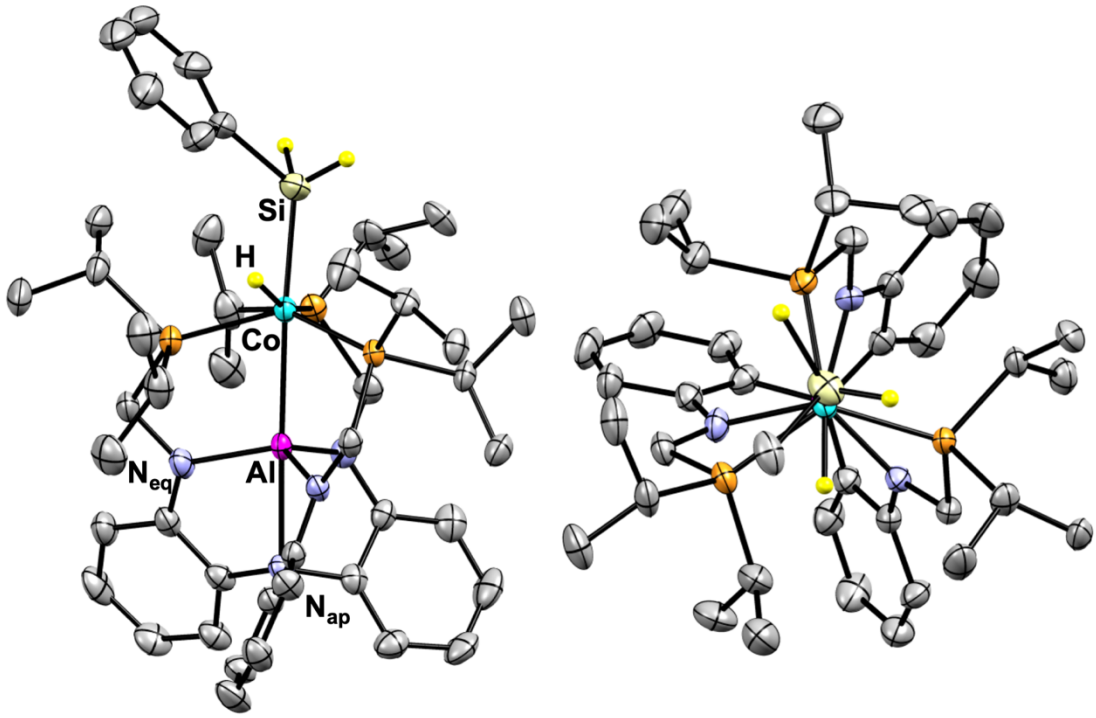

Figure 2.16: Molecular structure of **[1-H(PhSiH$_2$)]$^-$** at 50% thermal ellipsoid probability with selected hydrogen atoms and cation omitted for clarity. On the right, only the ipso carbon atom of the $PhSiH_2$ ligand is shown for clarity.

With a locked solution-state structure in mind, a view along the Co–Al bond distance reinforces that the SiH environments are unique with respect to the Ph ring of the

$PhSiH_2$ ligand. This topological feature observed for **[1-H(PhSiH$_2$)]$^-$** is largely the same for **[2-H(PhSiH$_2$)]$^-$** which was obtained as the K^+(18-crown-6)(THF) salt. Much like [1-**H(PhSiH$_2$)]$^-$**, **[2-H(PhSiH$_2$)]$^-$** crystallizes as large yellow-orange blocks in the orthorhombic space group *Pbca*, but with Z'=1. Notable is the persistent C-H interaction between the K^+(18-crown-6)(THF) unit and the aromatic rings of the ligand framework as shown in Fig 2.17.

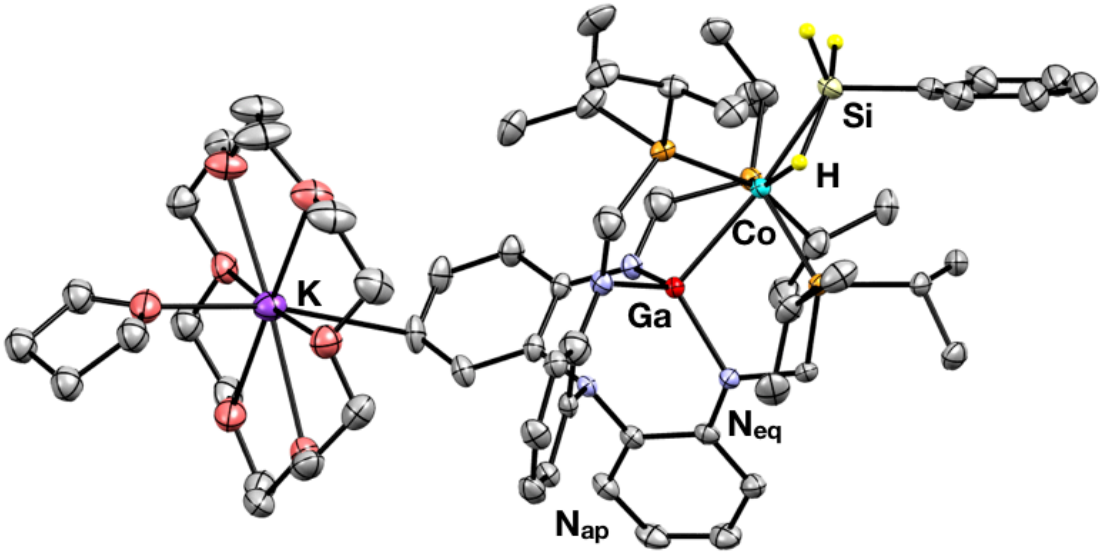

Figure 2.17: Molecular structure of [K(18-crown-6)(THF)]**[2-H(PhSiH$_2$)]** at 50% thermal ellipsoid probability showing selected hydrogen atoms and cation.

Generally, the metrics of both **[1-H(PhSiH$_2$)]$^-$** and **[2-H(PhSiH$_2$)]$^-$** appear to indicate a low spin Co^I coordination environment featuring a terminal silyl ligand. The identity of the silyl ligand is corroborated with comparison the Co-Si bonds with those in the literature (see Table 2.4).[62-67] For example, a triphosphinosilane ligand $^{Ph}P_3SiH$ was used to support a Co^I species with a Co-Si bond distance of 2.245(2) Å.[67] Similarly, N_2 and H_2 complexes supported by a trigonal phosphine-silatrane ligand showed Co-Si bond distances of 2.233(1) and 2.205(3), respectively.[23] There are also examples to the contrary in which $PhSiH_3$ acts as only a σ-donor. For example, the species [^{iPr}DBI]Fe(H_3SiPh)$_2$

features two distinct $PhSiH_3$ σ-only ligands where the longer Fe-Si bond distances of 2.4733(7) and 2.3266(8) clearly indicate that the SiH bond is preserved.[68] Hillhouse has reported an unsupported nickel hydrido-silyl species with a Ni-Si distance of 2.245(2) Å which is relevant to the discussion at hand.[63]

Table 2.4: Selected metrics for **[1-H(PhSiH₂)]⁻** and **[2-H(PhSiH₂)]⁻**

parameter	**[1-H(PhSiH₂)]⁻**	**[2-H(PhSiH₂)]⁻**
Co–M (Å)	2.579(5)	2.457(1)
r[a]	1.04	0.99
Avg. M–P (Å)	2.19(1)	2.20(1)
$M–N_{apical}$ (Å)	2.288(5)	2.473(1)
$M–N_{eq}$ (Å)	1.889(5)	1.950(1)
ΣP–Co–P (deg.)	346.4(2)	347.9(1)
ΣN_{eq}–M–N_{eq} (deg.)	346.5(2)	336.3(1)
$M–N_3$ plane (Å)	0.409	0.561
$Co–P_3$ plane (Å)	0.472	0.447
Co–Si (Å)	2.257(5)	2.255(1)

[a] Ratio of the Co–M bond length to the sum of respective covalent radii.[54-55]

It must be stressed that the interpretation of the $^1H/^{31}P$ NMR and X-ray crystal structures are only preliminarily assignments of **[1/2-H(PhSiH₂)]⁻** as low-spin Co^I hydrido-silyl complexes. There are a number of experiments that could be performed to further evidence this electronic structure. For example, a T_{1min} study of both the $PhSiH_2$ protons and the Co-H should shed light on these resonances. Furthermore, IR spectroscopy should indicate the extent of activation provided that the Co-H stretching frequency can be located. Nonetheless, there appears to be minimal precedent for a low-spin Co^I hydrido-silyl complex. Most examples of silyl ligands belong to tethered phosphine-silicon ligand frameworks where the σ-SiH interaction can be enforced geometrically.[10, 23, 69]

Furthermore, the majority of cobalt silyl complexes in the literature appear to exhibit Co^{III} (or higher) spin states, with the notable exception of the triphoshine-silyl ligand reported by Peters et al.[61-62, 64, 70] Lastly, it would be interesting to develop a catalytic scheme in which $PhSiH_3$ its derivatives could be transferred to alkenes. These results suggest that H-B oxidative addition might also be feasible for hydroboration chemistry.

2.5 Conclusions

Complexes **[1(H₂)]⁻** to **[3(H₂)]⁻** are rare examples of d^{10} dihydrogen adducts. Previously, the only well-defined examples were the $Ni^0(\eta^2–H_2)M$ species (M = B, Ga, In).[8-9, 31] In common, all the d^{10}-H_2 adducts feature a d^{10} center directly appended to a Lewis acidic group 13 (B, Al, Ga, or In) metalloligand. Based on this common design factor present in nearly all known d^{10} dihydrogen adducts to date, we propose that their stability is due to an apparent inverse *trans*-influence of the group-13 metalloligand, which acts as a σ-acceptor. To our knowledge, the inverse *trans*-influence has been applied primarily to actinide[71-73] (e.g. uranium) and lanthanide[74] complexes. It is worth mentioning that the relationship between the extent of H_2 activation and the strength of the Lewis acid-cobalt interaction is a superficial inverse *trans*-influence only. Care should be taken to not mistake this description with the well-established molecular orbital derived inverse *trans*-influence of the f block.[71]

However, the d^{10}-H_2 complexes reported do highlight the utility of the Z-type acceptor ligands in stabilizing unusual metal fragments. Namely, **[1(H₂)]⁻** to **[3(H₂)]⁻** are distinct from typical Kubas dihydrogen complexes, where the H_2 ligand is *trans* to a strong σ-donor such as CO.[4] This bonding has been rationalized using the anti-symbiotic effect,

where the strong metal−CO bond is favorably poised opposite to the weak metal−H_2 interaction.[75] Conversely, in **[1(H₂)]⁻** to **[3(H₂)]⁻** the H_2 ligand is *trans* to a strong σ-acceptor, allowing for symbiotic (H_2)→Co and Co→M bonding interactions that reinforce each other. This relationship is also not limited to these d^{10} cobalt complexes is well demonstrated by the isoelectronic NiML series. Under 1 atm H_2, NiAlL does not bind H_2 appreciably, whereas Ni(η^2–H_2)GaL binds H_2 reversibly. On the other hand, Ni(η^2-H_2)InL is stable to vacuum. In the present case, **[1(H₂)]⁻ to [3(H₂)]⁻** bind H_2 irreversibly and are thermally stable.

The ability to stabilize species such as **[1(H₂)]⁻** to **[3(H₂)]⁻** allowed for preliminary reactivity studies where the H_2 ligand can be displaced by donors such as N_2 and $PhSiH_3$ (for M = Al, Ga). The N_2 complexes complete a trio of reduced Co^{-I} dinitrogen complexes, **[1(N₂)]⁻** to **[3(N₂)]⁻**, and add to this growing class of complexes in the literature.[43] The N_2 species exhibiting a unique activation of the N_2 moiety that may be attributed to the σ-accepting ligands around cobalt. The ability of the 16e⁻ fragment [CoML]⁻ to activate weaker E-H bonds is demonstrated by the reaction of **[1(H₂)]⁻** and **[2(H₂)]⁻** with $PhSiH_3$ which results in what appears to be oxidative addition of the SiH bond across a Co^{-I} center to yield the unsupported Co^{I} hydrido-silyl complexes, **[1/2-H(PhSiH₂)]⁻**.

2.6 Experimental Section

General Considerations. Unless otherwise stated, all manipulations were performed under a purified Argon atmosphere using standard Schlenk techniques or inside of an MBraun glovebox maintained < 1 ppm O_2 and H_2O. Standard solvents were deoxygenated by sparging with Ar and dried by passing through activated alumina columns of an SG Water solvent purification system. Deuterated solvents were purchased from Cambridge Isotope Laboratories, Inc., degassed via freeze–pump–thaw cycles, and stored over activated 4 Å molecular sieves. All other reagents were purchased from commercial vendors and used without purification unless otherwise noted. Solutions of Li[$HBEt_3$] and K[$HBEt_3$] were purchased from Sigma–Aldrich and stored at –25˚C. 18–crown–6 was dried by recrystallization from acetonitrile, and heating *in vacuo* at 60˚C for 4 hours. HD gas was prepared by the addition of degassed D_2O (~ 1mL) to excess $LiAlH_4$ (~250mg) under vacuum at -78˚C and then trapping the generated gas in a pre-evacuated manifold. ^1H and ^{31}P NMR spectra were recorded on Bruker 400 MHz spectrometer. ^1H NMR were referenced to the internal solvent residual signal or an external reference for ^{31}P (H_3PO_4).[76] Longitudinal relaxation times (T_{1min}) were acquired using the standard inversion recovery pulse sequence method. The neutral ligand (N(*o*-($NHCH_2PiPr_2$)C_6H_4)$_3$ (H_3L), and LAl, LGa, and LIn were synthesized according to literature procedure.[31, 33] [PPN][$BArF_{24}$] was prepared utilizing the reported preparation but on a 10g scale.[41]

General Synthesis of [**1(H$_2$)**]$^-$ to **[3(H$_2$)]**$^-$anions as [K(18-crown-6)]$^+$ or Li^+ salts:

A solution of the appropriate metalloligand in THF (70 μmol, 3 mL THF) was added to a stirred suspension of $CoBr_2$ in THF (70 μmol, 3 mL THF). After the mixture turned

homogeneous, it was cooled to −78˚C, and a solution of K[HBEt$_3$] (1M in THF, 217 µmol, 3.1 equiv.) was added dropwise via microsyringe. Inspection of the reaction mixture showed a small amount of effervescence and the formation of a colorless precipitate (presumably KBr). The yellow-red solution was allowed to warm to room temperature over 12 hours in the glovebox coldwell. The solution was filtered into a vial containing 18-crown-6 (70 µmol) and shaken briefly. The solution was then reduced to 3 mL, and then 4 mL of n-hexane was added causing the precipitation of a microcrystalline precipitate. The solution was then reduced again to 3 mL, and 10 mL diethyl ether was added. The solid was isolated on a glass frit and washed with diethyl ether (M=Ga) or 1:1 DME/Pentane (M=Al, In) (5 x 2 mL) yielding the microcrystalline product, which was further dried in vacuo.

An identical procedure is employed for the isolation of the lithium salt, but Li[HBEt$_3$] is employed (1M, THF) and gives a similar yield. NMR spectra of these species showed no differences in THF-d$_8$ other than the presence of 18-crown-6 ^{1}H resonances. Single crystals of the lithium salts of amenable to single crystal diffraction were grown from DME/pentane for **[1(H$_2$)]**$^-$ and THF/pentane for **[2(H$_2$)]**$^-$ and for **[3(H$_2$)]**$^-$. These bright yellow crystals are extremely air sensitive and thus were mounted in STP oil on a glass slide inside of a glovebox. Upon exposure to air they immediately decompose and fracture.

Characterization of **[1(H$_2$)]**$^-$ to **[3(H$_2$)]**$^-$

[K(18-crown-6)]**[1(H$_2$)]** Yield (46 mg, 61 %). ^{1}H{^{31}P} NMR (ppm, THF-d$_8$, 400 MHz): δ 7.16 (d, J=7.4 Hz, aryl, 3H), 6.68 (t, J=7.6 Hz, aryl, 3H), 6.19 (d, J=7.8 Hz, aryl, 3H), 6.05 (t, J=7.2 Hz, aryl, 3H). 2.75 (br, $CH_2P(^iPr)_2$, 6H), 1.93 (br, C*H*$(CH_3)_2$, 3H) 1.71 (br,

C*H*(CH_3)$_2$, 3H), 1.39 (br, CH(*C*H_3)$_2$, 9H), 1.25(br, CH(*C*H_3)$_2$, 9H), 0.86 (br, CH(*C*H_3)$_2$, 9H), 0.61 (br, CH(*C*H_3)$_2$, 9H), -7.00 (br, Co (η^2–H_2), 2H). $^{31}P\{^1H\}$ NMR (ppm, THF-d_8, 162 MHz): δ 73.2. Elemental analysis consistently showed values that would result from phosphine oxidation of the ligand, or the equivalent to "[K(18-crown-6)]**[1(H$_2$)]** + 3O" and one molecule of DME. Anal. calculated for $C_{51}H_{86}AlCoKN_4O_9P_3$•$C_4H_{10}O_2$ (%) C 54.72, H 8.01, N 4.64. Found, C 54.80, H 7.82, N 4.45.

[K(18-crown-6)]**[2(H$_2$)]** Yield (55 mg, 65 %). $^1H\{^{31}P\}$ NMR (ppm, THF-d_8, 400 MHz): δ 7.14 (d, J=7.4 Hz, aryl, 3H), 6.68 (t, J=7.6 Hz, aryl, 3H), 6.23 (d, J=8.0 Hz, aryl, 3H), 6.06 (t, J=7.3 Hz, aryl, 3H), 2.75 (br, $CH_2P(^iPr)_2$, 3H), 2.60 (br, $CH_2P(^iPr)_2$, 3H), 1.89 (br, C*H*(CH_3)$_2$, 3H), 1.70 (br, C*H*(CH_3)$_2$, 3H). 1.37 (br, CH(*C*H_3)$_2$, 9H), 1.28 (br, CH(*C*H_3)$_2$, 9H), 0.82 (br, CH(*C*H_3)$_2$, 9H), 0.50 (br, CH(*C*H_3)$_2$, 9H), -7.74 (br, Co (η^2–H_2), 2H). $^{31}P\{^1H\}$ NMR (ppm, THF-d_8, 162 MHz): δ 84.5. Elemental analysis consistently showed values that would result from phosphine oxidation of the ligand, or the equivalent to "[K(18-crown-6)]**[2(H$_2$)]** + 3O" and two molecules of THF. Anal. calculated for $C_{51}H_{86}GaCoKN_4O_9P_3$ (%) C 52.81, H 7.47, N 4.83. Found, C 53.07, H 7.61, N 4.72.

[K(18-crown-6)]**[1(H$_2$)]** (3). Yield (51 mg, 71 %). The room-temperature ^1H NMR spectrum was complicated by intermediate site exchange, and the reported ^1H NMR data was recorded at -80˚C. ^1H NMR (ppm, THF-d_8, 400 MHz, -80˚C): δ 7.22 (d, J=7.0Hz, aryl, 3H), 6.64 (t, J=7.0Hz, aryl, 3H), 6.14 (d, J=7.4 Hz, aryl, 3H), 5.99 (t, J=6.9Hz, aryl, 3H), 2.97 (d, J = 9.4Hz, $CH_2P(^iPr)_2$, 3H), 2.49 (d, J= 10.5 Hz $CH_2P(^iPr)_2$, 3H), 1.97 (br, C*H*(CH_3)$_2$, 3H), 1.64 (br, C*H*(CH_3)$_2$, 3H), 1.44 (br, CH(*C*H_3)$_2$, 9H), 1.28 (br, CH(*C*H_3)$_2$

, 9H), 0.81 (br, CH(CH_3)$_2$, 9H), 0.43 (br, CH(CH_3)$_2$, 9H), -7.74 (br, Co (η^2–H_2), 2H). $^{31}P\{^1H\}$ NMR (ppm, THF-d_8, 162 MHz): δ 91.9. Elemental analysis consistently showed values that would result from phosphine oxidation of the ligand, or the equivalent to "[K(18-crown-6)]**[3(H$_2$)]** + 3O" and one molecule of DME. Anal. calculated for $C_{51}H_{86}InCoKN_4O_9P_3$•$C_4H_{10}O_2$ (%) C 51.58, H 7.56, N 4.37. Found, C 51.85, H 7.26, N 4.08

Synthesis of **[1(N$_2$)]**$^-$ to **[3(N$_2$)]**$^-$

The bis(triphenylphosphine)iminium salts of the N_2 cobaltate anions, **[1(N$_2$)]**$^-$ to **[3(N$_2$)]**$^-$ were synthesized via a common procedure which is shown explicitly below for M = Al as an example:

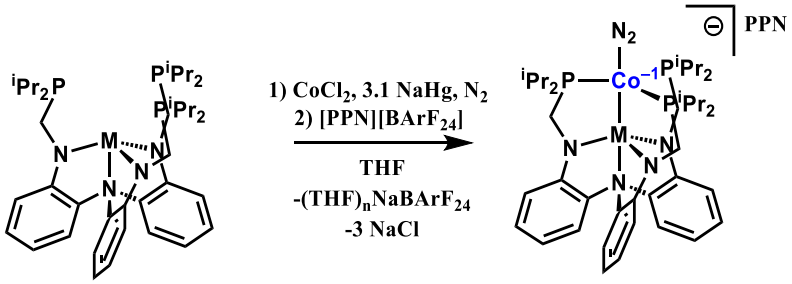

In an Ar glovebox, a 100mL Schlenk flask with Teflon valve was charged with a stir bar and a deep blue-green solution containing LAl (408.1mg, 0.580 mmol) and anhydrous $CoCl_2$ (75.2mg, 0.580mmol) in THF (20mL). This mixture is allowed to stir for 1-2 hours until homogeneous, at which point freshly prepared ca. 1% NaHg (41.3 mg Na, 1.79 mmol) is added at once. The atmosphere of the flask is subjected to static vacuum three times, and the atmosphere is replaced with 1 atm. of ultra-high purity N_2 (ca. 80mL N_2, 3 mmol, ca. 3-5 equiv.). The mixture is stirred overnight yielding a red-yellow solution and a grey

precipitate. The mixture is decanted, filtered, and reduced to 6mL at which point [PPN][$BArF_{24}$] (1g, 0.714mmol) is added as a solid along with a stir bar. The solution is stirred until solids begin to precipitate and then 15mL of Et_2O are added to deposit a microcrystalline yellow solid. The solid is collected on a fritted filter, washed liberally with Et_2O (2x10mL), then finally dried overnight under vacuum to yield 460mg (61% yield) of bright yellow crystalline [PPN]**[1(N_2)]** which is free of $NaBArF_{24}$ by ^{19}F and ^{1}H NMR. The material can be further purified by crystallization from THF/Et_2O or DME/Et_2O.

Characterization of [PPN]**[1(N_2)]:** $^{1}H\{^{31}P\}$ NMR (500 MHz, THF-d_8): δ 7.59-7.45 (m, 30H, PPN), 7.06 (d, J = 7.5 Hz, 3H, ArH), 6.60 (t, J = 7.6 Hz, 3H, ArH), 6.15 (d, J = 7.9 Hz, 3H, ArH), 5.97 (t, J = 7.4 Hz, 3H, ArH), 2.72 (s, 6H, CH_2), 2.37 (s, 3H, $CH(CH_3)_2$), 2.01 (s, 2H, $CH(CH_3)_2$), 1.31 (s, 18H $CH(CH_3)_2$)), 0.88 (s, 18H, $CH(CH_3)_2$)). $^{31}P\{^{1}H\}$ NMR (202 MHz, THF-d_8): δ 56.12 (3P), 21.00 (2P, PPN). IR (KBr): $\nu(N_2)$ = 1981 cm^{-1}. The spectroscopic properties of this species are identical to those previously reported for the (222-crypt)K^+ salt, for which elemental analysis has been obtained previously.

Characterization of [PPN]**[2(N_2)]**: Utilizing LGa (471.7mg, 0.63 mmol), $CoCl_2$ (81.9 mg, 0.63 mmol), and NaHg (44.9mg Na, 1.95 mmol) provided 500mg of a bright yellow crystalline solid [PPN]**[2(N_2)]** (57% yield). The material is recrystallized from DME/Et_2O layering at -30˚C. $^{1}H\{^{31}P\}$ NMR (500 MHz, THF-d_8): δ 7.59-7.45 (s, 30H, PPN), 7.02 (d, J = 7.4 Hz, 3H, ArH), 6.56 (t, J = 7.6 Hz, 3H, ArH), 6.13 (d, J = 7.9 Hz, 3H, ArH), 5.94 (t, J = 7.4 Hz, 3H, ArH), 2.79 (br, 3H, CH_2), 2.58 (br, 3H, CH_2), 2.35 (d, 3H, *CH*$(CH_3)_2$), 2.03 (d, 3H, *CH*$(CH_3)_2$) 1.29 (br, 18H, CH*$(CH_3)_2$*), 0.88 (br, 18H, CH*$(CH_3)_2$*).$^{31}P\{^{1}H\}$ NMR

(202 MHz, THF-d_8): δ 65.86 (3P), 21.00 (2P, PPN). IR (KBr): ν(N_2) = 1995 cm^{-1} Analysis calc. (found) for $[C_{36}H_{30}NP_2][C_{39}H_{60}N_6P_3GaCo]\bullet C_4H_{10}O_2$: C 64.85 (64.75), H 6.89 (7.10), N 6.70 (5.88). Elemental analysis reproducibly showed low analysis values for N content, which may be related N_2 loss.

Characterization of [PPN]**[3(N_2)]**: Utilizing LIn (400.5mg, 0.51 mmol), $CoCl_2$ (65.6mg, 0.51mmol), and NaHg (36mg Na, 1.57mmol) provided 360mg of a [PPN]**[3(N_2)]** as a yellow crystalline solid (50% yield). $^1H\{^{31}P\}$ NMR (ppm, THF-d_8, 500 MHz): δ 7.59 -7.45 (m, 30H, PPN), 7.10 (d, J = 7.6 Hz, 3H, ArH), 6.55 (t, J = 7.6 Hz, 3H, ArH), 6.12 (d, J = 8.0 Hz, 3H, ArH), 5.89 (t, J = 7.3 Hz, 3H, ArH), 2.80 (br, 6H, CH_2), 2.24 (s, 6H, $CH(CH_3)_2$), 1.12 (s, 36H, $CH(CH_3)_2$).$^{31}P\{^1H\}$NMR (162 MHz, THF-d_8) δ 73.67 (3P), 21.00 (2P, PPN). IR (KBr): ν(N_2) = 2021 cm^{-1}. Analysis calc. (found) for $[C_{36}H_{30}NP_2][C_{39}H_{60}N_6P_3InCo]$: C 63.52 (63.42), H 6.40 (6.66), N 6.91 (5.03). Elemental analysis reproducibly showed low analysis values for N content, which may be related N_2 loss.

In-situ generation of H_2 complexes from respective N_2 complexes: 2-6 mg of the [PPN] salts of **[1(N_2)]$^-$** to **[3(N_2)]$^-$** were dissolved in THF-d_8 (0.5mL) and transferred to a J-young NMR tube. The solution was freeze-pump-thawed once, and then H_2 admitted (1 atm. from pressure gauge) when the tube was frozen in liquid nitrogen (ca. 77K). The solution was warmed to room temperature and briefly mixed by means of a vortex mixer. Within the time the spectra could be acquired the substitution of H_2 for N_2 was complete by both ^1H and ^{31}P NMR spectroscopy. The spectral data for these is identical to those reported for the $Li(solv)_n$ and K(18-crown-6) salts other than the resonances attributed to the PPN^+ moiety

in both the ^{1}H and ^{31}P which is listed as follows: ^{1}H: 30H, m, 7.7-7.2 ppm and ^{31}P: 2P, 21.0 ppm.

In-situ generation of dinitrogen complexes from respective dihydrogen complexes: 2-6 mg of **[1(N₂)]⁻** to **[3(N₂)]⁻** (any salt) stirred overnight at room temperature in an N_2 glovebox. Analysis of the mixture shown complete conversion to the N_2 species by ^{1}H and ^{31}P NMR.

Synthesis of [K(18-crown-6)(THF)]**[1-H(PhSiH₂)]**: To a cooled solution (-78˚C) of [K(18-crown-6)(THF)]**[2(H₂)]** (20mg, 18.0µmol) in THF (2mL) was added $PhSiH_3$ (22µL, 180µmol, 10equiv) via microsyringe. The solution is allowed to warm to room temperature overnight giving a bright yellow solution. The ^{1}H NMR of the reaction mixture indicated that the reaction is quantitative. X-ray quality crystals were grown from THF/hexane layering stored in a -30˚C freezer overnight. $^{1}H\{^{31}P\}$ NMR (400 MHz, THF-d_8): δ 7.97 – 7.85 (d, J = 7.0 Hz, 2H, *o*-$PhSiH_2$), 7.09 (d, *J* = 7.5 Hz, 1H, ArH), 7.04 (t, *J* = 6.9 Hz, 2H, *m*-$PhSiH_2$), 7.00 (t, *J* = 7.0 Hz, 1H, *p*-$PhSiH_2$), 6.67 (d, *J* = 8.1 Hz, 3H, ArH), 6.24 (d, *J* = 8.0 Hz, 3H, ArH), 6.09 (d, *J* = 7.6 Hz, 3H, ArH), 5.31 (s, 1H, $PhSiH_2$), 4.98 (d, *J* = 7.0 Hz, 1H, $PhSiH_2$), 3.53 (s, 24H, 18-c-6), 3.01 (d, *J* = 11.9 Hz, 3H, CH_2), 2.49 (d, *J* = 11.9 Hz, 3H, CH_2), 2.19 (hept, *J* = 6.7 Hz, 3H, *CH*$(CH_3)_2$), 1.78 (hept, *J* = 6.7 Hz, 3H, *CH*$(CH_3)_2$), 1.24 (d, *J* = 7.2 Hz, 9H, CH*(CH₃)₂*), 1.13 (d, *J* = 6.9 Hz, 9H, CH*(CH₃)₂*), 1.05 (d, *J* = 7.3 Hz, 9H, CH*(CH₃)₂*), 0.65 (d, *J* = 7.3 Hz, 9H, CH*(CH₃)₂*), -14.83 (d, *J* = 7.4 Hz, 1H, CoH). The ^{1}H NMR spectra shows the following differences when coupled to ^{31}P nuclei: ^{1}H NMR (400 MHz, THF-d_8) δ 5.31 (q, *J* = 8.5 Hz, 1H, $PhSiH_2$), 4.98 (dq, *J* = 12.1, 7.3 Hz, 1H,

$PhSiH_2$), -14.83 (quintet, *J* = 10.3 Hz, 1H, CoH). $^{31}P\{^1H\}$ NMR (203 MHz, THF-d_8): δ 67.5.

Synthesis of $[K(DME)_4]$**[1-H(PhSiH$_2$)]**: For this preparation $[K(DME)_4]$**[1-(H$_2$)]** was used, which is the product of $KHBEt_3$, $CoCl_2$, and LGa as described previously, with the omission of 18-crown-6. A solution of $[K(DME)_4]$**[1(H$_2$)]** (17.2mg, 15.7μmol) was cooled in THF (2mL) to -78˚C at which point 2.1 μL of $PhSiH_3$ (17.3μmol) was added via microsyringe. On warming a small amount of effervescence is noticeable, and the solution become nearly transparent yellow. After stirring overnight, the volatiles are removed in vacuo and extracted into THF-d_8. The ^1H NMR shows that the reaction is quantitative. X-ray quality crystals were grown from DME/Pentane layering. $^1H\{^{31}P\}$ NMR (500 MHz, THF-d_8): δ 7.91 (d, J = 7.2 Hz, 2H,*o*-$PhSiH_2$), 7.13 (d, J = 7.5 Hz, 3H, ArH), 7.01 (t, J = 7.2 Hz, 2H, *m*-$PhSiH_2$), 6.95 (t, J = 7.2 Hz, 1H, *p*-$PhSiH_2$), 6.71 (t, J = 7.6 Hz, 3H, ArH), 6.26 (d, J = 7.9 Hz, 3H, ArH), 6.12 (t, J = 7.3 Hz, 3H, ArH), 5.28 (s, 1H, PhSi*H$_2$*), 4.94 (d, J = 7.8 Hz, 1H, PhSi*H$_2$*), 2.95 (d, J = 11.8 Hz, 3H, CH_2), 2.60 (d, J = 11.9 Hz, 3H, CH_2), 2.15 (hept, J = 7.8, 7.2 Hz, 3H, *CH*$(CH_3)_2$), 1.93 (hept, J = 7.4 Hz, 3H, *CH*$(CH_3)_2$), 1.23 (d, J = 7.2 Hz, 9H, CH*(CH$_3$)$_2$*), 1.11 (d, J = 7.0 Hz, 9H, CH*(CH$_3$)$_2$*), 1.08 (d, J = 7.3 Hz, 9H, CH*(CH$_3$)$_2$*), 0.69 (d, J = 7.3 Hz, 9H, CH*(CH$_3$)$_2$*), -14.22 (d, J = 8.3 Hz, 1H, CoH). The ^1H NMR spectra shows the following differences when coupled to ^{31}P nuclei: ^1H NMR (500 MHz, THF-d_8): δ 5.28 (q, J = 8.7 Hz, 1H, $PhSiH_2$), 4.94 (dq, J = 14.5, 7.7 Hz, 1H, $PhSiH_2$), -14.22 (quintet, J = 7.7 Hz, 1H, $PhSiH_2$). $^{31}P\{^1H\}$ NMR (203 MHz, THF-d_8): δ 58.77.

An improved preparation of protonate ligand, H_3L^{iPr}

Step 1: Tris(2-nitrophenyl)amine [N(*o*-$PhNO_2$)$_3$]: A mixture of 2-(nitrofluorobenzene) (30.5mL, 300 mmol, 4 equivalents), 2-nitroaniline (10g, 72.4 mmol), and K_2CO_3 (60g, 434.4 mmol) in 30mL of benchtop dimethyl sulfoxide were heated to 150˚C with a large football shaped stir bar under N_2. The mixture was maintained at this temperature for 72 hours, at which point the mixture is poured into a 1 L flask containing 500 mL of deionized water causing the precipitation of a large volume of yellow/orange solid. The solids are filtered through a large medium porosity fritted filter (150mL) and then washed once with 150mL of acetone to remove the bulk residual water. The solids are transferred back to a 500mL flask, where they are vigorously stirred with 100mL of acetone for 10-15min, and then again on a medium porosity frit. This procedure is repeated 2-3 times until the remaining material is bright yellow, and the washings are no longer orange/brown. After drying in vacuo, the yield is 18.8 g (68% theory) of a bright yellow microcrystalline solid. ^{1}H NMR (400 MHz, $CDCl_3$): ∂ 7.82 (dd, 3H, ArH, J = 6.3 Hz, 1.6 Hz), 7.51 (td, 3H, ArH, J = 5.7, 2.0 Hz), 7.25 (td, 3H, ArH, J = 5.7, 1.2 Hz), 7.20 (dd, 3H, J = 6.3, 1.2 Hz). ^{13}C NMR (100 MHz, $CDCl_3$): 144.1 138.9, 134.1, 128.6, 126.4, 126.2 *Note: the major byproduct of the reaction bis(2-nitrophenyl)amine, is an orange/brown solid, and can be recovered from the acetone washings if desired. The ^{1}H NMR of this species are as follows: ^{1}H NMR (400 MHz, $CDCl_3$): ∂ 11.03 (br, 1H, NH), 8.21 (d, 2H, ArH, J = 8.8 Hz), 7.66 (t, 2H, ArH, J = 8.3 Hz), 7.54 (t, 2H, ArH, J = 7.6 Hz), 7.10 (d, 2H, ArH 7.7Hz). ^{13}C NMR (100 MHz, $CDCl_3$): ∂ 138.8, 132.4, 135.1, 127.0, 122.1, 120.8.*

Step 2: Tris(2-aminophenyl)amine [N(*o*-$PhNH_2$)$_3$]: In a glovebox a mixture of tris(2-nitrophenyl)amine (19.26 g, 50.7 mmol) and 10% palladium on carbon (5.4g) were

added to a 500 mL round bottom Schlenk flask (with a Teflon stopcock) containing a large stir bar. To this mixture is added 250mL of anhydrous THF, and the headspace of the flask removed by briefly applying vacuum so that the solvent begins to boil. The flask is sealed, brought outside the glovebox, and interfaced to a Schlenk line with a bubbler that can sustain 1.2-1.5 atm of H_2 pressure. The flask is refilled with hydrogen gas, and then stirred vigorously until the reaction solution is colorless (typically 12 hours). The mixture is then filtered in a glovebox through a medium porosity frit lined with Celite filter aid, and then the solvent removed in vacuo. The solids are washed with 100 mL (4x25mL) of a 1:1 Pentane/Et_2O mixture on a fritted filter and finally dried at 50˚C for 1-2 hours to remove any remaining solvent. The yield is 10.5 g (75% theory) of a bright white solid. ^{1}H NMR (400 MHz, $CDCl_3$): ∂ 6.99 (td, 3H, ArH, J = 7.5 Hz, 1.5 Hz),6.93 (dd, 3H, ArH, J = 7.8, 1.2 Hz), 6.73 (dd, 3H, ArH, J = 7.2, 0.9 Hz), 6.71 (td, 3H, J = 7.5, 1.5 Hz), 3.70 (s, 1H, NH). ^{13}C NMR (125 MHZ, CD_3CN): ∂ 143.4, 133.2, 126.4, 118.6, 116.7.

Step 3: H_3L^{iPr}. In a glovebox a 100mL Schlenk tube is charged with neat diisopropylphosphine (10g, 84.6 mmol), powdered paraformaldehyde (2.541g, 84.6 mmol), and a large stir bar. The slurry is brought outside of the glovebox and heated neat at 60˚C for 12 hours at which point the mixture is now homogeneous. The mixture is brought back into the glovebox where tris(2-aminophenyl)amine (7.99g, 27.3 mmol) is carefully added as a solid. If needed a small amount of DMSO can be added to aid in transfer of the tris(2-aminophenyl)amine. DMSO is preferably not added. The mixture is then heated to 100˚C for 24 hours, at which point the mixture is homogeneous. If DMSO was used, it is removed by means of a secondary trap and heat gun. The mixture is then brought into a glovebox where it is extracted in 200 mL of diethyl ether and filtered to

remove any insoluble material. The solvent is removed in vacuo, and then remaining solid is washed with CH_3CN (50-100mL) to yield 15.0g (81%) bright white microcrystalline powder. ^1H NMR (300 MHz, C_6D_6): ∂ 6.99 (t, 3H, ArH, J=9Hz), 6.92 (d, 3H, ArH, J = 9 Hz), 6.65 (d, 3H, ArH, J = 9 Hz), 6.49 (t, 3H, ArH, J = 7 Hz), 4.11 (s, NH, 3H), 3.10 (d, $^2J_{HP}$ = 15 Hz, CH_2), 1.53 (br, 3H, C*H*Me$_2$), 1.30 (br, 3H, C*H*Me$_2$), 0.94 (d, 18H, CH*Me$_2$,* $^2J_{PH}$= 6Hz), 0.84 (d, 18H, CH*Me$_2$,* $^2J_{PH}$= 6Hz). ^{31}P NMR (C_6D_6, 121 MHz): ∂ 3.1 (s).

An improved preparation of Sodium tetrakis(3,5- bis(trifluoromethyl)phenyl)borate:

*Note: *It is imperative that all glassware and solvent be void of all water, as this leads to substantially decreased yields. It is recommended that all glassware be dried for > 4 h at temperatures exceeding 150˚C. $NaBF_4$ (Aldrich) is dried at 100˚C under vacuum overnight, 3,5-bis(trifluoromethyl)-bromobenzene (Combi-Blocks) is degassed and stored over 20% molecular sieves for one week before use. Mg^0 powder (Aldrich) is stored under inert gas. Solvents are kept dry by means of a solvent purification system, with [H_2O] not exceeding 10 ppm, and stored in Teflon stoppered Strauss flasks.*

In a glovebox a 1 L, three neck round bottom flask,c is charged with pre-dried $NaBF_4$ (2.704g, 0.0246 mol, 1 equivalent), fresh magnesium powder (3.85g, 0.158 mol, 6.4 equivalents), and a large football shaped stir bar. The flask is isolated by means of a vacuum adapter and two glass stoppers, then brought outside of the glovebox. Under a positive pressure of argon, a reflux condenser and a separatory funnel (250mL) are installed (the funnel has a fine-tuning addition stopcock). Approximately 600mL of diethyl ether are then transferred via cannula into the flask through the dropping funnel. The magnesium powder is activated by adding 1.8 mL of 1,2-dibromoethane (stored on sieves, under argon, in dark) and cautiously heating the mixture to reflux and cooling. This process is repeated 3-5 times until the solution has become turbid and the surface of the magnesium powder is visibly bight.

The separatory funnel is then filled with 150 mL of diethyl ether and then 3,5-bis(trifluoromethyl)-bromobenzene (40g, 0.136mol, 5.5 equivalents) is added via syringe. With stirring, the ArBr/Et_2O solution is added dropwise at a rate which sustains reflux of the solution. In the case where the reaction is allowed to cool, a heat gun is used to ensure

that the Grignard continues to form. The addition should take 1-2 hours. Once the addition is done the mixture is a brown/yellow color. To ensure complete consumption of the Grignard the mixture is refluxed (ca. 50˚C) for 2.5 hours, and then stirred overnight at room temperature.

The work-up should be completed in a day to ensure that the ensuring $NaBArF_{24}$ is free of moisture. The reaction mixture is poured onto a solution of 42.4g of Na_2CO_3 in 500 mL of H_2O and stirred for an hour. The mixture is poured through a glass funnel lined with glass wool directly into a 1L separatory funnel (sometime necessary to use two), and the organic layer is separated. The aqueous phase is extracted 3x100mL with diethyl ether, and the organic layers are combined, dried over Na_2SO_4 (no brine solutions!), and then filtered through a frit lined with Celite. The mixture is reduced to dryness by means of a rotary evaporator to an oil. At this point, the mixture is dried at 80-90˚C at pressures below 100mTorr leading to a yellow powder after ca. 1.5 hours. This powder is transferred to a Schlenk flask (in air), and a 200mL of dry benzene are transferred into the flask, which is then fitted with a dean-stark distillation head. The azeotropic distillation is performed (ca 120˚C) until only 50mL of benzene remain, at which point the system is cooled, the distillation head removed, and the solids dried to yield a off-white powder. This solid is brought into a glovebox, where it is washed with dichloromethane (3 x 20mL) with vigorous agitation. The solid material is then placed in a Schlenk flask and dried at 60˚C under vacuum for 24 hours. In this manner, 15.5 g (71% yield) of $NaBArF_{24}$. ^{1}H NMR (400 MHz, Acetone-d_6) δ 7.79 (s, 8H, *o*-ArH), 7.67 (s, 4H, *p*-ArH). ^{19}F NMR (376 MHz, Acetone-d_6) δ -63.28 (24F).

X-ray Crystallographic and Structure Refinement Details

Crystalline specimens of the species reported below were placed onto the tip of MiTeGen Dual-Thickness MicroLoop™ and then mounted on a Bruker Photon II CPAD diffractometer for data collection at listed temperature. The data collections were carried out using Mo Kα radiation (graphite monochromator). The data intensity was corrected for absorption and decay (SADABS).[77] Final cell constants were obtained from least-squares fits of all measured reflections. The structure was solved using SHELXT-16[78] and refined using SHELXL-16[79], which were executed from the SHELXLE graphical user interface.[80] A direct-methods solution was calculated which provided most non-hydrogen atoms from the E-map. Full- matrix least-squares/difference Fourier cycles were performed to locate the remaining non-hydrogen atoms. All non-hydrogen atoms were refined with anisotropic displacement parameters. Hydrogen atoms were placed in ideal positions and refined as riding atoms with relative isotropic displacement parameters. Surfaces depicting the residual electron density maps of **[1(H$_2$)]$^-$** to **[3(H$_2$)]$^-$** were generated using FCF data after a single refinement in OLEX2, set to their respective electron density level, and then rendered using POV-ray.[81]

Table 2.5: Crystallographic Details for Complexes **[1(H₂)]⁻** to **[3(H₂)]⁻**

Metric	**[1(H₂)]⁻**	**[2(H₂)]⁻**	**[3(H₂)]⁻**
chemical formula	$[C_{39}H_{60}N_4P_3AlCo][Li(C_4H_{10}O_2)_3]\bullet 2C_5H_{12}$	$[C_{39}H_{60}N_4P_3GaCo][Li(C_4H_8O)_4]$	$[C_{39}H_{60}N_4P_3InCo][Li(C_4H_{10}O_2)_3]\bullet C_6H_{14}$
formula weight	1112.16	1099.81	1185.88
crystal system	Monoclinic	Triclinic	Triclinic
space group	Pn	P-1	P-1
a(Å)	12.3678(18)	15.7589(11)	11.409(2)
b(Å)	13.938(2)	16.9042(14)	12.130(2)
c(Å)	36.575(6)	21.5439(17)	23.099(4)
α (deg)	90	83.330(3)	98.560(8)
β (deg)	93.498(7)	85.737(2)	90.383(10)
γ (deg)	90	87.113(3)	103.728(10)
V ($Å^3$)	6293.1(17)	5679.5(8)	3067.9(10)
Z	4	4	2
Z'	2	2	1
λ (Å), μ (mm^{-1})	0.71073, 0.410	0.71073	0.71073, 0.766
T(K)	173	125	127
θ	2.204 to 30.517	2.374 to 30.592	2.298 to 30.507
reflections collected	139482	128896	67842
unique reflections	32600	34833	18673
data/restraint/parameter	31541/5/1283/	34842/4/1217	18676/0/603
R1, wR2 ($I > 2\sigma(I)$)	0.0624, 0.1543	0.0529, 0.1427	0.0496, 0.1215

Table 2.6: Crystallographic Details for Complexes **[2(N₂)]⁻** and **[3(N₂)]⁻**

Metric	**[2(N₂)]⁻**	**[3(N₂)]⁻**
chemical formula	$C_{39}H_{60}N_6P_3GaCo]$ $[C_{36}H_{30}NP_2]•3C_4H_8O$	$C_{39}H_{60}N_6P_3InCo]$ $[C_{36}H_{30}NP_2]•3C_4H_8O$
formula weight	1587.33	1631.42
crystal system	Triclinic	Triclinic
space group	P-1	P-1
a(Å)	12.177(3)	12.2163(15)
b(Å)	18.604(4)	18.704(3)
c(Å)	20.729(5)	20.450(4)
α (deg)	111.648(3)	112.181(7)
β (deg)	101.917(3)	100.878(9)
γ (deg)	95.562(3)	95.913(8)
V (Å^3)	4192.8(16)	4170.3(11)
Z	2	2
λ (Å), μ (mm^{-1})	0.71073, 0.666	0.71073. 0.623
T(K)	173(2)	173(2)
θ	1.095 to 27.572	2.175 to 30.532
reflections collected	49230	112059
unique reflections	19021	25459
data/restraint/parameters	19021/1/866	25459/0/901
R1, wR2 (I > 2σ(I))	0.0681, 0.2117	0.0558, 0.1491

Table 2.7: Crystallographic Details for Complexes **[1-H(PhSiH$_2$)]$^-$** and **[2-H(PhSiH$_2$)]$^-$**

Metric	**[1-H(PhSiH$_2$)]$^-$**	**[2-H(PhSiH$_2$)]$^-$**
chemical formula	2 [$C_{16}H_{40}O_8K$] 2 [$C_{45}H_{68}N_4P_3SiAlCo$]	[$C_{12}H_{24}O_6K(C_4H_8O)$] [$C_{45}H_{68}N_4P_3SiGaCo$]
formula weight	2629.1	1288.18
crystal System	Orthorhombic	Orthorhombic
space group	$Pca2_1$	Pbca
a(Å)	20.6548(13)	22.3679(13)
b(Å)	22.1334(11)	19.6463(10)
c(Å)	30.609(2)	29.953(2)
α (deg)	90	90
β (deg)	90	90
γ (deg)	90	90
V (Å^3)	13993.1(15)	13162.9(13)
Z	16	8
Z'	2	1
λ (Å), μ (mm^{-1})	0.71073, 0.588	0.71073, 0.867
T(K)	123(2)	123(2)
θ	2.176 to 30.520	2.364 to 27.515
reflections collected	176878	77572
unique reflections	37803	15132
data/restraint/parameters	37803/1/1263	15132/0/689
R1, wR2 (I > 2σ(I))	0.0745, 0.1941	0.0558, 0.1203

Computational Methods

Density functional theory (DFT) calculations were performed by Dr. Jing Xie. These calculations were performed on the unrestricted singlet state of **[1(H$_2$)]**$^-$ to **[3(H$_2$)]**$^-$ molecules with the Gaussian 09 suite of programs.[82] Gas-phase optimizations were carried out using the M06-L functional, with def2-TZVPP (for Ni, Al, Ga, In, and the H-H motif)/def2-TZVP (for N, P)/def2-SVP (for C, H) basis sets at 0 K.[83-84] The Stuttgart SDD pseudo potential was also used for In.[85] Vibrational frequency analysis with the harmonic approximation was performed to characterize the nature of the stationary points. Gibbs free energies at 298.15 K were computed by adding zero-point vibrational energies and thermal corrections. Solvation effects were also considered by performing single-point calculations for all stationary points using the SMD solvation model and tetrahydrofuran as solvent.[86] The energies reported are free energies in solvent of tetrahydrofuran.

Three isomers of the dihydrogen adducts were optimized, Kubas-type complex, terminal dihydride, and bridging/terminal dihydride. Structure comparison between the calculated Kubas-type complexes and experimental metrics show that the calculated H-H bond distances are about 0.1 Å shorter than that obtained from J_{HD} values. Other bond distances are in good agreement with experimental crystal structures, with the largest difference of 0.05 Å. Since the structures are optimized under 0 K and the H-H distance were measured at room temperature, the temperature difference may give rise to the H-H bond distance discrepancy.

For each complex, the Kubas-type complex is energetically favored relative to both a terminal dihydride and a bridging dihydride. It is noteworthy that the terminal dihydrides are uphill by only 0.97, 0.43, and 0.80 kcal/mol for M = Al, Ga, and In, respectively.

Meanwhile, the H-H distance changes from 0.9 Å in Kubas-type complex to 1.8 Å in terminal hydride, which indicates that activating H-H to be stretched is easy. The bridging dihydride is 3.5 and 4.6 kcal/mol higher in energy than the Kubas-type complexes for M=Al and Ga, respectively. Trials of optimizing bridging/terminal dihydride for M = In converged to terminal dihydride.

Chapter 3

CO_2 hydrogenation via a $Co^{-I/I}$ cycle featuring two stable dihydrogen complexes

In part from:

Matthew V. Vollmer, Jingyun Ye, Jing Xie, Andrew Preston, John C. Linehan, Eric Wiedner, Aaron Appel, Laura Gagliardi, and Connie C. Lu. "CO_2 hydrogenation via a $Co^{-I/I}$ cycle featuring two stable dihydrogen complexes." Manuscript in preparation.

3.1 Overview

This chapter details the use of dihydrogen cobaltate complexes, $[(\eta^2\text{-}H_2)CoML]^-$ where M = Al, Ga, or In and L = $N((o\text{-}C_6H_4)NCH_2P^iPr_2)_3$ as catalysts for the additive-free hydrogenation of CO_2 to formate. The dinitrogen complexes, [PPN][(N_2)CoML] are utilized as pre-catalysts for this transformation, which are in turn studied by *in-operando* high-pressure NMR spectroscopy. A screening of the identity of the supporting metal atom on catalytic proficiency reveals that the identity of this support is vital to catalytic turnover, with M = Ga being the most effective catalyst under standard conditions. Further catalytic studies reveal that for M = Ga large turnover numbers (TONs) and rapid turnover frequencies (TOFs) are observed (19,000 and 27,000 hr^{-1} respectively). Notably weak bases such as DBU and ^{t}BuTMG can be used to maintain high turnovers.

The mechanism of this catalytic reaction is elucidated using stoichiometric studies and computational methods. Important findings include the isolation of a pair of square planar $16e^-$ hydrides, HCoML (M = Al, Ga) that bind H_2 reversibly to form a non-classical dihydrogen hydride complex $(\eta^2\text{-}H_2)$HCoML. The pK_a and free energy of H_2 binding affinity of $(\eta^2\text{-}H_2)$HCoML are measured experimentally and allow for a strong estimate of the hydricity of $[(\eta^2\text{-}H_2)CoML]^-$ to be obtained. The proposed mechanism is compared and contrasted to that reported for the isoelectronic d^{10} analog, $(\eta^2\text{-}H_2)$NiGaL and to the state-of-the-art CO_2 hydrogenation catalyst $(dmpe)_2$CoH.

3.2 Introduction

Among renewable energy schemes, the hydrogenation of CO_2 to formic acid is particularly attractive as it utilizes a vastly underdeveloped C_1 feedstock (CO_2) to produce a value-added commodity chemical and an energy-dense fuel.[1-4] The demand for formic acid and its derivatives is expected to climb as new state-of-the-art formic acid dehydrogenation catalysts are discovered and it follows that analogous CO_2 hydrogenation catalysis must also be developed.[5-8] Furthermore, the widespread proliferation of these technologies necessitates that these processes must be based on catalysts featuring abundant metal sources.[9] Recent years have seen remarkable activities for CO_2 hydrogenation by precious metals[2, 10-26], but examples featuring only base metals remain relatively limited in comparison.[27-38]

In a typical mechanistic scheme, CO_2 hydrogenation is composed of three vital elementary steps, namely (1) the transfer of a hydride to CO_2 (inner/outer-sphere), (2) the regeneration of the metal hydride and (3) formation/dissociation of formate.[39] The energetics of the former (1) can be inferred from the ability of L_nM-H unit to donate H^-, (thermodynamic hydricity, ΔG_{H^-}) when compared to that of formate (ΔG_{H^-} = 44 kcal/mol CH_3CN).[40-41] A detailed analysis of the hydricity of base metal sheds light on why base-metal catalyzed CO_2 reduction remains a challenge; only a handful complexes exhibit hydricity values below 44 kcal/mol. The second and third steps, catalyst regeneration and formate dissociation, are likewise non-trivial. For example, many d^8 Ni-H complexes are hydridic enough reduce CO_2 to formate but require sacrificial Si-H or B-H donors that regenerate the catalytically prerequisite hydride.[42-44] Among first-row transition metal complexes, there remain few examples of catalysts that can balance the interplay of

elementary steps to accomplish the hydrogenation of CO_2 under ambient conditions without stoichiometric additives. Many of these examples take advantage of iron and cobalt complexes as they form strong chelates with many phosphine ligands which substantially increase the hydricity of the M-H bond.[29, 38, 45-48]

Recent studies have uncovered that many cobalt complexes are excellent catalysts for CO_2 hydrogenation due to their unique hydridic properties and latent ability to activate H_2. For example, Beller has described the hydrogenation of CO_2 to formate (ca. 4000 turnovers) utilizing a tetraphosphine catalyst at high temperature and pressure (120˚C, 60 atm H_2:CO_2).[30] More impressive yet, is a related system in which CO_2 is hydrogenated directly to methanol utilizing an *in-situ* generated catalyst comprising of mixtures containing $Co(acac)_3$/triphos/Tf_2NH.[35] Himeda and Fujita explored the ability of Cp^*Co^{III} catalysts to mediate CO_2 hydrogenation to formate with turnovers reaching 60 at high temperatures and pressures (80-100˚C, 40 atm of H_2:CO_2).[27] Bernskeotter *et al.* have reported pincer-ligated cobalt complexes for CO_2 hydrogenation that exhibit staggering turnovers near 30,000, albeit large amounts of LiOTf and forcing conditions (68 atm, >45˚C) are needed to promote the reaction.[36] The deceptively simple catalyst system based on $(dmpe)_2CoH$ and Verkade's base (Vkd) remains the most active Co-based catalysts for CO_2 hydrogenation to formate. In this system the reaction kinetics are remarkable in that they surpass many precious metals both at ambient conditions (3,400 hr^{-1}, 1 atm H_2:CO_2) and at high pressures (74,000 hr^{-1} 20 atm H_2:CO_2). Moreover, $(dmpe)_2CoH$ also maintains high overall turnover numbers (2000-9400) as well.[32-33] Recent strides with similar bis(diphosphine)cobalt complexes have produced remarkably robust catalysts capable of utilizing more ubiquitous organic bases at low overall CO_2 pressures.[28]

We have recently highlighted that a direct Lewis acid-nickel (e.g. Ni-Ga) interaction allows for the stabilization of an anionic Ni-H that surmounts the barriers of hydricity and formate dissociation in CO_2 hydrogenation.[49] Encouraged by the improvement in CO_2 hydrogenation efficiency gained via a direct Ga-Ni interaction, we sought to explore the ability of an isoelectronic cobalt analog toward the same process.[50] We have recently succeeded in synthesizing such complexes by isolating a small family of thermally robust d^{10}, Co^{-I} dihydrogen complexes. In this study, we detail thermodynamic and stoichiometric studies that strongly support that these species engage in a scarcely realized $Co^{I/-I}$ redox couple that permits additive-free hydrogenation activity on-par with current state-of-the-art catalysts.[51]

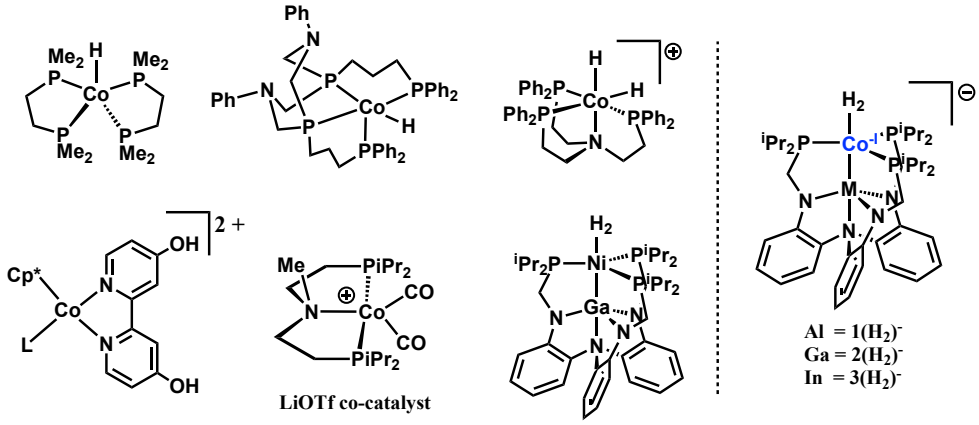

Figure 3.1: Left, Co and Ni catalyst for CO_2 hydrogenation to formate. Right, complexes explored in this body of work.

3.3 Results and Discussion

3.3.1 Catalytic CO_2 hydrogenation studies

Having established that a Co^{-I} dihydrogen complex is isolable for each member of the group 13 Lewis-acidic metalloligand family (LM, M = Al, Ga, In), we first screened the ability of **1-3(H$_2$)$^-$** to catalyze the hydrogenation of CO_2 to formate in the presence of

Verkade's base (Vkd) at high pressures. For synthetic ease we utilized the stable and crystalline PPN^+ (bis(triphenylphosphine)iminium) dinitrogen cobaltate complexes **1-3(N$_2$)$^-$** as pre-catalysts, as they are readily synthesized via NaHg reduction of LM/$CoCl_2$ and ion exchange with [PPN][$BArF_{24}$] (Figure 3.2). While complexes **1-3(N$_2$)$^-$** do not dissociate N_2 when exposed to extended vacuum/heat, the addition of H_2 at pressures as low as 1.8 atm rapidly produce [PPN][LMCo(H_2)], **1-3(H$_2$)$^-$** as shown in Figure 3.3. This exchange is noteworthy in light of the modestly activated N_2 unit (2010-1994 cm^{-1}), and the short reaction times needed to observe full substitution. Furthermore, the observation that this ligand exchange reaction is facile under modest pressure suggests that the complexes **1-3(N$_2$)$^-$** will behave as good pre-catalysts to generate **1-3(H$_2$)$^-$**, especially under

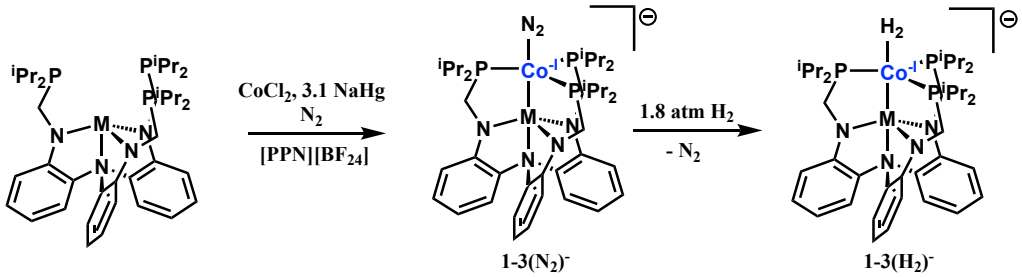

Figure 3.2: Synthesis of [PPN][**1-3(N$_2$)**] and their corresponding reaction with H_2

high pressures of H_2.

As complexes **1-3(N$_2$)$^-$** form **1-3(H$_2$)$^-$** under low pressures of H_2 we then examined the ability of these species to mediate the hydrogenation of CO_2. To this end we employed low catalyst concentrations of the desired cobalt species ($[Co]_{tot}$ < 0.25mM) with large excess of Verkade's base (800mM, 3200 theoretical turnovers) such that a detailed comparison with previously reported systems could be performed.[49] The catalytic experiments were performed at 34 atm of H_2:CO_2 and the pressure was held constant by means of a syringe pump directly attached to the high pressure PEEK NMR cell as

described in the literature.[52-53] An example of the changes in the ^{1}H NMR spectra of a typical reaction are shown in Figure 3.4.

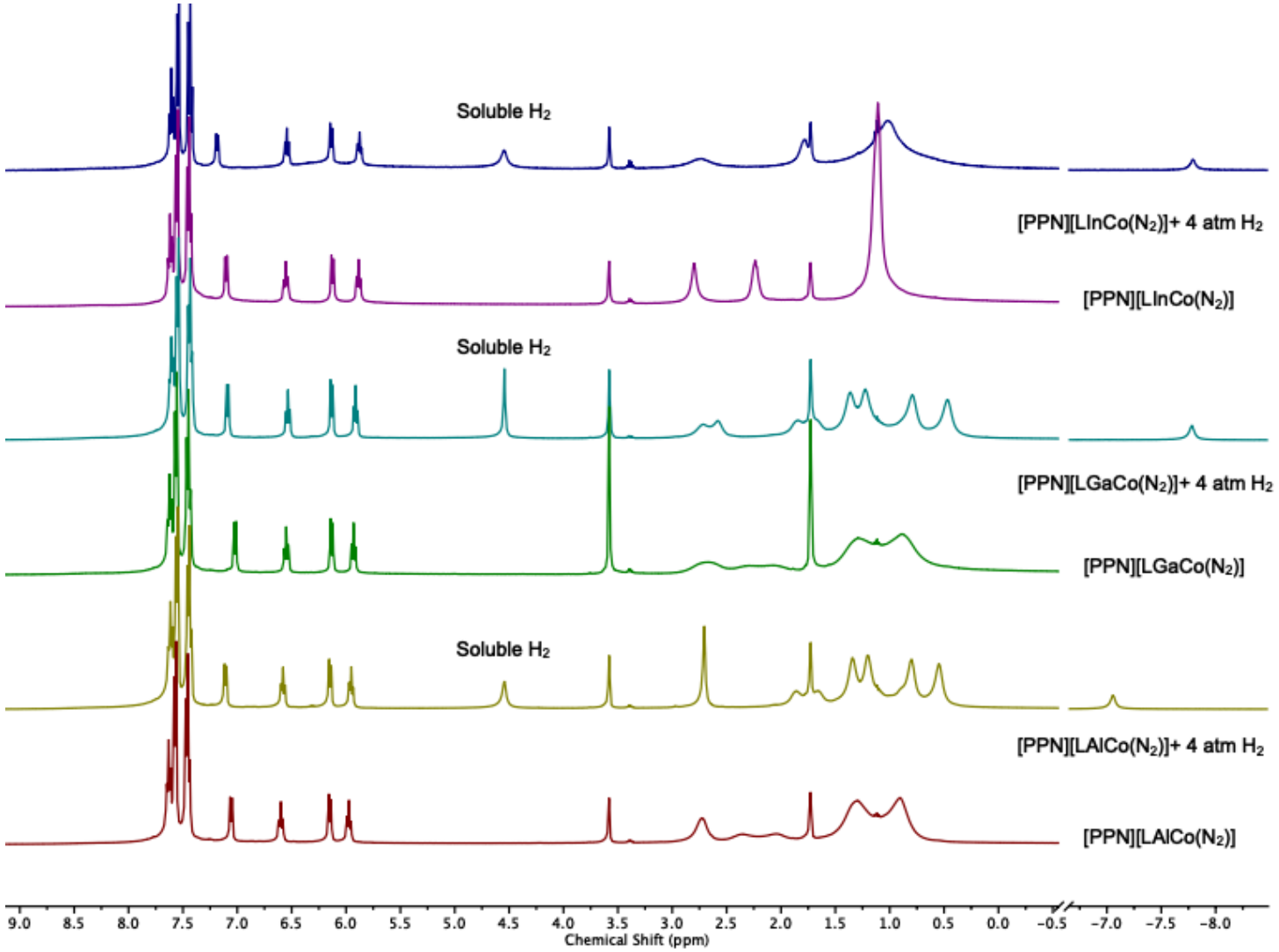

Figure 3.3: Overlay of the $^{1}H\{^{31}P\}$ NMR (THF-d_8) spectra showing that the addition of H_2 to **1-3(N$_2$)$^-$** generates **1-3(H$_2$)$^-$**.

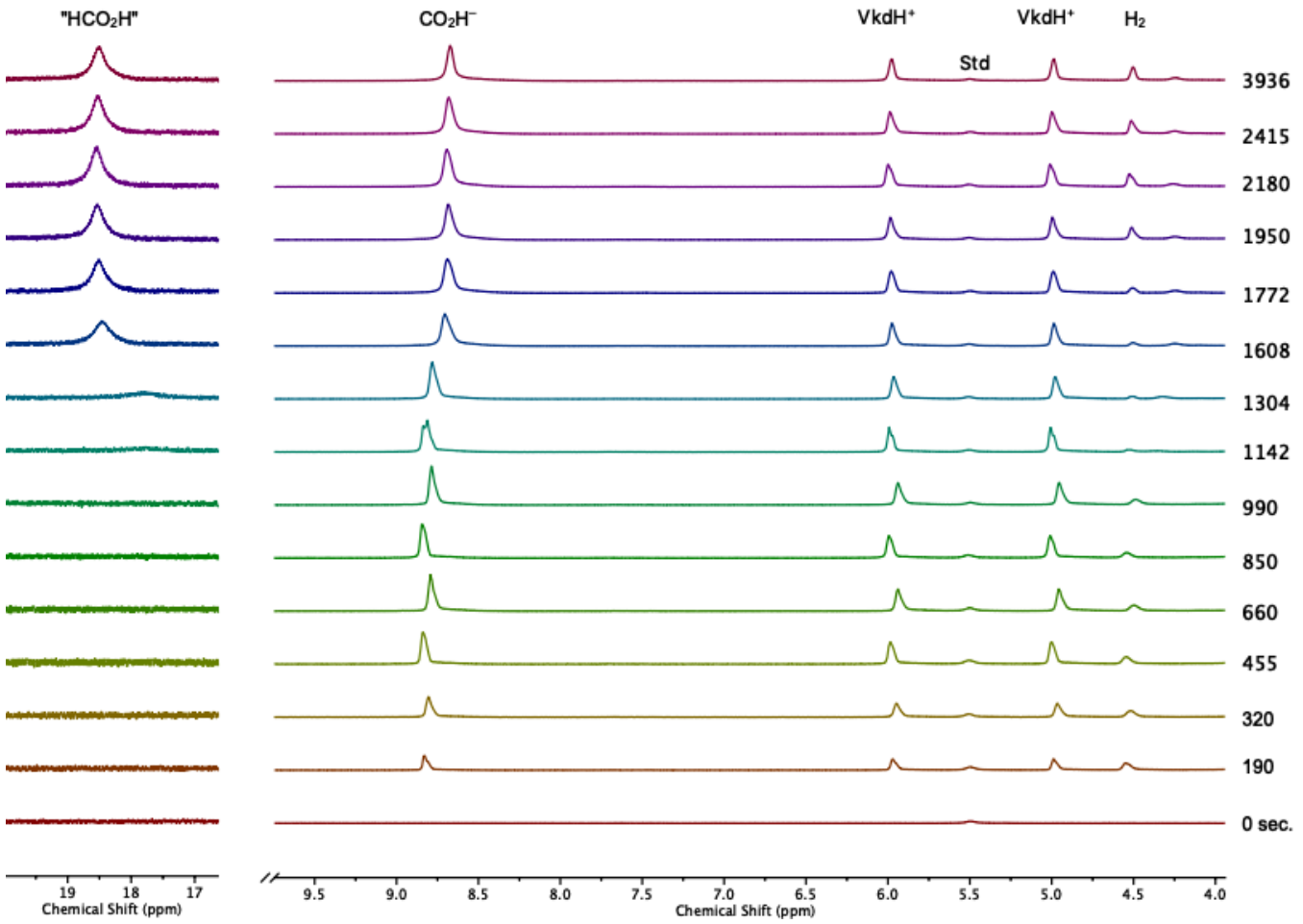

Figure 3.4: Kinetic traces showing the changes observed over the course of a catalytic reaction at 34 atm of H_2:CO_2 catalyzed using **2(N$_2$)**$^-$ and Verkade's base (800 mM).

The identity of the Lewis acid was found to have a large impact on both the yield of formate and the initial turnover frequency (TOF). Both **1(N$_2$)$^-$** and **2(N$_2$)$^-$** are active catalysts for the production of formate, operating at an initial TOFs of 1540 hr^{-1} and 10500 hr^{-1}, respectively, under standard reactions conditions (0.25mM catalyst 800mM base, 34 atm 1:1 H_2:CO_2), whereas **3(N$_2$)$^-$** does not detectably produce formate under catalytic, or stoichiometric, conditions. The effect of the supporting metal atom on the overall catalytic activity is directly observed in the figure below.

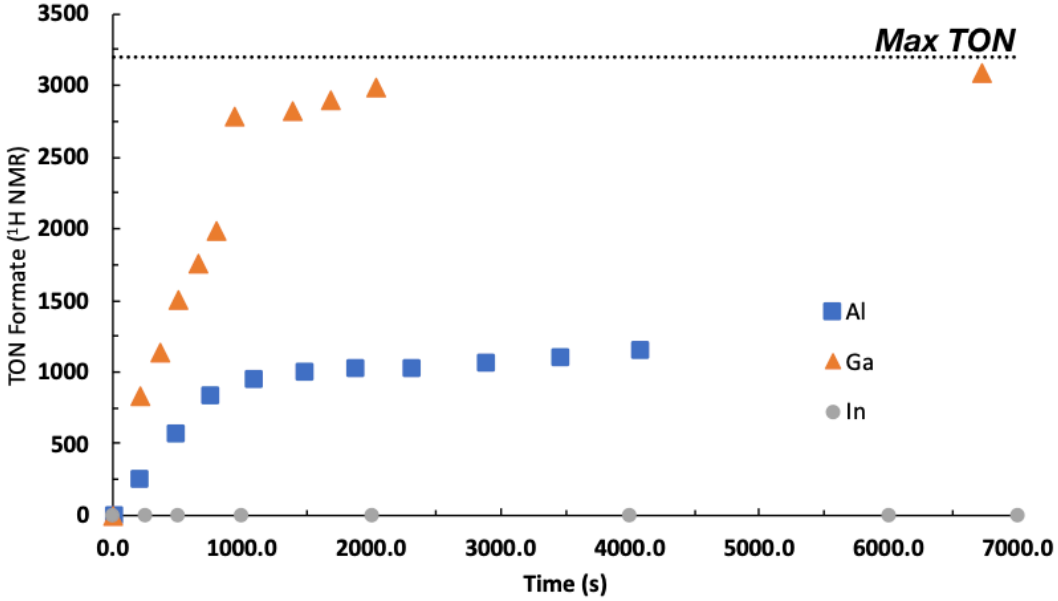

Figure 3.5: Plot showing the catalytic performance of **1-3(N$_2$)$^-$.** Conditions: 0.25 mM catalyst, 800 mM Vkd, 350µL THF-d_8, 34 atm 1:1 H_2:CO_2.

Further optimization of the catalysts system based on **2(N$_2$)$^-$** was achieved by lowering the catalyst concentration by an order of magnitude (to ensure mass transport limitations were not affecting catalyst performance), and gives rise to turnovers and TOFs comparable to the state-of-the-art CO_2 hydrogenation catalysts (entries 4 and 5).[27, 30, 32-33, 36] At higher catalysts loadings of **2(N$_2$)$^-$**, Barton's base ^{t}BuTMG (pKa = 28.4 in CH_3CN[54]) or DBU (pK_a = 24.3 in CH_3CN[54]) are effective in converting CO_2 to formate as well, at

TOFs of 2300 hr^{-1} and 1350 hr^{-1}, respectively. Notably, the performance of the **2(N_2)**$^-$ with these weak bases outperforms state-of-the-art catalysts such as $(dmpe)_2CoH$ under similar conditions[32]. Experiments performed with triethylamine (pK_a = 18.8 in CH_3CN[54]) yielded < 2.5 equivalents of formate over the course of 12 hours. The observation that catalyst activity decreases as a function of the pK_a of the base employed suggests that weak bases may alter the rate-limiting step of the catalytic mechanism.[39, 55] Worth noting is that a similar trend has been noted for the $(dmpe)_2CoH$ system, as the conjugate acid *cis*–$(dmpe)_2CoH_2^+$ is only reluctantly deprotonated by weak bases (pK_a = 33.7 in CH_3CN).[33]

Table 3.1: Catalytic CO_2 hydrogenation to formate using **1-3** under various conditions [a]

Entry	Catalyst	Loading (mM)	Base	P (atm)	CO_2:H_2	TOF (h^{-1})[b]	Turnovers[c]	% Yield
1	$1(N_2)^-$	0.25	Vkd	34	1:1	1540	1900[d]	59
2	$3(N_2)^-$	0.25	Vkd	34	1:1	0	0	0
3	$2(N_2)^-$	0.25	Vkd	34	1:1	10500	3100	> 99
4	$2(N_2)^-$	0.063	Vkd	34	1:1	23000	12400	> 99
5	$2(N_2)^-$	0.030	Vkd	34	1:1	27000	19200	70
6	$2(N_2)^-$	0.25	Vkd	17	1:1	5000	3150	> 99
7	$2(N_2)^-$	0.25	Vkd	1.8	1:1	530	950	30
8	$2(N_2)^-$	1.2	Vkd	1	1:1	64	160	55
9	$2(N_2)^-$	2.0	^{t}BuTMG	34	1:1	2300	480	> 99
10	$2(N_2)^-$	2.0[e]	DBU	34	1:1	1350	360	> 99
11	$2(N_2)^-$	20[f]	Et_3N	34	1:1	-	< 2.5[g]	< 5
12	$2(N_2)^-$	0.25	Vkd	34	3:1	13000	3150	> 99
13	$2(N_2)^-$	0.25	Vkd	34	1:3	2500	1200	37

[a] Reaction conditions: catalyst (0.020 mM to 20mM), 800mM base, 0.350mL THF-d_8 solution, 293K, Conditions applicable to all entries unless otherwise noted. [b] TOF is the initial slope of linear formate production vs time plot, typically acquired in first 15-20 min of the reaction. [c] Observed turnovers of formate based on ^{1}H NMR. [d] Recorded after 6 hours, conversion after 1 hour is ca. 700-900 TON, after which the initial rate drops dramatically. [e] Run without a capillary standard due to salt formation of [DBUH][CO_2H]. [f] Solution generated in-situ from equimolar $[H(OEt_2)_2][BArF_{20}]$. [g] Only super stoichiometric amount of CO_2H^- were detected over the course of 12 hours, single run.

We then performed more detailed mechanistic studies utilizing **2(N$_2$)$^-$** as it is the most active of the triad. Experiments conducted under standard conditions (Verkade's base, 34 atm), but with H_2:CO_2 mixtures shed light on the rate-limiting step. When H_2 rich gas is utilized (75% H_2), there is a sharp decrease in both initial rate and overall turnover whereas CO_2 rich mixtures (75% CO_2) nearly replicated the activity observed in 50:50 mixtures (entries 3, 12, 13). These observations may be consistent with a mechanism in which the transfer of H^- to CO_2 is rate limiting. Furthermore, the similarity between entries 12 and 3 suggests CO_2 saturation may occur at 34 atm of 3:1 CO_2:H_2. Similarly, the role of one (or both) of the gases in the rate determining step is directly observed by modulating the overall pressure, which leads to a steady decrease in the overall catalytic performance (entries 3, 6-8). Under ambient conditions (1-1.8 atm H_2:CO_2), **2(N$_2$)$^-$** produced formate at a steady rate (entries 7 and 8), but the sensitivity of the catalysts is reflected in the low overall TON.

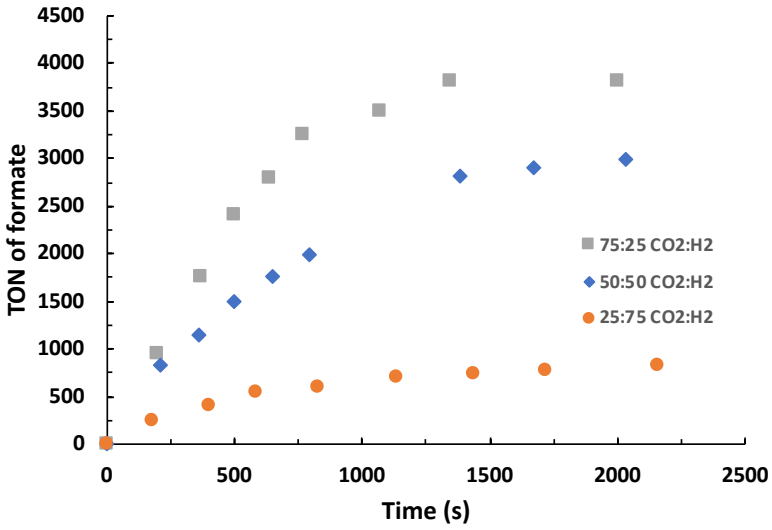

Figure 3.6: Overlay of different catalytic hydrogenation traces under various mixtures of H_2:CO_2 (34 atm). Conditions: 0.25 mM of **2(N$_2$)$^-$**, 800 mM Vkd.

At higher pre-catalyst concentrations (ca. 20 mM) the catalytic resting state in the presence of Verkade's base was identified as the anionic dihydrogen complex, **2(H₂)⁻** by both ^{31}P and ^{1}H NMR spectroscopy. With weaker bases we observed that deprotonation is rate limiting. This observation is supported by the identification of the intermediate species **2-H(H₂)**, the conjugate acid of **2(H₂)⁻**, which we wished to fully characterize (*vide infra).*

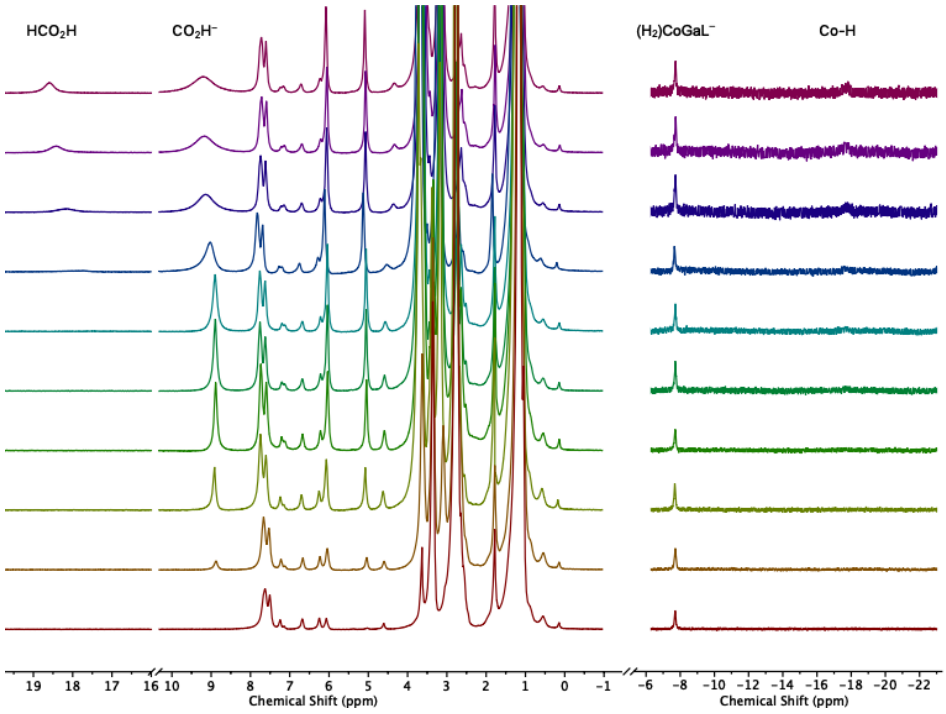

Figure 3.7: Time resolved ^{1}H NMR spectra of a non-catalytic run to identify catalyst resting state showing persistence of **2(H₂)⁻** (-7.7 ppm) throughout the course of the reaction. Conditions: 20 mM **2(N₂)⁻**, 800 mM Vkd. Towards the end of the reaction a new, unidentified M-H also appears near -15 ppm.

Resting state experiments performed at higher catalysts concentrations ($[Co]_{tot}$ = 20 mM) suggested that $CO_{(g)}$ is produced during catalysis and likely leads to catalyst decomposition. While a post-catalytic solution of **2(N₂/H₂)⁻** did not show any noticeable decomposition by ^{1}H NMR, heating this solution overnight at 55˚C produces a new species by both ^{1}H and ^{31}P NMR spectroscopies. We suspected that this species is the anionic carbonyl metallate, **2(CO)⁻**, based on the presence of $CO_{(g)}$ in the reaction headspace

(identified by GC-FID). Based on these collective observations, it is likely that $CO_{(g)}$ is produced in small quantities during the course of the reaction, which accounts for the deactivation of the catalyst. Furthermore, complex **2(CO)**$^-$ could be cleanly isolated from the room temperature reaction mixture of excess ethyl formate and **2(N$_2$)**$^-$. Complex **2(CO)**$^-$ exhibits an intense C-O stretching frequency at 1826 cm^{-1} which is consistent with a terminal carbonyl ligand.[56] Further validation of this catalyst decomposition products comes from an identical ^{31}P NMR resonance to those observed in Figure 3.7 as well as combustion analysis that validate the formulation of [PPN][**2(CO)**]. Unfortunately, the ^{13}C NMR resonance for the terminal carbonyl moiety could not be located, likely due to unresolvable coupling to 100% abundant, $I = 7/2$, cobalt atom.

3.3.2 Stoichiometric studies and catalytic intermediates

Given the high activity of **2(H₂)**⁻ to hydrogenate CO_2 we then turned to stoichiometric studies to shed light on the mechanism of CO_2 hydrogenation and to elucidate catalytic intermediates. As previously described, complex **2(N₂)**⁻ is fully converted to its corresponding dihydrogen complex, **2(H₂)**⁻, under pressures as low as 1.8 atm H_2 as seen by both ^{31}P and ^{1}H NMR spectroscopy (Figure 3.9, a). This supports the notion that **2(H₂)**⁻ forms readily under the catalytic conditions employed. Re-exposure of

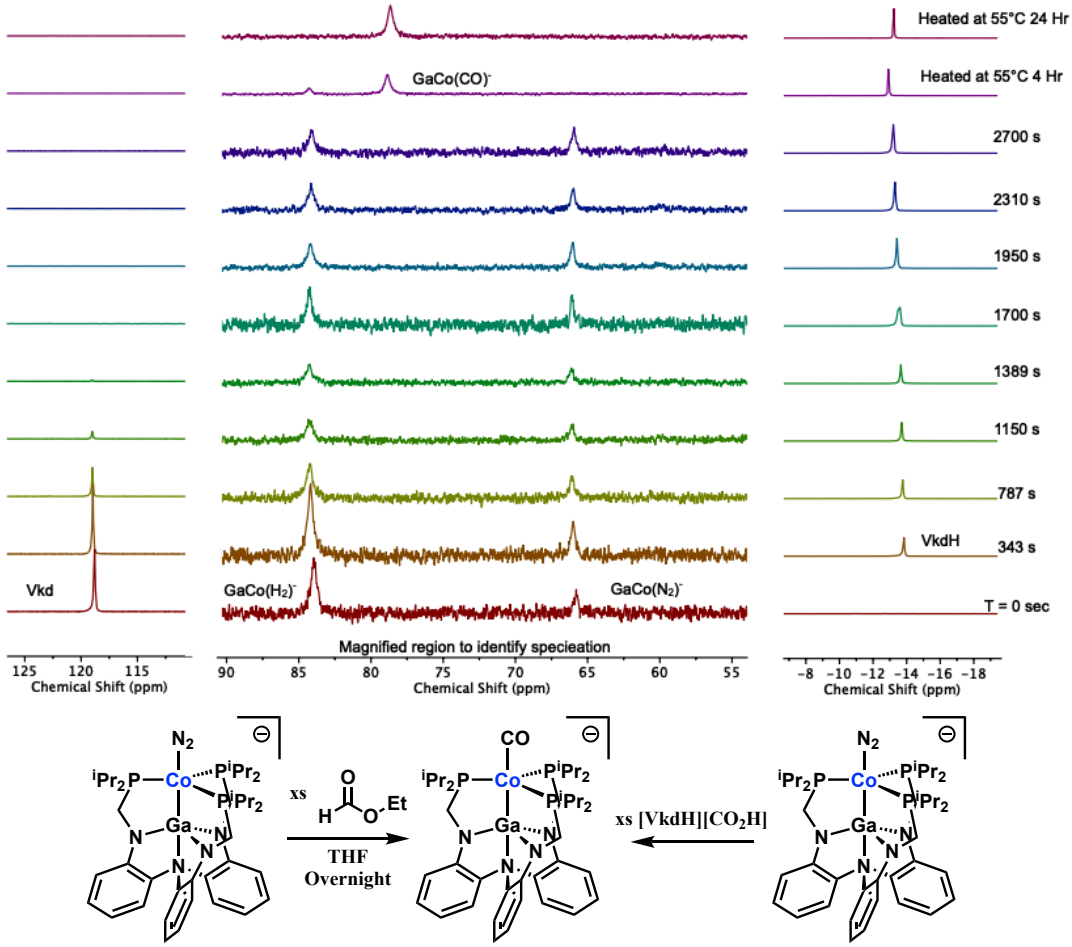

Figure 3.8: $^{31}P\{^{1}H\}$ NMR overlay used to identify catalyst speciation. Conditions: 20 mM [PPN][**2(N₂)**], 800 mM Vkd, 1.8 atm H_2:CO_2. Bottom, independent pathways that produce **2(CO)**⁻.

solutions containing **2(H₂)⁻** to an N_2 atmosphere regenerates **2(N₂)⁻** which suggests that N_2 coordination may inhibit catalysis, especially at lower pH_2.

Hydride transfer from **1/2(H₂)⁻** to CO_2 is rapid and quantitative at room temperature under 1.8 atm of 1:1 H_2:CO_2 and produces formate as the only product visible by ^{1}H NMR spectroscopy (Figure 3.9, b). This observation indicates dihydrogen complexes **1/2(H₂)⁻** are potent hydride donors for the hydride transfer to be thermodynamically feasible under ambient conditions ($\Delta G_{H^-} < 44$ kcal/mol). Furthermore, this reaction is synthetically useful if stoichiometric LiOTf is added which acts to facilitate the separation of the $LiCO_2H$ and [PPN][OTf] byproducts. In this manner, **1/2(N₂)⁻** can be used as precursors to produce **1/2-H(H₂)** and ultimately **1/2-H** (Figure 3.9 a → b → c).

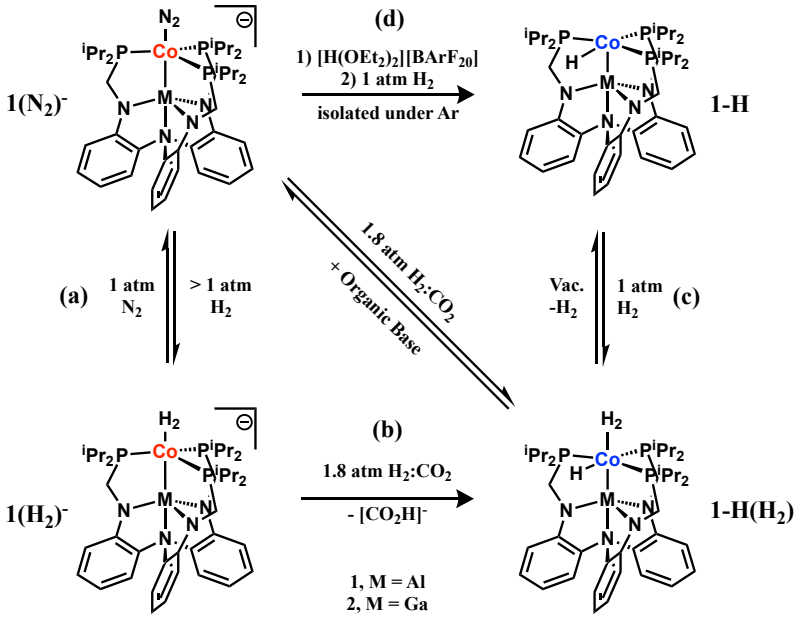

Figure 3.9: Stoichiometric reactions of **1/2(N₂)⁻** relevant to the catalytic CO_2 hydrogenation

Hydride transfer from **1/2(H$_2$)**$^-$ cleanly generates a new oxidized cobalt hydride species with a broad, *Co-H* resonance at -8.1 ppm (for **2**) (3 ^{1}H nuclei per ligand) in addition to a new, and broad, ^{31}P NMR resonance at 74 ppm. When the addition of the H_2:CO_2 mixture is performed at lower temperatures a deeply colored intermediate is formed which rapidly decays to yield colorless solutions of this new cobalt hydride species. Similar observations were noted for the analogous M = Al congener, with the only discrepancies being the location of the ^{31}P resonance (68.1 ppm) and the ^{1}H resonance of the new Co-H (-7.80 ppm).

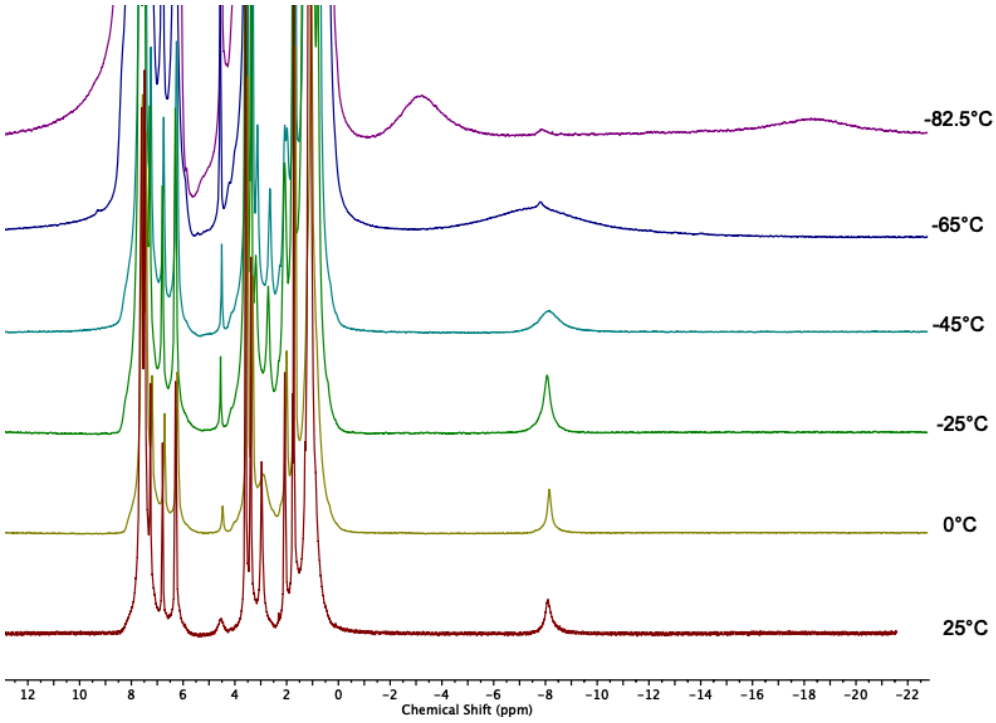

Figure 3.10: Variable temperature ^{1}H NMR spectra of **2-H(H$_2$)** in THF-d$_8$.

We have assigned the product of hydride transfer from **1/2(H$_2$)**$^-$ to be the non-classical dihydrogen-hydride complexes **1/2-H(H$_2$)** on the basis of their spectroscopic

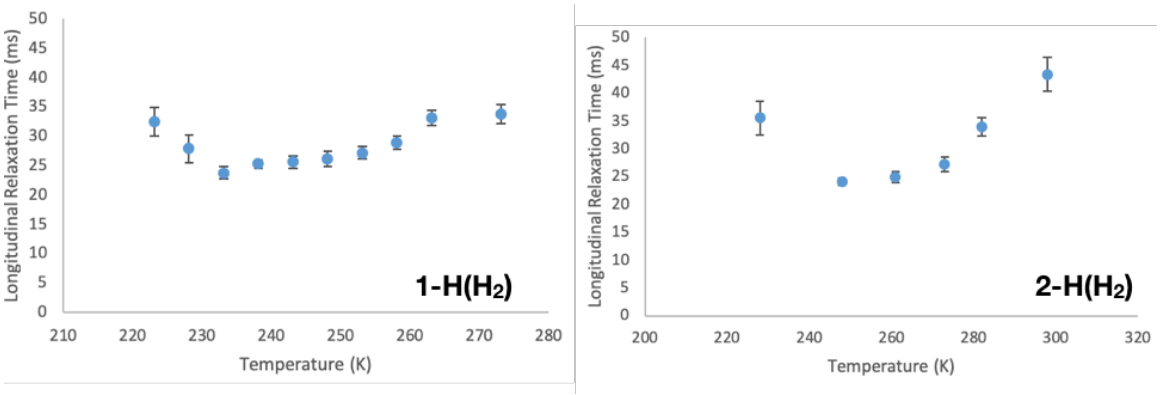

Figure 3.11: Variable temperature T_1 studies on the M-H resonance of **1-H(H_2)** and **2-H(H_2)**

behavior and independent generation (see Fig 3.9, d). Samples of an identical species can be prepared from the addition of $[H(OEt_2)_2][BArF_{20}]$ followed by the addition of 1 atm of H_2 and stirring overnight. The room temperature NMR spectrum of **2-H(H_2)** (THF-d_8 1 atm H_2) shows the expected ^{1}H NMR resonances of the ligand framework in addition to a broad resonance at -8.1 ppm that integrates to ca. 3 hydridic ^{1}H nuclei. Variable temperature ^{1}H NMR studies on **2-H(H_2)** showed the that the resonance at -8.1 ppm separates into two broad singlets with chemical shifts near -3 ppm and -15 ppm (at -83°C). This observation is consistent with M(H_2) and MH functionalities engaged in rapid exchange. A similar analysis for **1-H(H_2)** leads only to broadening of the M-H resonance. It is recognized that non-classical dihydrogen hydrides often exhibit rapid H_2/H exchange due to the intrinsically small barrier to breaking and reforming the H_2/H bonds.[57-59]

The identity of **2-H(H_2)** as dihydrogen-hydride complexes versus a classical trihydride is further evidence by a survey of spin-lattice relaxation times (T_1), for which a minimum of 24.9 ms was found at -25˚C (23.8 ms for **1-H(H_2)**). Notably, these values are within the norm of dihydrogen complexes and dihydrogen-hydride complexes alike; the enhanced spin-lattice relaxation time being a product of the large dipolar coupling of the

intact H_2 ligand bound to I = 7/2 Co.[50, 60-64] Working under the assumption that the procession of the H_2 ligand is rapid this T_{1min} corresponds to a d_{HH} ~ 0.91 Å after accounting for dipolar interaction between the adjacent ^{1}H and ^{59}Co nuclei (see Ch. 2).

Further validation of a non-classical dihydrogen-structure is garnered from DFT calculations (M06-L) which supported the notion that the mono-valent $MCo^{I}H(H_2)$ motif is more stable than its putative trivalent analog $MCo^{III}H_3$ by 5.3 and 2.2 kcal/mol for M =Al and Ga, respectively (see experimental section for more details). Furthermore, a close examination of the optimized structure of **1-H(H₂)** and **2-H(H₂)** reveals modest H_2 activation, with both species exhibiting d_{HH} values of 0.84 Å. The computationally determined d_{HH} values are in fair agreement with the d_{HH} extracted from T_1(min) measurements working under the premise of rapid procession of the H_2 ligand. Lastly, the

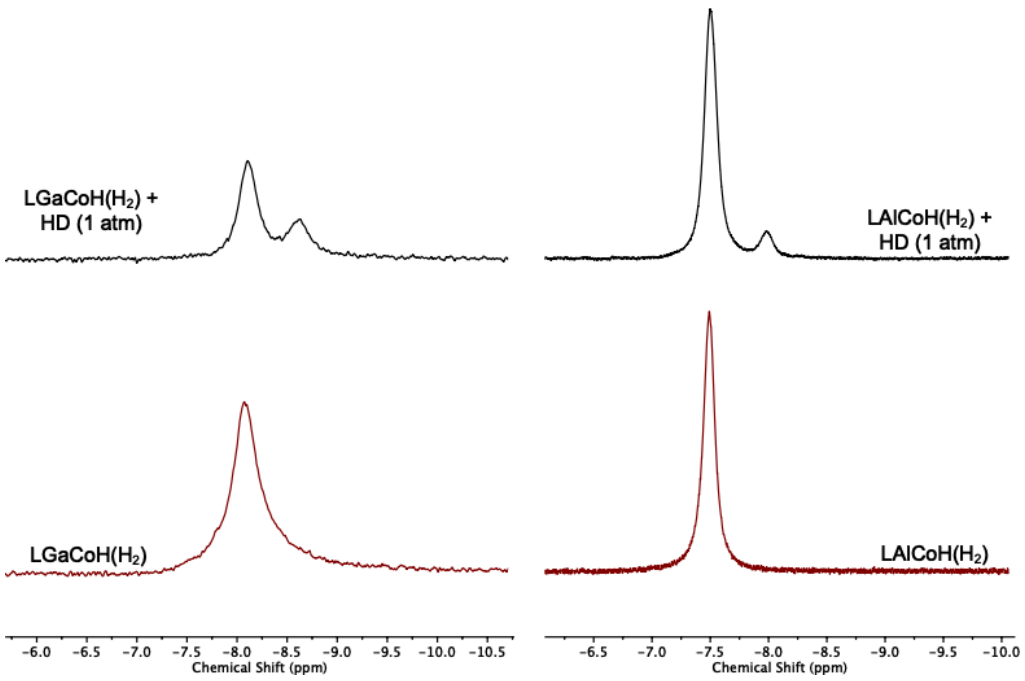

Figure 3.12: ^{1}H NMR of the Co-H in **1-H(H₂)** and **2-H(H₂)** showing the effect on deuterium incorporation on the Co-H resonance. Recorded at ca. -25˚C in THF-d_8.

$CoH(H_2)$ resonance is sensitive to deuterium incorporation, and exposure of solutions of **1/2-H(H_2)** to either HD or D_2/H_2 mixtures leads to isotopic chemical shift perturbation of the Co-H_n resonance arising from non-statistical incorporation of D in the Co-H positions, as shown in Fig 3.12.[65]

Further assignment of the formulation in **2-H(H_2)** comes from the thermally and chemically labile H_2 ligand. Removal of H_2 under vacuum gives rise to dark solutions of the square planar 16e$^-$ cobalt hydride, **2-H**, which is isostructural to the previously reported rhodium species, HRhGaL.[66] The ^{1}H NMR spectrum of **2-H** features a sharp M-H resonance that is complicated at room temperature due to partial signal coalescence. On cooling to -20˚C, the M-H resonance of **2-H** sharpens to reveal a doublet of triplets ($^2J_{H-P}$ = 82 *trans*, 52 *cis* Hz), strongly diagnostic of a square planar geometry. Similarly, the $^{31}P\{^1H\}$ NMR spectra revealed that near -20˚C the two *cis* phosphine environments also

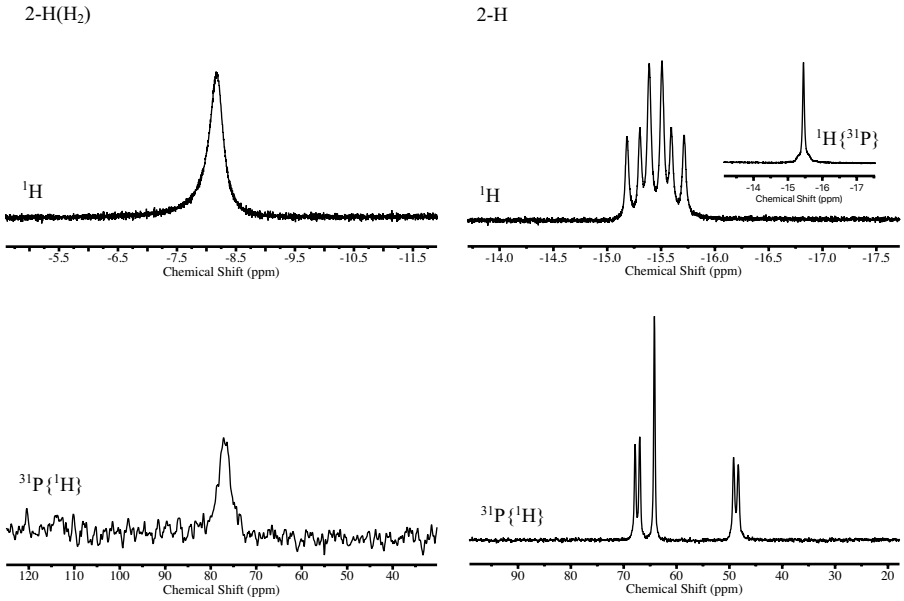

Figure 3.13: Selected NMR traces for **2-H(H_2)** and **2-H** recorded near -25˚C (THF-d_8 or toluene-d_8)

become inequivalent giving rise to three distinct $^{31}P\{^{1}H\}$ NMR environments with chemical shifts at 67.4 (d, J =142 Hz), 64.2 (App. s), and 48.8 (d, J = 142 Hz). A large ^{31}P coupling constant appears to arise from the two mutually *trans* phosphines, which are no longer related via time-averaged C_3 symmetry and become magnetically inequivalent. A similar set of observations are made for the analogous **1-H**, further validating its isoelectronic nature.

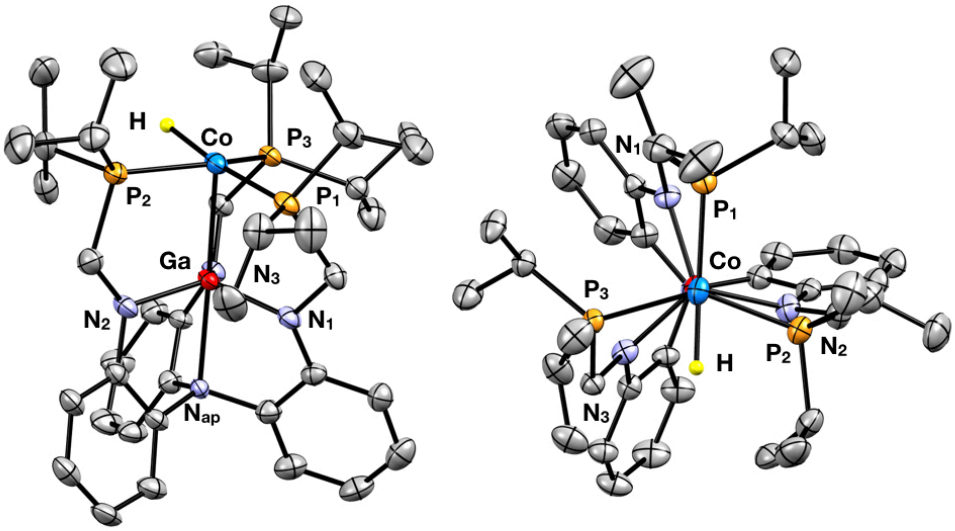

Figure 3.14: Molecular structure of **2-H** rendered at 50% probability. The righthand image is a projection viewed along the M-Ga vector. Selected hydrogens and crystallization solvent molecules omitted for clarity.

Isothermal diffusion of Et_2O/pentane mixtures containing **2-H** allowed for the growth of single crystals suitable for crystallographic analysis. Specimens of **2-H** crystallize as dark indigo plates in the triclinic space group P-1. The asymmetric unit contains two independent molecules (Z'=2) alongside a single molecule of diethyl ether. While both molecules feature bond metrics characteristic of a square planar metal hydride, only one of the molecules permits location of the hydride from the difference Fourier map, and thus this molecule will be discussed in detail (see experimental section for all metrics). The Co-Ga distance in **2-H** is fairly short at 2.413(1) Å, and is comparable to that observed

in Co^{-I} dihydrogen complex, $\mathbf{2(H_2)^-}$ which features a slightly shorter Co-Ga distance of 2.383(5) Å. The valence Co-P angles are strongly indicative of a distorted square planar environment with values of 107.58˚, 107.71˚, and 141.39˚, the latter encompassing the Co-H unit. Intriguingly, the sum of the P-Co-P angles, 356.7˚, indicates that there are only minor perturbations from a rigorously planar geometry despite the Co center lying 0.22 Å above the P_3 plane. Intriguingly, the hydride atom sits substantially further from this plane, though the error in this measurement is suspect in light of the small scattering factors for hydrogen (H-P_3 plane = 0.59Å). The Co-P bond distances are further reflective of the distorted square planar geometry, having values of 2.187, 2.201, and 2.215 Å, the latter

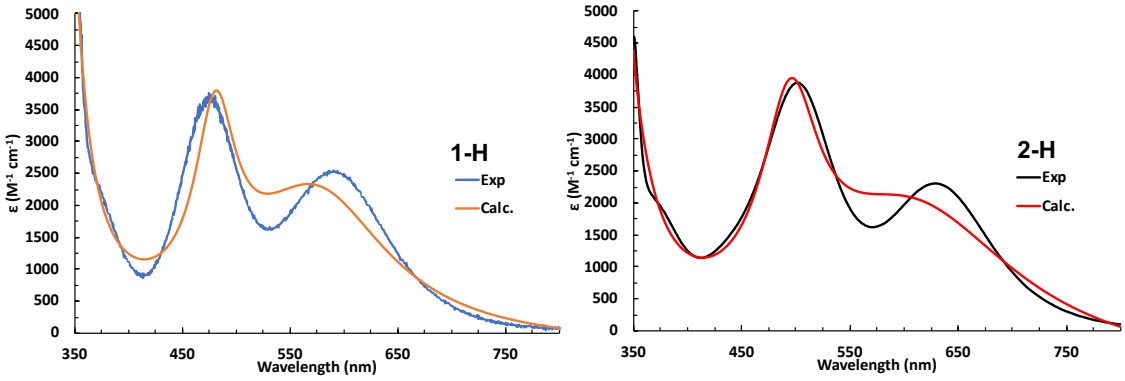

Figure 3.15: UV-vis spectra of **2-H** under argon in toluene (ca. 0.3 mM solutions).

oriented *trans* to the hydride ligand. The Co-P bond distances are collectively much longer than the corresponding Co^{-I} species $\mathbf{2(H_2)^-}$, supporting the notion that **2-H** is best described as an oxidized Co^{I} species.

The $16e^-$ hydrides **2-H** and **1-H**, are electronically unsaturated species, a notion which is supported by their UV-vis spectra (298K, toluene, Fig 3.14). Both **1-H** and **2-H** give rise to moderate intensity ($\epsilon > 2000$ M^{-1} cm^{-1}) visible transitions that are generally atypical of pure d-d transitions ($\epsilon < 500$ M^{-1} cm^{-1}). In the case of **2-H** these transitions occur at 500 nm ($\epsilon = 3900$ M^{-1} cm^{-1}) and at 630 nm ($\epsilon = 2300$ M^{-1} cm^{-1}), which produce the

purple/indigo color of its more concentrated solutions. The color of **1-H** is similar, resulting from transitions occurring at 480 nm (ϵ = 3600 M^{-1} cm^{-1}) and at 600 nm (ϵ = 2400 M^{-1} cm^{-1}). The experimental spectra for **2-H** and the values obtained from TD-DFT calculations (*vide infra*) are shown in Fig. 3.14.

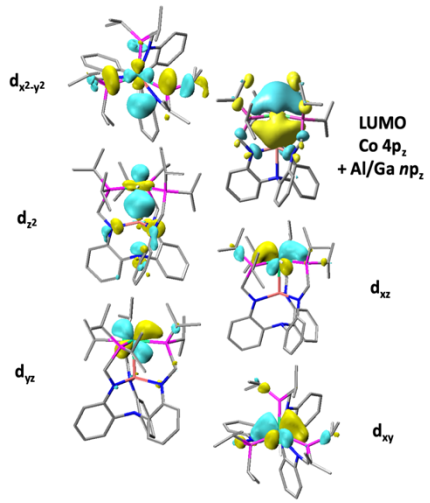

Figure 3.16: Molecular orbitals calculated for **2-H** (TD-DFT, M06-L, see appendix for full details). Orbitals for **1-H** are almost identical.

Puzzled by the appearance of these signatures, we turned to time-dependent density functional theory (TD-DFT, details in experimental section) in an effort to better understand the electronic structure of **1-H** and **2-H**. A fair fitting of the experimental UV-vis spectra were obtained by optimizing and studying the structure of **1-H** and **2-H** at the M06-L level of theory. A detailed analysis found that the transitions observed in the experimental spectrum are best described as HOMO and HOMO-1 transitions to a LUMO largely composed of cobalt $4p_z$ character (shown for M = Ga in Fig. 3.15). Notably, in a pseudo square planar coordination geometry, this hybrid LUMO lies lower in energy than the highly destabilized d_{x2-y2}. Analysis of the HOMO and HOMO-1 reveal that these orbitals are composed primarily of the cobalt-based d_{xz} and d_{z2} character, respectively. The transitions from the HOMO and HOMO-1 to the LUMO largely give rise to the observed

visible transitions, with the added intensity arising from the nature of the allowed 3d → 4p transition which are stabilized by the presence of 3p/4p Al/Ga orbitals. Of note, the LUMO of **1-H** and **2-H** are nearly identical to those observed in the nickel congener, NiGaL, for which we have shown is vital to the binding and acidity enhancement of the H_2 ligand as well as the isolation of formally Ni^{-I} complexes. [67-68]

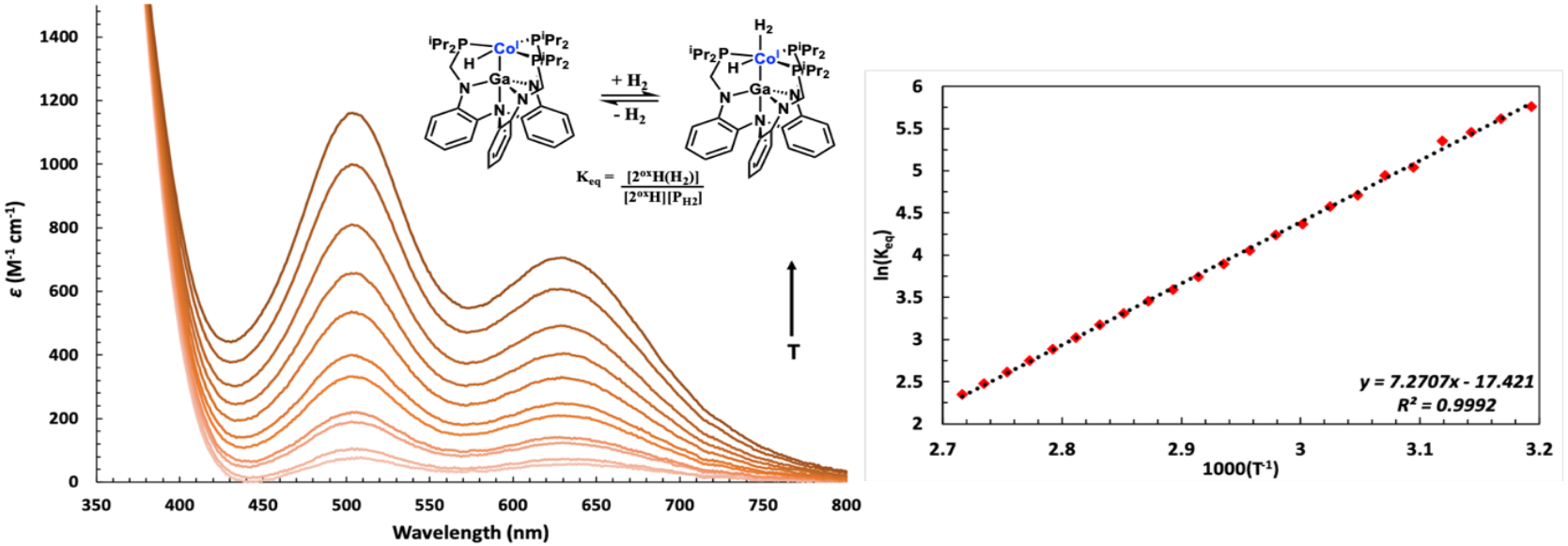

Figure 3.17: Left, variable temperature UV-vis traces under 10.0% H_2 in argon (40-90°C) for 2-H. Right, van't Hoff analysis of VT behavior (based on λ_{max} at 503 nm). The standard state refers to 1 atm of H_2 and 1M of all other species.

The binding of H_2 to **1/2-H** is reversible at room temperature, and heating solutions of **1/2-H(H_2)** leads to reformation of the **1/2-H**, which is conveniently monitored by UV-vis spectroscopy in toluene under 1 atm of 10% H_2 in Ar (or 25% for **1-H**). Noteworthy is the use of 10% H_2 in argon, as mixtures containing more H_2 required temperatures above 50˚C to observe the desired thermochromic behavior. From 40 to 95˚C, **2-H** exhibits thermochromic behavior. When subjected to a van't Hoff analysis this behavior reveals that the equilibrium shown in Fig 3.16 strongly favors the dihydrogen bound complex with an estimated K_{298} = 1200 ± 200 atm^{-1}. The ΔG° value of -4.2(1) kcal mol^{-1} is consistent with the equilibria almost entirely favoring **2-H(H_2)** under 1 atm of H_2.

Furthermore, the Δ*H*° of -14.5(1) kcal mol^{-1} and Δ*S*° = -34.8(2) cal mol^{-1} K^{-1} for **2-H** are within the values of H_2 binding commonly observed for non-classical dihydrogen complexes reported in the literature (Δ*H*° from -6.5 to -18 kcal mol^{-1} and Δ*S*° = -19 to -44 cal mol^{-1} K^{-1}).[67] We note, as have others, that care must be exercised not to directly compare these values as their standard states may be defined differently (here, 1 atm of H_2). Definitive conclusions regarding the strength of this binding event are limited because only a small number of molecular cobalt complexes reversibly bind H_2. Indeed only a handful of studies on such species exist, with Co^0 complex (TBP)Co(η^2-H_2) being the only species being studied in the manner discussed here.[69] A definitive comparison between **1-H** and **2-H**, can be drawn, as the latter binds H_2 more strongly than its aluminum analog, for which a similar VT UV-vis study revealed binding is favorable with Δ*G*˚ = -2.1 kcal/mol and an identical standard state.

The coordinated dihydrogen ligand in **2-H(H$_2$)** (and **1-H(H$_2$)**) is rendered acidic and can be deprotonated by exogenous base to regenerated **2(H$_2$)**$^-$. Unfortunately, the equilibrium constant cannot be measured in acetonitrile, as the H_2 ligand is rapidly (and irreversibly) displaced by weak donors such as CH_3CN. However, in THF-d_8 the equilibrium is conveniently monitored by ^{1}H NMR spectroscopy utilizing a small excess (1.5–2.0 equivalents) of the base ^{tBu}N(^{iPr}NHC^{Me}) (pK_a = 30.3 CH_3CN).[70] When performed at concentrations low enough to inhibit self-association in THF-d_8 ([Co]$_{tot}$ < 10 mM, 1 atm H_2) a K_{298K} = 0.072(1) can be extracted. Under the limiting assumption that the equilibria of **2(H$_2$)**$^-$ and **2-H(H$_2$)** with base would be similar in CH_3CN, one can estimate that the pK_a of **2-H(H$_2$)** is 31.3(1).

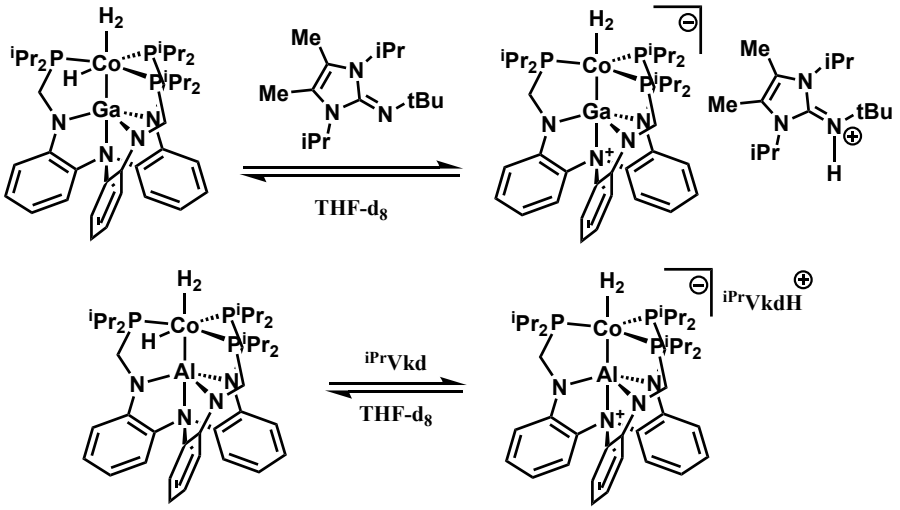

Figure 3.18: Reactions used to calculate the pK_a of **1-H(H$_2$)** and **2-H(H$_2$).**

A similar analysis, but with Verkade's base and **1-H(H$_2$),** allows for the observation of K_{eq} = 0.25(1) and ultimately a pK_a of 34.2(1) under the same assumptions made for **2-H(H$_2$)**. Notably, the pK_a of **1-H(H$_2$)** is higher than that of Verkade's base, indicating that the deprotonation of the modestly acidic H_2 ligand likely inhibits the hydrogenation of CO_2. Furthermore, despite being entirely isoelectronic cobalt hydrides, the local electronic

environment of **1-H(H_2)** and **2-H(H_2)** enhances the acidity of the H_2 ligand by nearly three orders of magnitude.

Table 3.2: System of equations utilized to calculate ΔG_{H-}

2-H(H_2) ↔ 2-H + H_2	$\Delta G°_{H2}$	(2)
BaseH^+ + 2(H_2)$^-$ ↔ 2-H(H_2) + base	$\Delta G°$=-RTln(K)	(3)
base + H^+ ↔ baseH^+	$\Delta G°$=-RTln(K)	(4)
H_2 ↔ H^+ + H^-	$\Delta G°$=76.0 kcal/mol	(5)
2(H_2)$^-$ ↔ 2-H + H^-	$\Delta G°_{H-} = \sum$(2)-(5)	(6)

With a detailed knowledge of both the pK_a and H_2 binding energy of **1-H(H_2)** and **2-H(H_2)** we can construct a series of equations that enable an estimation of the hydride donor ability of their conjugate bases, **1(H_2)$^-$** and **2(H_2)$^-$**. As the transfer of H^- in chemical systems produces a formally unsaturated center (e.g. **2-H)** the binding energy of H_2 must be accurately known to compensate for the additional thermodynamic leverage gained in the formation of **1/2-H(H_2)**. Performing this analysis allows one to derive the experimental hydricity values of **1(H_2)$^-$** and **2(H_2)$^-$** of 31.4(1) and 37.4(1) kcal/mol. Gratifyingly, isodesmic hydride transfer reactions between $(dmpe)_2CoH$ ($\Delta G°_{H-}$ = 36 kcal/mol) studied by DFT (M06-L) corroborate this measurement, with good agreement between both the absolute values and relative differences between the hydricity of **1(H_2)$^-$** and **2(H_2)$^-$** (calculated to be 33.5 and 38.3 kcal/mol, respectively).

3.3.3 Mechanism of CO_2 hydrogenation

The stoichiometric reactivity and acid/base properties of the **1(H_2)$^-$** and **2(H_2)$^-$** contrast with our recent report of CO_2 hydrogenation catalyzed by a d^{10} bimetallic Ni-Ga complex, **2-Ni** (e.g. NiGaL) and thus we sought to elucidate their mechanistic differences. For the sake of fair comparison, the direct analogy for M = Ga is discussed moving forward.

Both **2(H$_2$)$^-$** and **2-Ni** bind and activate H_2, as indicated by their diagnostic NMR signatures. However, despite their isoelectronic nature, these two species activate the H_2 ligand in different manners due to the combination of charge and π-basicity at their respective d^{10} centers (0.87 Å for **2-Ni**, 0.98(1) Å for **2(H$_2$)$^-$**). For example, we have found that when **2-Ni** binds H_2 it greatly enhances the acidity of the H_2 ligand (pK_a = 33.1 est. CH_3CN) when compared to that of free H_2 (~45). In contrast, the H_2 ligand in **2(H$_2$)$^-$** does not exhibit measurable acidic properties, as indicated by a lack of any observable reaction between this species with bases such as ^{iPr}Vkd (pK_a = 33.6), P$_4^t$Bu (pK_a = 42.4), or even ^{n}BuLi (pK_a > 45). This notion is further supported by DFT calculations which suggest that the deprotonation of **2(H$_2$)$^-$** by Verkade's base to generate a terminal, di-anionic hydride, is thermodynamically unfeasible (ΔG° = +24.5 kcal/mol, $\Delta G^\ddagger$ = +49.8 kcal/mol, M06-L, full ligand). The difficulty associated with this deprotonation is attributed to the inherent challenge in deprotonating an anionic species when compared to either neutral/cationic counterparts.[55] The contrasting difference between **2(H$_2$)$^-$** and **2-Ni** is also clearly apparent when considering their stability; **2(H$_2$)$^-$** is stable under vacuum and to at least 80˚C, whereas the dihydrogen complex of **2-Ni** only exists in equilibrium at room temperature.

While the Co^{-I} center in **2(H$_2$)$^-$** does not enhance the acidity of the anionic dihydrogen complex, it does enhance the hydricity of the species. This is directly evidenced by the measured value of ΔG_{H^-} = 37.4(1) kcal/mol obtained from base heterolysis experiments. Notably, the ΔG_{H^-} value of **2(H$_2$)$^-$** is more hydridic than many terminal base-metal hydride complexes in general (for example dppe$_2$NiH$^+$ or dppe$_2$CoH).[40-41, 71] Computational support for this measurement is also gleaned from isodesmic hydride transfer reactions between **2(H$_2$)$^-$** and (dmpe)$_2$Co$^+$ to provide **2-H** and (dmpe)$_2$CoH (ΔG_{H^-}

= 37 kcal/mol). Compared to deprotonation prior to hydride transfer, the direct transfer of H^- to CO_2 from **2(H₂)⁻** is substantially more facile and generates putative hydrido-formate species **2-H(CO₂H)⁻** where the formate ligand is bound in the apical position. Specifically, both the energy of activation and overall reaction energy to form **2-H(CO₂H)⁻** are substantially lower than the values observed for deprotonation (ΔG° = 3.8 kcal/mol, $\Delta G^\ddagger$ = 17.9 kcal/mol). The transfer of H^- to CO_2 from **2(H₂)⁻** occurs via transition state 2 (T.S. 2, Fig 3.18). Transition state 2 occurs late in the reaction coordinate, as indicated a fully cleaved dihydrogen ligand (d_{HH} = 2.18 Å) and a short formate C-H bond of 1.586 Å. The observation that hydride transfer requires further activation of the H_2 ligand in **2(H₂)⁻** is in line with the notion that the valance tautomer of **2(H₂)⁻**, namely **2H₂⁻**, lies within the error of theoretical calculations performed on **2(H₂)⁻**.[50] Furthermore, comparing the geometries of **2(H₂)⁻** and **2-H** reveals that the structure of T.S. 2 more strongly resembles an anionic hydride adduct of **2-H**, rather than **2(H₂)⁻** (see experimental section for comparison). Furthermore, the complementary transition state for CO_2 hydrogenation (T.S. 1 in Fig. 3.18) mediated by **2-Ni** is similar, supporting the notion that **2(H₂)⁻** behaves as a masked source of its valence tautomer, **2H₂⁻**. Further stabilization can be gained by dissociating the formate ligand from **2-H(CO₂H)⁻**, to generate **2-H** and free formate (ΔG° = + 0.5 kcal/mol), which are the experimentally observed products.

Once **2-H** has formed, theory predicts that H_2 binding is thermoneutral, suggesting that the energetic cost of formate/dihydrogen exchange is near negligible and likely facile at high pressures of H_2. Furthermore, the resting state of the CoGa bimetallic system is observed to be **2-H(H₂)** with weak bases (DBU, ^{t}BuTMG), wherein H_2 is strongly bound to cobalt (experimentally ΔG°_{H2} = -4.2 kcal/mol). The last step for catalysis to proceed is

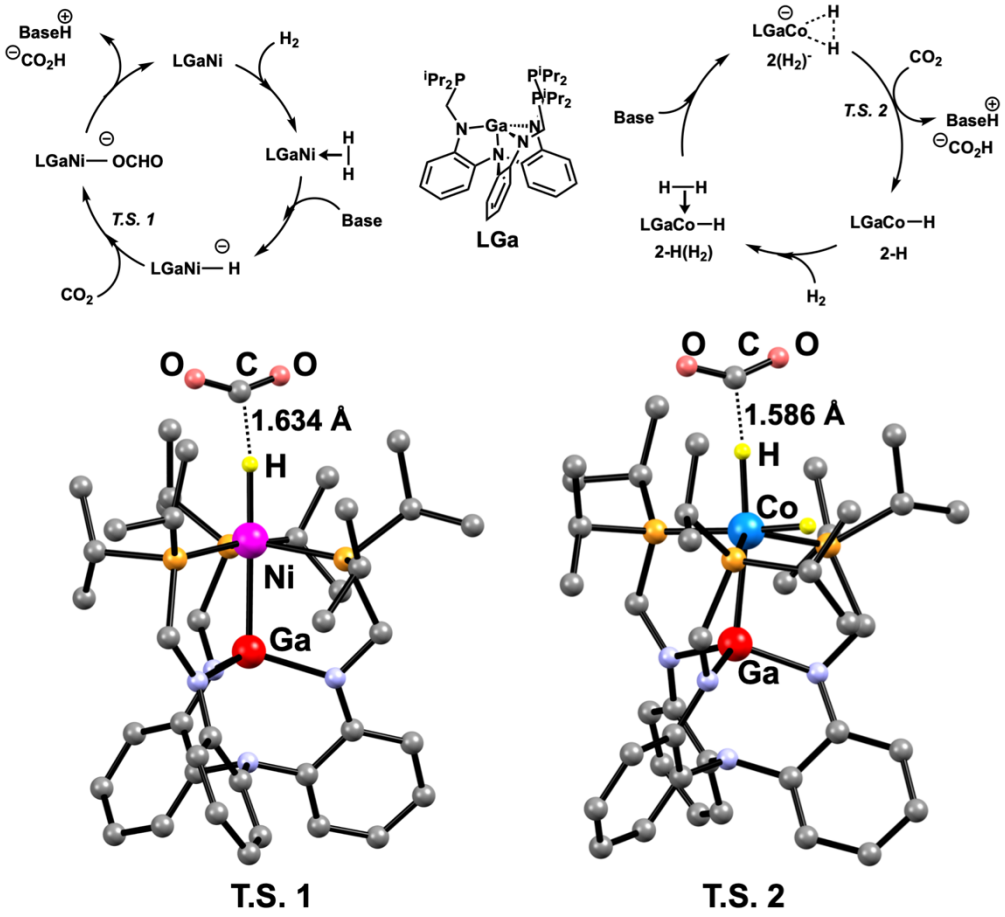

Figure 3.19: Top, comparative mechanisms between **2(H₂)**⁻ and **2-Ni**. Transition state structure of hydride transfer from key intermediates to CO_2 for both Ni and Co complexes.

the regeneration of **2(H₂)**⁻ by deprotonation of **2-H(H₂)** with base. Experimentally, DBU, ^{t}BuTMG, and Vkd are capable of deprotonating this modest acid (experimental pK_a = 31.3(1)). In line with this observation, the anionic dihydrogen complex, **2(H₂)**⁻ can be reformed directly from deprotonation with exogenous base ($\Delta G^{\dagger}$ = 48.4 kcal/mol), or the barrier can be greatly reduced by the addition of formate as a proton shuttle ($\Delta G^{\dagger}$ = 11.0 kcal/mol). More detailed energy profiles of these transformations can be found in the experimental section.

Given the unique $Co^{-I/I}$ redox cycle by which **2(H₂)⁻** mediates the hydrogenation of CO_2 to formate, a comparison with the $Co^{I/III}$ redox cycle observed for $(dmpe)_2CoH$ is also informative. For example, in the $(dmpe)_2Co^+$ system oxidative addition to form *cis*-$(dmpe)_2CoH_2^+$ is observed. The species *cis*-$(dmpe)_2CoH_2^+$ is a classical dihydride with modestly acidic behavior (pK_a = 33.7 CH_3CN) and deprotonation with strong base gives rise to $(dmpe)_2CoH$ which can generate formate with high efficiency (ΔG° = 36 kcal/mol). The present system is similarity hydridic (ΔG_{H^-} = 37.4(1) kcal/mol), but instead operates via two separate non-classical dihydrogen species **2(H₂)⁻** and **2-H(H₂)** where the H_2 bond remains intact. Moreover, in light of the difficulties in deprotonating **1-H(H₂)** it is apparent that the use of Lewis-acidic metalloligands to tune the electronic properties of the metal center is vital to catalyst proficiency. To this end, the LGa scaffold allows for **2-H(H₂)** to be 2 orders of magnitude more acidic than *cis*-$(dmpe)_2CoH_2^+$, which in turn facilitates catalyst efficiently with weaker bases such DBU and ^{t}BuTMG while retaining the strongly hydridic character of **2(H₂)⁻**.

3.4 Conclusions

Both aluminum and gallium act as Lewis-acidic supports for Co^{-I} complexes that catalyze the hydrogenation of CO_2 to formate. Key to proficient catalysis is the use of the gallium metalloligand as it is substantially more active than its aluminum congener and its indium analog is not a catalyst. Mechanistically, a simple set of elementary equations is proposed based on the observations made via stoichiometric transformations. First, the pre-catalyst, **2(N₂)⁻**, undergoes substitution with H_2 at low pressures to yield the anionic dihydrogen complex, **2(H₂)⁻**. The anionic dihydrogen complexes (**1**/**2(H₂)⁻**) are not acidic

and fail to react with bases as strong as $P_4{}^tBu$ or ^nBuLi, which is in contrast to their isoelectronic nickel counterparts. Despite possessing an intact H-H bond, **1(H₂)⁻** and **2(H₂)⁻** act as masked sources of H^- and provide a sufficient thermodynamic driving force to transfer H^- to CO_2 (6-10 kcal/mol) with concomitant formation of the $16e^-$ cobalt hydrides **1-H** and **2-H**. On the basis of theoretical studies, outer sphere hydride transfer occurs via a late transition state for **2(H₂)⁻** via a formal hydride adduct of **2-H** that results from oxidative addition of H_2 across the π-basic Co^{-I} center. DFT supports the notion that the oxidative addition of H_2 is facile and nearly thermoneutral (within the error of the theory employed), which is experimentally inferred from the ability of **1/2(H₂)⁻** to scramble H_2 and D_2.

The binding of hydrogen to coordinately unsaturated species **1-H** and **2-H** results in the formation of **1/2-H(H₂)** which are best described as a non-classical dihydrogen-hydride complexes on the basis of various NMR experiments. As indicated by VT UV-vis measurements, **1/2-H(H₂)** bind H_2 reversibly providing insight into the binding of H_2 at low-valent cobalt centers, which is scarcely realized for these frequently thermally labile species. Under H_2, **1/2-H(H₂)** are persistent catalytic intermediates and useful in that they are readily deprotonated by organic bases to regenerate the **1/2(H₂)⁻**.

It is informative to compare the present system to our previously reported Ni-mediated CO_2 reduction using **2-Ni**. In the case at hand, **1**/**2(H₂)⁻** mediate the reduction of CO_2 through a different mechanism that involves formal cobalt-based redox chemistry. The anionic dihydrogen complexes (Co^{-I}) transfers H^- to CO_2 and generate an oxidized Co^I center observable as either as **1/2-H(H₂)** or **1/2-H**. Furthermore, the H_2 ligand in **2(H₂)⁻** is not rendered acidic, but rather hydridic, upon coordination to the π-basic cobalt fragment and highlights the role of charge and π-basicity across the isoelectronic complexes **2-Ni**

and **2(H$_2$)$^-$** . The acidity of H_2 is important when comparing the oxidized species **1/2-H(H$_2$)** where the Co^I fragment activates the H_2 ligand such that it can easily undergo deprotonation with strong organic bases such as Vkd, ^{t}BuTMG, and DBU to regenerate **2(H$_2$)$^-$** re-establishing the Co^{-I} oxidation state. The difference in mechanism is attributed to the ability of Co vs. Ni to activate the H_2 ligand, as well as the charge localization of the hydride donor. The rational modification of the choice of metal allows for a significant enhancement in the acidity of the H_2 ligand in **2-H(H$_2$),** which in conjunction with the hydricity of **2(H$_2$)$^-$** allows for a well-balanced thermodynamic catalytic cycle to proceed, even with bases such as DBU and ^{t}BuTMG, to rapidly produce formate with impressive turnover numbers and frequencies that are comparable to many of the state-of-the-art cobalt complexes reported in the literature. Studies are ongoing to further optimize this catalytic mechanism such that higher stability and improved performance can be realized.

3.5 Experimental Section

General Considerations: Unless otherwise stated, all manipulations were performed under a dinitrogen or argon atmosphere inside a glovebox or using standard Schlenk techniques. Standard solvents were deoxygenated by sparging with N_2 and dried by passing through activated alumina columns of a SG Water solvent purification system. $NaK_{2.8}$ used for drying solvents was prepared by pressing desired amounts of Na and K metals together under argon, and then decanting any present slag (and cautiously quenching). Deuterated solvents were purchased from Cambridge Isotope Laboratories, Inc., degassed via freeze-pump-thaw cycles, and either stirred with NaK (THF-d_8 and Toluene-d_8) and distilled, or stored over activated 4 Å molecular sieves for 48 hrs (C_6D_6). Gas cylinders containing H_2, CO_2 or ~1:1 H_2/CO_2 were purchased from Matheson or Oxarc. Specific cylinders that were suspected of containing traces of water vapor (CO_2 and H_2/CO_2) were passed through an Agilent Oxygen Moisture Trap (Model OT-2-SS) drying column to minimize residual oxygen and moisture in the gas stream. GC analysis showed the mixture used for catalysis to be 48% H_2 and 52% CO_2 (~1:1 H_2/CO_2) after passing through the drying column. ^1H, ^{13}C, and ^{31}P NMR spectra were recorded on Bruker 500, or 400 MHz and Varian 500 MHz spectrometers and referenced to internal residual solvent (H_3PO_4 for ^{31}P NMR spectra).[72] IR spectra were obtained for solid samples in KBr pellets using a Bruker Tensor-37 FTIR with OPUS 6.5 software. The neutral ligand ($N(o\text{-}(NHCH_2PiPr_2)C_6H_4)_3$ (abbreviated as H_3L)[73], monometallic species (LAl, LGa, LIn) [74], [PPN]$BArF_{24}$[56], $H(OEt_2)_2BArF_{20}$/$H(OEt_2)_2BArF_{24}$[75-76], and guanidinium base $^{tBu}N(^{IPr}NHC^{Me})$[70], were synthesized according to literature procedures. tButyl-tetramethylguanidine (abbreviated as tBuTMG), 2,8,9-triisopropyl-2,5,8,9-tetraaza-1-phosphabicyclo[3,3,3]undecane

(Verkade's base, abbreviated as Vkd), and bis(triphenylphosphine)iminium chloride (PPNCl) were purchased from Aldrich. [PPN]Cl was recrystallized from dichloromethane to yield the solvate and then dried in vacuum at 60˚C before use. Lithium triflate was purchased from Strem. All other reagents were purchased from commercial vendors and used without purification unless otherwise noted. Elemental analyses were performed by Robertson Microlit Laboratories (Ledgewood, NJ).

Electrochemical experiments were performed utilizing a CHI instruments 620D potentiostat at 295 ± 3 K utilizing a three-electrode setup consisting of a 1mm PEEK-encased glassy carbon working electron, a Pt wire pseudo-reference electrode, and a graphite counter electrode. The working electrode was polished with 0.25 μm diamond polishing paste inside a glovebox and then rinsed with THF shortly before use. Experiments under 1 atm. of inert gas (N_2 or Ar) were conducted in a glovebox with the appropriate atmosphere. The experiments were performed a glass vial containing 2 mL of 0.1 M $[^nBu_4N][B(C_6F_5)_4]$ and an analyte concentration varying from 1-2.5 mM in addition to an internal standard of ferrocene (ca. 0.25mM). The THF used for CV experiments was dried over NaK, vacuum transferred, and stored in a PTFE plugged solvent bulb on 20% w/v molecular sieves. High pressure experiments were conducted using ultra-high purity H_2 gas in a modified Parr © reactor, that has been described previously.[77]

UV−vis experiments were carried out using either a Shimadzu UV-2401PC (PNNL) or Cary UV-50 (UMN) spectrophotometers both equipped with a variable-temperature cuvette holder attachment. For the Shimadzu instrument, the sample and solvent blank

temperatures were controlled with a PolyScience external cooling bath with recirculating 50:50 water/ethylene glycol solutions. For the Cary instrument, a similar variable temperature cuvette holder was utilized alongside a dual cell Peltier accessory with recirculating water bath. Samples were placed into 1.00 cm quartz cuvettes fitted with a greased stopcock and sealed inside a glovebox. Each heating accessory had temperature accuracy of +/- 0.1 ˚C, which routinely reached equilibrium after 5 minutes.

Synthesis of LAlCoH: In a glovebox containing N_2, [PPN][LAlCo(N_2)] (125mg, 0.1mmol) was suspended in 10mL of THF and subsequently cooled to -30°C in a freezer. To this solution was added a THF solution of [H(OEt_2)$_2$]$BArF_{20}$ (77.8 mg, 0.1 mmol, 2mL). Within minutes after the addition the solution developed a deep blue color. The mixture was stirred for 30 minutes at room temperature, and then the volatiles were removed. The remaining solid is extracted with hexane (2x15mL) and filtered away from a colorless microcrystalline solid. The hexane was removed in vacuum to yield 51mg (72% yield) of deep blue microcrystalline solid that was stored in a freezer at -30°C. A sample suitable for elemental analysis was recrystallized from minimal Et_2O at -30˚C. NMR samples prepared under N_2 showed complicated Co-H splitting patterns, suggestive of N_2 binding to LAlCoH. The data listed below are those acquired after preparing a sample in an argon glovebox. ^{1}H NMR (500 MHz, Toluene-d_8) δ 7.47 (d, *J* = 7.6 Hz, 3H, ArH), 7.11 (t, J = 7.5 Hz, 3H, ArH, center frequency coincident with Tol-d_8) 6.49 (t, *J* = 7.5 Hz, 3H, ArH), 6.45 (d, *J* = 7.9 Hz, 3H, ArH), 3.33 (br, 2H, CH_2), 3.09 (s, 4H, CH_2), 2.17-2.1 (br, 6H, *CH*(CH_3)$_2$), 1.00 (br, 36H, CH*(*CH_3*)*$_2$).), -15.18 (td, *J* = 102, 55 Hz).^{31}P{^{1}H} NMR (202

MHz, THF-d_8, -25°C) δ 62.66 (d, J = 137 Hz), 59.50, 44.90 (d, J = 137 Hz). Analysis calc. (found) for $C_{39}H_{60}N_4P_3AlCo$ • 0.5 Et_2O: C 61.42 (61.70), H 8.30 (8.05), N 6.99 (6.75).

Synthesis of GaCoH: In an argon filled glovebox, [PPN][LGaCo(N_2)] (148mg, 0.1 mmol) and LiOTf (28mg, 0.18mmol) was suspended in 20mL of THF and stirred to give a homogenous yellow solution. This solution was transferred to a Schlenk flask with Teflon plug, and the interfaced to a vacuum manifold. The headspace of the vessel was removed via a freeze-pump-thaw cycle and as the solvent began to thaw, the atmosphere was replaced with 1 atm. of 50:50 H_2:CO_2. While still cold, the initially bright yellow solution darkened to produce a dark green solution. On warming, the solution then reverts to a dull yellow color with concomitant formation of a colorless precipitate. After stirring for one hour at room temperature, the volatiles were removed at which point the color of the solution turns deep green. The residue was extracted into 20mL of diethyl ether, and filtered from a large amount of colorless precipitate, and reduced to dryness. After trituration with hexane 80.0 mg (92% yield) of a dichroic purple/green microcrystalline powder is obtained. $^1H\{^{31}P\}$ NMR (400 MHz, 298K, Toluene-d_8) δ: 7.50 (d, J = 7.6 Hz, ArH, 3H), 7.09 (t, J = 7.7 Hz, ArH, 3H), 6.50 (t, J = 7.5 Hz, ArH, 3H), 6.46 (d, J = 7.9 Hz, ArH, 3H), 3.24 (br, 2H, CH_2), 3.08 (s, 4H, CH_2), 2.40–2.13 (br, 6H, $CH(CH_3)_2$), 1.2-0.71 (br, 6H, $CH(CH_3)_2$, -15.68 (s, 1H, Co-H). At -18˚C the resonance for the Co-H sharpens with a slight chemical shift perturbation and the expected splitting pattern ^1H NMR (400 MHz, 255K, Toluene-d_8) δ -15.45 (td, J = 82.3, 47.5 Hz). $^{31}P\{^1H\}$ NMR {162 MHz, 298K, toluene-d_8) δ 64.9 (s, 3p). At -25˚C each phosphine environment is inequivalent $^{31}P\{^1H\}$ NMR {162 MHz, 248K, toluene-d_8) δ 67.40 (d, J = 142.2 Hz, 1P), 64.19 (s, 1p), 48.76 (d,

J = 142.2 Hz, 1P). Analysis calc. (found) for $C_{39}H_{61}N_4P_3GaCo$: C 58.01 (56.24), H 7.61 (7.87), N 6.94 (6.30). Repeated analysis repeatedly showed low values for carbon, which we associate to the highly air-sensitive nature of this species.

In-situ generation of LAlCoH(H_2) and LGaCoH(H_2)

Method A: H_2 addition to LMCoH. A solution of LMCoH (ca. 5mg in 0.5mL of toluene-d_8 or THF-d_8) was freeze-pump-thawed on a vacuum manifold, and the atmosphere was replaced with 1-2 atm. of H_2 (or HD/D_2 if needed). The color of the solution rapidly faded from deep blue/indigo to colorless as the H_2 dissolves into solution. The mixture is mixed by aid of a vortex mixer, and then the pressure of the cell remeasured to ensure the desired pressure has been met.

Method B: Treatment with H^+BArF_{20} followed by H_2. A solution of 5-8mg of [PPN][LMCo(N_2)] was treated with a stoichiometric amount of [H(OEt_2)$_2$]$BArF_{20}$ (typically 3-5mg) as a solution in THF-d_8/Toluene-d_8. The solids were rapidly solubilized, and then filtered (to remove any [PPN][$BArF_{20}$]) directly into a J. Young NMR tube at which point the atmosphere was replaced with 1-4 atm. H_2 as described in method B and the mixture stirred overnight at room temperature before analysis.

Method C: Treatment with 1:1 CO_2:H_2 (1.8 atm). 5 mg of [PPN][LMCo(N_2)] was dissolved in 0.5 mL of THF-d_8 and added to a J. Young NMR tube. This solution is exposed to static vacuum three times to remove the headspace of the tube, and then refilled with 14 psig as read from a bourdon gauge (ca. 1.8 atm). The solution was mixed by aid of a vortex

mixer wherein it gave rise to a nearly colorless solution and some colorless precipitate. Preforming this experiment with M = In lead to deposition of solids and an intractable mixture by ^{1}H NMR

Spectral Data for LGaCoH(H₂): ^{1}H NMR (500 MHz, THF-d_8, 25°C) δ 7.27 (d, J = 7.6 Hz, 3H, ArH), 6.79 (t, J = 7.6 Hz, 3H, ArH), 6.31 (d, J = 8.0 Hz, 3H, ArH), 6.27 (t, J = 7.5 Hz, 3H, ArH), 2.97 (s, 6H, CH_2), 2.07 (br p, J = 7.7 Hz, 6H, *CH*$(CH_3)_2$), 1.17 (s, 18H, CH*(CH-₃)₂*), 1.07 (s, 18H, CH*(CH₃)₂*), -8.08 (s, 3H). ^{1}H NMR (400 MHz, 298K Toluene-d_8) δ 7.59 (d, J = 7.6, 3H, ArH), 7.13 (t, J = 7.6 Hz, 3H), 6.6-6.47 (mult overlapping Ar-H, 6H), 2.92 (s, 6H), 1.79 (hept, J = 7.1 Hz, 6H, *CH*$(CH_3)_2$), 0.93 (s, 18H, CH*(CH₃)₂*), 0.84 (s, 18H, CH*(CH₃)₂*), -8.30 (s, 3H, $CoH(H_2)$).^{31}P{^{1}H} (202 MHz, THF-d_8) δ 75.6 (referenced internally to PPN^+ at 21.0 ppm). The ^{31}P NMR chemical shift does not appear to shift with changes in NMR solvent employed. Elemental analysis of this complex was not obtained due to facile loss of H_2.

Spectral Data for $LAlCoH(H_2)$ ^{1}H NMR (500 MHz, THF-d_8, -45°C) δ 7.00 (d, J = 7.2 Hz, 3H, ArH), 6.49 (t, J = 7.3 Hz, 3H, ArH), 5.95 (ap. t, J = 7.8 Hz, 6H, overlapping ArH), 2.72 (s, 3H, CH_2), 2.44 (s, 3H, CH_2), 1.70 (s, 6H, *CH*$(CH_3)_2$), 0.93 (s, 18H, CH*(CH₃)₂*), 0.63 (s, 9H, CH*(CH₃)₂*), 0.46 (s, 9H, CH*(CH₃)₂*), -7.80 (s, 3H). ^{1}H NMR (500 MHz, 298K, Toluene-d_8) δ 7.51 (d, J = 7.4 Hz, 3H, ArH), 7.10 (t, J = 8.8 Hz, 3H, ArH), 6.53 – 6.44 (m, 6H, Ar-H overlapping), 2.92 (s, 6H, CH_2), 1.81 (ap. q, J = 7.9 Hz, 6H, *CH*$(CH_3)_2$), 0.96 (s, 18H, CH*(CH₃)₂*), 0.87 (s, 18H, CH*(CH₃)₂*), -7.97 (s, 3H, $CoH(H_2)$). ^{31}P{^{1}H} (202 MHz, THF-d_8) δ 68.1 (referenced internally to PPN^+ at 21.0 ppm). The ^{31}P NMR chemical shift

does not appear to shift with changes in NMR solvent employed. Elemental analysis of this complex was not obtained due to facile loss of H_2.

Synthesis of [PPN][LGaCo(CO)]: To a stirred slurry of [PPN][LGaCo(N_2)] (56.3mg 41 μmol) was added an excess of ethyl formate (0.25 mL, mmol) at room temperature. Immediately the color of the solution fades to nearly colorless, which is accompanied by gas evolution. The solution is stirred for overnight at room temperature, and then the volatiles were removed in vacuo, and the solids washed with Et_2O (2x5mL) to yield 45 mg (80% yield) of a pale yellow solid. The material is then recrystallized from DME/Et_2O to provided analytically pure material. One recrystallized, this material is difficult to re-dissolve in THF and sometimes requires extended stirring or heating. ^{1}H NMR (400 MHz, THF-d_8) δ 7.74-7.42 (m, 30H, PPN^+ ArH), 7.07 (d, J = 7.5 Hz, 3H, ArH), 6.57 (t, J = 7.7 Hz, 3H, ArH), 6.16 (d, J = 8.0 Hz, 3H, ArH), 5.96 (t, J = 7.4 Hz, 3H, ArH), 2.65 (s, 6H, CH_2), 2.03 (s, 6H, *CH*(CH_3)$_2$), 1.4-0.67 (br, 36H, CH*(CH$_3$)$_2$*). The CO resonance could not be detected by ^{13}C NMR even during prolonged collection times, presumably due to coupling to ^{59}Co (I = 7/2, 100 %), which is well documented. ^{31}P{^{1}H} NMR (203 MHz, THF-d_8) δ 78.6 (3P), 21.00 (2P, PPN). IR (KBr, cm^{-1}) ν_{CO} = 1826 cm^{-1}. Analysis calc. (found) for [$C_{36}H_{30}NP_2$][$C_{40}H_{60}N_6P_3OGaCo$] • 0.5$C_4H_{10}O_2$: C 66.06 (65.92), H 6.75 (6.74), N 4.94 (5.00).

pK_a Measurements of LMCoH(H$_2$): Below is an example shown for pKa measurements of 2-H(H_2), analogous experiments were performed in an identical manner for M = Al . Under an atmosphere of argon, LGaCoH (9.6mg, 11.9 μmol) was dissolved in 1.5mL of THF-

d_8 and transferred to three J. Young NMR tubes. A separate stock solution was prepared by dissolving $^{tBu}N(^{IPr}NHC^{Me})$ (10.0 mg, 40.0 μmol, pK_a = 30.2 CH_3CN) in 250μL of THF-d_8 in a 1 mL vial. The desired quantity (35-45uL) of the base stock solution was added to each J. Young NMR tube, giving solution containing 1.2, 1.4, and 1.6 equivalents of base with respect to LGaCoH. The atmosphere of the NMR tube was replaced with H_2 via sequential freeze-pump-thaw and backfilling cycles. The atmosphere was ensured to be 1 atm by filling with 1 atm of H_2 (measured from digital gauge), briefly shaking, and then ensuring the total pressure was 1 atm (or 0-0.2 psig). In the case of M=Al, Vkd was utilized. Additionally, for M = Ga, the concentration of baseH^+ could not be directly measured by ^{1}H NMR due to fast exchange with the anionic dihydrogen complex, and the concentration of base was inferred from the formation of [^{t}BuN(^{iPr}NHC^{Me})H][LGaCo(H_2)] as indicated by the aromatic resonances of the ligand scaffold. In the case of M = Al, the concentration of protonated base (VkdH^+) was measured by both ^{1}H and ^{31}P NMR. The ^{1}H channel utilized the Vkd isopropyl resonance, or the VkdH^+ resonance. The ^{1}H and ^{31}P spectra agreed within 2-3%. The reaction was identified at equilibrium after the ratio of the products no longer changed and typically occurred after 6-9 days. For M = Al, an equilibrium constant K_{eq} = 0.25(1) was measured at 1 atm giving a pK_a of 34.2(1).

Table 3.3: Example of tabulated data used to calculate the pK_a and K_{eq} for base heterolysis mediated by **2-H(H_2)**

Trial	Conditions			Thermodynamic Results (pKa of LGaCoH(H_2)		
	p[H_2] atm	[Co]$_{tot}$ mM	[Base]$_{tot}$ mM	Measured K_{eq} (error)	Log(K_{eq})	pK_a LGaCoH(H_2)
A	1	7.50	9.01	0.0765	1.12	31.32
B	1	7.43	10.41	0.0735	1.13	31.33
C	1	7.36	13.26	0.0650	1.19	31.39

Average (St.Dev)	0.0717(6)	1.15(4)	31.3(1)

X-ray Crystallographic and Structure Refinement Details

Near black plates of **2-H** were placed onto the tip of MiTeGen Dual-Thickness MicroLoop™ and then mounted on a Bruker Photon II CPAD diffractometer for data collection at 100(2) K. The data collections were carried out using Mo Kα radiation (graphite monochromator). The data intensity was corrected for absorption and decay (SADABS).[78] Final cell constants were obtained from least-squares fits of all measured reflections. The structure was solved using SHELXT-16 and refined using SHELXL-16, which were executed from the SHELXLE graphical user interface.[79-80] A direct-methods solution was calculated which provided most non-hydrogen atoms from the E-map.[81] Full-matrix least-squares/difference Fourier cycles were performed to locate the remaining non-hydrogen atoms. All non-hydrogen atoms were refined with anisotropic displacement parameters. Hydrogen atoms were placed in ideal positions and refined as riding atoms with relative isotropic displacement parameters. Crystallographic data are summarized below.

Table 3.4: Crystallographic Data for **2-H**

Metric	Value
chemical formula	$C_{82}H_{131}Co_2Ga_2N_8OP_6$
Formula weight	1688.06
Crystal system	triclinic
space group	P-1
a(Å)	12.4071(13)
b(Å)	19.343(2)
c(Å)	19.588(2)
α (deg)	110.472(4)
β (deg)	97.544(4)
γ (deg)	101.928(3)
V (Å3)	4201.2(8)
Z	4
Z'	2
λ (Å), μ (mm^{-1})	0.71073, 1.185
T(K)	100(2)
θ	2.165 to 27.524
reflections collected	81337
unique reflections	19200
data/restraint/parameters	13773/0/915
R1, wR2 ($I > 2\sigma(I)$)	0.0788, 0.1657

Table 3.5: Compiled bond distance, angles, and averages for **2-H**.

Metric	1, Z'=2		Average (Å)
Co-Ga	2.4133(9)	2.3974(9)	2.405(1)
r	0.97	0.97	0.97
Co-P_1	2.1771(16)	2.1798(17)	2.178(2)
Co-P_2	2.2005(15)	2.2140(19)	2.214(1)
Co-P_3	2.2151(17)	2.2255(18)	
Ga-N_{apical}	2.283(4)	2.282(4)	2.283(4)
Ga-N_1	1.934(5)	1.933(5)	1.939(4)
Ga-N_2	1.938(5)	1.935(5)	
Ga-N_3	1.946(4)	1.947(4)	
Co-H	1.55(7)	Not placed	1.55(7)
Ga to N_3 plane	0.390	0.387	0.389
Co to P_3 plane	0.221	0.143	0.182
P_2-Co-P_3	141.38(7)	131.09(7)	
P_1-Co-P_3	107.71(6)	116.22(7)	
P_2-Co-P_1	107.59(6)	111.41(7)	
N_2-M-N_3	112.25(19)	115.19(19)	
N_1-M-N_3	115.41(19)	114.19(19)	
N_2-M-N_1	120.51(19)	118.95(19)	

Table 3.6: Comparative metrics listed for transition state, T.S. 2

Metric	Average (Å or deg)
Co-Ga	2.444
Co-P_1	2.187
Co-P_2	2.229
Co-P_3	2.269
Ga-N_{apical}	2.480
Ga-N_1	1.977
Ga-N_2	1.981
Ga-N_3	1.980
Co-H_{apical}	1.692
Co-H_{plane}	1.479
Ga to N_3 plane	0.578
Co to P_3 plane	0.342
P_2-Co-P_3	127.9˚
P_1-Co-P_3	112.5˚
P_2-Co-P_1	113.0˚
N_2-M-N_3	115.6˚
N_1-M-N_3	110.3˚
N_2-M-N_1	109.6˚

Catalysis Section:

High-Pressure Reactions in PEEK NMR Tubes: Carbon dioxide hydrogenation reactions at 34 atm. of ~1:1 H_2/CO_2 were performed in PEEK high pressure NMR spectroscopy tubes designed and built at Pacific Northwest National Laboratory, as reported previously.[53, 82] ***CAUTION: Operators of high-pressure equipment should take proper precautions to minimize the risk of personal injury***. In a typical catalytic experiment (0.25 mM [PPN][LGaCo(N_2)] catalyst, 800 mM Vkd base), a stock solution of [PPN][LGaCo(N_2)] (2.6 mg, 1.8 μmol) in 2 mL THF-d_8 (0.946mM) was prepared and then an appropriate aliquot (0.200mL) was added to a solution of Vkd in THF (ca. 180mg in 0.55mL) such that the total volume of the combined solutions was 0.750 mL. All manipulations were performed utilizing gas-tight micro syringes of appropriate volume. Note that preparations were adjusted accordingly to afford other concentrations of [PPN][LGaCo(N_2)] and/or other bases, including tBuTMG and DBU. Lastly, 350μL of the reaction solution was added to two different PEEK cells, which each contained a capillary of $CoCl_2$ in D_2O as an internal NMR reference. The PEEK cell was sealed and connected to a high-pressure line equipped with a vacuum pump and an ISCO syringe pump. The headspace was degassed by opening the PEEK cell to static vacuum (3 × 10 s). Gas was delivered to the cell from an ISCO syringe pump running constantly at desired pressure (typically 34 atm., continuous gas feed). The contents of the PEEK NMR spectroscopy cell were mixed using a vortex mixer for approximately 3 minutes until the pressure stabilized. After stabilization, the cell was inserted into the NMR spectrometer to acquire data for the first time point. The time for the catalysis experiments started upon initial exposure of the PEEK cell to the H_2/CO_2 gas mixture, and later time points corresponded to the start of

each NMR acquisition. ^{1}H NMR spectra were collected approximately every 3-5 minutes using the following parameters: 8 scans each, delay time of 1 s, acquisition time of 5 s, pulse width of 4 μs (20 degree pulse), and gain of 2 (total time of 48 s per spectrum). The concentration of the formate was determined by integration of the formate resonance relative to that of residual HDO (5.6 ppm) in the internal capillary standard of $CoCl_2$ in D_2O. ^{31}P spectra were acquired at the same time interval, with 4 scans per spectrum, a delay time of 5 s, and an acquisition time of 5 s (total time of 21 s per spectrum). The contents of the PEEK NMR spectroscopy cell were mixed using a vortex mixer when NMR spectra were not being collected to promote optimal dissolution of gas into the reaction solution throughout catalysis.

Note: For catalytic runs that utilized DBU, the kinetics traces of the reaction were found to only be reproducible in the absence of an internal capillary standard. This is likely attributed to the insolubility of the product [DBU][HCO_2] in THF at high concentrations (upwards of 500mM). Furthermore, the presence of the capillary potentially initiates the crystallization event, and thus was excluded in these experiments. However, as the catalysis was performed at high catalyst loadings (> 2mM), the PPN^+ residue was found to be a suitable replacement for reliable integration standard and gave reproducible results.

Computational Section:

Gaussian 09 calculations[83] were performed with the M06-L[84] density functional using a def2-SVP basis set for C and H atoms that remain invariant during the reaction, a def2-TZVP basis set for N and P, and a def2-TZVPP basis set for Co and Ga and the atoms involved in the reaction (C, O, H atoms in CO_2, CO, HCO_2^-, H^-, H_2O, H_2).[85-86] The structures of all species were optimized in the gas phase. Harmonic vibrational frequencies were computed to confirm the nature of all intermediates (no imaginary frequencies) and transition state structures (one imaginary frequency). The gas-phase Gibbs free energies, *G*, were calculated at T = 298.15 K and 1 atm pressure by using the harmonic approximation for the optimized structures. The solvation effect of tetrahydrofuran (THF) was included by performing single-point energy calculations at the gas-phase geometries using the SMD solvation model.[87] The relative solution-phase Gibbs free energies were calculated by adding solvation energies to the gas-phase relative Gibbs free energies. The Cartesian coordinates of all the structures and their associated electronic energies, enthalpies, and Gibbs free energies in both the gas phase and in solution are given in the Supporting Information. The energy values reported in the main text are Gibbs free energies (298.15 K, standard state of 1 atm for gases and 1 M for solutes) including the solvent effect of THF. TD-DFT calculations were performed in Gaussian 09 on the M06-L optimized structure with solvent considerations (SMD, Toluene[87]) to the calculated electronic transitions, which were fitted to the experimental spectra using the Orgin software package. The M06-D3[88] hybrid functional with D3 dispersion correction[89] with 6-311G(d,p) basis sets were used for all atoms.

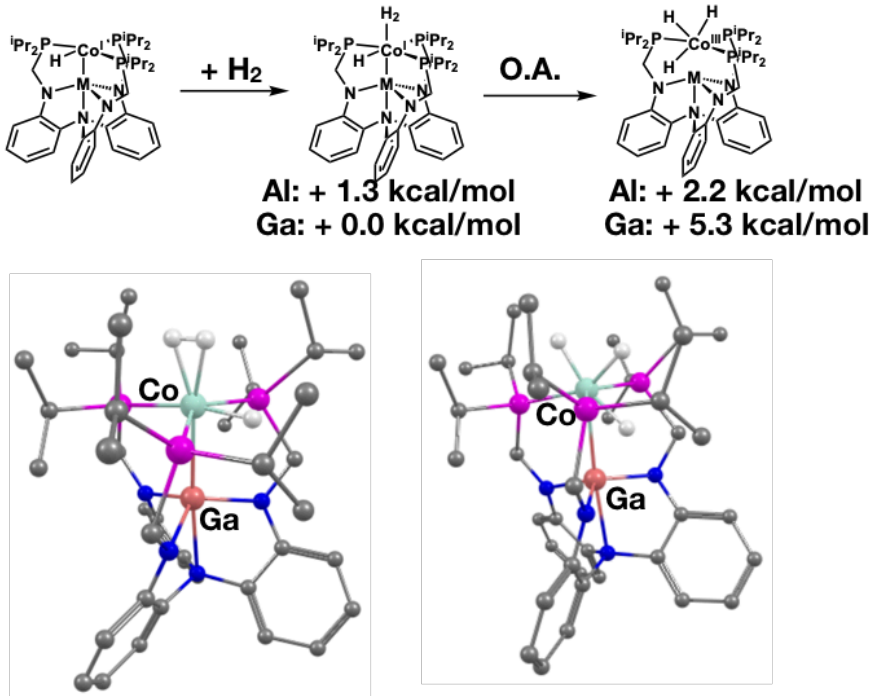

Figure 3.21: Free energy profile for H_2 binding and oxidative addition at HCoML. And examples of the corresponding structures of the (η^2-H_2)CoGaL and H_3CoGaL.

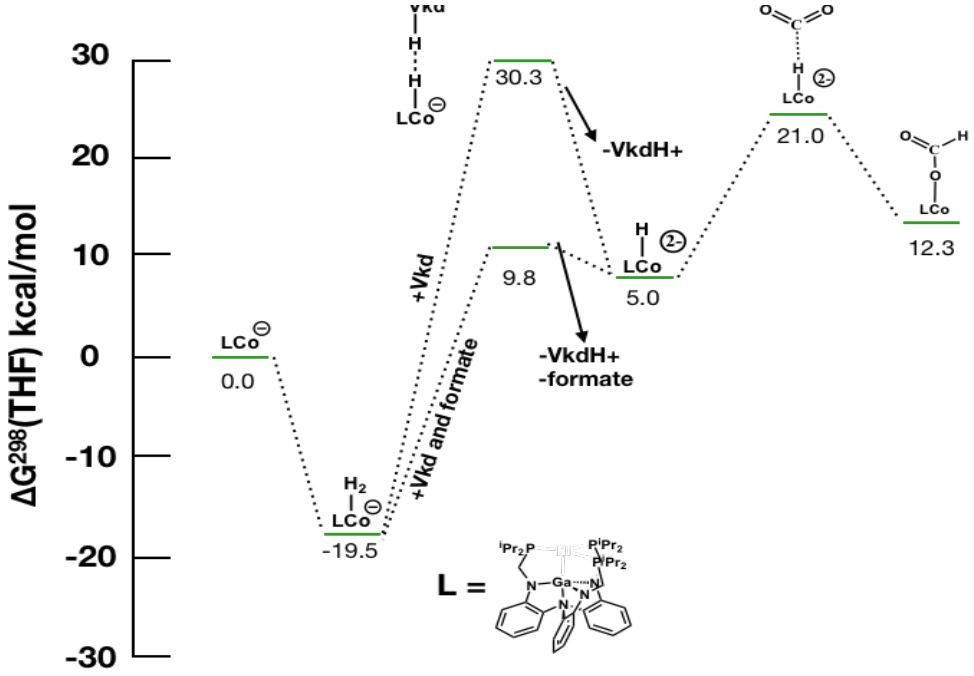

Figure 3.20: Gibbs free energy profile for CO_2 hydrogenation demonstrating challenge in deprotonation as the first step.

Chapter 4

Formal Ni^{-I} and Cu^{0} complexes supported by Lewis acids: synthesis, characterization, and reactivity

In part from:

Vollmer M. V.; Xie J., Cammarota R. C., Young Jr., V. G., Bill E., Gagliardi, L. Lu, C. C., Formal Nickelate(−I) Complexes Supported by Group 13 Ions. *Angew. Chem. Int. Ed.* **2018**, *57*, 7815-7819.

Vollmer, M. V.; Cammarota, R. C.; Lu, C. C. Reductive Disproportionation of CO_2 Mediated by Bimetallic Nickelate(−I)/Group 13 Complexes. *In press: Eur. J. Inorg. Chem.* ***2019****,* DOI: 10.1002/ejic.201801452.

4.1 Overview

Formal Ni^{-I} complexes have been isolated by employing group 13 metalloligands (M = Al and Ga). These $17e^-$ species were synthesized by one-electron reduction of the corresponding $Ni^0 \rightarrow M^{III}$ precursors, and were investigated by single-crystal X-ray diffraction, EPR spectroscopy, and quantum chemical calculations. Collectively, the experimental data support: (1) the strengthening of the Ni–M bond upon one-electron reduction and (2) the delocalization of the unpaired spin across the Ni and M atoms. Complementary quantum chemical studies are consistent with an electronic configuration featuring three σ-dative bonding electrons, $Ni(3d_z^2)^2 \rightarrow M(np_z)$ and $Ni(4p_z/4s)^1 \rightarrow M(np_z/s)$. The reactivity of these new bimetallic Ni^{-I}/group 13 complexes towards carbon dioxide is presented. The reaction of the anionic $[NiML]^-$ complexes with CO_2 (1 atm) results in reductive disproportionation of CO_2 to afford CO_3^{2-}, NiML, and the monocarbonyl adducts, (CO)NiML. The (CO)NiML complexes, where M is Al, Ga, or In, were independently synthesized and characterized. The extent of CO activation varies slightly across the different group 13 ions, where the CO stretching frequency increases for M = Al < Ga < In.

Preliminary results concerning the isolation and characterization of isoelectronic formally zero-valent copper species are also presented. The cationic copper species, $[CuML]BArF_{24}$ (Ar = 3,5–bis(trifluoromethyl)phenyl) were synthesized from the useful "naked copper," reagent $[Cu(1,5\text{-}COD)_2]BArF_{24}$ for which a scalable synthesis is presented. Lastly, preliminary studies concerning the oxidation of the NiML complexes shed light on the electronic structure of the $15e^-$ fragment, and complete the trio of aluminum supported nickel complexes, $[NiAlL]^{+/0/-}$.

4.2 Introduction

Metal complexes which exhibit negative oxidation states have fascinated inorganic chemists for a long time and have sparked interest beyond their unique electronic structures and reactivity.[1-4] While sub-valent oxidation states of are pervasive in the coordination chemistry of late transition metals (e.g. Co^{-I}, Fe^{-II})[5-10], very little is known about analogous oxidation states of nickel complexes. The Ni^{-I} atomic ion was first tentatively assigned as a minor byproduct of positive-ion bombardment in an apparatus using NiCr supports.[11] A rare example of a formal Ni^{-I} coordination complex is the 17-electron tricarbonyl anion, $[Ni(CO)_3]^-$, which is generated in an inert gas matrix below 10K.[12-13] The reduced analog to the nickel carbonyl anion, $[Ni(CO)_3]^{2-}$, has recently been structurally identified, but lacked complementary spectroscopic characterization and combustion analysis.[14] Several Li_2Ni olefin complexes, which are formally Ni^{-II}, have been isolated including $[Li(THF)]_2[(Ni(1,5\text{-cyclooctadiene})]$.[15-16] The stability of these molecules was attributed to their 18-electron noble-gas configuration and strongly polarized Ni-Li covalent bonds.

Of relevance, formal Cu^0 complexes, (TPB)Cu and $(Me_2\text{-cAAC})_2Cu$, have also been isolated (TPB = trisphosphinoborane and cAAC= cyclic alkyl amino carbene).[17-18] The unpaired spin in these molecules is delocalized across the Cu-B and C-Cu-C bond, with dominant radical character at the B and C atoms, respectively. We sought to target isoelectronic nickelate complexes using our previously reported NiML precursors (L = $[N(o\text{-}NCH_2P^iPr_2)C_6H_4]^{3-}$ M = Al, Ga, In) in which the Ni center is zero-valent with a d^{10} electron count.[19-21] We hypothesized that reduction of the NiML compounds may give rise to unique bonding and electronic structures because of (1) a pre-existing Ni→M bonding interaction, and (2) the better spatial overlap between the frontier orbitals of nickel and the

heavier group 13 elements. In this work, we report the anionic $[NiML]^-$ complexes for M = Al and Ga which feature a $\{NiM\}^{11}$ configuration. The combined experimental and theoretical work support the formulation of these complexes as formally Ni^{-1} in character and reveal an unexpected stabilization arising from a three-electron occupation of two distinct σ-type bonding interactions between Ni^{-I} and M^{III}.

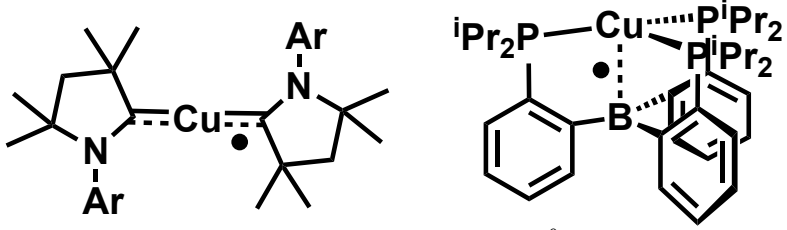

Figure 4.1: Recently synthesized species with formally Cu^0 centers.

4.3 Results & Discussion

4.3.1 Electrochemical characterization of the $\{NiM\}^{9\text{-}11}$ series

To examine the exciting postulate that formally Ni^{-I} complexes may be isolable, we first examined the previously reported series of bimetallic nickel complexes, NiML (**1** = Al, **2** = Ga, **3** = In**)** by cyclic voltammetry to see if a $\{NiM\}^{11}$ state was accessible. Gratifyingly, the electrochemical profile of the NiML members for each shows a reversible one-electron reduction process at −2.82, −2.48, and −2.34 V vs $Fc^{0/+}$, respectively (0.4 M TBA[PF_6] in THF, Fig 4.2 TBA = tetra(n-butyl)ammonium).[20] Neither the monometallic precursors, nor the mono-nickel control exhibit such as redox event suggesting this redox process intimately tied to the presence of the M–Ni interaction. Furthermore, the presence of a mono-valent $\{NiM\}^9$ state was also evidenced by cyclic voltammetry, with much milder oxidative events occurring at -0.74, -0.57, and -0.46 V vs $Fc^{0/+}$, respectively.[20] Thus, to compare and contrast the effect of the supporting metal atom on the electronic structure

of the oxidized and reduced counterparts we sought to chemically isolate and study these species by conventional solution state methods and computational methods.

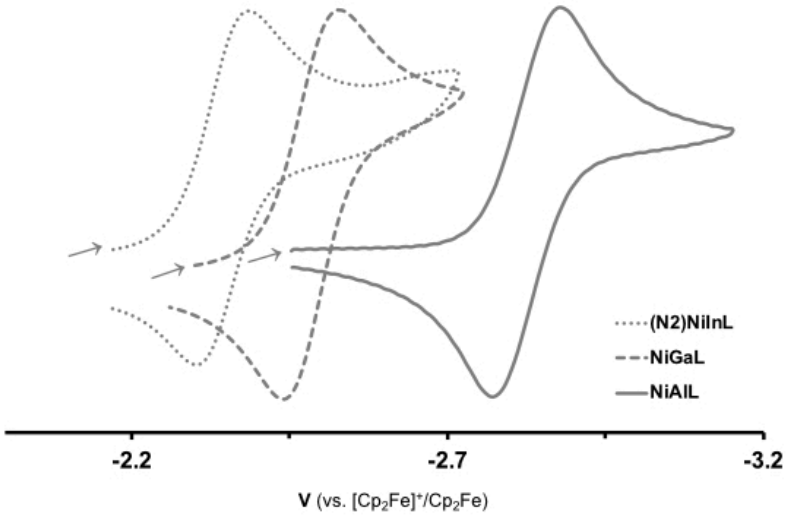

Figure 4.2: Cyclic voltammogram of **1-Ni**, **2-Ni,** and **3-Ni(N_2)**.

4.3.2 Synthesis and X-ray Crystallographic Studies {NiM}$^{10/11}$ complexes

In accordance with the harsh reducing potentials, the addition of strong reducing agents such as KC_8 or Li^0 to solutions of **1-Ni** and **2-Ni** in THF generates deep dark-red solutions of anions **1-Ni^{red}** and **2-Ni^{red}**. In the case of KC_8, the K^+ salt that is generated can be easily encapsulated with 222-crypt giving rise to [K(222-crypt)][**1/2-Ni^{red}**]. For crystallographic characterization of **2-Ni^{red}**, the Li(κ^4–12-crown-4)(κ^2–DME) salt was found to form when recrystallized from DME containing excess 12-crown-4.

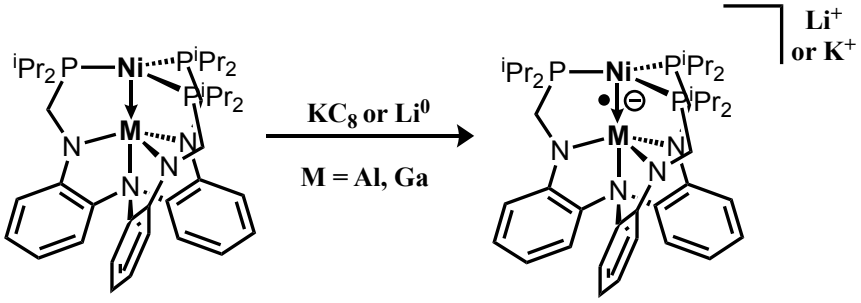

Figure 4.3: Synthesis of formally Ni^{I} complexes **1-Ni^{red}** and **2-Ni^{red}**.

Samples of **1-Ni^{red}** and **2-Ni^{red}** as either their Li^+ or K^+ salts are exceedingly oxygen and moisture sensitive and are best stored as solids at −30 °C under argon. To date, our attempts to isolate the analogous $[NiInL]^-$ complex have been unfruitful. Crystalline specimens of [K(222-crypt)]**[1-Ni^{red}]** suitable for crystallography studies can be grown from concentrated DME/Et_2O solutions layered with n-hexane. Alternatively, non-single crystals can be grown from layering a 1:1 mesitylene:THF mixture with n-hexane and permits a higher overall yield of polycrystalline material. Worth mentioning is that crystals of [K(222-crypt)]**[1-Ni^{red}]** were frequently twinned. However, the twinning present was caused purely through an inversion twin and the final refinement cycles could thus converge. Indeed, the final solution (see Fig. 4.4) gives satisfactory refinement statistics (R_1 = 0.0396, wR_2 = 0.1034) after removal of a badly disordered 1,2-dimethoxyethane solvent molecule. The final solution of [K(222-crypt)]**[1-Ni^{red}]** is obtained in the orthorhombic space group $Pna2_1$ and the image of the crystal structure is shown in Figure 4.4. The pertinent structure metrics are shown in Table 4.1.

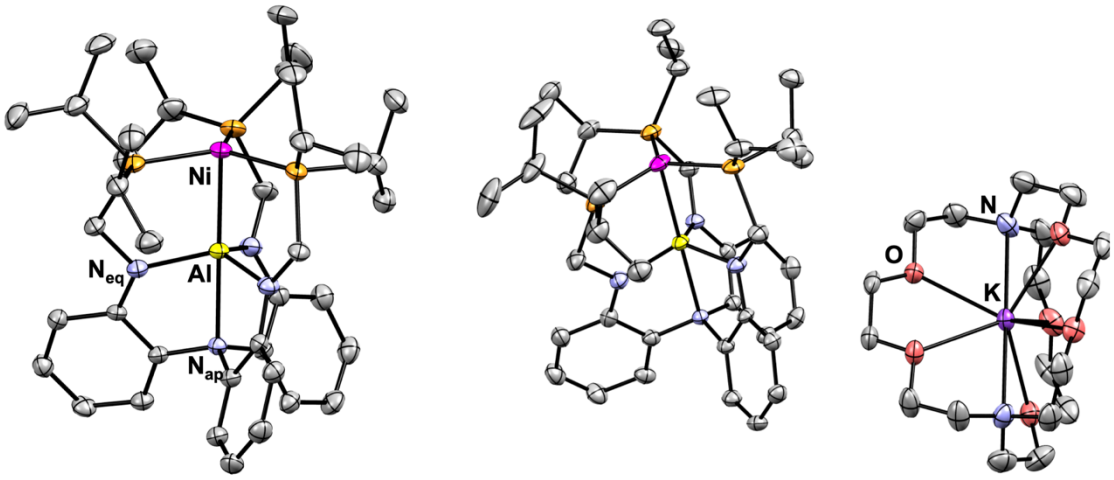

Figure 4.4: Molecular structure of [K(222-crypt)][**1-Ni^{red}**] rendered at 50% thermal ellipsoid probability. Right, cation anion pair; left, an expanded image of the anion

Crystals of [K(222-crypt)]**[2-Ni^{red}]** grown similarly to [K(222-crypt)]**[1-Ni^{red}]** exhibit crystalline properties, but they were found to possess a rhombohedral unit cell solution with unrealistic unit cell dimensions (*c* upwards of 110 Å, typically 10-20Å), and the final solution had inconsistent site occupancy factors for the proposed K^+ and **2^{red}** content. A reasonable hypothesis is that **2-Ni^{red}** and **2-Ni** co-crystallized to generate the erroneous chemical formula. Inspired by a recent report that used lithium to prepare highly-reduced Ln^{II} complexes, an ethereal solution **2-Ni** and Li^0 smear reacted quickly at room temperature to generate the deep purple-red color that is indicative of **2-Ni^{red}**. [21] Single-crystal red prisms were grown from vapor diffusion of Et_2O into a DME solution of **2-Ni^{red}** containing excess 12-crown-4, and were then investigated by X-ray diffraction. The resulting molecular structure of [Li(κ^4–12-crown-4)(κ^2–DME)]**[2-Ni^{red}]** is shown in Figure 4.5, with accompanying metrics are listed in Table 4.1. The final solution to [Li(κ^4–12-crown-4)(κ^2–DME)]**[2-Ni^{red}]** is in monoclinic space ground $P2_1/c$ and has two independent molecular pairs in the asymmetric unit (Z'=2).

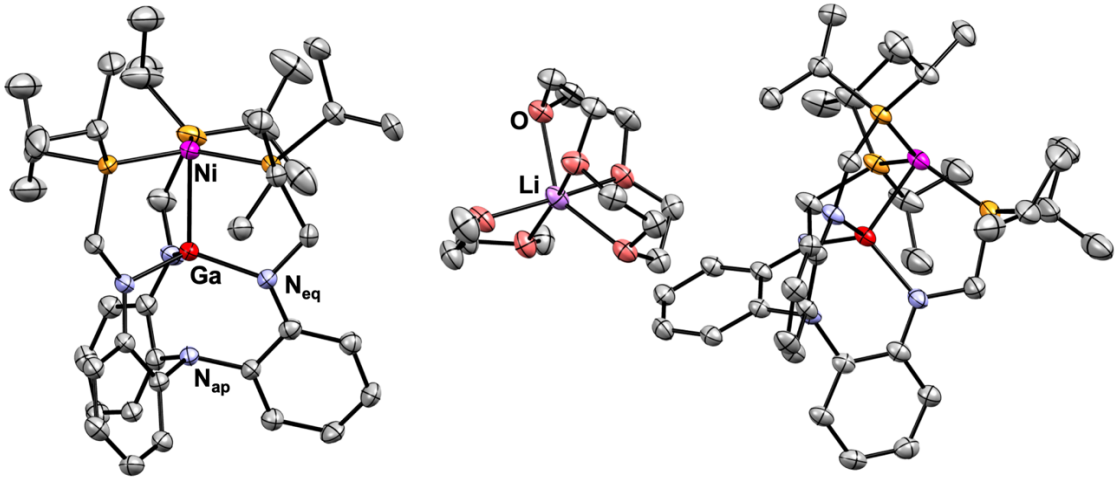

Figure 4.5: Molecular structure of **2-Ni^{red}** isolated as a Li(κ^4–12-crown-4)(κ^2–DME) complex rendered at 50% thermal ellipsoid probability. The right image highlights the cation. Hydrogen atoms and solvent molecules excluded for clarity.

Upon reduction, the Ni−M bond contracts by 0.06 Å and 0.04 Å respectively for **1-Ni^{red}** and **2-Ni^{red}**, resulting in a decrease in the formal shortness ratio (*r*) of the Ni−M bond length relative to the sum of their covalent radii.[22-23] Correspondingly, the M−N_{ap} distance drastically elongates by 0.16 Å and 0.21 Å Al and Ga, respectively, as the M^{III} ion moves further above the N_3–plane and closer to Ni (0.13 Å for Al, 0.12 Å for Ga). Reduction to the $\{NiM\}^{11}$ state also perturbs the metal-ligand bonds perpendicular to the Ni−M axis. The average Ni−P bond lengths decrease by 0.07 Å for **1-Ni^{red}** and 0.06 Å for **2-Ni^{red}** which is attributed to better π-backbonding from the more electron-rich Ni center in the $\{NiM\}^{11}$ state. In addition, the average M−N_{eq} bonds elongate upon reduction by a modest 0.03 Å and 0.02 Å for in **1-Ni^{red}** and **2-Ni^{red}**. This effect is likely tied to the increasing pyramidalization of the group 13 ion, as reflected by a decrease in the sum of the N_{eq}−M−N_{eq} angles (6.8˚ Al, 7.6˚ Ga). Interestingly, a subtle reorganization of the ligand framework also occurs upon reduction. The flexible PCH_2N-ligand arms can twist, as reflected by the P−Ni−M−N_{eq} dihedral angles. The average P−Ni−M−N_{eq} dihedral angle increases by 4.0˚ in **1-Ni^{red}** and 5.4˚ in **2-Ni^{red}**. Such twisting can accommodate a shorter Ni−M interaction and/or increasing pyramidalization of the group 13 center.

One counterargument is that the bridging amino-phosphine framework forces an interaction between the two metal centers. We would argue that this is not the case, as the ligand framework has been shown to be highly flexible, supporting bonds over a range of 0.7 Å (from 1.74 to 2.41 Å).[24] Furthermore, the elongation of the M–N_{apical} bond is often associated with the shortening of the M-M bond, as may be expected from a weak tris(arylamine) donor. The overall geometrical changes in both **1-Ni^{red}** and **2-Ni^{red}** support the notion that there is significant reduction at both the Ni (contraction of the Ni−P bonds)

and the Al center (increased pyramidalization) sites. Of interest, it appears that the Ni−M interaction strengthens in **1/2-Ni^{red}** upon reduction, which suggests that the additional electron populates a Ni−M bonding orbital. This observation is contrary to classical two-center three-electron bonds, where the bond weakens substantially upon reduction, due to population of an antibonding singly occupied molecular orbital (SOMO). A classic example of this motif is showcased by the He_2^+ with a formal bond order of 0.5.[25]

Table 4.1: Selected metrics for the series of **{NiM}$^{10/11}$** complexes

	1-Ni^{red}	**1-Ni**	**2-Ni^{red}**	**2-Ni**
Ni–M (Å)	2.389(1)	2.450(1)	2.340(6)	2.379(1)
r[a]	0.97	1.00	0.95	0.97
Ni−P[b] (Å)	2.136(1)	2.204(1)	2.155(1)	2.210(1)
M−N_{eq}[b] (Å)	1.904(3)	1.876(2)	1.969(1)	1.954(2)
M−N_{apical} (Å)	2.257(3)	2.099(2)	2.423(1)	2.216(3)
Ni to P_3-plane (Å)	0.11	0.13	0.12	0.13
M to N_3-plane (Å)	0.39	0.26	0.49	0.37
∑(∠P−Ni−P) deg	359.3(7)	359.0(1)	359.1(4)	359.01(9)
∑(∠N_{eq}−M−N_{eq}) deg	347.7(2)	354.5(2)	341.9(5)	349.5(3)
∠P−Ni−M−N_{eq}[b,c] deg	15.9	19.9	11.8	17.2

a) Ratio of Ni−M bond length to the sum of the Ni and M covalent radii.[22-23] b) Average value. c) Dihedral angles are reported as absolute values d) Z'=2, values listed are averaged

4.3.3 EPR spectroscopy of {NiM}$^{10/11}$ species

Solutions of **1-Ni^{red}** and **2-Ni^{red}** give rise to informative EPR signatures at room temperature as a result of their S = ½ nature (THF, 1mM, Fig. 4.6). For **1-Ni^{red}**, an isotropic signal at g = 2.067 comprised a 1:1:1:1:1:1 sextet of 1:3:3:1 quartets, results from coupling to an ^{27}Al nucleus (I = 5/2, A = 7.6 mT) and three equivalent ^{31}P nuclei (I = ½, A = 1.30 mT). The signal associated with **1-Ni^{red}** and the associated splitting diagram are shown in Fig. 4.6.

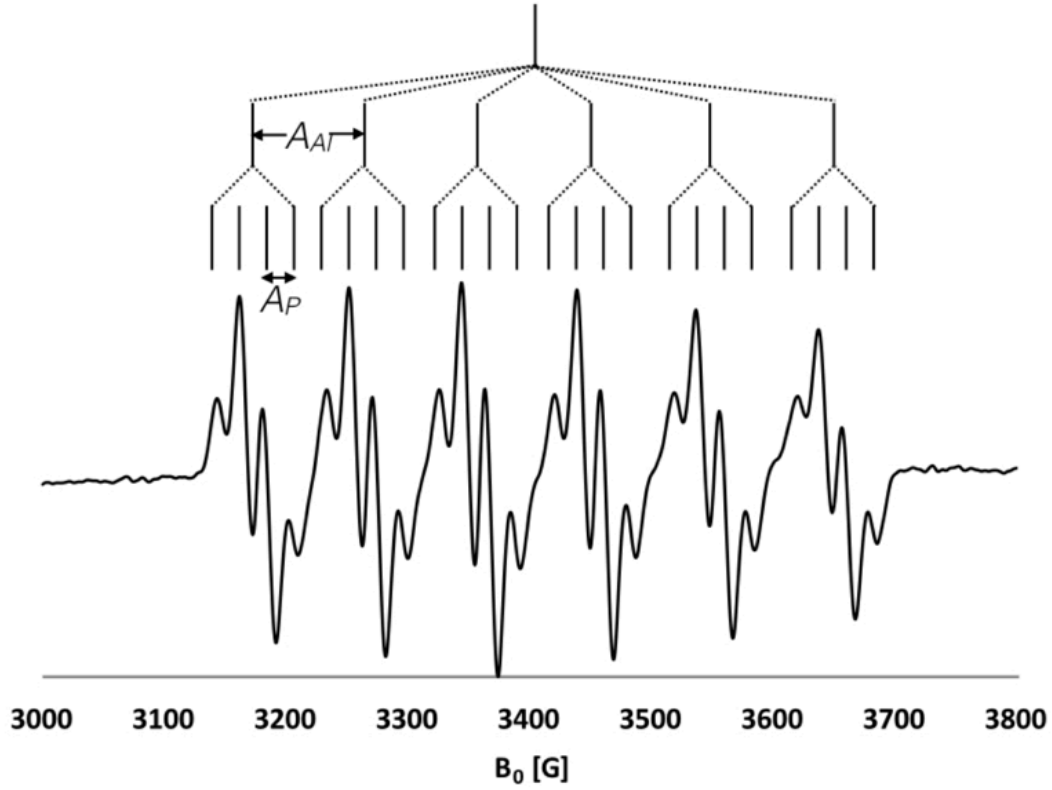

Figure 4.6: X-band EPR spectra of **1-Ni^{red}** (1mM, THF, 298K)

The EPR signal for **2-Ni^{red}** at g = 2.023 features two overlapping 1:1:1:1 quartets, which arise from coupling to two naturally occurring Ga isotopes: ^{69}Ga (60.4%, I = 3/2, 60.4%, A = 37.0 mT) and ^{71}Ga (39.6%, I = 3/2, A = 47.1 mT). The signal associated with **2-Ni^{red}** and the associated splitting diagram are shown in Figure 4.7. Additional super-hyperfine interactions can be resolved for the transition associated with the spin quantum number, $m_I = -½$ (Fig. 4.8). This transition has ~18 lines, which is more than the 8 lines expected for two overlapping ^{31}P-based quartets. Hence, we propose additional hyperfine interactions to the ^{14}N nuclei in **2-Ni^{red}**, which could be accurately modeled with four additional ^{14}N nuclei, three of which are equivalent, in accordance with the differing nitrogen sites in the ligand framework.

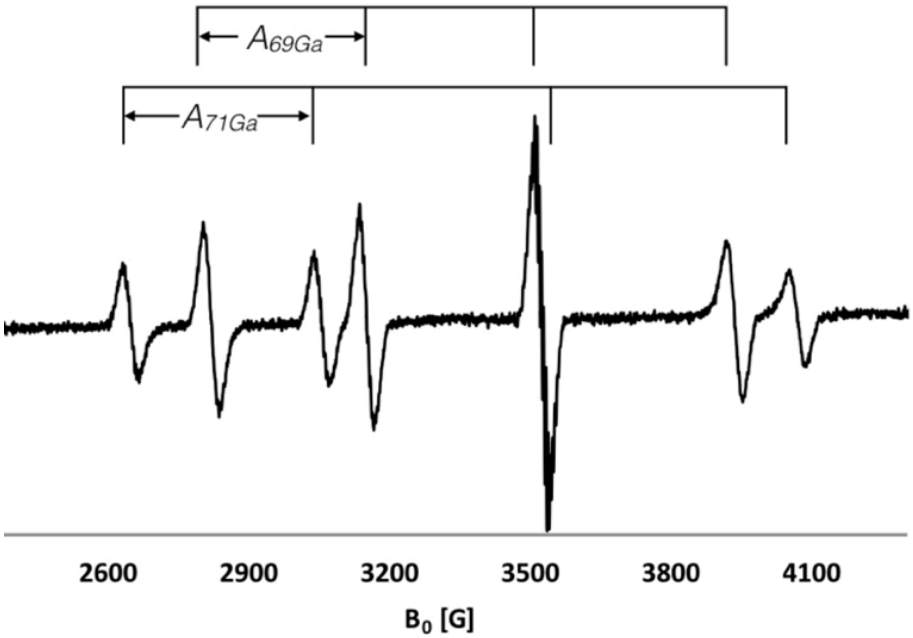

Figure 4.7: X-band EPR spectra of **2-Ni^{red}** (1mM, THF, 298K)

A simulation of the EPR signal for **2-Ni^{red}** with three equivalent ^{31}P couplings allowed us to estimate an A(^{31}P) value of ~1.2 mT, comparable to that of **1-Ni^{red}**. Low-temperature EPR spectra of **1-Ni^{red}** and **2-Ni^{red}** were also obtained, but no additional

parameters could be extracted. Lastly, the low natural abundance of ^{61}Ni (I = 3/2, 1.19%) precluded the detection of any Ni hyperfine interactions. Generally, there was excellent agreement between the experimental and fit spectra, as shown in Figure 4.8.

Mononuclear group 13 radical anions are unusual. The unstable species, $[AlH_3]^{\bullet-}$ and $[GaH_3]^{\bullet-}$, exhibit larger hyperfine couplings of 15.4 and 42 mT to the ^{27}Al and ^{69}Ga nuclei, respectively.[26-27] On the other hand, the corresponding hyperfine interactions in $[Al(SiMetBu_2)_3]^{\bullet-}$ and $[Ga(SiMetBu_2)_3]^{\bullet-}$ are diminished at 6.2 and 12.3 mT, respectively.[28] A two-coordinate Ga^{II} diboryl complex has an A_{iso}(^{69}Ga) of 24.4 mT.[29] Considering the large variation in hyperfine values for bona fide Al^{II} and Ga^{II} complexes, it is difficult to ascertain the electronic structures of **1-Ni^{red}** and **1-Ni^{red}** based solely on their respective A(^{27}Al) or A(^{69}Ga/^{71}Ga) values. However, the EPR parameters for **1-Ni^{red}** and **2-Ni^{red}** do suggest substantial spin character at both the group 13 and the Ni elements, for which the latter is inferred from the ^{31}P coupling.

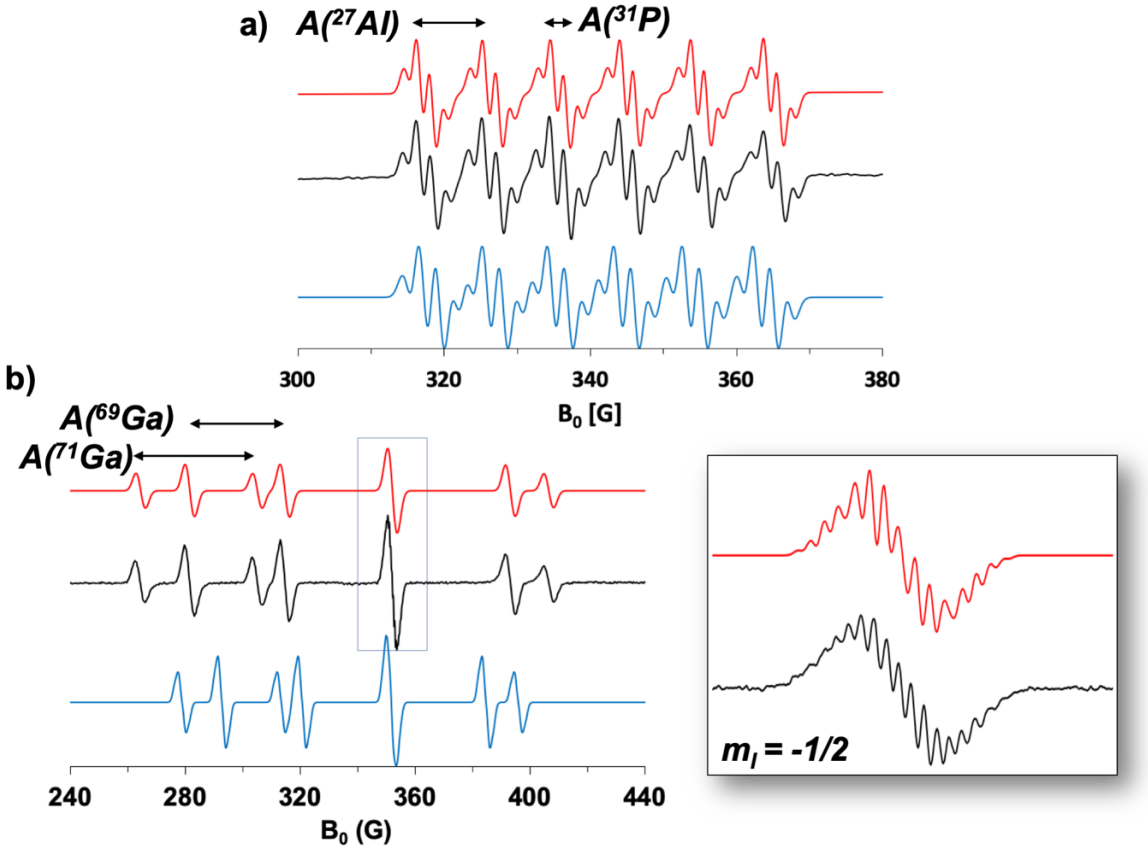

Figure 4.8: Overlaid EPR spectra for **1-Ni^{red}** (a) and **2-Ni^{red}** (b). Experimental (black, middle), fit (red, top), and calculated (bottom, blue) EPR parameters.

4.3.4 Computational Studies

To further elucidate the electronic structures of **1-Ni^{red}** and **2-Ni^{red}**, we utilized quantum chemical calculations, including density functional theory (DFT) and complete active space self-consistent field calculations (CASSCF).[30] Geometry optimizations of **1-Ni^{red}** and **2-Ni^{red}** were performed on the full structures (M06-L/DEF2, see experimental for full details), and the final geometries show good agreement with the X-ray structures (experimental Section Table 4.9 and 4.10).[31] To corroborate the theoretical findings, we calculated the EPR parameters for **1-Ni^{red}** and **2-Ni^{red}** as a means to validate the theory employed. The DFT-calculated parameters reproduce the experimental EPR signatures well, as shown in Figure 4.8, with the major discrepancies being the magnitude of $A(^{69/71}\text{Ga})$ in **2-Ni^{red}** (**$A(^{69}\text{Ga}_{\text{Exp}})$** = 1050 MHz; $A(^{69}\text{Ga}_{\text{Calc}})$= 866 MHz).[32-33] In the Mulliken spin-density plot of **2-Ni^{red}** (Fig. 4.9), the unpaired spin can be observed to reside at Ni, Al, and the three P atoms. Specifically, the spin is distributed across the Ni:Al:3P atoms in a ratio of 1.8:1.0:1.4. As further support, the SOMO of **1-Ni^{red}** shows significant Ni (35%), Al (13%), and P (30% total) character (Fig. 4.9). As in **1-Ni^{red}**, the spin density in **2-Ni^{red}** is similarly distributed with a Ni:Ga:3P ratio of 2.1:1.0:1.2. Likewise, the SOMO (nearly identical to that shown in Fig. 4.9) for **2-Ni^{red}** is comprised of Ni (38%), Ga (14%), and P (22% total) based orbitals. Notably, the SOMOs of **1-Ni^{red}** and **2-Ni^{red}** represent σ-bonding interactions between Ni (mainly $4p_z$) and the group 13 (ns and np) atoms, though the Ni−M bond is strongly polarized towards Ni in both cases. This observation reinforces the notion that chemical reduction reinforces the strength of the Ni-M bond.

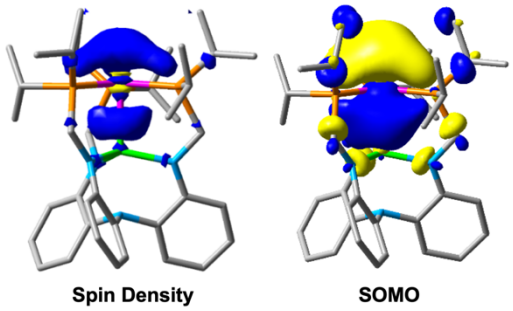

Figure 4.10: Contour plots for the Mulliken spin density and SOMO of **1-Ni^{red}**

Lastly, CASSCF calculations (performed on the DFT-optimized geometries of **1-Ni^{red}** and **2-Ni^{red}**) using an active space of 11 electrons in 12 orbitals were used to obtain a detailed composition of the SOMOs of **1-Ni^{red}** and **2-Ni^{red}**. In the set of natural orbitals, all five Ni 3d orbitals are doubly occupied, as one might infer from the nature of the d^{10} Ni^0 center in either **1/2-Ni**. The singly occupied natural orbital for both **1-Ni^{red}** and **2-Ni^{red}** qualitatively resembles the corresponding DFT-calculated SOMO in that they depict a σ-(Ni−M) bonding interaction. A notable difference, however, is that the natural orbital is more heavily Ni-based (~70%), with remaining contributions from Al (14%) or Ga (21%)

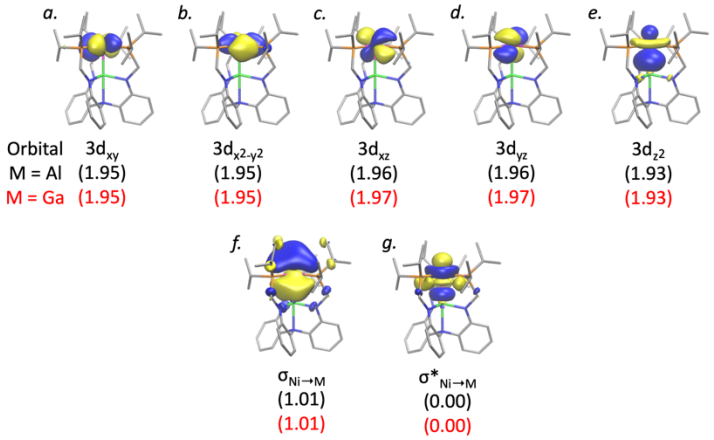

Figure 4.9: Natural orbitals obtained from a CASSCF(11e,12o) calculation of **1-Ni^{red}** . Occupation numbers (parentheses) indicate orbital occupancy. Black text for **1-Ni^{red}** and red for **2-Ni^{red}**.

and P-based orbitals (10 to 15%). An example of the orbitals obtained from CASSCF are shown in the figure below for **1-Ni^{red}**, which are nearly identical to those of **2-Ni^{red}**.

4.3.5 Reactivity of {NiM}^{11} towards CO_2

As discussed, **1-Ni^{red}** and **2-Ni^{red}** exhibited a reversible {NiM}$^{10/11}$ redox couple at −2.82 V (vs. Fc^+/Fc) and −2.48 V, respectively. These negative potentials should be suitable for reduction of CO_2 ($E°' = -1.90$ V vs. NHE for $CO_2 + e^- \rightarrow CO_2^{\bullet -}$).[34] Exposure of the K(crypt-222) salts of **1-Ni^{red}** and **2-Ni^{red}** to 1 atm CO_2 resulted in a color change from an intense dark-red to light brown within minutes (in THF-d_8). As shown in Figure 4.11, the products were determined to be K_2CO_3 and a 1:1 mixture of NiML (**1/2-Ni**) and (CO)NiML (**1/2-Ni(CO)**) based on the following data. The formation of K_2CO_3 is consistent with the observation of a precipitate during the reaction; and, repeating the reaction with labeled $^{13}CO_2$, the ^{13}C NMR spectra of the reaction mixture showed a ^{13}C resonance at 167.9 ppm. The ^{31}P and ^1H NMR spectra of the reaction mixtures showed the production of two ligand-containing products in ~1:1 ratio. In the case of **1-Ni^{red}**, two ^{31}P singlets were observed at 30.7 and 43.8 ppm, which are consistent with **1-Ni** and its carbonyl adduct, **1-Ni(CO)** (*vide infra*), respectively. Moreover, the crude IR spectrum from the reaction with **1-Ni^{red}** showed an intense band at 1953 cm^{-1}, which is diagnostic of a terminal end-on CO stretch. For the reaction with **1-Ni^{red}**, two ^{31}P singlets were observed at 37.6 and 55.5 ppm, which are consistent with **1-Ni** and its carbonyl adduct, **1-Ni(CO)** (*vide infra*), respectively; and, the latter is identified from a strong IR stretch at 1962 cm^{-1}. In labeled experiments with $^{13}CO_2$, the ^{13}C NMR analysis of the reaction solutions lend further support for the formation of the end-on CO adducts, **1-Ni(^{13}CO)** and **2-Ni(^{13}CO)**, both of which give rise to quartet signals at 209.9 and 211.9 ppm, respectively

($^2J_{CP}$ = 8 and 9 Hz). Correspondingly, their ^{31}P peaks also split into doublets. Collectivity, these observations support the reaction stoichiometry shown in Figure 4.11, where two

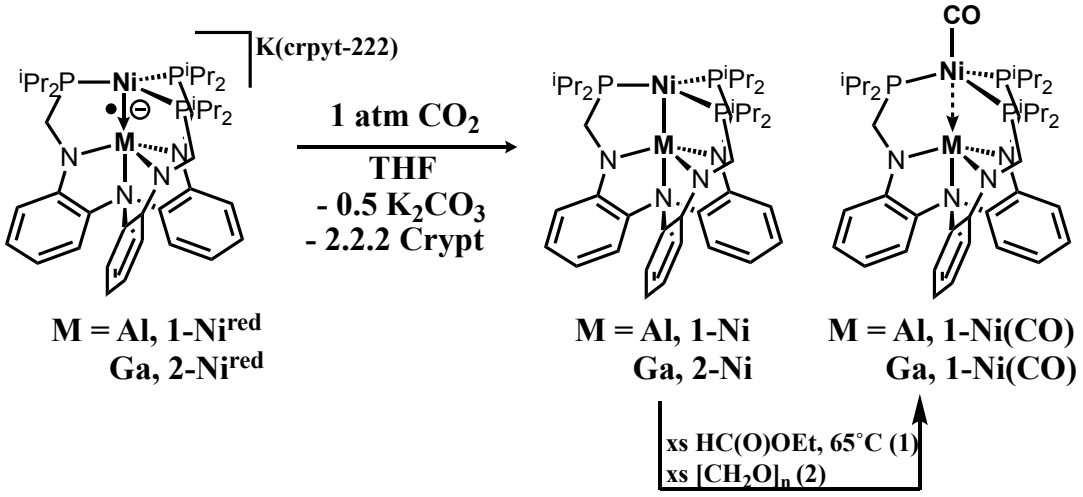

Figure 4.11: Reactivity of **1-Ni^{red}** and **1-Ni^{red}** towards CO_2

equivalents of CO_2 are reduced by two electrons (from two equivalents of $[NiML]^-$) to generate CO_3^{2-} and CO, in which the latter is trapped by **1/2-Ni** as the metal carbonyl.

To unambiguously assign the CO adducts **1-Ni(CO)** and **2-Ni(CO)** each were independently synthesized and structurally characterized. Addition of $CO_{(g)}$ (1 atm) to **1/2-Ni** gave intractable mixtures; and hence, alternative syntheses were sought. Heating excess ethyl formate and **1-Ni** at 65˚C for several days yielded **1-Ni(CO)** cleanly, while **2-Ni(CO)** was obtained in high yield by reaction of **1-Ni** and excess paraformaldehyde. The IR spectra and NMR data of the pure isolated complexes **1/2-Ni(CO)** are identical to the carbonyl products from the reactions of CO_2 and **1/2-Ni^{red}**. While our efforts to isolate the $\{Ni-In\}^{11}$ counterpart to **1-Ni^{red}** and **2-Ni^{red}** have been unsuccessful, the Ni−In carbonyl adduct, **3-Ni(CO)**, was isolated from a reaction of **3-Ni** with either ethyl formate (HC(O)OEt) or paraformaldehyde. The molecular structures of the (CO)NiML triad, are shown in Figure 4.12, and selected geometrical parameters, including bond lengths and

angles, are shown in Table 4.2 Compounds **1-Ni(CO)** and **2-Ni(CO)** both crystallize in the space group $P2_1/c$ with one hydrocarbon solvent molecule (pentane for **1-Ni(CO)**, hexane for **2-Ni(CO)**) in the unit cell. Species **3-Ni(CO)** crystallizes in space group $P2_1$.

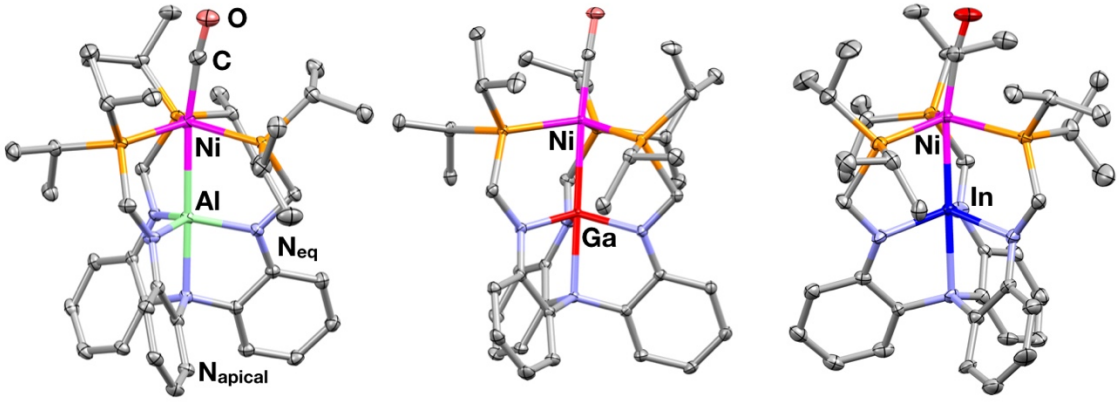

Figure 4.12: Molecular structures of the CO adducts (CO)NiML rendered at 50% thermal ellipsoid probability. Hydrogen atoms and solvent molecules omitted for clarity.

For both **1-Ni(CO)** and **2-Ni(CO)**, the Ni−M distances of 2.626(1) and 2.529(1) Å, respectively, are longer than the sums of the covalent radii of Ni and Al/Ga.[23] While the Ni−In distance of 2.523(1) Å in **3-Ni(CO)** remains shorter than the sum of the two metals' covalent radii, the Ni−M interaction in all of the CO adducts are attenuated compared to their unligated counterparts. Moreover, the Ni center adopts a more pyramidal geometry (toward CO) in **1-Ni(CO)** to **3-Ni(CO)** with Ni to P_3-plane distances of ~0.40 Å. Complexes **1-Ni(CO)** to **3-Ni(CO)** also have longer Ni−P bond lengths on average than the NiML compounds, by 0.03, 0.04 and 0.05 Å, respectively. The C−O bond lengths in **1-Ni(CO)** to **3-Ni(CO)** are similar at 1.15 Å (compared to 1.128 Å in free CO), which is consistent with the modest activation of the CO ligand as observed by IR spectroscopy (1953 to 1968 cm^{-1}, KBr pellet).

Table 4.2: Selected metrics for the series of carbonyl complexes **1** to **3-Ni(CO)**

Metric	**1-Ni(CO)**	**2-Ni(CO)**	**3-Ni(CO)**
Ni−M (Å)	2.626(1)	2.529(1)	2.523(1)
r [a]	1.07	1.03	0.95
Ni−C (Å)	1.805(2)	1.775(2)	1.755(6)
C−O (Å)	1.149(3)	1.148(2)	1.151(7)
Ni−P[b] (Å)	2.235(1)	2.249(5)	2.303(3)
M−N_{apical} (Å)	2.150(2)	2.292(2)	2.372(4)
M−N_{eq} [b] (Å)	1.881(2)	1.938(2)	2.113(6)
Ni to P_3-plane (Å)	0.36	0.36	0.42
M to N_3-plane (Å)	0.27	0.40	0.51
M−Ni−C deg.	170.8(1)	170.8(1)	169.3(1)
ν_{CO} (KBr, cm^{-1})	1953	1962	1968

a) Ratio of Ni−M bond length to the sum of the Ni and M covalent radii.[22-23] b) Average value

Nickel-mediated reductive disproportionation of CO_2 to CO and CO_3^{2-} is precedented, but examples remain limited. Of note is the rich CO_2 activation chemistry of low-valent Ni centers, which frequently produce CO/H_2O (electrocatalytically) or HCO_2^-.[35-49] Particularly relevant is the Ni^I *ß*-diketiminate complex, $K_2[L^{tBu}Ni(N_2^{2-})NiL^{tBu}]$, where $L^{tBu} = [HC(C(t\text{Bu})NC_6H_3(i\text{Pr})_2)_2]^-$, which has been shown to react rapidly with CO_2 to generate the hexanuclear carbonate cluster $K_6\{L^{tBu}NiCO_3\}_6$ and the monocarbonyl complex, $L^{tBu}NiCO$.[37] Expulsion of carbonate from $K_6\{L^{tBu}NiCO_3\}_6$ was accomplished using KC_8, providing a route back to the N_2-precursor, $K_2[L^{tBu}Ni(N_2)NiL^{tBu}]$.[47] Furthermore, the reductive CO_2 disproportionation of **1-Ni^{red}** and **2-Ni^{red}** parallel the reactivity of reduced transition carbonyl metallates, $[M(CO)_n]^{2-}$, where M = Fe / Ru (n = 4), Cr / Mo / W (n = 5).[50] Cooper and co-workers showed that the alkali salts of the $[M(CO)_n]^{2-}$ complexes react with CO_2 to generate alkali metal carbonates and neutral metal carbonyl complexes, $M(CO)_{n+1}$, where the additional CO ligand was established to derive from CO_2 based on ^{13}C-labeling studies. A mechanism was postulated whereby

$[M(CO)_n]^{2-}$ initially attacks CO_2 to yield a *C*-bound metallocarboxylate intermediate, $MC(O)O^-$. A subsequent addition of a second equivalent of CO_2 to the metallocarboxylate would yield the di-CO_2 intermediate, $MC(O)OC(O)O^-$, which can undergo C-O cleavage to release CO_3^{2-} and provide the neutral carbonyl product, $M(CO)_{n+1}$.[40]

Adapting this mechanism to the reaction shown in Figure 4.13, we propose nickel metallocarboxylate and $NiC(O)OC(O)O^-$ intermediates. To accumulate the two-electron equivalents necessary to reduce CO_2 to CO_3^{2-}, one might propose an initial disproportionation of $[NiML]^-$ to NiML and $[NiML]^{2-}$, where the latter is directly akin to the $[M(CO)_n]^{2-}$ dianions. However, the monoanionic **1-Ni^{red}** and **2-Ni^{red}** compounds already require quite harsh potentials to form via the one-electron reduction of **1/2-Ni^{red}** (for M = Al, $E_{½} = -2.82$ V vs. Fc^+/Fc; M = Ga, $E_{½} = -2.48$ V), which makes the possibility of $[NiML]^{2-}$ thermodynamically unfeasible. Instead, we propose an initial reaction between monoanionic $[NiML]^-$ and CO_2 to generate a Ni^I metallocarboxylate, which then is further reduced by another equivalent of **1/2-Ni^{red}** to generate a dianionic nickel diolate. The latter species could then attack a second CO_2 molecule to generate the Ni di-CO_2 intermediate, which then decays to CO_3^{2-} and neutral (CO)NiML. Attempts to spectroscopically observe the proposed diolate complex at low temperature using $^{13}CO_2$ were unsuccessful and lead to the described 1:1 mixture of complexes within minutes.

Unfortunately, in the NiML systems, the stability of the (CO)NiML products precludes the possibility of turnover via CO release. While CO release can be challenging from a low-valent Ni center, Lee and co-workers recently demonstrated this feat using an acridine-based PNP Ni^0 carbonyl complex.[42] In their system, two-electron reduction of the Ni^{II} CO adduct results in a severely distorted Ni^0 CO adduct, where the CO ligand is

displaced out of the square plane. This geometrical distortion allows CO_2 to bind to the Ni^0 center, after which CO is released followed by formation of a Ni^{II} metallocarboxylate species. Hence, future work will investigate whether the reduced carbonyl adducts, $[(CO)NiML]^-$ are accessible species, and if so, their behavior with respect to CO dissociation.

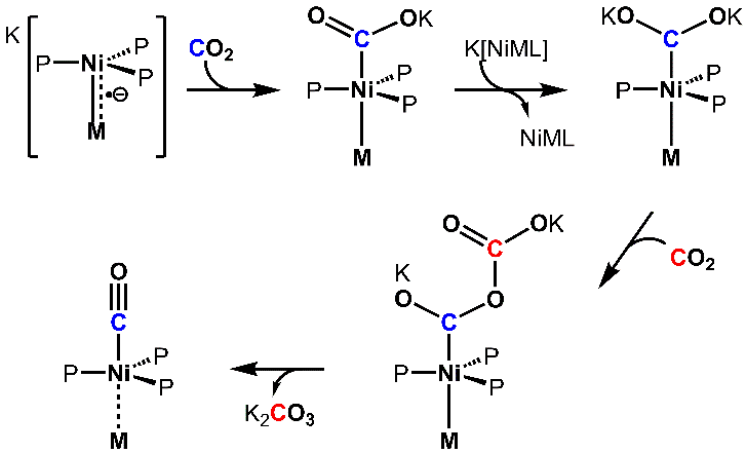

Figure 4.13: Proposed mechanism for the reaction between **1/2-Ni^{red}** and CO_2

4.3.6 Preliminary results with formally $Cu^0$and Ni^I species

Excited by the observation that the use of the Lewis-acidic metalloligand AlL and GaL allowed for the isolation of formally Ni^{-I} complexes, the isolation and characterization of isoelectronic copper species were then targeted. Initial attempts to synthesize a copper halide bimetallic of the form XCuML resulted in poorly soluble materials. For reasons unclear, attempts to prepare halide abstracted species such as $[CuML]^+$ failed as well using either $CuX/NaBArF_{24}$ or $[Cu(NCCH_3)_4]PF_6$. An extensive search of the literature revealed that recent progress in the stabilization of Cu^+ fragments has been made possible by the use of weakly coordinating anions.[51] Thus a new starting material [(1,5-

$COD)_2Cu][BArF_{24}]$ was sought in order to permit the isolation of the desired bimetallic species.

It is well known that copper forms π-complexes with many simple alkenes.[52] Even so, the $[(1,5\text{-}COD)_2Cu]^+$ fragment has received little attention as a precursor to low-coordinate copper complexes, which likely stems from a lack of an appropriately soluble salt (frequently encountered as insoluble/unstable ClO_4^- or BF_4^-). It is appreciated that $BArF_{24}$ salts confer high solubility in low dielectric solvents such as THF, Et_2O, or dichloromethane. The homoleptic olefin complex $[(1,5\text{-}COD)_2Cu][BArF_{24}]$ is readily synthesized by simply mixing the pentameric copper aryl species CuMes[53] (Mes = 2,4,6-trimethylphenyl) with the electrophilic acid $[(H(OEt_2)_2][BArF_{24}]$[54] in the presence of dry 1,5-cyclooctadiene.

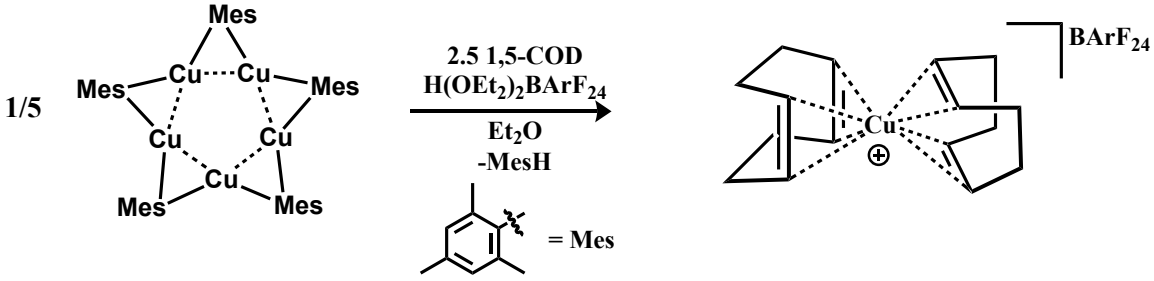

Figure 4.14: Synthesis of $[Cu(1,5\text{-}COD)_2]BArF_{24}$ from $[CuMes]_5$

The ^1H NMR spectrum of $[Cu(1,5\text{-}COD)_2]BArF_{24}$ when compared to free 1,5-cyclooctadiene indicates that the Cu^I center is a weak Lewis acid.[51] For example, the olefinic C-H residues of $[Cu(1,5\text{-}COD)_2]^+$ appear at higher chemical shifts (∂ 5.55ppm) than the respective C-H residues in free 1,5-cyclooctadiene (∂ 5.50ppm). This suggests that the Cu^+ fragment should be labile to substitution, as the olefins are minimally activated. This is further inferred by comparisons with the olefinic residues in $Ni(COD)_2$ that occur at much more upfield shifts (C-H, 4.3 ppm), while still retaining "naked-nickel," character.

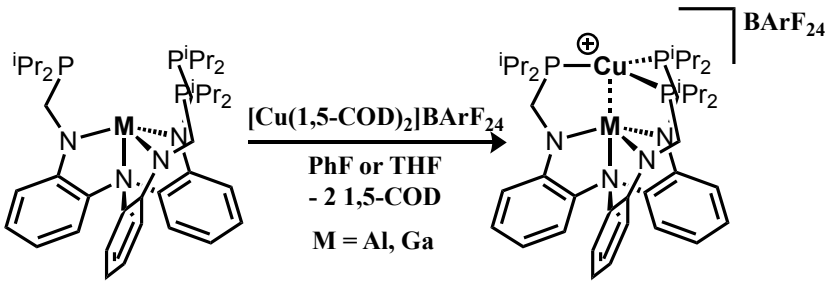

Figure 4.15: Synthesis of **1-Cu** and **2-Cu**

In line with this assessment, the addition of $[Cu(1,5\text{-}COD)_2][BArF_{24}]$ to solutions of AlL or GaL results in rapid substitution of the diene ligands and generation of the cationic fragments **1-Cu** and **2-Cu**. The addition of $[Cu(1,5\text{-}COD)_2][BArF_{24}]$ to solutions containing InL at any temperature results in the formation of a metastable violet/indigo solution that decays to an intractable mixture over a few hours. Regardless, **1-Cu** and **2-Cu**, are isolated cleanly in high yield as bright yellow and orange powders respectively. The ^{1}H NMR spectra of **1-Cu** and **2-Cu** show the expected signals for the H_3L^{iPr} ligand in addition to a single ^{31}P resonance at 17.3 ppm and 23.0 ppm, respectively. The single sharp ^{31}P resonance is indicative of C_3 solution state symmetry.

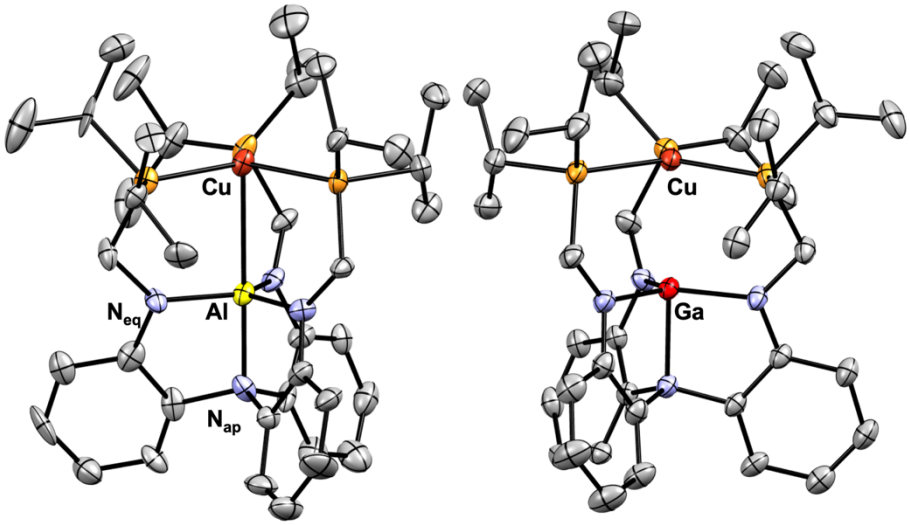

Figure 4.16: Molecular structure of **1-Cu** and **2-Cu** rendered at 50% probability. Hydrogen atoms and solvent molecules excluded for clarity.

Single crystals can be grown of both **1-Cu** and **2-Cu** (prepared by Brendan J. Graziano). Unfortunately, the anionic fragment exhibited disorder around the numerous CF_3 groups, and the structure was not able to reach a converged solution (thus table 4.3 has no ESD values). Worth noting is that the cationic fragments of **1-Cu** and **2-Cu** show minimal disorder and thus a discussion of the preliminary structure metrics are warranted. In the future, studies should attempt to utilize more rigid $BArF_{20}$ or BFI anions due to their tight molecular packing and lack of CF_3 groups. (BFI = N,N'-bis(tris(pentafluorophenyl)–borane)imidazolate, $BArF_{20}$ = tetrakis(pentafluorophenyl)borate). Of note, simple anions such as PF_6^- of BF_4^- were found unsuitable for the chemistry described here.

Table 4.3: Selected metrics for the series of copper complexes **1/2-Cu**

Metric	**1-Cu**[b,c]	**2-Cu**[b,c]
Ni–M (Å)	2.767	2.705
r[a]	1.09	1.06
Avg. Ni–P (Å)	2.285	2.290
Avg. M–N_{eq} (Å)	1.863	1.895
M–N_{apical} (Å)	1.99	2.047
Ni to P_3-plane (Å)	0.16	0.13

M to N_3-plane (Å)	0.05	0.11
∑(∠P−Ni−P) deg	358.6	358.8
∑(∠N_{eq}−M−N_{eq}) deg	359.8	359.0
∠P−Ni−M−N_{eq}[d] deg	16.8	14.9

a) Ratio of Ni−M bond length to the sum of the Ni and M covalent radii.[22-23] b) Preliminary structure, esd omitted as structure is not converged. c) Z'=2 values listed averaged. d) dihedral angles reported as absolute values.

The preliminary structure metrics of **1-Cu** and **2-Cu** reveal a modest (at best) interaction between the Cu^I center and the respective Lewis acids (2.767 and 2.705 Å for M = Al, Ga). The structures of cations **1-Cu** and **2-Cu** suggest that the d^{10} copper ion exists in a nearly perfect trigonal ligand field with minimal influence from the supporting ligand framework. This can be inferred from looking at the sum of the P–Cu–P and N_{eq}-M-N_{eq} angles; which approach 360˚ suggesting minimal perturbations to the Cu center. This is also reflected in the Cu-P_3 plane and M-N_3 plane distances, for which one might infer that the Lewis acidic metalloligand is reluctant to interact with the cationic Cu^I center. It is worth mentioning that the strength of the interaction is expected to be weaker in **1-Cu** and **2-Cu** than in corresponding Ni and Co complexes on the basis of the higher energy Cu based d-orbitals, as well as the localized cationic change on the Cu^+ center. The poor π-basic properties of Cu^I are apparent when comparing the isostructural d^{10} series of complexes $[Co(1,5\text{-}COD)_2]^-$, $Ni(1,5\text{-}COD)_2$, and $[Cu(1,5\text{-}COD)_2]^+$ for which average olefinic C-C bond lengths vary greatly from 1.416(7)[55], 1.391(2)[56], and 1.33(2) Å respectively.[51-52] The progressively elongated C-C bond when compared to free 1,5-COD (1.34 Å) is indicative of increasingly proficient π-backbonding.

With a stable and isolable Cu^{I} synthon in hand, we then sought to examine if a $Cu^{+/0}$ redox event could be achieved akin to the isoelectronic Ni^{0} complexes. Gratifyingly, the addition of one equivalent of KC_8 to the pale solutions **1-Cu** and **2-Cu** of results in the formation of deep red/maroon solutions that are reminiscent of the analogous $\{NiM\}^{11}$ complexes. In line with this observation, the ^{1}H NMR spectra of the reaction mixtures of **1-Cu** and **2-Cu** with reducing agents shows no resolvable resonances other than the NMR solvent employed. These observations are consistent with an $S = ½$ spin state, working under the limiting assumption that the $\{NiM\}^{11}$ and $\{CuM\}^{11}$ complexes have similar electronic structures.

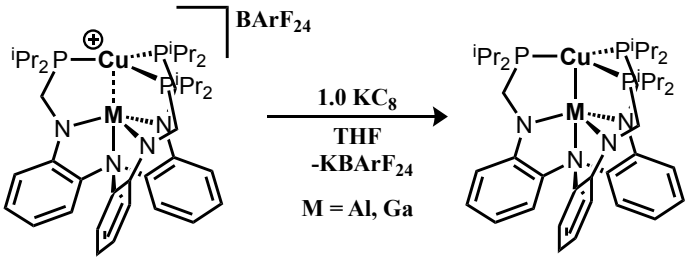

Figure 4.17: Synthesis of $\{CuM\}^{11}$ complexes **1-Cu^{red}** (M = Al) and **2-Cu^{red}** (M = Ga)

Bright-red crystals of **1-Cu^{red}** and **2-Cu^{red}** can be grown from saturated Et_2O (M = Al) or toluene (M=Ga) solutions at -30˚C. Images of their respective crystal structures are shown in the figure below (samples prepared by Brendan J. Graziano following initial characterization). Each species crystallizes in the triclinic space group *P-1*, and the pertinent structural parameters are shown in Table 4.4.

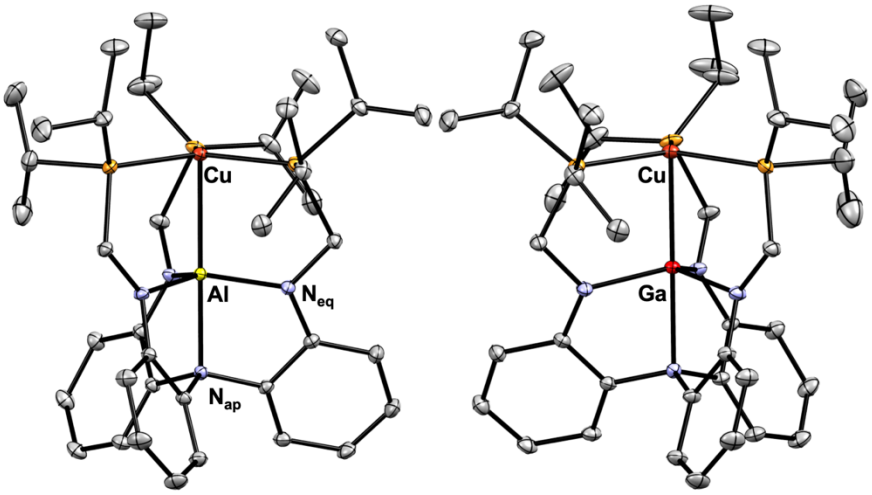

Figure 4.18: Molecular structures rendered at 50% probability of $\{CuM\}^{11}$ complexes **1-Cu^{red}** (left) and **2-Cu^{red}** (right). Hydrogen atoms and solvent molecules omitted for clarity.

The most immediate structural change upon reduction from **1-Cu** and **2-Cu** is the dramatic contraction of the Cu–M interaction. In both cases, the Cu–M distances changes by upwards of 0.23 Å indicating a strong perturbation in bonding between the oxidized and reduced species (Table 4.4). The local coordination environment around the Cu atom is minimally perturbed, with both the Cu–P_3 plane and average Cu–P distances not changing dramatically. Conversely, there is a sharp change in the local coordination environment around the Lewis acidic ion. There are considerable deviations from the ideal trigonal symmetry exhibited in **1-Cu** and **2-Cu**, which are reflected in both the changes in the sum of N_{eq}–M–N_{eq} bond angles (4.8˚, 8.6˚ resp.) as well as a dramatic repositioning of M with respect to the N_3 plane (Δ_{Al} = 0.20 Å, Δ_{Ga} = 0.25 Å). In contrast to the isoelectronic Ni complexes, there is minimal overall reorganization of the ligand framework as indicated by the change in dihedral angels. Taken together, the repositioning of M and contraction of the Cu–M interaction suggests that the reduction is largely accommodated by the Lewis acid. Lastly, reduction to the $\{CuM\}^{11}$ state has a noticeable effect on the average Cu-P

bond lengths, which shortens akin to the $\{NiM\}^{10/11}$, likely due to increased π-backbonding to the phosphine ligands.

Table 4.4: Selected metrics for the series of copper complexes **$\{1/2\text{-Cu}\}^{10/11}$**

Metric	**1-Cu**[b,c]	**1-Cu^{red}**	**2-Cu**[b,c]	**2-Cu^{red}**
Ni–M (Å)	2.767	2.530(4)	2.705	2.454(1)
r[a]	1.09	1.0	1.06	0.96
Avg. Ni−P (Å)	2.285	2.249(4)	2.290	2.270(1)
Avg. M−N_{eq} (Å)	1.863	1.892(1)	1.895	1.957(1)
M−N_{apical} (Å)	1.99	2.084(1)	2.047	2.195(1)
Ni to P_3-plane (Å)	0.16	0.18	0.13	0.14
M to N_3-plane (Å)	0.05	0.25	0.11	0.355
∑(∠P−Ni−P) deg	358.6	359.2	358.8	358.9
∑(∠N_{eq}−M−N_{eq}) deg	359.8	355.0	359.0	350.4
∠P−Ni−M−N_{eq}[d] deg	16.8	16.0	14.9	14.9

a) Ratio of Ni−M bond length to the sum of the Ni and M covalent radii.[22-23] b) Preliminary structure, esd omitted as structure is not converged. c) Z'=2 values listed averaged. d) dihedral angles reported as absolute values.

Drawing parallels between the isoelectronic $\{NiM\}^{11}$ complexes it is attractive to describe the ground state electronic structure of **1-Cu^{red}** and **2-Cu^{red}** as possessing a formal Cu^0 oxidation state. As discussed, there is scant evidence for the formally zerovalent copper oxidation state. Molecular compounds that appear to exhibit Cu^0 character have been shown to have ground state configurations that are more indicative of Cu^I than Cu^0. Examples of such species include the spin-coupled radicals reported by Bertrand[18] and Peters (see Fig. 4.1).[17] Furthermore, the structure of the matrix-isolated $Cu(CO)_3$ is believed to be D_{3h} symmetric with the unpaired electron residing in a $4p_z$ orbital.[57] In the present case, it is important to acknowledge the fact that the inherent electronegativity of the series of complexes still holds in the order: $\chi_B > \chi_{Ni} \sim \chi_{Cu} > \chi_{Ga} > \chi_{Al}$. Thus to a first approximation, it would appear that the similar Pauling electronegativities between Cu and Ni would support the postulate that **1-Cu** and **2-Cu** are best described as possessing a large degree of Cu^0 character. Working under the limiting assumption that the composition of

the orbitals in the isoelectronic $\{NiM\}^{11}$ and $\{CuM\}^{11}$ complexes are similar (Section 4.3.4) the frontier orbitals of $\{CuM\}^{11}$ likely possess substantial copper character.

4.3.7 EPR spectroscopy of $\{CuM\}^{11}$ complexes

As the EPR spectra of the $S = ½$ $\{NiM\}^{11}$ species were found to be informative with respect to the electronic structure, we sought to characterize **1-Cu^{red}** and **2-Cu^{red}** by similar means. The EPR spectra of **1-Cu^{red}** recorded at 40K (1mM in THF) gives rise to a unique 9-line pattern that is appropriately modeled by utilizing axial Cu and Al hyperfine tensors, as shown in the figure below.

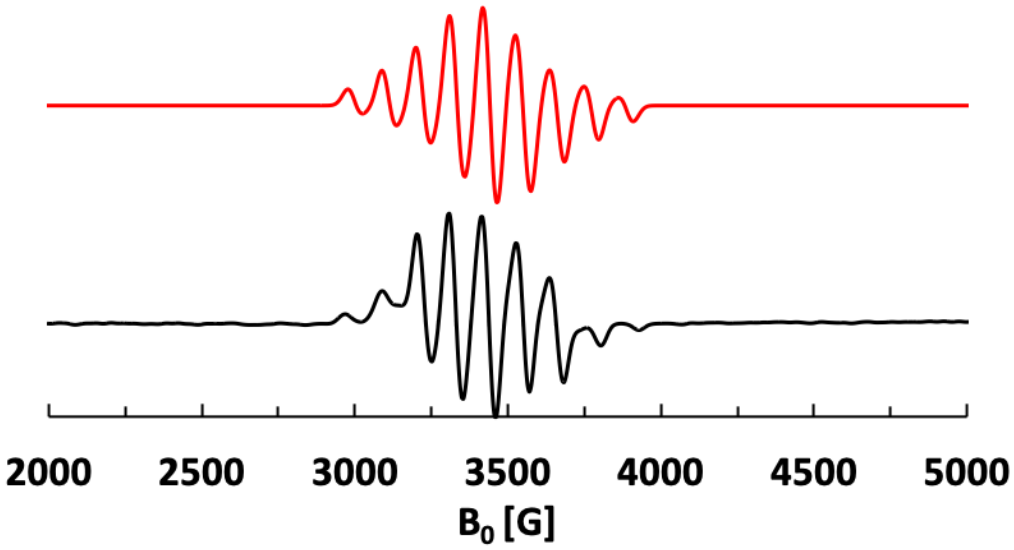

Figure 4.19: EPR spectra of **1-Cu^{red}** (1mM, THF, 40K). Modeled (top, red) and experimental (bottom, black) traces.

The preliminary simulation reveals that a largely anisotropic coupling between both the $I = 5/2$ (100% abundant) ^{27}Al nuclei and the $^{63/65}Cu$ (60:40 abundance, $I = 3/2$) contribute to give the unique pattern at $g = 2.04$. Of note, the values of hyperfine tensors are quite large, as was observed for the analogous **1-Ni^{red}** complex. The tensor that describes the hyperfine coupling are: $A(^{27}Al) = \{4.3, 0.6, 0.6\}$ mT and $A(^{63}Cu) = \{4.8, 1.8,$

1.8} mT. Unfortunately, room temperature EPR data for direct comparison to **1-Ni^{red}** have not been achieved to date.

The room temperature EPR spectra of **2-Cu^{red}** is also informative, but only a preliminary fit has been achieved to date. There is inherent difficulty in simulating EPR data for **2-Cu^{red}** which is a consequence of the number of isotopically active nuclei ($^{63/65}$Cu, ^{69}Ga, 3x^{31}P, 4x^{14}N). The EPR spectra (modeled at g_{iso} = 2.029) do however show that there is a large hyperfine interaction with Ga visually approaches that observed for **2-Ni^{red}** (A_{69Ga} = 37mT). This hyperfine tensor is strongly axial, as indicated by the difference in the magnitudes of A(^{69}Ga) tensor components: {44.9, 8.16, 8.16} mT. Furthermore, the signal contains many more lines than that anticipated for the two spin active isotopes of gallium, and thus coupling to naturally abundant ^{63}Cu and ^{65}Cu must be considered. The hyperfine interaction with Cu is similarly axial with values for A(^{63}Cu) of {146, 0.2, 0.2} mT. The EPR spectra recorded thus far for **2-Cu^{red}** are shown in the figure below alongside the best simulation to date. The shape and width of the signal are not dissimilar from those reported for **2-Ni^{red}**. Better room temperature data acquisitions should lead to datasets that are easier to interpret so that conclusions can be drawn between the {NiM}^{11} and {CuM}^{11} complexes.

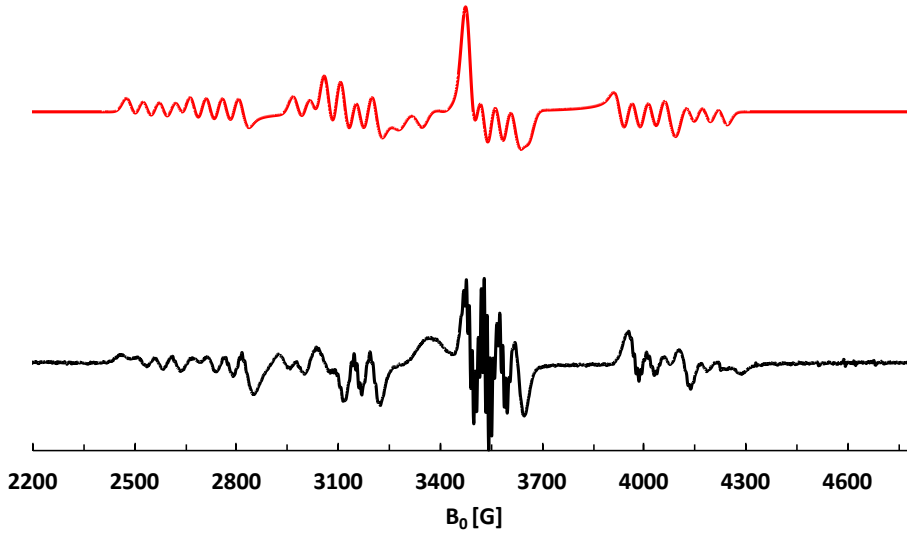

Figure 4.20: EPR spectra of **2-Cu^{red}** (1mM, THF, 298K). Modeled (top, red) and experimental (bottom, black) traces.

4.3.8 Preliminary results with {NiM}^{9}

With definitive characterization in hand for both the neutral {NiM}^{10} and {NiM}^{11} complexes, characterization of cationic Ni^{I} complexes were sought to complete the redox series available in the NiML configuration. To this end, the reaction between the neutral nickel precursors, **1-Ni** and **2-Ni**, and soluble ferrocenium salts of weakly coordinating anions were explored in detail so that comparisons between the three redox states for each complex could be drawn. Notably, we have been unable to synthesize an unligated Ni^{I} cation to date due to solvent binding (MeCN).

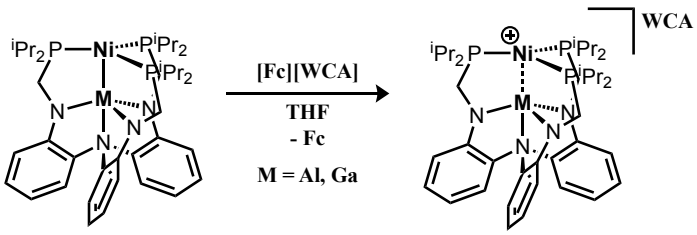

Figure 4.21: Synthesis of cations **1/2-Ni^{ox}**.

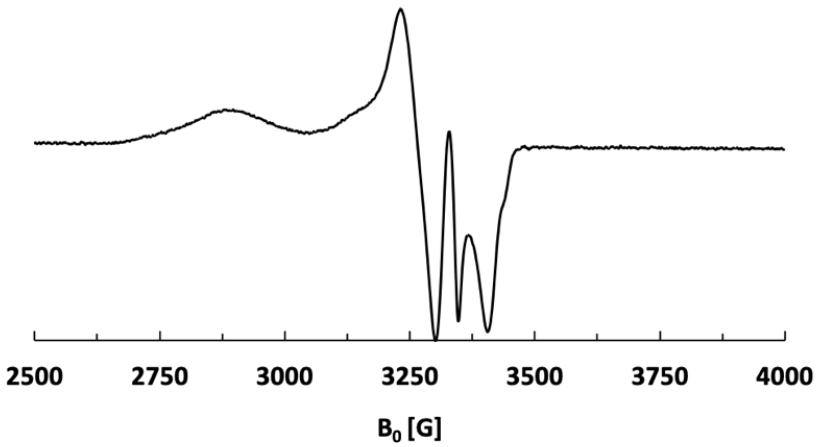

Figure 4.22: X-Band EPR spectrum for **1-Ni^{ox}** (ca. 1mM, THF, 40K)

Conveniently, the addition of one equivalent of [Fc][WCA] (but not PF_6, BF_4 etc.) to solutions of **1-Ni** or **2-Ni** results in the formation of dark yellow/green (M =Al) and red/yellow (M=Ga) solutions with the formation of THF soluble paramagnetic materials as indicated by ^{1}H NMR spectroscopy. Consistent with a postulated $S = ½$ center, the ^{1}H NMR spectrum of **1-Ni^{ox}** gives rise to paramagnetically shifted resonances from 120 to -5 ppm, as shown in Figure 4.23. Similar results were noted for the oxidation of the gallium

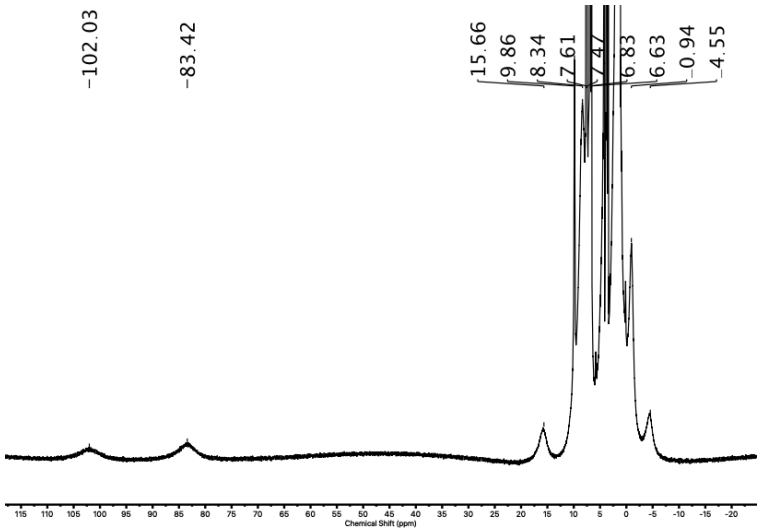

Figure 4.23: ^{1}H NMR spectrum of **1-Ni^{ox}** (400 MHz, THF-d_8)

congener **2-Ni**, however the species has yet to be adequately characterized in both solution and in the solid state and thus will not be explicitly discussed.

The identity of **1-Ni^{ox}** was further identified from its EPR spectra which is supports the assignment of an $S = 1/2$ center. The removal of an electron from the ground state computed electronic structure of **1-Ni** should result in removal of an electron from the degenerate $d_{x2-y2}d_{xy}$ orbital manifold. Thus, a reasonable hypothesis is that the resulting EPR spectra should appear to be more rhombic in character due to the anisotropy in the x/y plane frontier orbitals (where z is defined colinear with the Ni-Al vector). Accordingly, the EPR spectra of **1-Ni^{ox}** shows what appears to be a rhombic signal with three distinct *g* values of [2.36, 2.11, 2.05]. It is not yet clear if the signal found near the center of if the signal due to unresolved coupling or excess ferrocenium salt.

Due to the highly rigid nature of the BFI anion, single crystals of [**1-Ni^{ox}**][BFI] were grown by layering a fluorobenzene solution with pentane. In this manner, large prismatic yellow-green plates of [**1-Ni^{ox}**][BFI] were able to be grown and analyzed by single crystal x-ray diffraction. The molecular structure of the complex, as well as the tabulated X-ray diffraction data, are shown in the respective figure and tables below. Worth noting is that despite numerous attempts, single crystals suitable for diffraction could not be obtained utilizing the $BArF_{24}$ anion.

Specimens of [**1-Ni^{ox}**][BFI] crystallize in the monoclinic space group $P2_1/c$ with one molecule of disordered fluorobenzene in the unit cell. In comparison with the other redox members of the {NiAl}$^{9\text{-}11}$ series, it is immediately apparent that the Ni-M interaction is the weakest of the trio, as might be expected based on exceptionally electron poor Ni center in **1-Ni^{ox}**. By comparison to the rest of the series of complexes, the Ni center in **1-Ni^{ox}** sits even further out of the P_3 plane than in either of its other redox partners. In accordance with the elongation of the Ni-Al interaction, the Al atom must also sit progressively closer to the N_3 plane as well when compared to **1-Ni^{red}** and **1-Ni**. It is notable in light of these structural changes that a large degree of trigonal symmetry is retained. This is directly evidenced by the sum of the N-Al-N and P-Ni-P angles which still total close to 360˚.

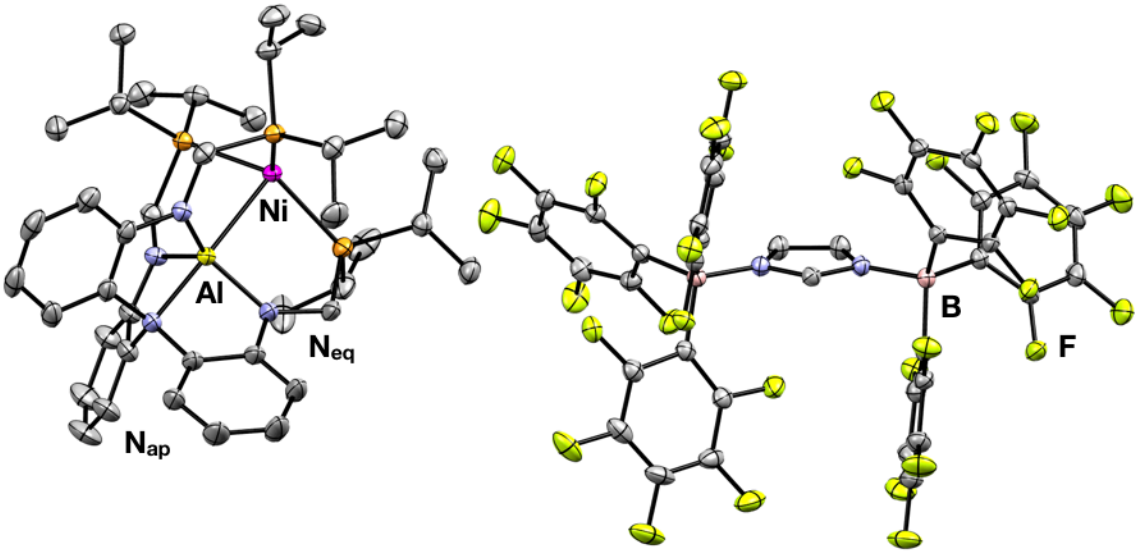

Figure 4.24: Molecular structure of [**1-Ni^{ox}**][BFI] showing both the cationic and anionic fragments. Thermal ellipsoids draw at 50% probability, hydrogen atoms and crystallization solvent omitted for clarity.

Lastly, there is a notable "bend," in the ligand framework that acts to accommodate these various changes, as evidenced by the continually increasing average P-Ni-M-N_{eq} torsion angle from **1-Ni^{red}** to **1-Ni^{ox}.** The identity of **1-Ni^{ox}** as a d^9 Ni^I species is also

substantiated by the dramatic elongated of the average Ni–P bond length across the $\{NiM\}^{9-11}$ series of complexes. Explicitly, the average Ni–P bond length contracts from 2.285(5) Å in **1-Ni^{ox}** to 2.204(1) Å in **1-Ni** and finally 2.136(1) Å in **1-Ni^{red}**, a change of 0.149 Å. Of note, one of the Ni–P bonds in **1-Ni^{ox}** is substantially shorter than the other corresponding distances. Given that the frontier orbitals are comprised of approximately degenerate $d_{x2-y2}d_{xy}$ orbitals, its stand to reason that this deviation may arise from a pseudo-Jahn Teller distortion. Indeed such reasoning has been employed for the d^9 cobalt-borane complexes reported by Peters, (TPB)Co(η^2–H_2). [58]

Table 4.5: Selected metrics for the **{NiM}$^{9-11}$** redox family

Metric	**1-Ni^{red}**	**1-Ni**	**1-Ni^{ox}**
Ni–M (Å)	2.389(1)	2.450(1)	2.567(1)
r[a]	0.97	1.00	1.05
Avg. Ni−P[b] (Å)	2.136(1)	2.204(1)	2.285(5)
M−N_{eq}[b] (Å)	1.904(3)	1.876(2)	1.852(1)
M−N_{apical} (Å)	2.257(3)	2.099(2)	2.019(2)
Ni to P_3-plane (Å)	0.11	0.13	0.18
Al to N_3-plane (Å)	0.39	0.26	0.13
∑(∠P−Ni−P) deg	359.3(7)	359.0(1)	358.0(1)
∑(∠N_{eq}−M−N_{eq}) deg	347.7(2)	354.5(2)	358.5(1)
∠P−Ni−M−N_{eq}[b,c] deg	15.9	19.9	23.3

a) Ratio of Ni−M bond length to the sum of the Ni and M covalent radii.[22-23] b) Average value. c) Dihedral angles are reported as absolute values

4.4 Conclusion

Isolable examples of odd-electron bonds between transition metals and heavier main group elements are extremely rare. Typically, odd-electron metal-ligand bonds are known for O, N, or S donors where the unpaired spin residues in the π manifold.[25, 59-67] To our knowledge the only other similar species Cu(TPB), which is formally isoelectronic to the $\{Ni–M\}^{11}$ system (see Fig 4.1).[17] We note, however, that the Cu−B interaction is fundamentally different from the Ni−M interactions of the heavier group 13 congeners.

Upon reduction of the cationic precursor $[Cu(TPB)]^+$, a polar one-electron bond is formed in Cu(TPB) where none had existed beforehand. The natural atomic orbital population analysis spin densities of 0.13 and 0.57 at the Cu and B atoms, respectively, indicate that the σ-(Cu−B) bond is polarized towards B, and as such, it has been described as a B→Cu σ-dative bond between a borane radical ($BR_3^{\bullet -}$) and Cu^I. By contrast, reduction of the NiML precursors further strengthens the Ni−M interaction beyond the pre-existing $Ni(3d_{z2})^2 \rightarrow M$ dative bond. The SOMO and spin density contours support a σ-(Ni−M) bond that is polarized towards Ni, supporting Ni^{-I} character. This reversal of the spin polarization can be rationalized by considering electronegativity (X) differences, where $\chi_B > \chi_{Ni} \sim \chi_{Cu} > \chi_{Ga} > \chi_{Al}$.[68] Thus based on electronegativity, the d^{10} nickel center is forced to accept the majority of the added electron density in **1-Ni^{red}** and **2-Ni^{red}**. Importantly, the total number of Ni−M bonding electrons in the $[NiML]^-$ complexes sum to 3 across two centers. Therefore, the $\{Ni-M\}^{11}$ compounds are exceptional cases of 2c/3e-bonds in which all 3 electrons participate in polar σ-bonding interactions. This stand in stark contrast to traditional 2c/3e-bonds in which a formal 0.5 order bond is typically observed.[69-71]

To understand these unusual $\{Ni-M\}^{11}$ species, one may consider three limiting resonance forms, as depicted in Figure 4.25. If the one-electron reduction is localized at a single metal site, then two different metalloradicals are possible: M^{II} as in structure A, or Ni^{-I} as in structure C. B is an intermediate structure, where the reducing equivalent is shared by both Ni and M as a bonding electron. Structure A can be ruled out based on the following arguments: (1) Substantial changes to the coordination bonds around Ni strongly indicate reduction at Ni (and not solely at M). (2) Significant Ni-based spin density, which is inferred from the ^{31}P-hyperfine values and corroborated by theory, is inconsistent with

A. (3) The Ni→M bonding interaction does not weaken as implied by the $Ni^{0}\rightarrow M^{II}$ bonding in A.

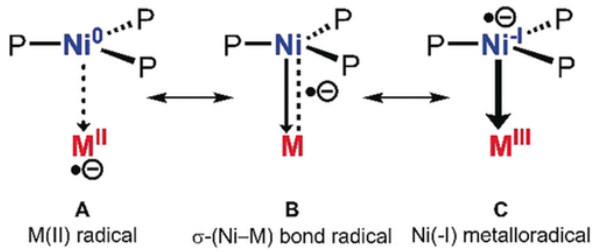

Figure 4.25: Three limiting resonance structures for complexes **1-Ni^{red}** and **2-Ni^{red}**

Structure B is a reasonable resonance structure as it accounts for the delocalization of spin density across both Ni and M centers. Moreover, the presence of the one-electron polar σ-(Ni−M) and the two-electron $Ni(3d_{z2})^{2}\rightarrow M$ dative bond reinforces the observed shortening of the Ni−M interaction. In structure C, the highly reduced Ni^{-I} center could also generate shorter Ni−M bonds via two distinct dative bonds to the Lewis acidic M^{III} center: $Ni(3d_{z2})^{2}\rightarrow M$ and $Ni(4s/p_{z})^{1}\rightarrow M$. Spin density at the P and M atoms may be attributed to strong π- and σ-backbonding interactions, respectively, from the electron-rich Ni center to these ligands.

In summary, we have investigated a unique pair of complexes in which the $\{MNi\}^{10}$ unit undergoes chemical reduction to produce reduced complexes featuring a $\{MNi\}^{11}$ configuration. X-ray crystallography, EPR, and chemical theory support the notion that much of this reduction occurs at the Ni center at an orbital with π symmetry. This unique orbital produces a net two-center three-electron bond that exhibits a formal bond order of greater than one. Collectivity, both theory and experiment agree that these reduced species are best described at formally Ni^{-I} where the unpaired electron lies in predominantly Ni based orbitals, with non-negligible contributions from the Lewis acid.

Given the unique and exciting electronic structure that Lewis acidic metalloligands engender at low-valent nickel centers, this strategy was expanded to include isoelectronic copper complexes. The synthesis of the $\{CuM\}^{10/11}$ species is not immediately trivial and is greatly facilitated by the new starting material $[Cu(1,5\text{-}COD)_2][BArF_{24}]$ which provides rapid access to **1-Cu** and **2-Cu**. These $16e^-$ copper fragments have been shown to undergo single electron reduction to generate species that are isoelectronic to their nickel analogous. Drawing parallels between these nickel and copper complexes allows for one to speculate that the oxidation state of **1-Cu^{red}** and **2-Cu^{red}** may be best described as Cu^0. This formulation is noteworthy in light of the lack of characterization of such species. Furthermore **1-Cu^{red}** and **2-Cu^{red}** offer a solution stable isoelectronic analog to $Cu(CO)_3$, which is notably isolable to the CH_3• radical.

Future studies should explore the in-depth characterization of the room temperature EPR spectra of **1-Cu^{red}** and **2-Cu^{red}** such that strong comparison with **1-Ni^{red}** and **2-Ni^{red}** can be made. Furthermore, the accessibility of an anionic state (e.g. $\{CuM\}^{12}$) should be investigated by cyclic voltammetry studies, to assess the limitation of the LM scaffold in stabilizing low-valent copper complexes.

Lastly, for M = Al, the redox series $\{NiM\}^{9\text{-}11}$ has been completed by characterizing **1-Ni^{ox}** in both solution and the solid-state. The **1-Ni^{ox}** species exhibits an $S = 1/2$ spin state as evidenced by its EPR spectrum and paramagnetically shifted ^{1}H NMR resonances. Oxidation of **1-Ni** ultimately results in weakening of the Ni–Al interaction in **1-Ni^{ox}** due to abstraction of an electron from the $d_{x2\text{-}y2}d_{xy}$ manifold. This electronic modification gives rise to a distorted geometry at the d^9 nickel center, which likely occurs through a pseudo-Jahn Teller distortion.

4.5 Experimental Section

General Considerations: Unless otherwise stated, all manipulations were performed under a purified Ar atmosphere using standard Schlenk techniques or inside of an inert atmosphere glovebox with < 1.0 ppm O_2 and H_2O. Standard solvents were deoxygenated by sparging with Ar and dried by passing through activated alumina columns of an SG Water solvent purification system. Deuterated solvents were purchased from Cambridge Isotope Laboratories, Inc., degassed via freeze-pump-thaw cycles, and stored over activated 4 Å molecular sieves. THF-d_8 was dried over NaK, freeze-pump-thawed, and vacuum transferred into a Schlenk flask filled with ca. 20% w/v sieves. Mesitylene was dried over pre-activated 4 Å molecular sieves. All other reagents were purchased from commercial vendors and used without purification unless otherwise noted. ^{1}H and ^{31}P NMR spectra were recorded on Bruker 400 MHz spectrometer. Perpendicular-mode X-band EPR spectra were recorded at low (20 to 40 K) or ambient (298 K) temperature with a Bruker ESP 300 spectrometer equipped with an Oxford ESR 910 liquid-helium cryostat and an Oxford temperature controller. EPR spectra were simulated utilizing Easyspin with the functions pepper (frozen solution) and garlic (fluid state), and refined using esfit until a satisfactory model was obtained.[72] Cyclic voltammetry was conducted using a CH Instruments 600 electrochemical analyzer. The one-cell setup utilized a glassy carbon working electrode, platinum wire counter electrode, and vitreous carbon auxiliary electrode. Analyte solutions were prepared in a THF solution of tetra-*n*-butylammonium hexafluorophosphate (0.4 M) and referenced internally to the $FeCp_2/FeCp_2^+$ redox couple. NMR shifts were referenced to the internal solvent residual signal (for ^{1}H spectra) or an external H_3PO_4 reference (for ^{31}P spectra).[73] The neutral ligand ($N(o\text{-}(NHCH_2P^iPr_2)C_6H_4)_3$

(H_3L)[19], and bimetallic complexes, NiML (M = Al, Ga, In)[20], were synthesized according to literature procedures. 4,7,13,16,21,24-Hexaoxa-1,10-diazabicyclo[8.8.8]hexacosane (2.2.2-cryptand, or crypt–222) was purchased from Sigma–Aldrich and dried under vacuum for 12 hours at room temperature before use. Potassium graphite (KC_8) was stored at –30˚C to prolong its shelf life. Elemental analyses were performed by Robertson Microlit Laboraties, Inc. (Ledgewood, NJ). Ultra-high purity CO_2 was passed through a CO_2 specific gas drying column immediately before use. $^{13}CO_2$ was purchased from Sigma-Aldrich and used without further purification. All other materials were prepared according to their literature procedures.

Syntheses of [K(crypt-222)][1-Ni^{red}]: A solution of **1-Ni** (50 mg, 65μmol) and crypt–222 (24.6 mg, 65μmol) in 4 mL of 1:1 mesitylene/THF was cooled to –30˚C and then added to a similarly cooled vial of solid KC_8 (8.8 mg, 65μmol). The mixture was shaken for 5-10 min by hand causing the consumption of the golden KC_8 and deposition of black graphite. The mixture was filtered using a glass fiber pipet, giving rise to a deep-red solution. The mixture was then carefully layered with diethyl ether (12 mL) and stored at –30˚C for 48 hours providing nearly black hexagonal prisms (54.6 mg, 76% yield). Crystals suitable for X-ray diffraction were grown from layering a DME solution with /hexanes at –30˚C. ^{1}H NMR (THF-d^8, 400 MHz): δ 7.29 (fwhm = 40 Hz, 6H), 3.49 (12H, $NCH_2CH_2OCH_2$), 3.47 (12H, $NCH_2CH_2OCH_2$), 2.49 (12H, $NCH_2CH_2OCH_2$). Anal. calculated for $C_{57}H_{96}AlKN_6NiO_6P_3$•$C_4H_8O$ (%) C 58.56, H 8.38, N 6.72. Found, C 58.81, H 8.26, N 6.67. UV-VIS (in THF): (nm, ε [mol^{-1} cm^{-1}]) 348 (11,100), 429 (7,900), 484 (6,300). The

synthesis of this compound can also be performed utilizing 18-crown-6 but crystals grown from this method were unsuitable for x-ray diffraction studies.

Syntheses of [K(crypt-222)][2-Ni^{red}]: The synthesis is analogous to [K(crypt–222)][NiAlL]. **2-Ni** (21.6 mg, 26.8 μmol) was added to KC_8 (3.6 mg, 26.8 μmol) at -30˚C in THF in the presence of crypt–222 (10.1 mg, 26.8 μmol) to provide nearly black hexagonal prisms of the title complex (12.5 mg, 32 % yield). ^{1}H NMR (ppm, THF-d_8, 400 MHz): δ 7.29 (fwhm = 40 Hz, 6H), 3.49 (12H, $NCH_2CH_2OCH_2$), 3.46 (12H, $NCH_2CH_2OCH_2$), 2.48 (12H, $NCH_2CH_2OCH_2$). Anal. calculated for $C_{57}H_{96}GaKN_6NiO_6P_3$•0.5 C_9H_{12} (%) C 57.60, H 8.02, N 6.56. Found, C 57.67, H 7.92, N 6.44. UV-VIS (in THF): (nm, ε [mol^{-1} cm^{-1}]) 328 (29,000), 408 (2,750), 465 (3,400), 484 (6,300), 527 (2,500).

Synthesis of [Li(12-crown-4)(DME)][2-Ni^{red}]: A solution of **2-Ni** was stirred in 1,2-dimethoxyethane (49.3 mg, 61 μmol, 8 mL) with a glass-coated stir bar until dissolved and then transferred to a vial containing a smear of elemental lithium metal. 12-crown-4 (30 μL, 180 μmol) was added directly to the stirring mixture, and then the reaction was stirred for an additional 2 h. The solution was reduced to ca. 4 mL in vacuo and then filtered to give a deep scarlet-red solution. Diethyl ether (~10 mL) was added, and the mixture stored at −30˚C for 4 h to yield dark scarlet crystals. The crystals were washed with diethyl ether (3 x 2mL) and dried in vacuo to give 18.4 mg (30% yield) of a crystalline solid. Vapor diffusion of diethyl ether into a concentrated DME solution provided large prisms of **2^{red}** suitable for X-ray diffraction. The spectroscopic properties of this salt are identical to those

reported previously for the K(crypt-222) salt of **2-Ni^{red}**. If stored at -30˚C under argon, samples of this complex are stable for upwards of six months.

Reaction of 1/2-Ni^{red} with CO_2. A resealable NMR tube was charged with a 0.5 mL THF-d_8 solution of [K(crypt-222)]**[1-Ni^{red}]** or [K(crypt-222)]**[2-Ni^{red}]** (ca. 10mg). The solution was degassed via a freeze-pump-thaw cycle, and the atmosphere replaced with CO_2. Immediately, a color change from deep red to yellow-brown (for **1^{red}**) or red-brown (for **2^{red}**) was observed. The ^{1}H NMR spectra showed the consumption of the paramagnetic precursor, and the formation of NiML and (CO)NiML in a 1:1 ratio. In the case of **1-Ni^{red}**, the volatiles were removed and crystallization from a concentrated pentane solution yielded single crystals containing crypt-222, **1-Ni**, and **1-Ni(CO)**.

Synthesis of 1-Ni(CO): A solution of **1-Ni** (25 mg, 32 μmol) and ethyl formate (250 μL) in C_6D_6 (0.750 mL) was heated in resealable NMR tube at 65˚C until full conversion was observed by ^{31}P NMR spectroscopy (ca 4. days). After the volatiles were removed in vacuo, the crude was dissolved in ca. 1 mL of pentane and stored at −30˚C to afford large colorless crystals of **1-Ni(CO)** (9.8 mg, 35% yield). Using a reaction vessel with a small headspace is critical for the reaction to occur. Multiple attempts to scale up the reaction using a 100mL Schlenk flasks were unsuccessful, and only **1-Ni** was recovered. Elemental calc. (found) for $C_{40}H_{60}AlN_4NiOP_3$•0.8C_5H_{12}: C 62.23 (61.95), H 8.26 (8.13), N 6.60 (6.28). ^{1}H{^{31}P} (400 MHz, C_6D_6): δ 7.48 (d, J = 6.9 Hz, 3H, aryl), 7.12 (t, J = 7.78 Hz, 3H, aryl), 6.54−6.51 (m, 6H, aryl), 2.99 (br, 3H, CHH′), 2.81 (br, 3H, CHH′), 2.12 (br, 3H, *CH*(CH_3)$_2$), 1.95 (br,

3H, *CH′*(CH_3)$_2$), 1.20−0.9 (br, 36H, CH_3). $^{31}P\{^1H\}$ (162 MHz, C_6D_6): δ 43.6. IR (KBr pellet): ν_{CO} = 1953 cm^{-1}. $^{13}C\{^1H\}$ (100.5 MHz, THF-d_8): δ 209.9 (q, J = 8 Hz, Ni−^{13}CO).

Synthesis of 2-Ni(CO):. A mixture of **2-Ni** (46mg, 57 μmol) and paraformaldehyde (25 mg, 0.833 mmol) in benzene (4 mL) were stirred for 12 h and then filtered and reduced in vacuo to yield a bright yellow powder. The solids were then dissolved in minimal benzene. Vapor diffusion of hexane into the solution and storage at −30˚C yielded 18.5 mg (40% yield) of nearly colorless crystals suitable for single-crystal diffraction studies. The crystals were washed with hexane and briefly dried in vacuo. Elemental calc. (found) for $C_{40}H_{60}GaN_4NiOP_3 \cdot C_6H_{14}$: C 60.02 (60.36), H 8.10 (8.16), N 6.09 (6.10). $^1H\{^{31}P\}$ NMR (400 MHz, C_6D_6): δ 7.45 (d, J = 7.4 Hz, 3H, aryl) 7.20 (t, J = 7.6 Hz, 3H, aryl), 6.63−6.59 (m, 6H, aryl), 3.13 (br, 3H, CHH′), 2.74 (br, 3H, CHH′), 2.08 (m, 3H, CH(CH_3)$_2$), 1.90 (m, 3H, CH′(CH_3)$_2$), 1.20−0.6 (br, 36H, CH_3). $^{31}P\{^1H\}$ NMR (162 MHz, C_6D_6): δ 55.7 ppm. IR (KBr pellet): ν_{CO} = 1962 cm^{-1}. $^{13}C\{^1H\}$ (100.5 MHz, THF-d_8): δ 211.9 (q, J = 9 Hz, Ni-^{13}CO)

Synthesis of 3-Ni(CO):. A mixture of **3-Ni** (43 mg, 51 μmol) and paraformaldehyde (11.7 mg, 0.4 mmol) were stirred for 2 h in benzene (4 mL) and then filtered and reduced in vacuo to yield a yellow powder. The solids were then dissolved in minimal toluene. Vapor diffusion of hexane into the solution and storage at −30˚C for 12 h yielded 22.3 mg (50% yield) of nearly colorless crystals suitable for single-crystal diffraction studies. The crystals were washed with hexane and briefly dried in vacuo. Elemental calc. (found) for $C_{40}H_{60}InN_4NiOP_3 \cdot 0.8\ C_6H_{14}$: C 56.74 (57.06), H 7.57 (7.21), N 5.91 (5.88). $^1H\{^{31}P\}$ NMR

(400 MHz, C_6D_6): δ 7.45 (d, J = 7.4 Hz, 3H, aryl), 7.23 (t, J = 7.4 Hz, 3H, aryl), 6.66 (d, J = 8.0 Hz,3 3H, aryl), 6.60 (t, J = 7.4Hz, 3H, aryl), 3.08 (br, 6H, CH_2), 1.96 (m, 6H, $CH(CH_3)_2$), 1.00−0.8 (br, 36H, CH_3). ^{31}P NMR (162 MHz, C_6D_6): δ 66.9. IR (KBr pellet): ν_{CO} = 1968 cm^{-1}.

Preparation of $[H(OEt_2)_2][BArF_{24}]$: In a 100 mL Erlenmeyer flask fitted with a fresh septum was dissolved anhydrous $NaBArF_{24}$ (2.0145g, 2.3 mmol) in 50 mL of diethyl ether. This solution is then cooled to -78˚C and then 2.4 mL of HCl in Et_2O are added via syringe causing immediate precipitation of NaCl in the form of a fine powder. The mixture is stirred at -78˚C for 30 min, and then filtered through a chilled frit lined with celite. The volume of the solution is reduced to 5 mL and then layered with 15 mL of n-hexane forming a clathrate. Vigorous shaking induces crystallization of $[H(OEt_2)_2][BArF_{24}]$. The mother liquor is decanted and then the crystalline solid is dried giving 2.08g (90% yield) of $[H(OEt_2)_2][BArF_{24}]$, which is stored at -30˚C to prevent decomposition. ^1H NMR (400 MHz, CD_2Cl_2): δ 7.72 (s, 8H, *o*-CH $BArF_{24}$), 7.57 (s, 8H, *p*-CH $BArF_{24}$), 3.98 (q, *J* = 7.2 Hz, 8H, CH_2 of $(Et_2O)H^+$), 1.38 (t, *J* = 7.1 Hz, 12H, CH_3 of $(Et_2O)H^+$), the H^+ was not observed likely due to HD exchange with CD_2Cl_2.

Synthesis of $[Cu(1,5\text{-}COD)_2][BArF_{24}]$: A mixture of $[CuMes]_5$ (100mg, 0.547mmol) and dried 1,5-cyclooctadiene (167µL, 1.3675 mmol) are stirred in Et_2O (10mL) and subsequently cooled to -78˚C. To this mixture is added 554.2 mg of $[H(OEt_2)_2][BArF_{24}]$ (0.547 mmol) in 2 mL of Et_2O, and the solution is then stirred at room temperature for 4 hours to give a translucent solution with a small amount of yellow precipitate (likely trace

[(1,5-COD)CuCl]$_2$). The volume is reduced to 4-5 mL, and then the solution filtered and layered with 10 mL n-hexane inducing the formation of a clathrate. Shaking the mixture results in crystallization of the title compound as a bright white crystalline solid. The solid is isolated by decanting the mother liquor, and then washed with n-hexane and dried to afford 527 mg (84% yield) of [Cu(1,5-COD)$_2$][BArF$_{24}$]. The ^{1}H NMR of this material are identical to those the reported on [Cu(1,5-COD)$_2$][OTf] and [Cu(1,5-COD)$_2$][Tf$_2$N]. ^{1}H NMR (400 MHz, THF-d_8): δ 7.79 (s, 8H, *o*-CH BArF$_{24}$), 7.58 (s, 4H, *p*-CH BArF$_{24}$), 5.69 (s, 8H, *CH*-CH$_2$), 2.38 (s, 16H, CH-*CH$_2$*). ^{19}F NMR (376 MHz, THF-d_8): δ -63.4 (s, 24F).

Synthesis of 1-Cu and 2-Cu: These species are synthesized via an identical procedure; thus, it is only shown explicitly for M = Al. To a stirred solution of LAl (100mg, 0.142 mmol) in THF (4mL) is added a solution of [Cu(COD)$_2$]BArF$_{24}$ (162mg 0.142mmol, 2mL THF). This immediately gives rise to a bright yellow solution. The mixture is stirred for 3 hours at room temperature and the volatiles are removed in vacuo. The mixture is triturated with 1:1: Et$_2$O:C$_6$H$_6$ to yield a yellow powder. The mixture is washed with 6 mL of pentane and dried to give 210 mg (90%) of [CuAlL][BArF$_{24}$]. The yield for M = Ga is similar at 94%.

M = Al ^{1}H NMR (400 MHz, THF-d_8): δ 7.76 (s, 8H, *o*-CH BArF$_{24}$), 7.59 (d, *J* = 7.8 Hz, 3H, ArH), 7.54 (s, 9H, *p*-CH BArF$_{24}$), 7.07 (t, *J* = 7.7 Hz, 3H, ArH), 6.72 – 6.51 (m, 6H, ArH overlapping), 3.50 (s, 6H, CH$_2$), 2.54 (s, 6H, *CH*Me$_2$), 1.40 – 1.16 (br, 36H, CH*Me$_2$*). ^{31}P NMR (162 MHz, THF-d_8): δ 17.30 (s, 3P).

M = Ga ^{1}H NMR (400 MHz, THF-d_8, δ): 7.79 (s, 8H, *o*-CH $BArF_{24}$), 7.66 (d, J = 7.9 Hz, 3H, AH), 7.57 (s, 4H, *p*-CH BF_4), 7.09 (t, J = 7.8 Hz, 3H, ArH), 6.66 – 6.59 (m, 6H, ArH overlapping), 3.67 (s, 6H, CH_2), 2.60 (s, 6H, *CH*Me_2), 1.42-1.22 (br, 36H, CH*Me*$_2$). ^{31}P NMR (162 MHz, THF-d_8): δ 22.98 (s, 3P).

Synthesis of 1-Cu^{red} and 2-Cu^{red}: These species were synthesized via a common procedure and thus is only shown explicitly for 2-Cu^{red}. A solution of LGa in THF (100.8mg, 0.135mmol, 15mL) is added dropwise to a stirred slurry of CuBr in THF (19.3mg, 0.135mmol, 2mL) giving rise to a pale-yellow solution. KC_8 (17.5mg, 0.129 mmol) is then added as a solid and the solution becomes dark red. The solution is stirred for one hour, filtered, and then reduced to dryness in vacuum. Trituration with benzene (3mL) affords 68 mg (65% yield) of a red flakey solid. [2-Cu]$BArF_{24}$ may be substituted with similar results, and the yield with 1-Cu^{red} is similar. Neither **1-Cu^{red}** nor **2-Cu^{red}** appear to exhibit any resolvable paramagnetically shifted ^{1}H NMR resonances and are thus characterized by EPR. X-ray quality crystals were grown from concentrated toluene (**2-Cu^{red}**) or diethyl ether solutions (**1-Cu^{red}**).

Synthesis of [Fc][BFI]: To a solution of 122.8 mg of Li[BFI] (0.112 mmol) in 10mL DCM is added 30.5 mg of [Fc][BF_4] (0.112 mmol). Stirring overnight gives rise to a colorless precipitate ($LiBF_4$) and a deep blue solution. The solution is dried in vacuo, and then extracted into a minimal amount of THF, and again reduced in vacuo before 4mL of toluene are added. Removal of the solvent yields 119 mg (84% yield) of a microcrystalline blue powder that is free of residual dichloromethane. ^{1}H NMR (400 MHz, THF-d_8): δ 32.88

(s, 10H), 7.59 (s, 1H), 6.96 (s, 2H). ^{19}F NMR (376 MHz, THF-d_8): δ -133.2 (d, J = 21 Hz), -161.7 (t, J = 20 Hz), -167.0 (t, J = 19 Hz).

Synthesis of [1-Ni^{ox}][BFI] A solution of **1-Ni** in THF (6 mg, 11.7μmol, 2mL) is treated with [Fc][BFI] (10mg, 7.8 μmol). There is an immediate color change to bright green/yellow. Removal of the volatiles and washing with n-hexane affords ca. 10mg of the title complex. X-ray quality crystals can be grown from layering PhF with pentane. The EPR and NMR spectroscopy of this complex are consistent with the formation of a S =1/2 species. ^{1}H NMR (400 MHz, THF-d_8): δ 102.03, 83.42, 15.66, 9.86, 8.34, 7.61, 7.47, 6.83, 6.63, -0.94, -4.55. ^{19}F NMR (376 MHz, THF-d_8): δ -132.9 (d, J = 22 Hz), -161.4 (t, J = 20 Hz), -166.6 (t, J = 20Hz).

X-ray crystallographic and structure refinement details.

Crystalline specimens of the listed complexes were placed onto the tip of MiTeGen Dual-Thickness MicroLoop™ and then mounted on a Bruker Photon II CPAD diffractometer for data collection at the desired temperature (100-123K). The data collections were carried out using Mo Kα radiation (graphite monochromator). The data intensity was corrected for absorption and decay (SADABS).[74] Final cell constants were obtained from least-squares fits of all measured reflections. The structure was solved using SHELXT-16 and refined using SHELXL-16[75-76], which were executed from the SHELXLE graphical user interface.[77] A direct-methods solution was calculated which provided most non-hydrogen atoms from the E-map. Full- matrix least-squares/difference

Fourier cycles were performed to locate the remaining non-hydrogen atoms. All non-hydrogen atoms were refined with anisotropic displacement parameters. Hydrogen atoms were placed in ideal positions and refined as riding atoms with relative isotropic displacement parameters. The collection performed for **3-Ni(CO)** revealed a small component of inversion twinning and thus a BASF refinement was utilized to achieve a satisfactory model (final BASF = 0.17451). The Platon squeeze function was used to remove disordered solvent molecules from [Li(12-crown-4)(DME)]**2-Ni^{red}** (1,2-dimethoxyethane) and **3-Ni(CO)** (hexane).[78]

Table 4.6: Crystallographic Details for Complexes **1-Ni^{red}**

Parameter	**[K(crypt-222)][NiAlL]**	**2-Ni^{red}**
chemical formula	$[C_{18}H_{36}KN_2O_6][C_{39}H_{60}AlN_4NiP_3]\bullet C_6H_{14}$	2 $(C_{39}H_{60}GaN_4NiP_3)$ • $2(C_{12}H_{26}LiO_6)$ • $0.5(C_4H_{10}O_2)$
formula weight	1265.25	1566.71
crystal System	orthorhombic	monoclinic
space group	$Pna2_1$	$P2_1/c$
a(Å)	23.573(3)	25.5653(12)
b(Å)	13.5810(17)	23.4957(11)
c(Å)	24.698(3)	22.6159(10)
α (deg)	90	90
β (deg)	90	112.467(2)
γ (deg)	90	90
V ($Å^3$)	7907.1(17)	12553.7(10)
Z	4	8, Z' = 2
λ (Å), μ (mm^{-1})	0.71073, 0.410	0.71073, 0.850
T(K)	100	100(2)
θ	2.288 to 27.526	2.133 to 27.541
reflections collected	200932	245124
unique reflections	18216	28926
data/restraint/parameters	18216/1/728	28926/0/1245
R_1, wR_2 ($I > 2\sigma(I)$)	0.0396, 0.1034	0.0648, 0.1727

Table 4.7: Crystallographic Details for Complexes **2-Ni^{red}** and **1-Ni(CO)** to **3-Ni(CO)**

Parameter	**1-Ni(CO)**	**2-Ni(CO)**	**3-Ni(CO)**
chemical formula	$C_{40}H_{60}AlN_4NiOP_3 \bullet C_6H_{14}$	$C_{40}H_{60}GaN_4NiOP_3 \bullet C_6H_{14}$	$C_{40}H_{60}InN_4NiOP_3$
formula weight	877.69	906.40	879.37
crystal system	monoclinic	monoclinic	monoclinic
space group	$P2_1/c$	$P2_1/c$	$P2_1$
a (Å)	11.8725(5)	11.7707(8)	11.7281(5)
b (Å)	15.9978(6)	15.9707(11)	16.1472(7)
c (Å)	24.2895(9)	24.2154(17)	11.9776(5)
α (deg)	90	90	90
β (deg)	101.3350(10)	101.136(2)	103.4390(10)
γ (deg)	90	90	90
V (Å^3)	4523.4(3)	4466.5(5)	2206.16(16)
Z	4	4	2
D_{calcd} (g cm^{-3})	1.289	1.348	1.325
λ (Å), μ (mm^{-1})	0.71073, 0.594	0.71073, 1.171	0.71073, 5.986
T (K)	100(2)	103(2)	123(2)
θ range (deg)	2.450 to 30.534	2.176 to 30.545	1.896 to 36.115
reflections collected	13818	96446	23188
unique reflections	11284	13664	7625
data/restraints/parameters	11284/0/520	13664/0/517	7625/1/464
R_1, wR_2 ($I > 2\sigma(I)$)	0.0541, 0.1521	0.0376, 0.0869	0.0455, 0.1265

Table 4.8: Crystallographic Details for Complexes **1/2-Cu^{red} and 1-Ni^{ox}**

Parameter	**1-Cu^{red}**	**2-Cu^{red}**	**1-Ni^{ox}**
chemical formula	$C_{41}H_6AlCuN_4O_{0.5}P_3$	$C_{42.5}H_{63.5}CuGaN_4P_3$	$C_{78}H_{63}AlB_2F_{30}N_6NiP_3$
formula weight	805.40	856.64	1854.56
crystal system	triclinic	triclinic	monoclinic
space group	P-1	P-1	$P2_1/c$
a (Å)	11.2148(7)	11.344(4)	18.8421(9)
b (Å)	14.0921(10)	14.194(4)	15.1154(8)
c (Å)	14.3396(9)	14.285(5)	32.0750(16)
α (deg)	70.906(2)	70.274(17)	90
β (deg)	82.680(2)	79.551(17)	90.747(2)
γ (deg)	80.584(2)	82.067(14)	90
V (Å^3)	2106.0(2)	2122.0(12)	9134.4(8)
Z	2	2	4
D_{calcd} (g cm^{-3})	1.270	1.341	1.349
λ (Å), μ (mm^{-1})	0.71073, 0.688	0.71073, 1.283	0.71073, 0.378
T (K)	100(2)	100(2)	100(2)
θ range (deg)	2.247 to 33.194	2.294 to 36.427	2.136 to 28.719
reflections collected	36969	57673	223465
unique reflections	15940	20377	23642
data/restraints/ parameters	15940/3/492	20377/0/483	23642/0/1102
R_1, wR_2 ($I > 2\sigma(I)$)	0.0336, 0.0867	0.0330, 0.0867	0.0410, 0.1351

Special details concerning the data collection of 1-Ni^{red}: Crystals of **1-Ni^{red}** were grown from DME/hexane at –30˚C. Multiple crystalline samples showed varying extents of twinning, which were discovered via poor unit cell indexing and subsequently via CELL_NOW. The sample collected was refined using a BASF TWIN refinement and inversion twin law {-1 0 0; 0 -1 0; 0 0 -1}. The final solution was allowed to freely refine and provided a BASF value of 0.03540 corresponding to a minor component of inversion twinning. In addition, substantial disorder of two DME (1,2-dimethoxyethane) molecules were also present, and these were omitted from the final solution utilizing the PLATON Squeeze function.

Geometry Optimizations The geometries of the $[NiML]^-$ anions for M = Al and Ga were fully optimized in the gas phase using Gaussian 09 software[79] and the M06-L local functional[80] with def2-series basis sets, where def2-TZVPP basis set was used for Ni, Al, and Ga; def2-TZVP basis set was used for N and P; and def2-SVP basis set was used for C and H atoms.[81] Vibrational frequency calculations were performed to confirm the stationary point nature of the structures.

Electron Paramagnetic Resonance Calculations We computed EPR parameters (g-tensors) and hyperfine coupling constants (A-tensors) where the spin-orbit relativistic effects were included via ZORA (zeroth-order regular approximation) formalism in conjunction with all-electron basis sets in the TZ2P library.[82] The calculations were performed using the generalized gradient approximation (GGA) with the Perdew-Burke-

Ernzerhof (PBE) exchange correlation functional implemented in the Amsterdam Density Functional (ADF 2017) program.[32, 83] The choice of PBE/TZ2P method is based on the its good performance of EPR parameter computing on iron (Fe) dinuclear metalloradicals compounds.[65] The element Ga has two abundant isotopes, ^{69}Ga and ^{71}Ga. EPR computations only gives the A-tensor of ^{69}Ga and multiply this value by a factor of 1.2706 gives the A-tensor of ^{71}Ga. This factor is calculated as below.

$$factor = \frac{A(^{71}Ga)}{A(^{69}Ga)} = \frac{\mu(^{71}Ga)/I(^{71}Ga)}{\mu(^{69}Ga)/I(^{69}Ga)} = \frac{2.56227/_{1.5}}{2.01659/_{1.5}} = 1.27060$$

where μ, the nuclear magnetic moment, is +2.01659(5) nm and +2.56227(2) nm for ^{69}Ga and ^{71}Ga, respectively, and I, the nuclear spin, is 3/2 for both isotopes.

TD-DFT calculations with solvent considerations (SMD[84], THF) were performed on the M06-L optimized structure to obtain the absorption spectra of the NiML^{-} compounds. The M06-D3[80] hybrid functional with D3 dispersion correction with 6-311G(d,p) basis sets were used for all atoms.[85] Gaussian 09 software was used. To be noted, the SOMO (singly occupied molecular orbital) of **1-Ni^{red}** anion compound is essentially the same as the LUMO (lowest unoccupied molecular orbital) of **1-Ni** neutral compound. Since **1-Ni^{red}** is an open-shell compound, the excitation of alpha-spin electrons and of beta-spin electrons are separated.

Complete Active Space Self Consistent Filed Calculation (CASSCF[30]) calculations with 11 electrons in 12 orbitals were performed on the M06-L/DEF2-optimized structures of **1-Ni^{red}** and **2-Ni^{red}** using the MOLCAS-8.1[86] package with relativistic basis sets of atomic

natural orbitals types; that is, ANO-RCC-VDZ were used for N, P, C, and H atoms and ANO-RCC-VTZP[87] were used for Ni and Ga atoms.

Table 4.9: Bond metric comparisons for DFT(M06-L)-optimized structures of {NiM}$^{10/11}$

	NiAlL		**NiAlL$^-$**		difference (anion - neutral)	
Å	expt.	M06-L	expt.	M06-L	expt.	M06-L
Ni-Al	2.450(1)	2.488	2.389(1)	2.404	-0.061	-0.084
Ni-P	2.204(1)	2.194	2.136(1)	2.148	-0.068	-0.046
M-N_{eq}	1.876(2)	1.878	1.904(3)	1.916	0.028	0.038
M-N_{apical}	2.099(2)	2.100	2.257(3)	2.241	0.158	0.141
Ni to P_3-plane	0.13	0.13	0.11	0.14	-0.020	0.010
M to N_3-plane	0.26	0.23	0.39	0.38	0.130	0.153
∑(∠ P–Ni–P)	359.0(1)	359	359.25(7)	359	0	0
∑(∠N_{eq}-M-N_{eq})	354.5(2)	356	347.7(2)	348	-7	-7
∠ P-Ni-M-N_{eq}	19.94(6)	19	15.9(1)	16	-4	-3

	NiGaL		**NiGaL$^-$**		difference (anion - neutral)	
Å	expt.	M06-L	expt.	M06-L	expt.	M06-L
Ni-Ga	**2.379(1)**	**2.431**	2.340(6)	**2.353**	-0.039	-0.077
Ni-P	2.210(1)	2.211	2.155(1)	2.170	-0.055	-0.040
M-N_{eq}	1.954(2)	1.952	1.969(1)	1.996	0.015	0.044
M-N_{apical}	2.216(3)	2.217	2.423(1)	2.381	0.207	0.164
Ni to P_3-plane	0.13	0.16	0.12	0.19	-0.01	0.028
M to N_3-plane	0.37	0.34	0.49	0.51	0.120	0.166
∑(∠P–Ni–P)	359.01(9)	358	359.1(4)	358	0	-1
∑(∠N_{eq}-M-N_{eq})	349.5(3)	351	341.9(5)	341	-8	-10
∠P-Ni-M-N_{eq}	17.2(1)	16.488	11.8	14	-5	-2

Table 4.10: Experimental/calculated EPR parameters of **1^{red}** and **2^{red}**

	NiAlL$^-$			**NiGaL$^-$**	
	Expt.	PBE/TZ2P		Expt.	PBE/TZ2P
g1	2.0668	2.0018	g1	2.023	2.0025
g2	2.0668	2.0244	g2	2.023	2.0325
g3	2.0668	2.0245	g3	2.023	2.0326
A (^{27}Al)	219.7421	236.5	A (^{69}Ga)	1050	865.8
			A (^{71}Ga)	1334.1	1100.1
A (^{31}P)	37.7141[a]	-44.611[b]	A (^{31}P)	34.60[a]	-37.332[b]

Chapter 5

Zero-valent nickel organometallics supported by Lewis acid metalloligands: synthesis, catalysis, and thermodynamics

5.1 Overview

Building on previous studies of the CO_2 hydrogenation catalyzed by a bimetallic Ni-Ga complex, this chapter seeks to elucidate the physical properties that are modulated by the presence of varying Lewis acids in the NiML motif (M = Al, Ga, In). As the binding of dihydrogen to these NiML complexes has been described elsewhere, this chapter focuses on understanding the acidity of the neutral dihydrogen complexes, (η^2-H_2)NiML, and the hydricity of their base heterolysis products, [H–NiML]$^-$. In order to do this in a systematic fashion, the remaining members of the triad are synthesized and subsequently characterized utilizing single crystal X-ray diffraction and NMR and IR spectroscopies. Hydride transfer and base heterolysis experiments reveal that while the (η^2-H_2)NiML complexes are best described as weak acids, their base heterolysis products, [H–NiML]$^-$, are amongst the strongest hydride donors of well-studied transition metal complexes. The role of these physical properties in the catalytic CO_2 hydrogenation performance is presented and reveals the importance of balanced elementary steps in catalysis. In conjunction with previous studies related to the NiML system, a comprehensive landscape regarding the thermodynamics of the Ni-H bond is also developed.

Inspired by the ability of the NiML scaffold to stabilize anionic hydrides, an investigation of other organometallic complexes is explored. Namely, the synthesis and characterization of a unique anionic methyl complex, [Me-NiGaL]$^-$, is presented. While alkyl complexes of nickel are not uncommon, few exhibit oxidation states below Ni^I. The preliminary reactivity of this unique species towards a library of small molecules is presented and sheds light on the basicity of the [Me–Ni^0]$^-$ unit.

5.2 Introduction

Metal hydrides are key intermediates in chemical transformations that cover nearly all areas of chemical catalysis.[1-3] While the metal–hydrogen bond is topologically simple, it is well appreciated that metal hydrides can exhibit a large continuum of chemical behavior that includes protonic (H^+), hydridic (H^-), and radical ($H\bullet$) reaction motifs.[4-5] Comprehensive studies regarding the thermodynamic characterization of metal hydrides have emerged over the years and the detailed knowledge gained has resulted in catalytic improvements.[5-10] Despite the wealth of information uncovered for d^6–d^8 metal hydride systems, quantitative data regarding the acidity and hydricity of d^{10} metal centers remains underdeveloped. This is likely a direct consequence of the relative instability of these reactive species with respect to decomposition and oligomerization (most commonly encountered for Cu, Ag, and Au).[11] It stands to reason that the development of a detailed relationship of the thermodynamic parameters of such species may aid in the rational design of catalytic systems in which these species function as reactive intermediates. Such studies should have widespread utility, considering the prevalence of group 11 metal hydrides to mediate organic transformations.[12-17]

We have previously reported that the neutral Ni^0 complex NiGaL, **2**, is a more efficient catalyst for the hydrogenation of CO_2 than any other nickel complex reported to date.[18-19] The efficiency of this catalyst is attributed to the potent hydricity of the d^{10}-Ni^0, anionic hydride, $[HNiGaL]^-$ [**2–H**]$^-$, which forms during catalysis. Having shown that the transannular M–Ni interaction is a vital tool to modulate the electronic structure of Ni (possibly via an *inverse–trans* influence[20]), we were intrigued to examine what effects the identify of this Lewis–acidic residue imparts to the Ni–H bond. In this body of work, we

report the synthesis and characterization of two anionic d^{10} nickel hydrides and detailed thermodynamic measurements pertaining to their M–H bonds. Ultimately, these values can be used to rationalize the activity of these species for the catalytic hydrogenation of CO_2 to formate under ambient conditions.

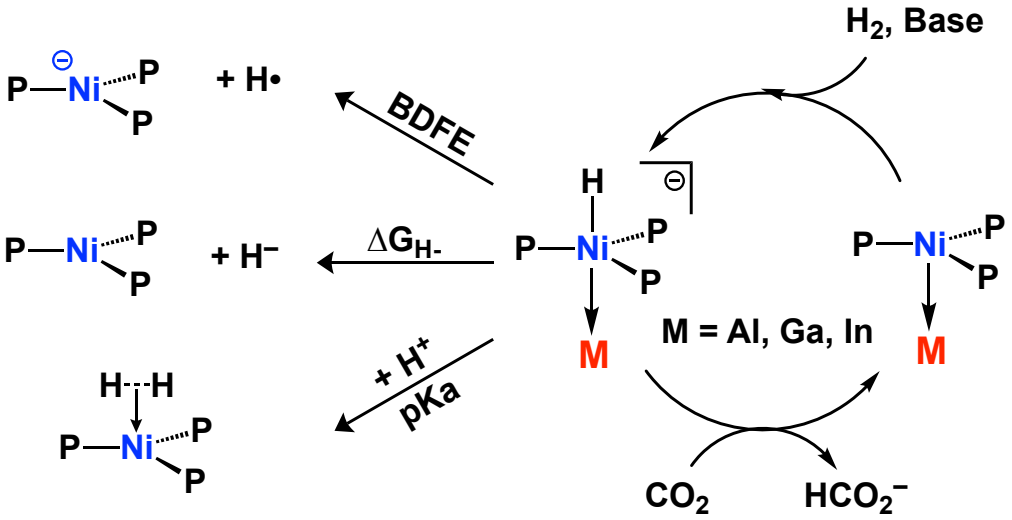

Figure 5.1: The differential modes of reactivity exhibited by synthesized anionic hydrides

5.3 Results and Discussion

5.3.1 Catalytic CO_2 Hydrogenation

Building on initial studies of the CO_2 hydrogenation catalyzed by **2**, we sought to examine the differences engendered by modulating the identity of the supporting metal ion in the NiML scaffold.[19] To this end, the catalytic hydrogenation of CO_2 was examined using **1** and **3** in the presence of the Verkade's superbase (Vkd) under 1 atm of 50:50 H_2:CO_2. Complexes **1–3** each act as catalysts towards the reduction of CO_2 to produce formate, but with varying efficiencies. The catalytic reaction studied is shown in Figure 5.2.[21]

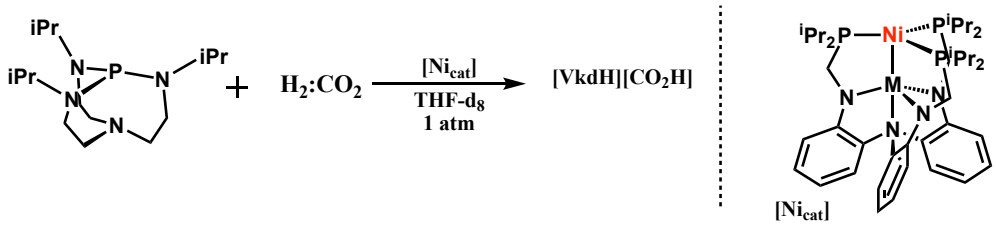

Figure 5.3: Catalytic hydrogenation reaction studied for comparison of supporting metals

For direct comparison, we utilized relatively high catalyst loading ($[Ni_{tot}]$ = 8 mM) in the presence of a large excess of Verkade's base (800 mM, pK_a = 33.6), allowing for a maximum theoretical turnover number of 100 equivalents of formate.[22-23] As Figure 5.3 shows, the initial turnover frequency is dependent on the identity of M, being the highest for Ga (25 hr^{-1}), followed by In (7.9 hr^{-1}), and finally Al (4.9 hr^{-1}). Notably, these turnover frequencies still outperform many other nickel complexes for the hydrogenation of CO_2 to formate.[24-28]

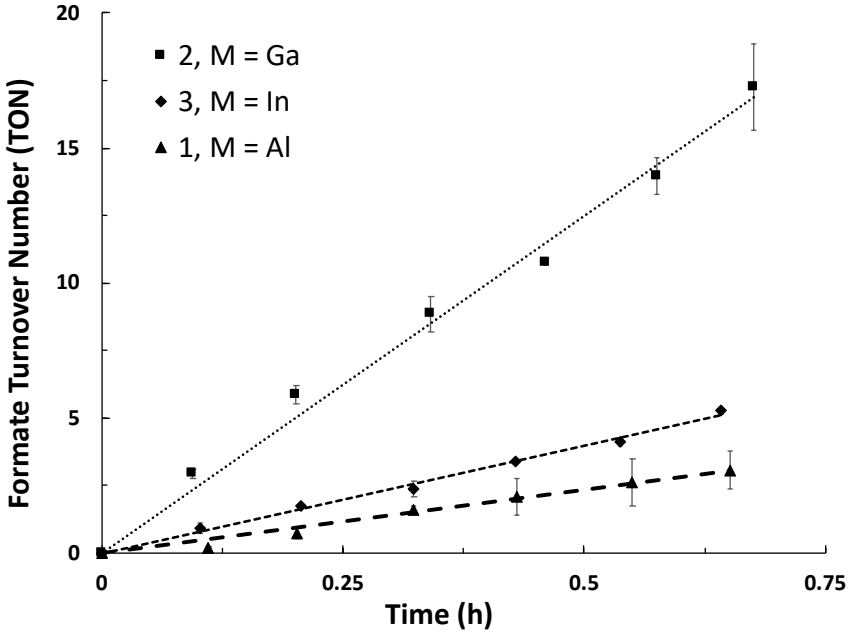

Figure 5.2: Plot showing the initial turnover frequencies for formate production utilizing complexes **1–3.** Conditions: THF–d_8 (0.5 mL), 1 atm H_2:CO_2, $[Ni]_{tot}$ = 8 mM, [Vkd] = 800 mM.

The ability of each of these species to mediate the hydrogenation of CO_2 to formate is reflected in the overall turnover number (TON), shown in Table 5.1. Complex **2** nearly reaches completion with an overall TON of 90 ± 4. This value is closely matched with complex **3**, yielding 87% of the theoretical production of formate. In contrast, **1** does not perform as well as either **2** or **3**, yielding a modest 43% of the theoretical yield of formate in the form of [VkdH][CO_2H].

Table 5.1: Catalytic performance of **1–3** for CO_2 hydrogenation

Catalyst	Initial TOF (h^{-1})	Max TON	% Yield Formate
NiGaL, **2**	25 (± 1)	90 (±4)	90 (±4)
NiInL, **3**	7.9 (± 0.3)	87 (±1)	87 (±1)
NiAlL, **1**	4.9 (± 0.6)	43 (±5)	43 (± 1)

Catalytic reaction performed in THF–d_8 (8 mM Ni, 800 mM Vkd) under 50:50 CO_2:H_2 in a J. Young NMR tube. TON defined as equivalent of formate per that of catalyst. TOF is the linear slope of the early timepoints of the plot of TON vs. time.

To understand the difference in catalytic competency between **1-3** towards CO_2 hydrogenation we sought to independently examine each of the elementary steps in the proposed mechanism (shown for M = Ga in Fig. 5.4) to rationally design new catalysts.

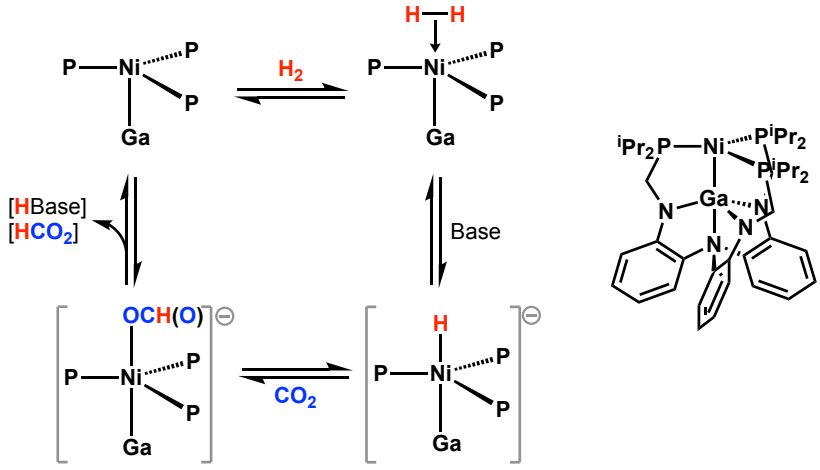

Figure 5.4: Proposed mechanism by which **2** mediates the hydrogenation of CO_2. Adapted from reference 19.

The first step, H_2 binding, has been independently examined by Dr. Ryan C. Cammarota. Importantly, the ability of complexes **1–3** to bind dihydrogen is substantially different across the series with values of $\Delta G^{\circ}_{H_2}$ of 1.6(2), 0.6(2), and –3.0(7) kcal mol^{-1}, respectively.[21] To further elucidate the differences between **1-3**, we sought also determine the impact of the supporting metal on the acidity (pK_a) and hydricity ($\Delta G^{\circ}_{H^-}$) of the dihydrogen complexes, (η^2–H_2)NiML, and anionic hydrides $[HNiML]^-$, respectively.

5.3.2 Synthesis of anionic hydrides M = Al, In

To understand the role of the supporting metalloligand in catalysis, we first wished to examine if Lewis acids other than M = Ga could support the highly reducing nature of the anionic hydride motif found in [**2–H**]$^-$. Using identical conditions reported for the synthesis of [PPN][**2–H**], we were able to complete the trio of isoelectronic anionic hydrides wherein the nickel center is supported by either Al or In.

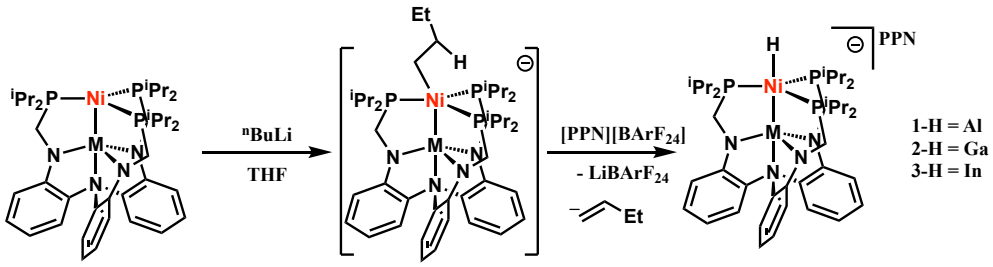

Figure 5.5: Synthesis of anionic hydrides [**1–H**]$^-$ to [**3–H**]$^-$.

Presumably, the formation of the terminally bound hydrides results from the ß–hydride elimination of a putative 18e$^-$ σ–butyl complex.[29] The addition of one equivalent of ^{n}BuLi to stirred THF solutions of **1-3** at –78˚C produced a drastic color change from brown (**1**) or purple (**3**) to light orange. Subsequent metathesis and precipitation in diethyl ether utilizing [PPN][$BArF_{24}$] yields soluble $LiBArF_{24}$ and insoluble salts [PPN][**1–H**] and

[PPN][**3–H**] in 25% and 75% respective yields. The low yield of [PPN][**1–H**] is attributed to its very hydridic nature, and a propensity to decompose to **1** over time (*vide infra*). Like the parent compound [PPN][**2–H**], the ^{1}H and ^{31}P NMR of both [PPN][**1–H**] and [PPN][**3–H**] are diagnostic of an apically bound terminal hydride.[19] This is most apparent in the case of [PPN][**1–H**], where a broad doublet ^{31}P resonance at 63.8 ppm ($^{2}J_{PH}$ = 33 Hz) collapses into a singlet upon selective ^{1}H decoupling. Likewise, the ^{1}H NMR spectrum of [PPN][**1–H**] shows a characteristic ^{1}H NMR resonance at -5.3 ppm that is resolved as a quartet resonance featuring a $^{2}J_{PH}$ = 35.1 Hz. It is worth noting that one may expect larger coupling values in the event that the H^{-} and phosphine ligands were coplanar, as is observed for the square planar species HRhAlL ($^{2}J_{PH}$ = 107 Hz for *trans* P).[30] The NMR data on the

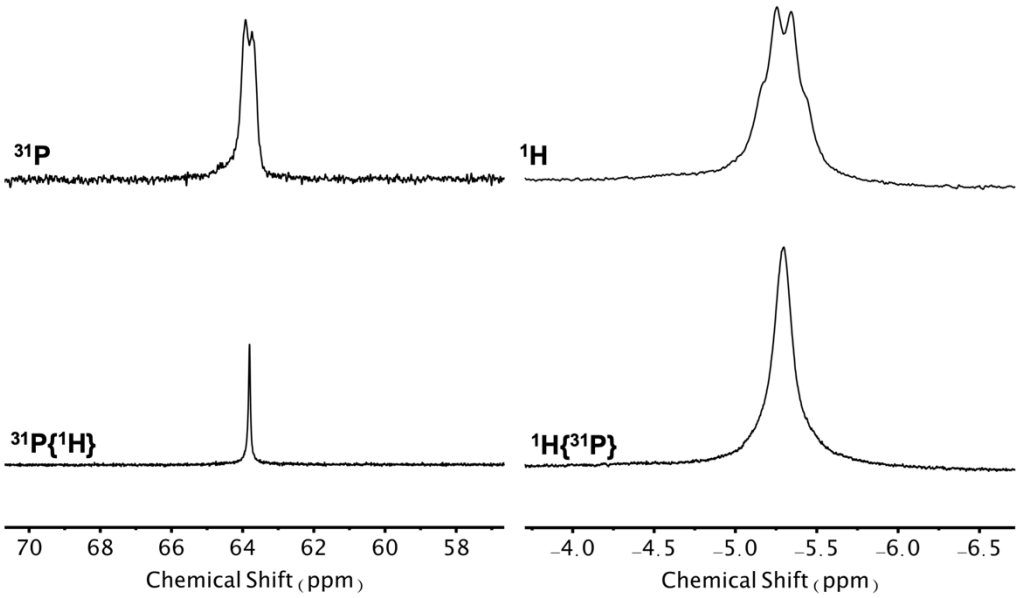

Figure 5.6: Selected NMR spectra insets for [PPN][**1–H**] showing both ^{31}P and ^{1}H frequencies.

analogous indium species, [PPN][**3–H**] are similar to those found for both the Al and Ga congeners, with the exception that the ^{1}H–^{31}P couplings are not resolved. There is however a ^{31}P resonance at 82.5 ppm in addition to a ^{1}H resonance near –6.2 ppm.

The IR spectra of the anionic hydrides, $[H–NiML]^–$, reveal that the M–H stretching frequency is very strongly perturbed by the identity of M. The M–H stretching frequency for the series continually decreases from 1714 $cm^{–1}$ to 1696 $cm^{–1}$ and finally 1646 $cm^{–1}$ for M = In, Ga, and Al, respectively. Each of these stretching frequencies was confirmed by independent synthesis by either hydrogen atom exchange with 4 atm of D_2 (M = Ga, In) or by base heterolysis with D_2 and the strong base $P_4{}^tBu$ (pK_a = 42.4 MeCN, M = Al, *vide infra*). The Ni–H stretches are noteworthy as they are atypical of most Ni–H complexes, which is a consequence of their hydridic nature and low formal oxidation state. Specifically, the Ni–H stretching frequency for [PPN][**1–H**] is, to our knowledge, the lowest frequency reported for a terminal Ni–H complex.[31]

5.3.3 Structural Studies M = Al, In

Single crystals of [PPN][**1–H**] and [PPN][**3–H**] can be grown from THF/pentane mixtures and shed further light on the electronic structures of these unique species. [PPN][**1–H**] crystallizes in the space group $P2_1/c$ and the hydrogen atom can be located from the difference Fourier map (albeit the accuracy of the Ni–H bond length is suspect). The Ni–Al interaction in [PPN][**1–H**] is shorter than that of the precursor species **1** (Ni–Al = 2.450(1) Å) supporting the notion that stability of this molecule is related to stabilization of the $H^–$ charge via a 3c–4e bonding motif. This is corroborated by elongation of the N_{ap}–Al distance from 2.099(1) in **1** to 2.296(2) Å in $[\mathbf{1–H}]^–$. Furthermore, it is apparent that the electronic rich Ni center in [PPN][**1–H**] relies on stabilization via π–backbonding to the alkyl phosphine ligands, which is reflected in a decrease in the average Ni–P distances from 2.204(1) to 2.145(1) Å (ΔNi–P = 0.06 Å). Intriguingly, the $H^–$ ligand enforces a large

pyramidalization of both the Ni atom in the P_3 pocket and the Al atom in N_3 as observed in the by their respective atom to plane distances (compared to **1**).[32]

Table 5.2: Selected metrics for **1**, [**1–H**]$^-$, **3**, and [**3–H**]$^-$

Measure	**1**[32]	[PPN][**1–H**]	**3**[18]	[PPN][**3–H**]
M–Ni	2.450(1)	2.431(1)	2.457(1)	2.432(1)
R[a]	1.00	0.99	0.92	0.91
Avg. Ni–P[b]	2.204(1)	2.145(1)	2.252(1)	2.211(1)
M–N_{ap}	2.099(2)	2.296(2)	2.309(6)	2.422(3)
M–N_{eq}[b]	1.876(2)	1.913(1)	2.119(4)	2.140(2)
Ni to P_3 plane	0.13	0.20	0.38	0.28
M to N_3 plane	0.26	0.43	0.54	0.59

[a] Defined as the interatomic distance divided by the sum of the respective covalent radii. [b] Averages across each unique metric. See Table 5.9 and 5.10 for collection details and metrics.

The hydride ligand in [PPN][**1–H**] enforces a modest change in the Ni–P_3 plane distance of 0.07 Å compared to **1**. On the other hand, there is a large change when comparing the Al–N_3 plane distance between these two species (Δ = 0.17 Å). This vertical displacement for the Lewis acidic Al atom is likely the major contributing factor to the elongation of the M–N_{eq} bonds distances which elongate from an average 1.876(2) to

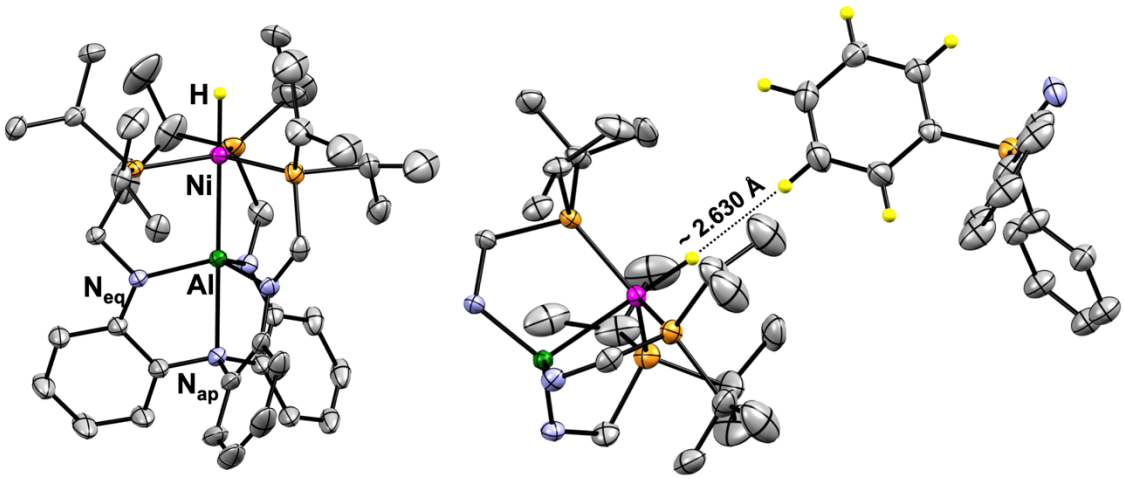

Figure 5.7: Molecular structure of [PPN][**1–H**] rendered at 50% thermal ellipsoid probability. Selected hydrogen atoms omitted for clarity.

1.913(1) Å upon installation of the hydride ligand. Noteworthy is a pronounced non–classical dihydrogen bonding interaction (e.g. H•••H) between a meta-PPN phenyl proton and the hydride ligand in [**1–H**]$^{-}$. This short contact is estimated to be ~ 2.63 Å from difference Fourier map, and may contribute to Ni–P_3 plane distance. This persistent interaction also hints at the hydridic nature of the hydride ligand in [PPN][**1–H**]**.**

Single crystals of [PPN][**3–H**] can likewise be grown from THF/hexane mixture are form in the space group $P2_1/c$, making it isomorphous to both Al and Ga congeners. The interaction between Ni and In is shortened (2.432(1)Å) when compared **3**. The observed structural changes for [PPN][**3–H**] are largely the same as observed for [PPN][**2–H**] and [PPN][**1–H**] and include the contraction in the Ni–P distances (Δ = 0.04 Å), an elongation of the N_{ap}–In (Δ = 0.11 Å) and N_{eq}–In bonds (Δ= 0.03 Å), and a deviation of In from the N_3 plane (Δ = 0.05 Å). One notable difference between the structural parameters observed of [PPN][**2–H**] and [PPN][**1–H**] is the Ni–P_3 plane distances. Upon careful

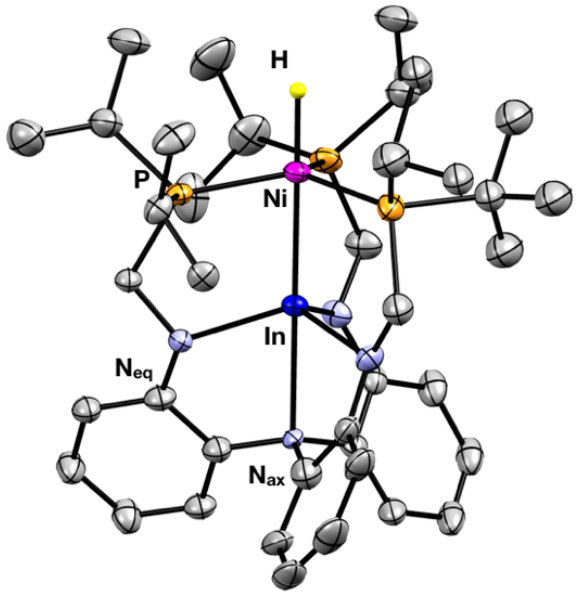

Figure 5.8: Molecular structure of [PPN][**3–H**] rendered at 50% thermal ellipsoid probability. PPN cation, selected hydrogen atoms, and solvent molecules excluded for clarity.

inspection, the Ni atom in [PPN][**3–H**] resides closer to the P_3 plane than it does in **3** (Δ = –0.1 Å). This observation is in contrast to the similar distances for [PPN][**1–H**] where the Ni atom becomes slightly more pyramidal to accommodate the additional ligand (Δ = +0.07 Å). This difference in geometry might reflect the ability of the Lewis–acidic metalloligand scaffold to effectively distribute the charge of the hydride.

5.3.4 Proton and hydride transfer experiments

To first bracket the ability of [**1–H**]$^-$ and [**3–H**]$^-$ to behave as hydride donors, we first examined the hydride transfer reaction between both **1** and **3** with [PPN][**2–H**] for which a $\Delta G^\circ_{H^-}$ = 31.3(5) kcal/mol has been measured (THF-d_8). In the case of **3**, relatively rapid hydride transfer occurred over the course of two days yielding resonances consistent with a complete transfer from [PPN][**2–H**] to **3**.[33-34] This observation suggests that the thermodynamic hydricity ($\Delta G^\circ_{H^-}$) of [PPN][**3–H**] is at least 34 kcal/mol ($\Delta\Delta G^\circ_{H^-}$ > 2.7 kcal/mol, assuming 1:10 product ratio). More intriguing is the lack of hydride transfer between [PPN][**2–H**] and **1** over the course of three weeks, suggesting $\Delta G^\circ_{H^-}$ for [**1–H**]$^-$ is less than 28.6 kcal/mol.

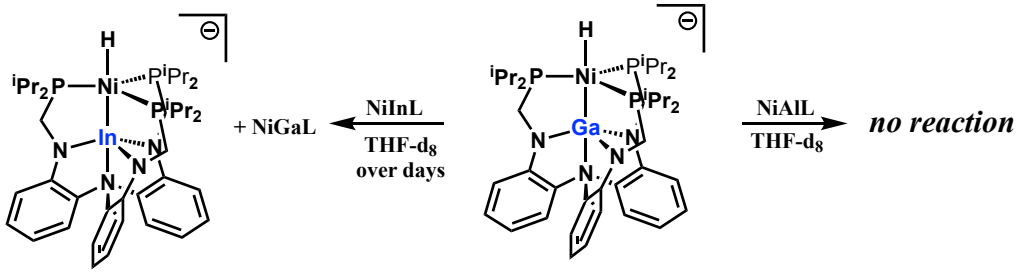

Figure 5.9: Preliminary hydride transfer reactions using [PPN][**2–H**], **1** and **3.**

To further validate the observations resulting from hydride transfer, we then sought to unambiguously determine the thermodynamic hydricity of [**1–H**]$^-$ and [**3–H**]$^-$ utilizing the base heterolysis method. It is worth noting that we are unable to utilize MeCN or PhCN

as solvents for these measurements, due to irreversible binding (M=In) and undesired reactivity (M=Al). To meaningfully compare the thermodynamic hydricity between [**1–H**]$^-$ and [**3–H**]$^-$ with those reported in the literature, we are forced to work under the limiting assumption that any of the equilibria discussed henceforth would be similar between THF and MeCN.

The addition of a small excess (5–15 equiv.) of the strong base ^{tBu}N(^{iPr}NHC^{Me}) (pK_a = 30.2 in MeCN[35]) to solution of **3** under 1 atm H_2 results in an equilibrium (K_{eq} = 0.02(1) at 1 atm H_2) with [**3–H**]$^-$. This equilibrium is stable for 1–2 weeks under ambient conditions and can conveniently be followed by both ^{31}P and ^{1}H NMR spectroscopies. Notably, the chemical shift of the Ni–H observed for [^{tBu}N(^{iPr}NHC^{Me})H][**3–H**] does not differ from isolated [PPN][**3–H**] suggesting that these ions exist as solvent–separated ion pairs. One caveat to this measurement is that the concentration of ^{tBu}N(^{iPr}NHC^{Me}) must be estimated from the amount of [**3–H**]$^-$ produced, as the free base and its conjugate acid appear to be in rapid equilibrium as judged by ^{1}H NMR spectroscopy.

From the equilibrium of **3–(H$_2$)** with ^{tBu}N(^{iPr}NHC^{Me}) we can then extract a pK_a of 31.9 ± 0.1 (est. MeCN scale).[36] This pK_a can then be used to calculate the thermodynamic hydricity of [**3–H**]$^-$ (equations 1 – 5) in combination with the free energy of H_2 binding

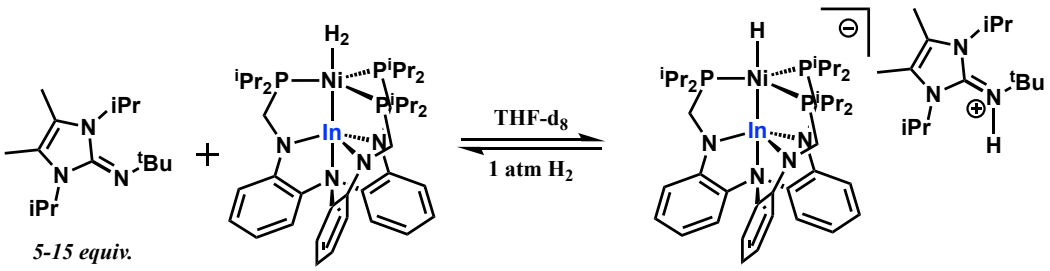

Figure 5.10: Base heterolysis reaction between ^{tBu}N(^{iPr}NHC^{Me}) and **3–(H$_2$)** provides [**3–H**]$^-$**.**

(Eq. 1, $\Delta G^{\circ}_{H_2}$ = -3.0(7) kcal/mol) and the self–heterolysis of H_2 in MeCN (Eq. 4) to calculate a hydricity of 37.5 ± 0.2 kcal/mol for [**3–H**]$^-$.[34]

Table 5.3: System of equation used to calculate thermodynamic hydricity of [PPN][**1–H**] and [PPN][**3–H**].

$M(H_2) \leftrightarrows M + H_2$	$\Delta G^{\circ}_{H_2} = -1.364\log(K_{eq})$	Eq. 1
$MH^- + H\text{–}Base^+ \leftrightarrows M(H_2) + Base$	$\Delta G^{\circ} = -1.364\log(K_{eq})$	Eq. 2
$H^+ + Base \leftrightarrows H\text{–}Base^+$	$\Delta G^{\circ} = -1.364pK_a$	Eq. 3
$H_2 \leftrightarrows H^+ + H^-$	ΔG° = 77.6 kcal/mol	Eq. 4
$MH^- \leftrightarrows M + H^-$	$\Delta G^{\circ}_{H^-}$	Eq. 5

In line with a pK_a of 31.9 ± 0.1 for **3–(H$_2$)**, the addition of Vkd (pK_a = 33.6 MeCN) to solutions of **3–(H$_2$)** in THF–d_8 results in the quantitative formation of [VkdH][**3–H**] by both ^{1}H and ^{31}P NMR spectroscopy. The use of weaker bases such as phosphazene base ^{tBu}NP(pyrr)$_3$ (pK_a = 28.4 MeCN) also produced [**3–H**]$^-$ to a measurable extent.[37] Moreover, the reaction between **3** and (dmpe)$_2$RhH ($\Delta G^{\circ}_{H^-}$ = 26.6 kcal/mol) rapidly produces NMR spectra that indicate quantitative formation of [(dmpe)$_2$Rh][**3–H**]. This observation is consistent with a large difference in thermodynamic hydricity between the donor and acceptor ($\Delta\Delta G^{\circ}_{H^-}$ = -10.9 kcal/mol).

To further characterize [**1–H**]$^-$ we turned to the hydride transfer reactions between **1** and the strong hydride donors (depe)$_2$RhH ($\Delta G^{\circ}_{H^-}$ = 28.3 kcal/mol) and (dmpe)$_2$RhH ($\Delta G^{\circ}_{H^-}$ = 26.6 kcal/mol).[34, 38] For the less hydridic rhodium hydride, (depe)$_2$RhH, no hydride transfer was observed over the course of 4 weeks suggesting that for [**1–H**]$^-$, $\Delta G^{\circ}_{H^-}$ < 28.3 kcal/mol. In line with this hypothesis solutions of **1** and (dmpe)$_2$RhH are found to exists in equilibrium. However, due to decomposition over the long equilibration periods, we were only able to measure an imprecise K_{eq} of approximately 0.2(1) which corresponds

to $\Delta G^{\circ}_{H^-}$ of 25.4 ± 1.0 kcal/mol. The observation that K_{eq} for the reaction shown in Figure 5.11 is less than 1 suggests that [**1–H**]$^-$ is a stronger hydride donor than $(dmpe)_2RhH$.

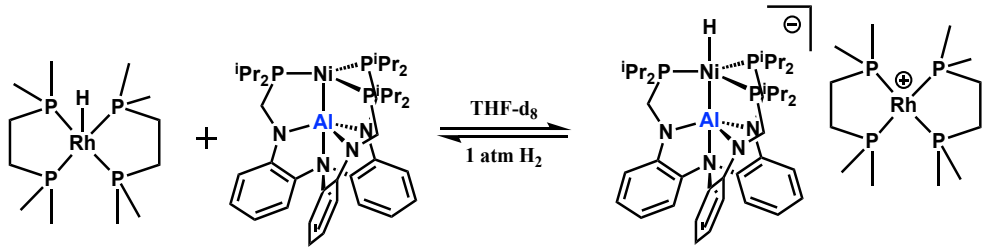

Figure 5.11: Hydride transfer between **1** and $(dmpe)_2RhH$ provides an equilibrium with [**1–H**]$^-$.

To gain more insight into the thermodynamics of the M = Al system, we then performed complimentary base heterolysis experiments to more precisely determine the hydricity of [**1–H**]$^-$. Ultimately, more exotic bases were needed to find a reliable pK_a measurement of **1–(H₂)**. We find that even a forty-fold excess of Vkd (pK_a 33.6 in MeCN) to **1** under 4 atm H_2 does not produce any amount of the desired anionic hydride, [**1–H**]$^-$. This supports the notion that the pK_a of **1–(H₂)** is greater 36 units in MeCN. Conveniently, base heterolysis utilizing **1** and N,N'–bis(imidazolyl)guanidine, $^{iPr}BIG^{NH}$, (pK_a(THF) =

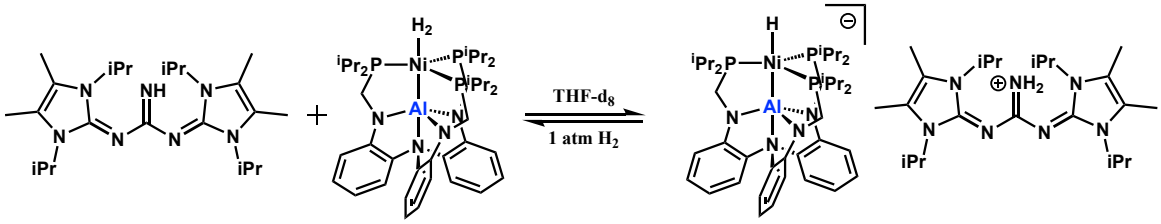

Figure 5.12: Base heterolysis with **1** and $^{iPr}BIG^{NH}$ provides an equilibrium with [**1–H**]$^-$ 27.8, pK_a(MeCN) ~ 35.8) under 1 atm H_2 results in an immediate equilibrium that is stable for approximately one week.[39] This measurement results in a more reliable pK_a value of 36.7 ± 0.1 (est. MeCN). This equilibrium is reversible, and the addition of [$P_4{}^tBuH$][**1–H**] to THF solutions of $[(dmpe)_2Rh]OTf$ generates primarily **1** and $(dmpe)_2RhH$.

Other strong bases fully deprotonate **1–(H_2)** as well; examples include $P_4{}^tBu$ (pK_a = 42.7), $^nBuNP_1(tmg)_3$ (pK_a = 38.7), and $Me_2CP(dma)_3$ (pK_a = 37.7).[36] The hydricity of [**1–H**]$^-$ can again be calculated utilizing equations 1–5, alongside the measured contributions for H_2 binding ($\Delta G^\circ_{H_2}$ = + 1.6 kcal/mol). Thus, we are able to estimate the thermodynamic hydricity of [**1–H**]$^-$ to be 26.2 ± 0.1 kcal/mol.

5.3.5 Discussion

On inspection, it is apparent that the identity of the Lewis–acid metalloligand has a pronounced effect on the thermodynamic parameters of the [Ni–H]$^-$ unit. This is most directly observable in the large span of thermodynamic hydricity measurements recorded for the [HNiML]$^-$ from 26.2(1) to 36.7(2) kcal/mol (Al to In). Prior to the report of [PPN][**2–H**] ($\Delta G^\circ_{H^-}$ = 31.3(5) kcal/mol), the strongest hydride donor of a first–row metal complex was the macrocyclic cobalt species bearing pendant amines, $Co(P_4N_2)H$ ($\Delta G^\circ_{H^-}$ = 31.8 kcal/mol).[40] The magnitude for which M modulates $\Delta G^\circ_{H^-}$ spans upwards of 10 kcal/mol, suggesting the Lewis-acid/metal interaction may be a valuable tool for catalysts optimization.[10, 27, 41-43]

The thermodynamic hydricity of [**1–H**]$^-$ is significant in that in reaches a region of hydride donor strengths only observed in photoexcited states (Cp*Ir(bpy)H$^+$) or precious metal complexes (e.g. dmpe$_2$RhH, (terpy)Ru(bpy)H$^-$).[7, 33-34] Having determined the thermodynamic hydricity the [HNiML]$^-$ family, we then wished to examine the comprehensive thermodynamic landscape of the anionic M–H bond. To determine the bond dissociation free energy (BDFE) of the Ni–H bond in complexes the [HNiML]$^-$ family, we reference a previously reported study in which we reported the reduction potentials of complexes **1–3** to yield their S = ½ paramagnetic radical anions (see Chapter 4).[44] Using this reduction event, one can then construct a thermodynamic scheme, in which the BDFE of the Ni–H bond can be directly measured by relating the reduction of **1–3**, the hydricity of the corresponding anionic hydride, and the oxidation of H$^-$ to H•. This notion is graphically captured in Figure 5.13

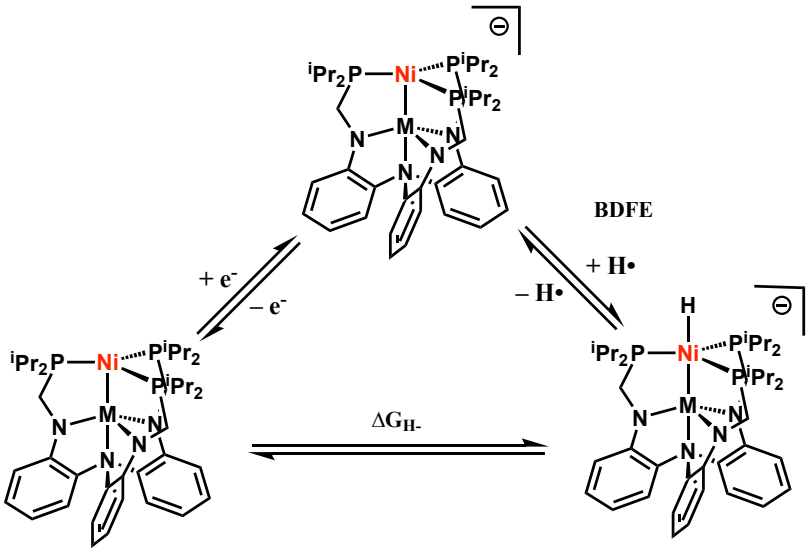

Figure 5.13: Relations of electrochemical reduction and hydricity to the bond dissociation free energy of anionic hydrides [HNiML]$^-$.

Table 5.4: Equations used to calculate the BDFE of the Ni-H bond

$[LMNiH]^- \leftrightarrows LMNi + H^-$	ΔG°_{H-}	Eq. 6
$LMNi + 1e^- \leftrightarrows [LMNi\bullet]^-$	$\Delta G^\circ = -23.06(E^\circ)$	Eq. 7
$H^- \leftrightarrows 1e^- + H\bullet$	ΔG° = -26.0 kcal/mol	Eq. 8
$MH^- \leftrightarrows M\bullet^- + H\bullet$	BDFE	Eq. 9

Interestingly, there are only minor perturbations of the Ni–H bond strengths within the $[HNiML]^-$ family (Table 5.5). The apparent scaling relationship occurs between the counteracting ΔG°_{H-} and reduction potentials (to $[LMNi]^{\bullet-}$). This is most apparent in the case of **[1–H]**$^-$, wherein the thermodynamic hydricity is remarkably low (26.2 kcal/mol), but the reduction potential needed to produce the radical anion $[NiAlL]^{\bullet-}$ is quite harsh (-2.82 V vs Fc). Conversely, [**3–H**]$^-$, the weakest hydride donor of the family of complexes, is the most easily reduced under electrochemical conditions, indicating the ability of the metalloligand scaffold is critical to stabilizing the anionic charge introduced by the hydride ligand.

Table 5.5: Comparative metrics for **1–3** and their derivatives

Species	**NiML**		**(η^2–H_2)NiML**			**[H–NiML]$^-$**		
Metal	$E_{1/2}^{(0/-)}$ V v Fc	$E_{1/2}^{(0/+)}$ V vs Fc	pK_a MeCN	$\Delta G^\circ_{H_2}$ kcal mol^{-1}	d_{HH} (Å)	ΔG°_{H-} kcal mol^{-1}	BDFE kcal mol^{-1}	ν_{NiH} cm^{-1}
Al	–2.82	–0.74	36.7(1)	1.6(2)	0.84	26.2(1)	64.9 ± 1	1646
Ga	–2.48	–0.57	33.1(2)	0.6(2)	0.86	31.3(5)	62.5 ± 1	1696
In	–2.34	–0.36	31.9(1)	–3.0(7)	0.91	37.5(2)	65.5 ± 1	1714

One question that Table 5.5 does not immediately answer is the relative order of catalytic performance (Ga > In > Al, see Table 5.1). In order to explain this, we must examine the thermodynamics of each step in the proposed catalytic cycle to gain more direct insight. The first step of the cycle, H_2 binding, has been examined and reveals a large bias in the binding affinity of H_2 by complexes **1–3**.[21] In the case of In, the H_2 binding is strong enough such that at 1 atm, nearly all of the nickel species exists as **3–(H_2)**. In the case of M = Ga, roughly half of the nickel species exists as **2–(H_2)** under 1 atm H_2. Lastly,

the binding affinity of **1** towards H_2 is even less favorable, such that roughly 3% of total nickel content in solution exists as the corresponding dihydrogen adduct, **1–(H_2)**, under 1 atm H_2. Thus, one could reasonably conclude that simply as a function of H_2 binding affinity that **1** should be the slowest catalyst, a notion that is mirrored experimentally (Fig 5.2, Table 5.1).

Once (η^2–H_2)NiML forms in solution, it must then be deprotonated by exogenous base to yield the anionic hydride, [H–NiML]$^-$. As Table 5.4 shows, the pK_a values of (η^2–H_2)NiML follow a logical trend that mirrors the extent which the species activates H_2 (as probed by d_{HH}).[45] To this end, the (η^2–H_2)NiML complexes are best regarded as weak acids, with values between 31.9(1)–36.7(1) on the acetonitrile scale.[46] Despite their modest acidity, a number of neutral bases can be used to form [**1–H**]$^-$ through [**3–H**]$^-$ [36] The pK_a values support the notion that turnover for **1** should be hindered by an acid/base mismatch which inhibits [**1–H**]$^-$ from forming in reasonable quantities. Conversely, the deprotonation of **3–(H_2)** should be more facile under the catalytic conditions employed and should not inhibit catalytic turnover as suggested by the full deprotonation of **3–(H_2)** with stoichiometric Vkd.

The next portion of the catalytic cycle, hydride transfer to CO_2, is largely determined by the differential thermodynamic hydricity of formate and the corresponding metal hydride.[7, 33, 47] For [**1–H**]$^-$ through [**3–H**]$^-$ this reaction is expected to have a thermodynamically favorable reaction energy (17.9 kcal/mol for [**1–H**]$^-$ to 7.3 kcal/mol for [**3–H**]$^-$) of transferring a hydride to formate ($\Delta G^\circ_{H^-}$ = 44 kcal/mol). However, hydricity is not the sole identifier for catalyst performance. This is most evident for the poor catalytic activity of **1**, which despite the challenge in forming [**1–H**]$^-$, would be expected to most

favorably transfer a hydride to CO_2. Indeed, the addition of CO_2 to [PPN][**1–H**]$^-$ does generate a new formate species nearly identical to previously reported [PPN][**2–CO_2H**] by NMR spectroscopy within seconds of gas mixing. However, the prohibitively high pK_a and scare amount of **1–(H_2)** prohibit catalytically competent concentrations of [**1–H**]$^-$ from forming.

When considering the role of hydricity in determining catalytic activity, it is interesting to compare the activity of **2** and **3**. Both species bind H_2 appreciably at room temperature are their respective anionic hydrides are sufficiently hydridic to produce formate with a considerable driving force. In light of the acidity of **3–(H_2)** relative to **2–(H_2)**, why then is **2** a better catalysis for the hydrogenation of CO_2 to formate when H_2 binding, deprotonation, and hydride transfer are favorable for both **2** and **3**? We suspect that formate binding may inhibit **3** from further catalytic turnover. Recent studies reported by Dr. Ryan C. Cammarota reveal an unexpected kinetic influence inherent to the In supporting metalloligand when compared to Ga. Namely, the rate of ligand substitution is approximately 2 orders of magnitude faster for M = Ga versus In (for example between [2-CO_2H] and 2-MeCN).[21] Thus, once catalytic amounts of formate are produced in solution, slow substitution reactions with [**3–CO_2H**]$^-$ may inhibit further turnover. In line with this hypothesis, the resting state identified for M = In is [**3–CO_2H**]$^-$ rather than **3–(H_2)** or [**3–H**]$^-$. Studies examining the ways in which this kinetic hinderance can be limited are ongoing.

5.4 Stabilizing organometallics groups with M = Ga

5.4.1 Stabilization of a Ni(0) methyl complex [MeNiGaL]$^-$

Given the unique ability of the Lewis acidic metalloligand scaffold to support anionic, 18e$^-$ Ni(0) fragments, we were interested to see if groups other than a hydride could be stabilized by the LGa metalloligand. To this end, we first synthesized the anionic chloride, [PPN][ClNiGaL], [**2–Cl**]$^-$, which was originally identified as an impurity between the reaction of [PPN][**2–H**] with CO_2.[19] Synthesis of this anionic chloride complex is facile and can be performed in a one-pot reaction of LGa, Ni(1,5–COD)$_2$, and [PPN]Cl in THF at room temperature. The product separates from THF after 2–3 hours as a bright orange powder in 70% yield. Performing analogous reactions with LIn lead to similar results. However, when LAl was utilized, only **1** was recovered. Although [**2–Cl**]$^-$ is only sparingly soluble in THF, the ^{1}H and ^{31}P NMR spectra are in agreement with the crystallographically determined trigonal symmetry of the complex.

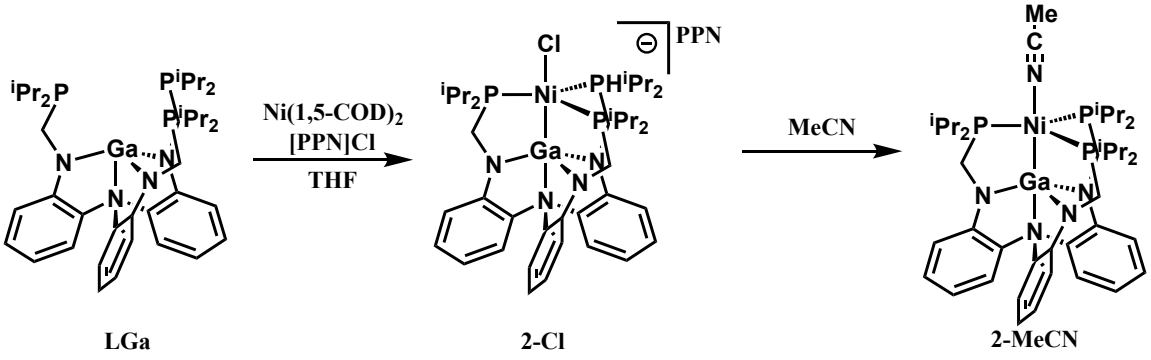

Figure 5.14: Synthesis of [PPN][**2–Cl**] and its instability in MeCN

The ^{1}H NMR spectrum of [**2–Cl**]$^{-}$ indicates a C_3 symmetric complex with the observation of the four diagnostic aromatic protons of the ligand base. This notion is strengthened by the observation of a single ^{31}P NMR resonance at 34.4 ppm in addition to those of the PPN^{+} cation at 21.0 ppm. In attempts to utilize other NMR solvents such as CD_2Cl_2 or MeCN, oxidation and substitution were observed, respectively. In the case of MeCN, dissolution of [**2–Cl**]$^{-}$ resulted in the formation of large yellow crystals of the acetonitrile complex, **2–MeCN**, which was crystallographically characterized. For comparison, the metrics of [**2–Cl**]$^{-}$ and **2–MeCN** are shown in Figure 5.15 and Table 5.6.

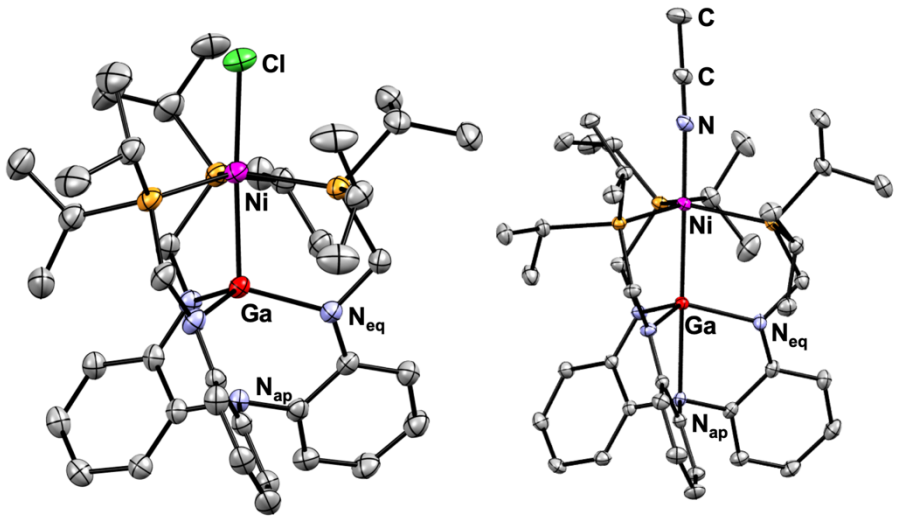

Figure 5.15: Molecular structures of [**2–Cl**]$^{-}$ and **2–MeCN** rendered at 50% probability with respective cationic fragment and recrystallization solvents omitted for clarity.

Complex [**2–Cl**]$^{-}$ crystallizes in triclinic space group P–1 without any co-crystallized solvent. The intermetallic Ni–Ga distance is quite similar to that observed in the neutral bimetallic NiGaL, **2**. This similarity is puzzling, as one might anticipate the large electronegative chloride ligand to quench the ability of nickel to act as a Lewis base towards gallium. In addition to the short Ni–Ga interaction, other metrics support the notion that the Ni–Ga bond remains intact. For example, there is a severe deformation of the

gallium atom from the N_3 plane (0.51 Å) when compared with that of the parent complex (0.37 Å). This structural change is corroborated by the Ga–N_{ap} bond distance which elongates 0.14 Å from **2** to [**2–Cl**]$^-$**.** The nickel center in [**2–Cl**]$^-$ moves to accommodate this structural change, as evidenced by the deviation of nickel–P_3 plane distances (0.32 Å) when compared to **2** (0.13 Å). The apparent pyramidalization of the nickel center is further evidenced by a large deviation from ideal trigonal symmetry, as evidenced by the sum of the P–Ni–P bond angles. This pyramidalization is likely what leads to the observed elongation of the P–Ni bonds in [**2–Cl**]$^-$ when compared to that of **2**. Intriguingly, there does not appear to be any structurally authenticated species in which a halide is bound to a formal Ni^0 center. However, spectroscopic evidence for the anionic halide complex [^{n}Bu$_4$N][XNi(CO)$_3$] (X = Cl, Br, I) exists, though these species are unstable and redistribute their ligands to form elemental Ni, ^{n}Bu$_4$NX, and Ni(CO)$_4$.[48]

Table 5.6: Selected comparative metrics for [PPN][**2–Cl**], **2–MeCN**, and **2**.

Complex	[PPN][**2-Cl**]	**2-MeCN**	**2**
Ni−M	2.376(1)	2.427(1)	2.379(1)
r[a]	0.97	0.98	0.97
Ni–P	2.246(1)	2.218(1)	2.210(1)
Ga–N_{apical}	2.359(2)	2.343(1)	2.216(3)
Ga–N_{eq}[b]	1.956(2)	1.958(3)	1.954(2)
∑P–Ni–P	344.0(1)	354.5(1)	359.0(1)
∑N–Ga–N	340.6(1)	344.4(1)	349.5(3)
Ni to P_3 plane	0.32	0.31	0.13
Ga to N_3 plane	0.51	0.45	0.37
Ni–X	2.335(9)	1.949(1)	–

[a] Defined as the interatomic distance divided by the sum of the respective covalent radii. [b] Averages across each unique metric. See Table 5.11 and 5.13 for collection details and metrics.

The lability of the chloride ligand in [**2–Cl**]$^-$ to substitution is immediately apparent when this material is dissolved in MeCN. Doing this results in solubilization of [PPN]Cl and deposition of large yellow single crystals of the acetonitrile complex, **2–MeCN**.

Complex **2–MeCN** crystallizes in monoclinic space group $P2_1/c$ alongside one MeCN solvent molecule. In comparison to [**2–Cl**]$^-$ the nickel center in **2–MeCN** is similarly pyramidal, which is evidenced by the Ni–P_3 plane distance. The MeCN–Ni bond (1.949 Å) is shorter than the variety of Ni^{II} species such as $[(MeCN)_6Ni]^{2+}$ (ca. 2.075(3)) presumably due to the presence of the three alkyl phosphine donors and the formally zero–valent nickel center.

Given that the chloride in [**2–Cl**]$^-$ is labile to substitution by modest donors such as MeCN, we then sought to examine if this material was a suitable precursor to form organometallic complexes of Ni^0. To this end, the reaction of [**2–Cl**]$^-$ with a variety of organometallic reagents was canvased. For example, the reaction of [**2–Cl**]$^-$ with $KHBEt_3$ leads rapidly (and near quantitatively) to [PPN][**2–H**] on comparison with the reported spectroscopic data. Generating a more insoluble halide byproduct (KCl vs. LiCl in original synthesis) leads to a purer [PPN][**2–H**]. For example, solutions of [PPN][**2–H**] do not show traces of [**2–Cl**]$^-$ when exposed to CO_2 (e.g. to generate [**2–CO_2H**]$^-$).

The reaction of [PPN][**2–Cl**] with a variety of carbanionic reagents was subsequently explored with hopes of producing a family of Ni^0 organometallics species. So far, only the addition of MeMgCl/MeMgBr and MeLi produced tractable mixtures. On the other hand, reactions of PhMgBr, BnMgBr, $TMSCH_2Li$, and $^tBuCH_2Li$ produced solutions containing predominantly **2** as the only tractable product. It is probable that the

sterically encumbering isopropyl groups of the phosphine ligand promote dissociation of the organic fragment after metathesis.

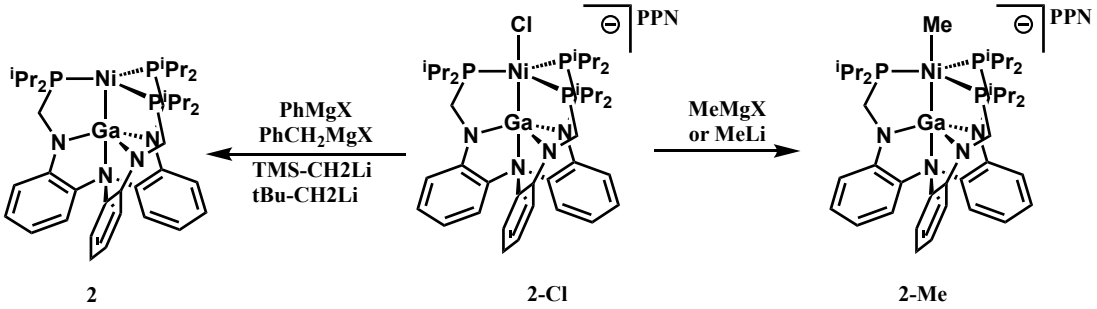

Figure 5.16: Metathesis reaction of [**2–Cl**]$^-$ with various carbon nucleophiles

The reaction of [**2–Cl**]$^-$ with either MeMgX or MeLi leads to a new species assigned as the Ni^0 methyl complex [**2–Me**]$^-$. This methyl complex exhibits a sharp ^{31}P NMR resonance at 44.1 ppm in addition to the PPN$^+$ resonance at 21.0 ppm. The ^{1}H NMR spectrum of [**2–Me**]$^-$ shows an upfield resonance at –0.56 ppm that is observed as a quartet with $^2J_{HP}$ = 8.5 Hz (THF-d$_8$). When the signal is decoupled from the ^{31}P nuclei, this resonance collapses into a singlet. Single crystals of [**2–Me**]$^-$ can be grown from diffusion of diethyl ether into concentrated THF solutions. Figure 5.17 and Table 5.7 detail the metrics of the structure.

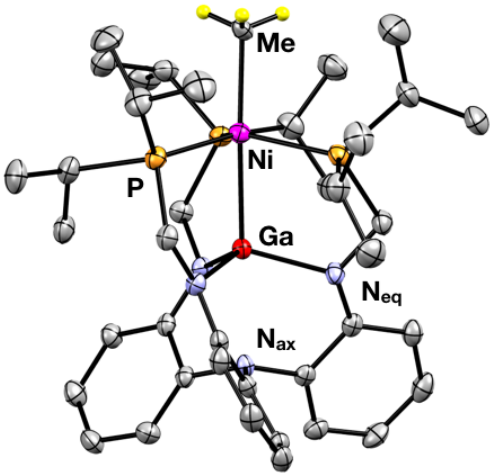

Figure 5.17: Molecular structure of [PPN][**2–Me**] rendered at 50% probability. The PPN$^+$ cation and selected hydrogen atoms are excluded for clarity.

Crystals of [PPN][**2–Me**] crystallize in the triclinic space group P–1 with a single anion/cation pair per unit cell. Initial inspection reveals the Ni–Ga distance is shorter than the sum of the respective covalent radii, and a long Ni–Me bond distance of 2.110(2) Å. There are limited examples of Ni^0 methyl complexes in the literature, but two prominent examples allow for a comparison of the Ni–Me bond metrics. For example, the reactive zero–valent nickel olefin complex, $Ni(C_2H_4)_3$, reacts with methyllithium to form the bridging organometallic species $(C_2H_4)_2Ni(\mu–Me)Li(PMDTA)$ (where PMTDA is N,N,N',N'',N''–pentamethyl–diethylenetriamine) which features a Ni–Me bond distance of 2.012(5)Å and a short Ni–Li interaction of 2.722(8) Å.[49-50] Worth noting is that the related complex, $(CDT)Ni^0$ (CDT is all–*trans*–1,5,9–cyclododecatriene*)* has been shown by ^1H and ^{13}C NMR spectroscopy to interact similarly with methyl lithium yielding a terminal methyl complex. Related is the Ni^{II} complex reported by Milstein *et al.* which is supported by a doubly deprotonated pyridine-diphosphine pincer platform, $[Li(DME)_3][(PNP^{IPr}**)NiMe]$.[51] This species features a square planar nickel center and a Ni–Me distance of 1.954(2) Å. Collectively, the Ni–Me bond in [**2–Me**]$^-$ more strongly resembles that of $(C_2H_4)_2Ni(\mu–Me)Li(PMDTA)$ supporting the assignment that [**2–Me**]$^-$ is indeed Ni^0 species with a methyl ligand.

Comparison of the metrics of [**2–Me**]$^-$ with those of the related anionic hydride are also of interest (Table 5.7). It is apparent that the Ni–Ga interaction is needed to stabilize formation of the Ni–X fragment by examination of the short Ni–Ga interactions, and large deviations of Ga and Ni from their respective planes. This structural pyramidalization is also reflected in the elongation of the N_{apical} bond distance, which is nearly 0.2 Å longer than that observed in **2**. When comparing [**2–Me**]$^-$ to [**2–H**]$^-$ the average Ni–P bond

distance is considerably longer in [**2–Me**]$^-$ (Δ = 0.06 Å). One possible explanation for this deviation is gleaned from the Ni–P_3 plane distance in [**2–Me**]$^-$ in which the Ni center sits 0.14 Å further from the P_3 plane than in [**2–H**]$^-$. This deviation likely inhibits π-backbonding from the nearly pyramidal Ni center by disturbing the overlap of the $d_{x^2-y^2}/d_{xy}$ orbitals of nickel with the π-accepting orbitals of the phosphine ligands. In line with this hypothesis is the difference in ^{31}P shifts of [**2–H**]$^-$ (75.6 ppm) and [**2–Me**]$^-$ (44.4 ppm), which may reflect the phosphine ligands in [**2–Me**]$^-$ are more shielded than in [**2–H**]$^-$. Worth mentioning is that the tensor that describes the chemical shifts of these species is likely highly dependent on a variety of other factors.

Table 5.7: Selected comparative metrics for [PPN][**2–Me**] and [PPN][**2–H**]

Complex	[PPN][**2–Me**]	[PPN][**2–H**]
Ni−M	2.379(1)	2.355(1)
r[a]	0.97	0.96
Ni–P	2.224(1)	2.164(1)
Ga–N_{apical}	2.408(2)	2.426(2)
Ga–N_{eq}	1.970(2)	1.977(2)
∑P–Ni–P	353.0(1)	354.5(1)
∑N–Ga–N	337.9(1)	338.72
Ni to P_3 plane	0.341	0.199
Ga to N_3 plane	0.545	0.537
Ni–X	2.110(2)	1.53(4)

[a] Defined as the interatomic distance divided by the sum of the respective covalent radii. [b] Averages across each unique metric. See Table 5.9, 5.10, and 5.13 for collection details and metrics.

5.4.2 Small Molecule Reactivity Screening

Given the exciting ability to stabilize the Ni^0 methyl complex [**2–Me**]$^-$ we canvased the reactivity of this unique species with other small molecule substrates. In accordance with the pK_a differences of methane (CH_4, > 55) and dihydrogen (H_2, 44–49, THF), [**2–Me**]$^-$ reacts with H_2 gas (1–4 atm) rapidly to produce CH_4 with concomitant formation of [**2–H**]$^-$. Repeating this same reaction in a J. Young NMR tube but with D_2 gives rise to [**2–**

D]$^-$ and CH_3D, the latter identified by characteristic deuterium coupling ($^2J_{HD}$ = 1.7 Hz). Given the inherent basicity of the methyl group, we then sought to utilize the anionic methyl ligand in [**2–Me**]$^-$ towards the activation of other E–H groups including C–H, B–H, and Si–H bonds.

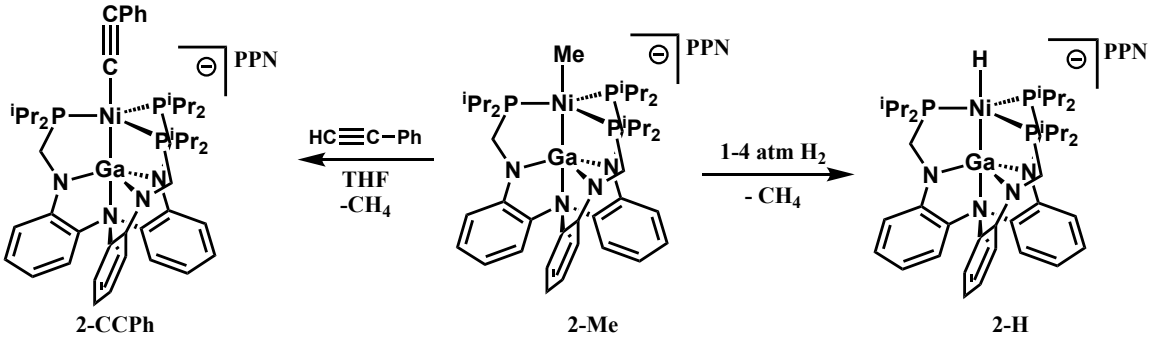

Figure 5.18: Reaction of [PPN][**2–Me**] yields anionic hydride [**2–H**]$^-$.

The reaction of [**2–Me**]$^-$ with phenyl acetylene (pK_a = 25) proceeds over 12 hours to provide a bright yellow solution of the anionic acetylide species, [**2–CCPh**]$^-$. The formation of this species is observed by inspection of the ^{1}H NMR spectrum (THF-d_8) for which an absence of the Ni–Me resonance is noted. Furthermore, there is the introduction of two visible triplet aromatic resonances in the ^{1}H NMR that are assigned to the meta and para position of the new acetylide ligand (the ortho position is coincident with another of the aryl ligand). Furthermore, the ^{31}P NMR reflect the nature of a strong sigma donor with a new resonance at 48.6 ppm in addition to those of the PPN cation at 21.0 ppm.

Species [PPN][**2–CCPh**] crystallizes in triclinic space group P–1 alongside one molecule of THF. The pertinent metrics, alongside those [**2–Me**]$^-$ are shown in Table 5.8. Upon substitution of the methyl ligand with the acetylide ligand in [**2–CCPh**]$^-$, there is an elongation of the Ni–Ga interaction but the interaction remains shorter than the sum of the respective covalent radii. The average Ni–P bond distances are somewhat shorter than in

those in [**2–Me**]$^-$, but not dissimilar. The geometry of the nickel center in [**2–CCPh**]$^-$ and in [**2–Me**]$^-$ are similar, with the nickel center sitting substantially out of the P_3 plane. In order to maintain the short Ga–Ni interaction, the gallium atom must be strongly distorted from ideal trigonal symmetry as reflected by the sum of the N_{eq}–Ga–N_{eq} angles that fall short of 340˚ in both cases. In comparison with the Ni–Me bond in [**2–Me]**$^-$, the Ni–C bond in [**2–CCPh**]$^-$ is considerably shorter at 1.914(4) Å. This is likely a consequence of the hybridization of the acetylide moiety (sp) in comparison with that of the methyl ligand (sp^3). The C_1–C_2 bond length of the phenyl acetylide ligand (1.222(5) Å) is slightly longer than the expected length of 1.200 Å for an sp–sp carbon–carbon bond, which likely reflects involvement of the alkyne π-orbitals delocalizing negative charge within the complex.

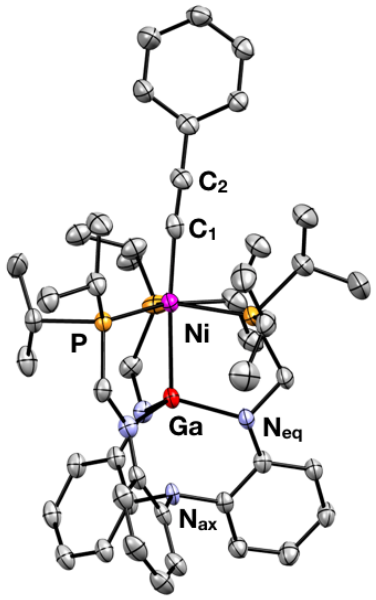

Figure 5.19: Molecular structure of [**2–CCPh**]$^-$ rendered at 50% thermal ellipsoid probability. PPN cation, crystallization solvent molecules, and hydrogen atoms are omitted for clarity.

Table 5.8: Comparative bond metrics between [PPN][**2–Me]** and [PPN][**2–CCPh**]

Complex	[PPN][**2–Me**]	[PPN][**2–CCPh**]
Ni–M	2.379(1)	2.418(1)
r[a]	0.97	0.98
Ni–P	2.224(1)	2.218(1)
Ga–N_{apical}	2.408(2)	2.438(3)
Ga–N_{eq}	1.970(2)	1.958(3)
∑P–Ni–P	353.0(1)	354.7(4)
∑N–Ga–N	337.9(1)	337.9(1)
Ni to P_3 plane	0.341	0.297
Ga to N_3 plane	0.545	0.543
Ni–X	2.110(2)	1.914(4)
C_1–C_2	–	1.222(5)

[a] Defined as the interatomic distance divided by the sum of the respective covalent radii. [b] Averages across each unique metric. See Table 5.11, 5.12, and 5.13 for collection details and metrics.

Organometallic functionalities other than the acetylide and methyl groups can also be installed in the apical binding pocket of **2** via E–H bond activation. To this end, [**2–Me**]$^-$ was treated with $PhSiH_3$ in hopes of generating an unsupported nickel–silyl species. Indeed, the addition of one equivalent of $PhSiH_3$ (excess leads to production of [**2–H**]$^-$) at low-temperature results in a small amount of gas evolution and the clean generation of a new product. Methane was not unequivocally evidenced by ^{1}H NMR spectroscopy, but it is a likely product in light of the inherent basicity of the methyl ligand in [**2–Me**]$^-$. The ^{1}H NMR spectrum of this species is shown on the below.

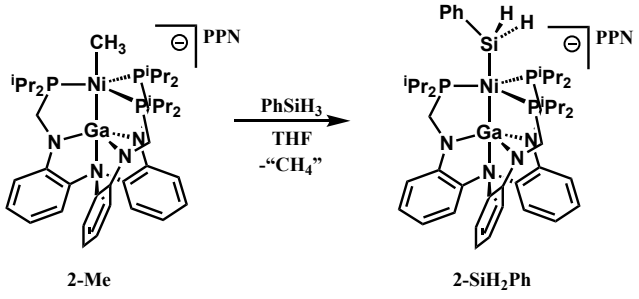

2-Me **2-SiH_2Ph**

Figure 5.20: Reaction of [PPN]**[2–Me]** with $PhSiH_3$ provides [PPN][**2–SiH_2Ph**]

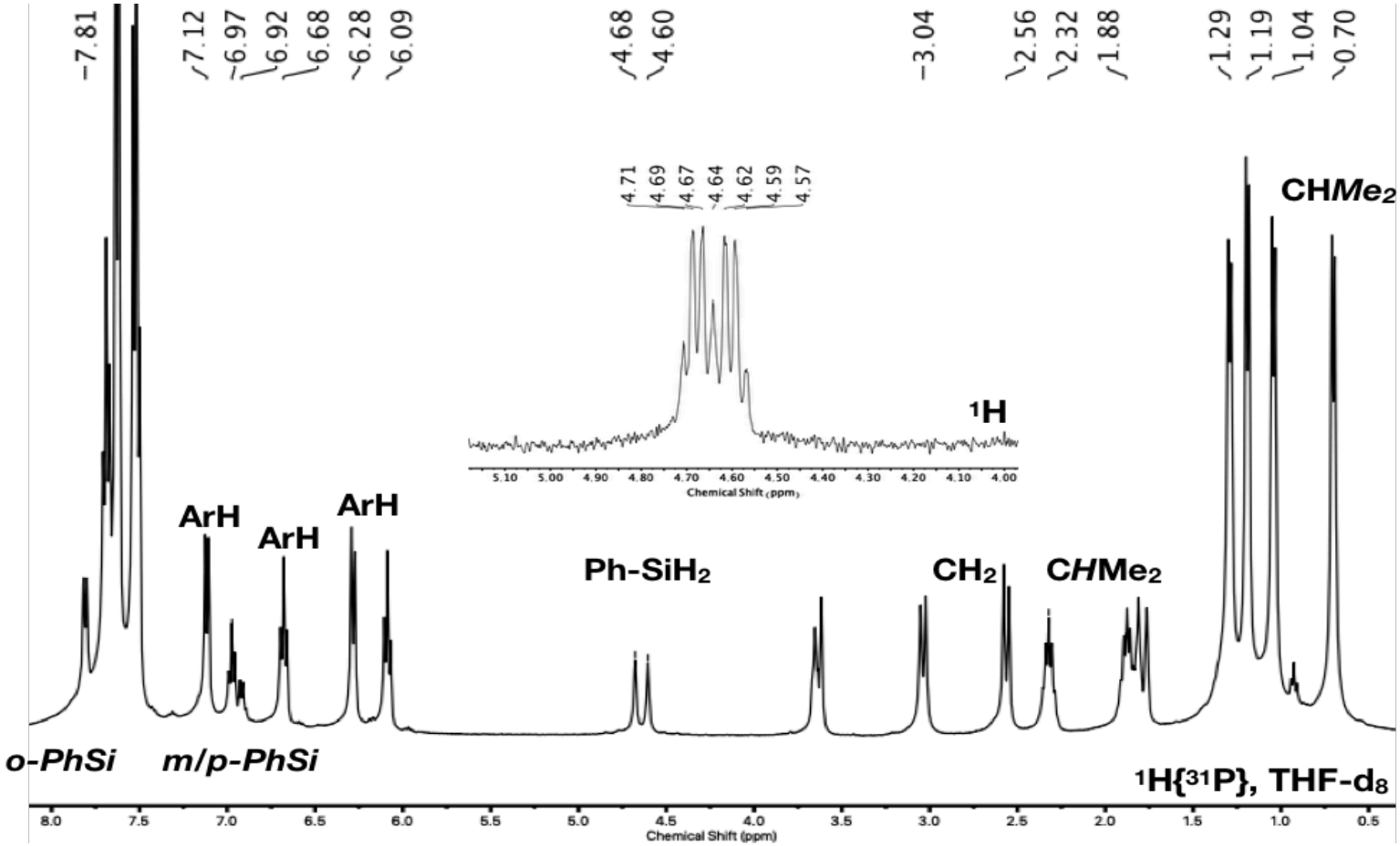

Figure 5.21: ^{1}H and $^{1}H\{^{31}P\}$ NMR spectra of [PPN][**2–SiH$_2$Ph**] (THF-d$_8$, 298K)

The spectroscopic behavior of [**2–SiH$_2$Ph**]$^-$ is informative and lends insight into its formulation. On comparing the ^{1}H NMR of [**2–Me**]$^-$ and [**2–SiH$_2$Ph**]$^-$ it is immediately apparent that the methyl ligand has left in some form, likely as methane (however generating PhSiH$_n$Me$_{3-n}$ cannot be excluded). Akin to the isoelectronic cobalt hydrido–silyl species reported in Chapter 2 (e.g. LGaCoH(SiH$_2$Ph)$^-$) the entire ligand framework has become stereochemically rigid as evidenced by ^{1}H NMR spectroscopy. The ^{1}H NMR spectrum of [**2–SiH$_2$Ph**]$^-$ give rise to the expected 12 signals of the H$_3$L framework. Due to the rigidity of the apical ligand, the methyl group (CH*Me$_2$*), methine (C*H*Me$_2$), and methylene (CH$_2$) groups become diastereotopic. The presence of the silyl ligand is inferred from new aromatic resonances at 7.81, 6.97 and 6.92 ppm, whose multiplicities and integrations correspond to ortho, meta, and para functionalities respectively. The remaining silicon bound protons are observed at chemical shifts of 4.68 and 4.60 ppm, respectively (Δ = 32 Hz). When the ^{1}H NMR spectrum is decoupled from ^{31}P nuclei, these resonances appear as singlets. When coupled to the ^{31}P nuclei, they resolve nicely into a pair of overlapping quartets with $^3J_{PH}$ = 8 Hz. Given the symmetry of the ^{1}H (^{31}P coupled) resonances observed it is attractive to propose a large germinal coupling between the SiH$_n$ protons. However, it is more probable that these two resonances belong to the respective Si–H moieties, whose symmetry is broken by the non–trigonal nature of the quasi-tetrahedral phenyl group of the phenyl silane residue. Single crystals of [**2–SiH$_2$Ph**]$^-$ can be grown from THF/Et$_2$O but samples repeatably exhibited substantial disorder and hence are not discussed.

Given that [**2–Me**]$^-$ reacts cleanly with $PhSiH_3$, we last examined if an unsupported boryl complex was feasible via B-H activation.[29, 52-53] To this end, we examined the reaction between HBPin (4,4,5,5–Tetramethyl–1,3,2–dioxaborolane) and [**2–Me**]$^-$. Addition of HBPin at low temperatures leads to the immediate formation of a bright yellow solution. ^{1}H NMR spectroscopy indicated that the HBPin has been consumed, as inferred from the absence of the board quartet centered near 3.7 ppm for HBPin.[54] Unfortunately, the ^{31}P NMR spectrum of the reaction reveals that the new nickel–containing product is exclusively [PPN][**2–H**]. The ^{11}B containing product is still of interest, as it appears to result from formal methyl transfer. The ^{11}B NMR of the reaction mixture shows a relativity broad resonance at 33.6 ppm which is in excellent agreement with the methyl ester, MeBPin (reported at 33.5 ppm).[54] Further indication of MeBPin as a product comes from analysis of the ^{1}H NMR spectrum of the mixture which shows two new singlet signals at 1.20 and 0.13. These signals integrate 4:1, respectively, and corresponding to the MeB and BPin portions of MeBPin. The presence of MeBPin by ^{1}H NMR spectroscopy following workup is attributed to a high boiling point (ca. 120˚C/1 atm).[54]

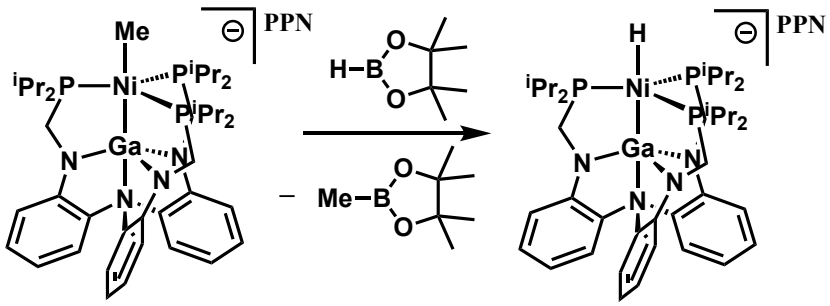

2-Me **2-H**

Figure 5.22: Reaction of [**2–Me**]$^-$ with HBPin lead to formation of [**2–H**]$^-$ and methyl transfer

5.5 Conclusions

The use of group 13 metalloligands is vital in conferring Lewis acidity to low valent nickel complexes. The ability of group 13 elements aluminum, gallium, and indium to produce modestly Lewis acidic centers is apparent for the ability to both bind and activate H_2 (in (η^2–H_2)Ni complexes) and to stabilize the reducing nature of their base heterolysis products ([HNiML]$^-$). In line with the observation that M electronically modifies Ni^0 in **1-3**, the ability of the corresponding base heterolysis products, [HNiML]$^-$, to act as hydride donors is similarly modulated. Importantly, complexes [**1–H**]$^-$ to [**3–H**]$^-$ are strong hydride donors with $\Delta G^\circ_{H^-}$ values lower than most 3d metals, and even stronger than some of the strongest precious metal species (e.g. $dmpe_2RhH$). Intriguingly, the hydricity values of [**1–H**]$^-$ to [**3–H**]$^-$ are insufficient to explain the differences in catalytic CO_2 hydrogenation for which **2** (M = Ga) remains the most active catalysts of the series. These studies have revealed that CO_2 hydrogenation is a careful interplay of H_2 activation (pK_a), H_2 binding, and hydride donor strength ($\Delta G^\circ_{H^-}$).

The ability of the LM (M = Al, Ga, In) scaffold to stabilize the reducing nature of the terminal hydride ligand in [**1–H**]$^-$ to [**3–H**]$^-$ suggests that other organometallic groups may be stabilized. This was examined explicitly for M = Ga, where the conferred Lewis-acidity of **2** was leveraged to isolate terminal chloride, silyl, acetylide, and methyl fragments of a formally Ni^0 center. In the case of the anionic methyl complex, [**2–Me**]$^-$ a preliminary survey of small molecule reactivity reveals a highly basic nature and a propensity to eliminate methane. The methyl ligand in [**2–Me**]$^-$ reacts with small molecules such as H_2, $PhSiH_3$, PhCCH, and HBPin rapidly to produce unique Ni^0 products atypically observable atypical of low-valent Ni.

5.6 Experimental Section

General procedures: Unless otherwise stated, all manipulations were performed under a purified argon atmosphere using standard Schlenk techniques or inside of an MBraun glovebox maintained at < 1 ppm O_2 and H_2O. Standard solvents were deoxygenated by sparging with Ar and dried by passing through activated alumina columns of an SG Water solvent purification system. Deuterated solvents were purchased from Cambridge Isotope Laboratories, Inc. or Sigma–Aldrich and degassed via freeze–pump–thaw cycles, then stored over activated 4 Å molecular sieves for 48 hours prior to use. The following reagents were purchased from Strem Chemicals and used as received: bis(triphenylphosphine) iminium chloride, 1,2–bis(dimethylphosphino)ethane, 1,2–bis(diethylphosphino)ethane, 1,5–cyclooctadiene rhodium chloride dimer, bis(1,5–cyclooctadiene)-nickel. Solutions of M[$HBEt_3$] (M = Li, Na, K), Verkade's superbase (Vkd), phosphazene bases P_4tBu and P_1tBu, and D_2 gas were purchased from Sigma–Aldrich. ^{1}H and ^{31}P NMR spectra were recorded on Bruker 400 MHz spectrometer. ^{1}H NMR were referenced to the internal solvent residual signal or an external reference for ^{31}P (H_3PO_4). Infrared spectra were recorded on a Bruker Tensor 30 instrument. The neutral ligand (N(*o*–($NHCH_2P^iPr_2$)C_6H_4)$_3$ (H_3L)[32], metalloligands ML (M = Al, Ga, In)[18, 32], bimetallic nickel complex (**1-3**)[18, 32], and bis(diphopshine) rhodium complexes $(diphos)_2RhH$ were synthesized according to literature procedures.[38] We find, in accordance with previous reports, that $(diphos)_2RhH$ are very reactive species, and are best stored as solids at –30˚C being prepared as needed.[38] The lipophilic N-heterocyclic carbene bases $^{iPr}NHC^{Me}N^{tBu}$ and $^{iPr}BIG^{NH2}$ were prepared as reported. [35 39]

Synthesis of [PPN][1–H]. A solution of **1** in THF (114 mg, 138 μmol, 8mL) is cooled to –78˚C and subsequently treated with ^{n}BuLi (138 μmol, 2.5M, 62.4 μL) immediately giving rise to a bright orange solution. The mixture is allowed to warm to room temperature overnight, before being treated with solid [PPN][$BArF_{24}$] (415 mg, 283 μmol). The solution is concentrated to 2 mL, then 15mL of diethyl ether is added to precipitate the product. Filtration of the resulting solid and washing with diethyl ether (2 x 5mL) furnishes a bright yellow powder (101 mg, 25 % yield). ^{1}H NMR (ppm, THF–d_8, 400 MHz): 7.66–7.45 (multi, 30H, PPN, ArH), 7.18 (d, J = 7.4Hz, 3H, ArH), 6.63 (t, J = 7.4 Hz, 3H, ArH), 6.20 (d, J = 7.7 Hz, 3H, ArH), 6.01 (t, J = 7.4 Hz, 3H, ArH), 2.68 (s, 6H, CH_2), 1.83–1.61 (br, 6H, *CH*(CH_3)$_2$), 1.2–0.42 (v br, ~ 36H, CH*(CH$_3$)$_2$*), –5.3 (br q, J = 35.1 Hz, 1H, Ni–H). ^{31}P NMR (ppm, THF–d_8, MHz): 63.8 (br d, J = 33 Hz, 3P, NiP_3), 21.0 (s, 2P, PPN)FTIR (KBr pellet): 1646 cm^{-1} (Ni–H). Similar complexes may be isolated as $P_4{}^{tBu}H^+$ or K(222–crypt)$^+$ salts by the addition of H_2 to solutions of **1** containing either $P_4{}^{t}$Bu or KO^{t}Bu, respectively. Solutions of the PPN^+ and K^+ salts of this hydridic compound slowly decompose at room temperature to yet unidentified materials, solids stored under argon at –30˚C show no changes over the course of 1–2 months. Both the PPN^+ and 222–crypt potassium salts of these complexes failed to produce satisfactory analyses, however, the salt prepared from $P_4{}^{t}$Bu could be prepared in analytically pure form in higher overall yield (ca. 65%). Anal Calc. for [$P_4{}^{t}$BuH][**1–H**], [$C_{22}H_{64}N_{13}P_4$][$C_{39}H_{61}N_4P_3AlNi$] (%) C 52.4, H 9.0, N 17.0. Found: C 52.6, H 9.6, N 16.6.

Synthesis of [PPN][3–H]. Prepared analogously to [PPN][**1–H**] from **3** (114 mg, 138 μmol), ^{n}BuLi (138 μmol, 2.5M, 62.4 μL), and [PPN][$BArF_{24}$] (415mg, 283μmol).

Yield (101 mg, 75 % yield). ^{1}H NMR (ppm, THF–d_8, 400 MHz): ^{1}H{^{31}P} NMR (ppm, THF–d_8, 400 MHz): 7.62–7.44 (m, $[PPN]^+$, 30 H), 7.22 (d, *J*=7.5 Hz, aryl, 3H), 6.57 (t, *J*=7.5 Hz, aryl, 3H), 6.16 (d, *J*=7.9 Hz, aryl, 3H), 5.91 (t, *J*=7.3 Hz, aryl, 3H), 2.71 (br, C*H*$_2$P(^{i}Pr)$_2$, 6H), 1.83 (br, C*H*(CH$_3$)$_2$, 6H), 1.07 (br, CH(*CH$_3$*)$_2$, 36H), −6.17 (br, Ni*H*, 1H). ^{31}P{^{1}H} NMR (ppm, THF–d_8, 162 MHz): 82.5 (s, 3P, $[HNiInL]^-$), 21.0 (s, 2P, $[PPN]^+$). FTIR (KBr pellet): 1714 cm^{-1} (Ni–H). This compound appears to be stable for extended periods of time under argon at –30˚C. Attempts to obtain satisfactory analysis for the PPN^+ or 2.2.2cryptand potassium salts of this material failed, however satisfactory results were obtained for the P$_4$^{t}BuH salt. Anal Calc. for [P$_4$^{t}BuH][**3–H**], [$C_{22}H_{64}N_{13}P_4$][$C_{39}H_{61}N_4P_3InNi$] (%) C 49.3, H 8.5, N 16.0. Found: C 48.8, H 8.8, N 15.4.

Synthesis of [1–D]$^-$: The base heterolysis reaction utilizing 1 atm D_2, equimolar P$_4$^{t}Bu, and **1** was used to synthesize spectroscopically pure [P$_4$^{t}BuH][**1–D**] which shows identical ^{1}H and ^{31}P NMR as described above, with the absence of a M–H resonance.

Synthesis of [3–D]$^-$: Exposing a solution of [PPN][**3–H**] to 4 atm D_2 results in no change by ^{31}P NMR and disappearance of the Ni–H resonance by ^{1}H NMR. This material can likewise be obtained by the base heterolysis utilizing 1 atm D_2 and equimolar P$_4$^{t}Bu, and **3**.

Synthesis of [PPN][2–Cl]: A solution of LGa (201.5 mg, 0.27 mmol) and Ni(1,5-COD)$_2$ (74 mg, 0.27 mmol) in THF (10mL) were stirred for 2–3 hours before being added to a solid sub–stoichiometric amount of PPNCl (115.0 mg, 0.202 mmol). The solution was

stirred overnight at room temperature resulting in the deposition of a finely divided orange powder. The product was further precipitated by addition of 20mL of Et_2O and then filtered. The resulting solid washed liberally with Et_2O (2x20mL) and then C_6H_6 (2x3mL) to provide 196 mg of an orange microcrystalline solid (70 % yield based on PPNCl). Crystals suitable for X–ray diffraction were grown from diffusion of Et_2O into a concentrated THF solution. This material is very poorly soluble in THF and reacts with both dichloromethane and acetonitrile. ^{1}H NMR (ppm, THF–d_8, 400 MHz): 7.69 (ap t, J = 7.1 Hz *p*–PPN, 6H), 7.63(dd, J = 7.8 Hz, 13 Hz, *m*–PPN, 12H), 7.52 (dt, J = 2.6, 7.6 Hz, *o*–PPN), 7.10 (d, J=7.5 Hz, 3H, ArH), 6.67 (t, J = 7.7Hz, 3H, ArH), 6.22 (d, J = 8.0 Hz, 3H, ArH), 6.08 (t, J = 7.1 Hz, 3H, ArH), 3.0–2.42 (br, 9H, overlapping CH_2 and $CH(CH_3)_2$), 2.16 (br, 3H, $CH(CH_3)_2$), 1.54–0.63 (br, 36H, $CH(CH_3)_2$). ^{31}P NMR (ppm, THF–d_8, 162 MHz): 34.4 (br s, 3P, complex), 21.0 (br s, 2P, PPN). Anal Calc. (found) for $[C_{36}H_{30}P_2N][C_{39}H_{60}N_4P_3NiGaCl]$ (%) C 65.26 (55.4), H 6.57 (5.8), N 5.07 (4.3).

Synthesis of 2-MeCN: [PPN][**2–Cl**] (25 mg, mmol) were suspended in 1 mL of MeCN and stirred for 5–10 min before being filtered to provide a yellow solution. Allowing this solution to stand for 1 day at room temperature provided large yellow crystals identified as **2–MeCN** which were suitable for X–ray diffraction. The NMR data recorded in THF–d_8 are consistent with a strongly bound acetonitrile adduct under ambient conditions. ^{1}H NMR (ppm, CD_3CN, 400 MHz): 7.19 (d, J =7.7 Hz, 3H, ArH), 6.87 (t, J = 8.0 Hz, 3H, ArH), 6.37 (d, J = 8.0 Hz, 3H, ArH), 6.30 (t, J = 7.7 Hz, 3H, ArH), 2.90 (br, 6H, CH_2), 2.25 (br, 6H, $CH(CH_3)_2$), 2.12 (s, 3H, *MeCN*), 1.5–0.79 (br, 36H, $CH(CH_3)_2$). ^{31}P NMR (ppm,

CD_3CN, 162 MHz): 40.7. Elemental analysis has not been obtained for this complex to date.

Synthesis of [PPN][2–Me]: A solution of [PPN][**2-Cl**] (58.9mg, 42.7 μmol) in THF (mL) was cooled to –30˚C. To this solution is added a small excess of a solution of 3M MeMgCl in Et_2O (21.2 μL, 63.6 μmol) and the mixture warmed to room temperature. Over the course of 2–3 hours the insoluble [PPN][**2-Cl**] is slowly consumed and the solution becomes homogeneous and deep orange. After stirring overnight, 1,4–dioxane (1mL) is added to precipitate any remaining magnesium salts, and then filtered. The solution is reduced to dryness and washed liberally with Et_2O (2 x 10mL) to provide 46 mg (78 % yield) of a yellow–orange solid. Crystals suitable for X–ray diffraction studies were grown from THF/Et_2O diffusion. ^{1}H NMR (ppm, THF–d_8, 400 MHz): 7.63 (ap t, J = 7.1 Hz *p*–PPN, 6H), 7.57 (dd, J = 7.8 Hz, 13 Hz, *m*–PPN, 12H), 7.46 (dt, J = 2.6, 7.6 Hz, *o*–PPN), 7.06 (d, J=7.2 Hz, 3H, ArH), 6.56 (t, J = 7.4 Hz, 3H, ArH), 6.16 (d, J = 8.0 Hz, 3H, ArH), 5.95 (t, J = 7.2 Hz, 3H, ArH), 2.78 (br, 6H, *CH_2*), 2.52 (br, 6H, *CH_2*), 2.35 (br, 3 H, *$CH(CH_3)_2$*) 1.96 (br, 3 H, *$CH(CH_3)_2$*) 1.22 (br, 18 H, CH*$(CH_3)_2$*), 0.89 (br, 9 H, CH*$(CH_3)_2$*), 0.78 (br, 9 H, CH*$(CH_3)_2$*), –0.59 (q, J = 8.5 Hz, Ni–CH_3). ^{31}P NMR (ppm, THF–d_8, 162 MHz MHz): 44.1 (s, 3P), 21.0 (s, 2P, PPN) Anal Calc. (found) for $[C_{36}H_{30}NP_2][C_{40}H_{63}N_4P_3NiGa]$ (%) C 67.13 (65.2), H 6.89 (6.9), N 5.15 (5.0). Repeated combustion for this complex exhibited low carbon values, which is in agreement of the reactivity of this species with oxygen and moisture.

Synthesis of [PPN][2–SiH_2Ph]: A J. Young NMR tube was charged with 24 mg (17μmol) of [PPN][**2–Me**] in ca. 0.5 mL THF–d_8. This solution was cooled to –78˚C and then 22μL of a solution of $PhSiH_3$ in THF–d_8 (10 μL $PhSiH_3$ in 100μL, 17μmol) causing an immediate lightening of the solution. The ^1H NMR of the mixture showed clean conversion to the desired species in quantitative yield. The material is recrystallized from THF/Et_2O or THF/Pentane to yield crystal suitable for combustion analysis. The yield of crystalline material was not determined. $^1H\{^{31}P\}$ NMR (ppm, THF–d_8, 400 MHz): 7.81 (d, J = 6.9 Hz, 2H, *o*–PhSi*)*, 7.69 (t, J=7.3 Hz, 6H, *p*–PPN), 7.63 (d, J = 7.5 Hz, 12H , *o*–PPN), 7.52 (t, J = 7.6 Hz, 12H, , *m*–PPN), 7.12 (d, J = 7.12, 3H, ArH), 6.97 (t, J = 7.1 Hz, 2H, *m*–PhSi), 6.92 (t, J = 7.0, 1H, *p*–PhSi), 6.68 (t, J =7.3 Hz, 3H, ArH), 6.28 (d, J = 7.8 Hz, ArH, 3H), 6.1 (t, J = 7.2 Hz, 3H, ArH), 4.64 (d, J_{HH} = 28.9Hz, $PhSiH_2$, with ^{31}P coupling a d of quartets is visible with J_{PH} of 8 Hz, 2H), 3.04 (d, J = 12.1 Hz, 3H, CH_2), 2.56 (d, J= 12.1 Hz, 3H, CH_2), 2.32 (q, J = 7.1 Hz, 3H, $CH(CH_3)_2$), 1.88 (q, J = 7.4 Hz, 3H, $CH(CH_3)_2$), 1.29 (d, J = 6.9 Hz, 9 H, $CH(CH_3)_2$), 1.19 (d, J = 6.7 Hz, 9 H, $CH(CH_3)_2$), 1.04 (d, J = 6.9 Hz, 9 H, $CH(CH_3)_2$), 0.70 (d, J = 7.0 Hz, 9 H, $CH(CH_3)_2$). ^{31}P NMR (ppm, THF–d_8, 162 MHz): 48.1 (s, 3P), 21.0 (s, 2P). Anal Calc. (found) for $[C_{36}H_{30}NP_2][C_{45}H_{67}N_4P_3NiGaSi]\bullet C_4H_{10}O$ (%) C 66.9 (66.4), H 7.1 (6.7), N 4.6 (4.8).

Synthesis of [PPN][2–CCPh]: To a stirred solution of [PPN][**2–Me**] in THF (25mg, 18.4μmol, 5mL) is added a small excess of phenyl acetylene (3μL, 27.3μmol). The resultant mixture is stirred with initial evolution of gas. The reaction is then stirred overnight to ensure a complete reaction, at which point the volatiles are removed under reduced pressure. The material is washed extensively with Et_2O and pentane to yield 20.0

mg (75% yield) or a bright yellow powder. X–ray quality crystals were grown from THF/Et_2O layering. ^1H NMR (400 MHz, THF–d_8): δ 7.68 (t, J = 7.5 Hz, 6H, p–PPN), 7.61 (d, J = 7.6 Hz, 12H, m–PPN), 7.50 (t, J = 7.6 Hz, 12H, o–PPN), 7.12 (d, J = 7.6 Hz, 4H, overlapping o–PhCC and ArH), 6.97 (t, J = 7.5 Hz, 3H, m–PhCC), 6.74 (t, J = 7.4 Hz, 1H, p–PhCC), 6.66 (t, J = 7.5 Hz, 3H, ArH), 6.23 (d, J = 7.9 Hz, 3H, ArH), 6.05 (t, J = 7.3 Hz, 3H, ArH), 2.8–2.7 (b, 6H, CH_2), 2.4–2.2 (b, 6H, C*H*Me_2), 1.3–1.0 (v. br, 36H, CH*Me₂*). $^{31}P\{^1H\}$ NMR (162 MHz, THF–d_8): δ 48.62 (3P), 21.00 (2P, PPN). Anal Calc. (found) for $[C_{36}H_{30}NP_2][C_{47}H_{67}N_4P_3NiGa]$ (%) C 68.9 (69.1), H 6.6 (6.9), N 4.8 (4.5).

Reaction of [PPN][2–Me] with HBPin: To a stirred solution of [PPN][**2–Me**] in THF (25mg, 18.4μmol, 3mL) is directly added 4μL HBpin (27.6μmol) and the reaction mixture stirred overnight to give a light orange solution. The volatiles were removed under reduced pressure and then the material was extracted into THF–d_8. The ^{31}P NMR showed [PPN][**2–H**] as the only nickel containing product. The ^{11}B NMR resolved a broad resonance at 33.6 ppm, consistent with the formation of MeBPin. In agreement with this, the ^1H NMR shows two new signals for MeBPin. ^1H NMR (400MHz, THF–d_8): ∂ 1.20 (12H, BPin), 0.13 (br, 3H, MeB).

Reaction of [PPN][2–Me] with H_2 or D_2*:* A J–Young NMR tube was charged with 10 mg of [PPN][MeNiGaL] (10 mg, 7.2 μmol) and ca. 0.5 mL THF–d_8, the tube was sealed, and the atmosphere replaced with 1 atm of H_2 (or D_2) by a freeze pump thaw cycle. The ^{31}P NMR and ^1H NMR show consumption of the alkyl species, in addition to the formation of reported [PPN][HNiGaL] and CH_4 (of CH_3D in the case of D_2).

X–ray Crystallographic and Structure Refinement Details

Crystals suitable for X–ray diffraction were placed onto the tip of MiTeGen Dual–Thickness MicroLoop™ and then mounted on a Bruker Photon II CPAD diffractometer for data collection at 100 K. The data collections were carried out using Mo Kα radiation (graphite monochromator). The data intensity was corrected for absorption and decay (SADABS).[55] Final cell constants were obtained from least–squares fits of all measured reflections. The structure was solved using SHELXT–16[56] and refined using SHELXL–16[57], which were executed from the SHELXLE graphical user interface.[58] A direct–methods solution was calculated which provided most non–hydrogen atoms from the E–map. Full– matrix least–squares/difference Fourier cycles were performed to locate the remaining non–hydrogen atoms. All non–hydrogen atoms were refined with anisotropic displacement parameters. Hydrogen atoms were placed in ideal positions and refined as riding atoms with relative isotropic displacement parameters. Images were rendered utilizing POV–ray.[59] In addition, if substantial disorder of THF molecules was present, these were omitted from the final solution utilizing the PLATON squeeze function.[60] Crystallographic data are summarized below.

Table 5.9: Summarized crystallographic details for [PPN][**1–H**] and [PPN][**3–H**]

chemical formula	[PPN][**1–H**]	[PPN][**3–H**]
Formula weight	1304.11	1376.58
Crystal system	monoclinic	monoclinic
space group	$P2_1/c$	$P2_1/c$
a (Å)	22.7023(19)	22.683(2)
b (Å)	13.8362(10)	13.9047(17)
c (Å)	25.469(2)	25.559(3)
α (deg)	90	90
β (deg)	103.910(3)	103.796(3)
γ (deg)	90	90
V ($Å^3$)	7765.6(11)	7828.8(14)
Z	4	4
λ (Å), μ (mm^{-1})	0.71073, 0.405	0.71073, 0.677
T (K)	123(2)	123(2)
θ	2.209 to 30.558	2.200 to 30.536
reflections collected	143862	67839
unique reflections	23748	23656
data/restraint/parameters	23748/0/792	23656/0/775
R1, wR2 ($I > 2\sigma(I)$)	0.0510, 0.1353	0.0664, 0.1711

Table 5.10: Compiled bond metrics for anionic hydrides [PPN][**1–H**] and [PPN][**3–H**]

Complex	[PPN][**1–H**]	[PPN][**3–H**]
Ni–M	2.431(1)	2.4317(5)
r	0.99	0.91
Ni–P	2.145(1)	2.207(1)
	2.150(1)	2.207(1)
	2.140(1)	2.219(1)
$M–N_{apical}$	2.296(2)	2.422(3)
$M–N_{eq}$	1.912(2)	2.136(3)
	1.913(2)	2.139(3)
	1.914(2)	2.146(3)
P–Ni–P	119.79(2)	119.04(4)
	116.92(2)	115.73(4)
	120.81(2)	120.42(4)
N–M–N	114.99(7)	113.72(12)
	115.71(7)	113.40(12)
	114.81(7)	111.24(13)
Ni to P_3 plane	0.20	0.28
M to N_3 plane	0.43	0.59
Ni–H	1.45(3)	1.57(6)
M–Ni–H	179.3(12)	179.0(2)

Table 5.11: Summarized crystallographic details for [**2–Cl**]$^-$ and [**2–Me**]$^-$

chemical formula	[PPN][**2–Cl**]	[PPN][**2–Me**]
Formula weight	1380.24	1359.83
Crystal system	triclinic	triclinic
space group	P–1	P–1
a (Å)	11.0701(10)	11.0268(7)
b (Å)	15.5176(14)	15.6076(9)
c (Å)	20.4534(17)	20.4675(11)
α (deg)	78.610(3)	78.437(2)
β (deg)	76.850(3)	77.173(2)
γ (deg)	88.219(3)	88.750(2)
V (Å^3)	3353.6(5)	3363.9(3)
Z	2	2
λ (Å), μ (mm^{-1})	0.71073, 0.889	0.71073, 0.847
T (K)	100(2)	123(2)
θ	2.247 to 27.612	2.266 to 28.339
reflections collected	15562	16735
unique reflections	15562	16735
data/restraint/parameters	10434/0/801	12452/0/806
R1, wR2 (I > 2σ(I))	0.0453, 0.0968	0.0435, 0.1123

Table 5.12: Summarized Crystallographic details for **2–MeCN** and [**2–CCPh**]$^{-}$

chemical formula	**2–MeCN**•CH_3CN	[PPN][**2–CCPh**]
Formula weight	888.35	1445.91
Crystal system	monoclinic	monoclinic
space group	$P2_1/c$	P –1
a (Å)	11.6176(8)	13.3605(13)
b (Å)	20.6583(12)	17.3002(16)
c (Å)	18.3232(12)	17.6091(17)
α (deg)	90	83.205(3)
β (deg)	100.358(2)	80.507(3)
γ (deg)	90	78.549(3)
V (Å^3)	4325.9(5)	3919.1(7)
Z	4	2
λ (Å), μ (mm^{-1})	0.71073, 1.207	0.71073, 0.731
T (K)	123(2)	123(2)
θ	2.466 to 30.524	2.355 to 27.485
reflections collected	89415	17968
unique reflections	13213	17968
data/restraint/parameters	13213/0/501	13676/0/867
R1, wR2 (I > 2σ(I))	0.0308, 0.0767	0.0543, 0.1228

Table 5.13: Compiled bond metrics for anionic Ga-Ni complexes

Complex	[PPN][**2–Cl**]	[PPN][**2–Me**]	**2–MeCN**	[PPN][**2–CCPh**]
Ni−Ga	2.376(1)	2.380(1)	2.428(1)	2.418(1)
r	0.97	0.97	0.99	0.98
Ni–P	2.221(1)	2.195(1)	2.236(1)	2.219(1)
	2.257(1)	2.239(1)	2.255(1)	2.222(1)
	2.258(1)	2.239(1)	2.264(1)	2.212(1)
$Ga–N_{apical}$	2.359(2)	2.408(2)	2.3425(13)	2.438(3)
$Ga–N_{eq}$	1.949(3)	1.961(2)	1.9455(14)	1.958(3)
	1.952(2)	1.968(2)	1.9500(14)	1.958(3)
	1.967(2)	1.980(2)	1.9525(13)	1.959(3)
P–Ni–P	122.43(4)	116.92(3)	120.459(18)	117.51(4)
	116.86(4)	122.21(3)	119.217(18)	118.05(4)
	114.70(4)	113.91(3)	114.865(18)	119.14(4)
N–Ga–N	110.87(11)	109.80(8)	114.15(6)	114.06(11)
	112.27(11)	111.56(9)	112.76(6)	111.25(11)
	117.42(11)	116.52(8)	117.50(6)	112.58(11)
Ni to P_3 plane	0.320	0.341	0.306	0.297
Ga to N_3 plane	0.507	0.545	0.451	0.543
Ni–X	2.335(1)	2.110(2)	1.949(1)	1.914(4)
Ga–Ni–X	175.55(3)	174.63(7)	176.81(4)	172.17(10)

References for Chapter 1:

1. Conway, B. E.; Tilak, B. V.; Eley, D. D.; Pines, H.; Weisz, P. B. *Advances in Catalysis*. 1992; Vol. 38, p 18.

2. MacKay, D. J. C. *Sustainable Energy—Without the Hot Air*. 2009.

3. Olah, G. A.; Prakash, G. K. S.; Goeppert, A. *J. Am. Chem. Soc.* **2011,** *133*, 12881-12898.

4. Tester, J. W.; Drake, E. M.; Golay, W. W.; Driscoll, M. J.; Peters, W. A. *Sustainable Energy*. 2005.

5. Yara International. Leading Ammonia Exporting Countries Worldwide in 2016 (in Million Metric Tons). www.statista.com/statistics/982846/ammonia-exporting-countries-worldwide/ (accessed 31 Mar 2019).

6. Erisman, J. W.; Sutton, M. A.; Galloway, J.; Klimont, Z.; Winiwarter, W. *Nature Geoscience*. **2008,** *1*, 636.

7. BP *Statistical Review of World Energy 2018*; BP: 2018; pp 1-56.

8. Glebova, O. *Gas to Liquids: Historical Development and Future Prospects*; Oxford Institute for Energy Studies: 2013; pp 1-53.

9. Alvarado, M. *IHS Chemical Bulletin*. **2016**, 10-11.

10. Johnson, D. *Global Methanol Market Review*; IHS Inc.: 2012.

11. World Population Prospects: The 2017 Revision, Key Findings and Advance Tables. United Nations Department of Economic and Social Affairs: Population Division: 2017

12. Manabe, S.; Wetherald, R. T. *J. Atm. Sci.* **1975,** *32*, 3-15.

13. Lewis, N. S.; Nocera, D. G. *Proc. Natl. Acad. Sci. U.S.A.* **2006,** *103*, 15729.

14. Odom, A. L.; McDaniel, T. J. *Acc. Chem. Res.* **2015,** *48*, 2822-2833.

15. Hunt, A. J.; Farmer, T. J.; Clark, J. H. CHAPTER 1 Elemental Sustainability and the Importance of Scarce Element Recovery. In *Element Recovery and Sustainability*, The Royal Society of Chemistry: 2013; pp 1-28.

16. Appel, A. M.; Bercaw, J. E.; Bocarsly, A. B.; Dobbek, H.; DuBois, D. L.; Dupuis, M.; Ferry, J. G.; Fujita, E.; Hille, R.; Kenis, P. J. A.; Kerfeld, C. A.; Morris, R. H.; Peden, C. H. F.; Portis, A. R.; Ragsdale, S. W.; Rauchfuss, T. B.; Reek, J. N. H.; Seefeldt, L. C.; Thauer, R. K.; Waldrop, G. L. *Chem. Rev.* **2013,** *113*, 6621-6658.

17. Roche, A. E.; Sutton, M. M.; Bohme, D. K.; Schiff, H. I. *J. Chem. Phys.* **1971,** *55*, 5480-5484.

18. van der Ham, C. J. M.; Koper, M. T. M.; Hetterscheid, D. G. H. *Chem. Soc. Rev.* **2014,** *43*, 5183-5191.

19. Chirik, P. J. *Acc. Chem. Res.* **2015,** *48*, 1687-1695.

20. Smith, K. M. *Organometallics*. **2005,** *24*, 778-784.

21. Connelly, N. G.; Geiger, W. E. *Chem. Rev.* **1996,** *96*, 877-910.

22. Holland, P. L. *Dalton Trans.* **2010,** *39*, 5415-5425.

23. Lee, Y.; Mankad, N. P.; Peters, J. C. *Nat. Chem.* **2010,** *2*, 558-565.

24. Rodriguez, M. M.; Bill, E.; Brennessel, W. W.; Holland, P. L. *Science*. **2011,** *334*, 780-783.

25. Hoang, T. K. A.; Antonelli, D. M. *Adv. Mater.* **2009,** *21*, 1787-1800.

26. Hoffman, B. M.; Lukoyanov, D.; Yang, Z.-Y.; Dean, D. R.; Seefeldt, L. C. *Chem. Rev.* **2014,** *114*, 4041-4062.

27. Hulley, E. B.; Welch, K. D.; Appel, A. M.; DuBois, D. L.; Bullock, R. M. *J. Am. Chem. Soc.* **2013,** *135*, 11736-11739.

28. Kubas, G. J. *Comments Inorg. Chem.* **2013,** *33*, 102-121.

29. Kubas, G. J. *J. Organomet. Chem.* **2014,** *751*, 33-49.

30. Stephan, D. W. *Acc. Chem. Res.* **2015,** *48*, 306-316.

31. Tsay, C.; Peters, J. C. *Chem. Sci.* **2012,** *3*, 1313-1318.

32. Beller, M.; Bornscheuer, U. T. *Angew. Chem. Int. Ed.* **2014,** *53*, 4527-4528.

33. Leitner, W. *Angew. Chem. Int. Ed. Engl.* **1995,** *34*, 2207-21.

34. Marks, T. J. *Bonding Energetics in Organometallic Compounds*. American Chemical Society: 1990; Vol. 428, p 324.

35. Armentrout, P. B. Periodic Trends in Transition Metal Bonds to Hydrogen, Carbon, and Nitrogen. In *Bonding Energetics in Organometallic Compounds*, American Chemical Society: 1990; Vol. 428, pp 18-33.

36. Darensbourg, M. Y.; Llobet, A. *Inorg. Chem.* **2016,** *55*, 371-377.

37. Hong Enriquez, R. P.; Do, T. N. *Life*. **2012,** *2*, 274-285.

38. Fausto Da Silva, J. J. R.; Williams, R. J. P. *The biological chemistry of the elements: The inorganic chemistry of life*. Oxford University Press; : 1997.

39. Dux, E. *Chem. Rev.* **2009,** *19*, 11-15.

40. Erisman, J. W.; Sutton, M. A.; Galloway, J.; Klimont, Z.; Winiwarter, W. *Nat. Geosci.* **2008,** *1*, 636-639.

41. Modak, J. M. *Resonance*. **2002,** *7*, 69-77.

42. Karton, A.; Taylor, P. R.; Martin, J. M. L. *J. Chem. Phys.* **2007,** *7*, 69-77.

43. Jones, A.; McNicol, B. D. *J. Catal.* **1977,** *47*, 384-8.

44. Hoffman, B. M.; Lukoyanov, D.; Dean, D. R.; Seefeldt, L. C. *Acc. Chem. Res.* **2013,** *46*, 587-595.

45. Spatzal, T.; Aksoyoglu, M.; Zhang, L.; Andrade, S. L. A.; Schleicher, E.; Weber, S.; Rees, D. C.; Einsle, O. *Science*. **2011,** *334*, 940.

46. Hoffman, B. M.; Dean, D. R.; Seefeldt, L. C. *Acc. Chem. Res.* **2009,** *42*, 609-619.

47. Howard, J. B.; Rees, D. C. *Proc. Natl. Acad. Sci. U. S. A.* **2006,** *103*, 17088-17093.

48. Peters, J. C.; Mehn, M. P. In *Bio-organometallic approaches to nitrogen fixation chemistry*, Wiley-VCH Verlag GmbH & Co. KGaA: 2006; pp 81-119.

49. Seefeldt, L. C.; Hoffman, B. M.; Dean, D. R. *Annu. Rev. Biochem.* **2009,** *78*, 701-722.

50. Igarashi, R. Y.; Laryukhin, M.; Dos Santos, P. C.; Lee, H.-I.; Dean, D. R.; Seefeldt, L. C.; Hoffman, B. M. *J. Am. Chem. Soc.* **2005,** *127*, 6231-6241.

51. Lukoyanov, D.; Yang, Z.-Y.; Barney, B. M.; Dean, D. R.; Seefeldt, L. C.; Hoffman, B. M. *Proc. Natl. Acad. Sci. U. S. A.* **2012,** *109*, 5583-5587.

52. Lindahl, P. A. *J. Inorg. Biochem.* **2012,** *106*, 172-178.

53. Lubitz, W.; Ogata, H.; Ruediger, O.; Reijerse, E. *Chem. Rev.* **2014,** *114*, 4081-4148.

54. Schilter, D.; Camara, J. M.; Huynh, M. T.; Hammes-Schiffer, S.; Rauchfuss, T. B. *Chem. Rev.* **2016,** *116*, 8693-8749.

55. Arioez, C.; Wittung-Stafshede, P. *Q. Rev. Biophys.* **2018,** *51*, e4/1-e4/39.

56. Zhang, L.-M.; Morrison, C. N.; Kaiser, J. T.; Rees, D. C. *Acta Crystallogr., Sect. D: Biol. Crystallogr.* **2015,** *71*, 274-282.

57. Umena, Y.; Kawakami, K.; Shen, J.-R.; Kamiya, N. *Nature*. **2011,** *473*, 55-60.

58. Ferreira, K. N.; Iverson, T. M.; Maghlaoui, K.; Barber, J.; Iwata, S. *Science*. **2004,** *303*, 1831-1838.

59. Service, R. J.; Hillier, W.; Debus, R. J. *Biochemistry*. **2010,** *49*, 6655-6669.

60. Tommos, C.; Babcock, G. T. *Biochim. Biophys. Acta, Bioenerg.* **2000,** *1458*, 199-219.

61. Bartlett, J. E.; Baranov, S. V.; Ananyev, G. M.; Dismukes, G. C. *Philos. Trans. R. Soc., B*. **2008,** *363*, 1253-1261.

62. Chen, C.; Kazimir, J.; Cheniae, G. M. *Biochemistry*. **1995,** *34*, 13511-26.

63. Tyryshkin, A. M.; Watt, R. K.; Baranov, S. V.; Dasgupta, J.; Hendrich, M. P.; Dismukes, G. C. *Biochemistry*. **2006,** *45*, 12876-12889.

64. Lee, C.-I.; Lakshmi, K. V.; Brudvig, G. W. *Biochemistry*. **2007,** *46*, 3211-3223.

65. Kanady, J. S.; Tsui, E. Y.; Day, M. W.; Agapie, T. *Science*. **2011,** *333*, 733-736.

66. Tsui, E. Y.; Agapie, T. *Proc. Natl. Acad. Sci. U.S.A.* **2013,** *110*, 10084.

67. Park, Y. J.; Ziller, J. W.; Borovik, A. S. *J. Am. Chem. Soc.* **2011,** *133*, 9258-9261.

68. Fourmond, V.; Baffert, C.; Sybirna, K.; Dementin, S.; Abou-Hamdan, A.; Meynial-Salles, I.; Soucaille, P.; Bottin, H.; Leger, C. *Chem. Commun.* **2013,** *49*, 6840-6842.

69. Kubas, G. J. *Chem. Rev.* **2007,** *107*, 4152-4205.

70. Shafaat, H. S.; Ruediger, O.; Ogata, H.; Lubitz, W. *Biochim. Biophys. Acta, Bioenerg.* **2013,** *1827*, 986-1002.

71. Shomura, Y.; Higuchi, Y. *Rev. Inorg. Chem.* **2013,** *33*, 173-192.

72. Kampa, M.; Pandelia, M.-E.; Lubitz, W.; van Gastel, M.; Neese, F. *J. Am. Chem. Soc.* **2013,** *135*, 3915-3925.

73. Liu, T.; DuBois, D. L.; Bullock, R. M. *Nat. Chem.* **2013,** *5*, 228-233.

74. Ogo, S.; Ichikawa, K.; Kishima, T.; Matsumoto, T.; Nakai, H.; Kusaka, K.; Ohhara, T. *Science*. **2013,** *339*, 682-684.

75. Siegbahn, P. E. M.; Tye, J. W.; Hall, M. B. *Chem. Rev.* **2007,** *107*, 4414-4435.

76. Khusnutdinova, J. R.; Milstein, D. *Angew. Chem. Int. Ed.* **2015,** *54*, 12236-12273.

77. Barnett, B. R.; Moore, C. E.; Rheingold, A. L.; Figueroa, J. S. *J. Am. Chem. Soc.* **2014,** *136*, 10262-10265.

78. Chakraborty, S.; Brennessel, W. W.; Jones, W. D. *J. Am. Chem. Soc.* **2014,** *136*, 8564-8567.

79. Comanescu, C. C.; Iluc, V. M. *Organometallics*. **2014,** *33*, 6059-6064.

80. Doyle, L. E.; Piers, W. E.; Borau-Garcia, J. *J. Am. Chem. Soc.* **2015,** *137*, 2187-2190.

81. DuBois, D. L. *Inorg. Chem.* **2014,** *53*, 3935-3960.

82. Filonenko, G. A.; Smykowski, D.; Szyja, B. M.; Li, G.; Szczygiel, J.; Hensen, E. J. M.; Pidko, E. A. *ACS Catal.* **2015,** *5*, 1145-1154.

83. Moore, C. M.; Dahl, E. W.; Szymczak, N. K. *Curr. Opin. Chem. Biol.* **2015,** *25*, 9-17.

84. Morris, R. H. *Acc. Chem. Res.* **2015,** *48*, 1494-1502.

85. Gordon, J. C.; Kubas, G. J. *Organometallics*. **2010,** *29*, 4682-4701.

86. Liu, Y.-C.; Chu, K.-T.; Jhang, R.-L.; Lee, G.-H.; Chiang, M.-H. *Chem. Commun.* **2013,** *49*, 4743-4745.

87. Mulder, D. W.; Ratzloff, M. W.; Shepard, E. M.; Byer, A. S.; Noone, S. M.; Peters, J. W.; Broderick, J. B.; King, P. W. *J. Am. Chem. Soc.* **2013,** *135*, 6921-6929.

88. Kubas, G. J. *Proc. Natl. Acad. Sci. U.S.A.* **2007,** *104*, 6901.

89. Bercaw, J. E.; Labinger, J. A. *Proc. Natl. Acad. Sci. U.S.A.* **2007,** *104*, 6899.

90. Paparo, A.; Okuda, J. *Coord. Chem. Rev.* **2017,** *334*, 136-149.

91. Aresta, M.; Nobile, C. F.; Albano, V. G.; Forni, E.; Manassero, M. *J. Chem. Soc., Chem. Commun.* **1975**, 636-7.

92. Aresta, M.; Nobile, C. F.; Sacco, A. *Inorg. Chim. Acta*. **1975,** *12*, 167-78.

93. Laplaza, C. E.; Cummins, C. C. *Science*. **1995,** *268*, 861-3.

94. Laplaza, C. E.; Johnson, M. J. A.; Peters, J.; Odom, A. L.; Kim, E.; Cummins, C. C.; George, G. N.; Pickering, I. J. *J. Am. Chem. Soc.* **1996,** *118*, 8623-8638.

95. Luca, O. R.; Crabtree, R. H. *Chem. Soc. Rev.* **2013,** *42*, 1440-1459.

96. He, T.; Tsvetkov, N. P.; Andino, J. G.; Gao, X.-F.; Fullmer, B. C.; Caulton, K. G. *J. Am. Chem. Soc.* **2010,** *132*, 910-911.

97. Gregor, L. C.; Chen, C.-H.; Fafard, C. M.; Fan, L.; Guo, C.; Foxman, B. M.; Gusev, D. G.; Ozerov, O. V. *Dalton Trans.* **2010,** *39*, 3195-3202.

98. Chakraborty, S.; Lagaditis, P. O.; Förster, M.; Bielinski, E. A.; Hazari, N.; Holthausen, M. C.; Jones, W. D.; Schneider, S. *ACS Catalysis*. **2014,** *4*, 3994-4003.

99. Liu, T.; Chen, S.; O'Hagan, M. J.; Rakowski DuBois, M.; Bullock, R. M.; DuBois, D. L. *J. Am. Chem. Soc.* **2012,** *134*, 6257-6272.

100. Wiese, S.; Kilgore, U. J.; Ho, M.-H.; Raugei, S.; DuBois, D. L.; Bullock, R. M.; Helm, M. L. *ACS Catal.* **2013,** *3*, 2527-2535.

101. Helm, M. L.; Stewart, M. P.; Bullock, R. M.; DuBois, M. R.; DuBois, D. L. *Science*. **2011,** *333*, 863.

102. Berry, J. F.; Lu, C. C. *Inorg. Chem.* **2017,** *56*, 7577-7581.

103. Zhou, Y.-Y.; Hartline, D. R.; Steiman, T. J.; Fanwick, P. E.; Uyeda, C. *Inorg. Chem.* **2014,** *53*, 11770-11777.

104. Zhou, Y.-Y.; Uyeda, C. *Science*. **2019,** *363*, 857-862.

105. Krogman, J. P.; Foxman, B. M.; Thomas, C. M. *J. Am. Chem. Soc.* **2011,** *133*, 14582-14585.

106. Napoline, J. W.; Krogman, J. P.; Shi, R.; Kuppuswamy, S.; Bezpalko, M. W.; Foxman, B. M.; Thomas, C. M. *Eur. J. Inorg. Chem.* **2013,** *2013*, 3874-3882.

107. Greenwood, B. P.; Forman, S. I.; Rowe, G. T.; Chen, C.-H.; Foxman, B. M.; Thomas, C. M. *Inorg. Chem.* **2009,** *48*, 6251-6260.

108. Wu, B.; Gramigna, K. M.; Bezpalko, M. W.; Foxman, B. M.; Thomas, C. M. *Inorg. Chem.* **2015,** *54*, 10909-10917.

109. Wu, B.; Hernandez Sanchez, R.; Bezpalko, M. W.; Foxman, B. M.; Thomas, C. M. *Inorg. Chem.* **2014,** *53*, 10021-10023.

110. Zhao, Q.; Harris, T. D.; Betley, T. A. *J. Am. Chem. Soc.* **2011,** *133*, 8293-8306.

111. Hernandez Sanchez, R.; Zheng, S.-L.; Betley, T. A. *J. Am. Chem. Soc.* **2015,** *137*, 11126-11143.

112. Harris, T. D.; Betley, T. A. *J. Am. Chem. Soc.* **2011,** *133*, 13852-13855.

113. Powers, T. M.; Betley, T. A. *J. Am. Chem. Soc.* **2013,** *135*, 12289-12296.

114. Powers, T. M.; Fout, A. R.; Zheng, S.-L.; Betley, T. A. *J. Am. Chem. Soc.* **2011,** *133*, 3336-3338.

115. Di Francesco, G. N.; Gaillard, A.; Ghiviriga, I.; Abboud, K. A.; Murray, L. J. *Inorg. Chem.* **2014,** *53*, 4647-4654.

116. Guillet, G. L.; Sloane, F. T.; Dumont, M. F.; Abboud, K. A.; Murray, L. J. *Dalton Trans.* **2012,** *41*, 7866-7869.

117. Murray, L. J.; Weare, W. W.; Shearer, J.; Mitchell, A. D.; Abboud, K. A. *J. Am. Chem. Soc.* **2014,** *136*, 13502-13505.

118. Zhang, S.; Fallah, H.; Gardner, E. J.; Kundu, S.; Bertke, J. A.; Cundari, T. R.; Warren, T. H. *Angew. Chem. Int. Ed.* **2016,** *55*, 9927-9931.

119. Lee, Y.; Anderton, K. J.; Sloane, F. T.; Abboud, K. A.; Garcia-Serres, R.; Murray, L. J. *J. Am. Chem. Soc.* **2015,** *137*, 10610-10617.

120. Amgoune, A.; Bourissou, D. *Chem. Commun.* **2011,** *47*, 859-871.

121. Maity, A.; Teets, T. S. *Chem. Rev.* **2016,** *116*, 8873-8911.

122. Corma, A.; García, H. *Chem. Rev.* **2003,** *103*, 4307-4366.

123. Stephan, D. W.; Erker, G. *Angew. Chem. Int. Ed.* **2015,** *54*, 6400-6441.

124. Galstyan, G.; Knapp, E.-W. *J. Comp. Chem*. **2015,** *36*, 69-78.

125. Yano, J.; Kern, J.; Sauer, K.; Latimer, M. J.; Pushkar, Y.; Biesiadka, J.; Loll, B.; Saenger, W.; Messinger, J.; Zouni, A.; Yachandra, V. K. *Science*. **2006,** *314*, 821-825.

126. Friedel, C.; Crafts, J. M. *J. Chem. Soc*. **1877,** *32*, 725-791.

127. Li, F.; Van Heuvelen, K. M.; Meier, K. K.; Münck, E.; Que, L. *J. Am. Chem. Soc.* **2013,** *135*, 10198-10201.

128. Massey, A. G.; Park, A. J. *J. Organomet. Chem.* **1964,** *2*, 245-250.

129. Erker, G. *Dalton Trans.* **2005**, 1883-1890.

130. Jacobsen, H.; Berke, H.; Döring, S.; Kehr, G.; Erker, G.; Fröhlich, R.; Meyer, O. *Organometallics*. **1999,** *18*, 1724-1735.

131. Ewen, J. A.; Jones, R. L.; Razavi, A.; Ferrara, J. D. *J. Am. Chem. Soc.* **1988,** *110*, 6255-6256.

132. Giardello, M. A.; Eisen, M. S.; Stern, C. L.; Marks, T. J. *J. Am. Chem. Soc.* **1995,** *117*, 12114-12129.

133. Yang, X.; Stern, C. L.; Marks, T. J. *J. Am. Chem. Soc.* **1991,** *113*, 3623-3625.

134. Welch, G. C.; San Juan, R. R.; Masuda, J. D.; Stephan, D. W. *Science*. **2006,** *314*, 1124-1126.

135. Ullrich, M.; Lough, A. J.; Stephan, D. W. *J. Am. Chem. Soc.* **2009,** *131*, 52-53.

136. Welch, G. C.; Stephan, D. W. *J. Am. Chem. Soc.* **2007,** *129*, 1880-1881.

137. Devillard, M.; Declercq, R.; Nicolas, E.; Ehlers, A. W.; Backs, J.; Saffon-Merceron, N.; Bouhadir, G.; Slootweg, J. C.; Uhl, W.; Bourissou, D. *J. Am. Chem. Soc.* **2016,** *138*, 4917-4926.

138. Fong, H.; Moret, M.-E.; Lee, Y.; Peters, J. C. *Organometallics*. **2013,** *32*, 3053-3062.

139. Gunderson, W. A.; Suess, D. L. M.; Fong, H.; Wang, X.; Hoffmann, C. M.; Cutsail, G. E., III; Peters, J. C.; Hoffman, B. M. *J. Am. Chem. Soc.* **2014,** *136*, 14998-15009.

140. Harman, W. H.; Lin, T.-P.; Peters, J. C. *Angew. Chem. Int. Ed.* **2014,** *53*, 1081-1086.

141. Moret, M.-E.; Peters, J. C. *Angew. Chem. Int. Ed.* **2011,** *50*, 2063-2067, S2063/1-S2063/25.

142. Suess, D. L. M.; Tsay, C.; Peters, J. C. *J. Am. Chem. Soc.* **2012,** *134*, 14158-14164.

143. Chen, C.-H.; Gabbai, F. P. *Dalton Trans.* **2018,** *47*, 12075-12078.

144. You, D.; Gabbai, F. P. *J. Am. Chem. Soc.* **2017,** *139*, 6843-6846.

145. Pan, B.; Gabbai, F. P. *J. Am. Chem. Soc.* **2014,** *136*, 9564-9567.

146. Gabbai, F. P. *Angew. Chem. Int. Ed.* **2003,** *42*, 2218-2221.

147. Parkin, G. *Organometallics*. **2006,** *25*, 4744-4747.

148. Harman, W. H.; Peters, J. C. *J. Am. Chem. Soc.* **2012,** *134*, 5080-5082.

149. Bouhadir, G.; Bourissou, D. *Chem. Soc. Rev.* **2016,** *45*, 1065-1079.

150. Power, P. P. *Chem. Rev.* **2003,** *103*, 789-810.

151. Tsoureas, N.; Hamilton, A.; Haddow, M. F.; Harvey, J. N.; Orpen, A. G.; Owen, G. R. *Organometallics*. **2013,** *32*, 2840-2856.

152. Tsoureas, N.; Haddow, M. F.; Hamilton, A.; Owen, G. R. *Chem. Commun.* **2009**, 2538-2540.

153. Tsoureas, N.; Bevis, T.; Butts, C. P.; Hamilton, A.; Owen, G. R. *Organometallics*. **2009,** *28*, 5222-5232.

154. Suess, D. L. M.; Peters, J. C. *J. Am. Chem. Soc.* **2013,** *135*, 4938-4941.

155. Schindler, T.; Lux, M.; Peters, M.; Scharf, L. T.; Osseili, H.; Maron, L.; Tauchert, M. E. *Organometallics*. **2015,** *34*, 1978-1984.

156. Nesbit, M. A.; Suess, D. L. M.; Peters, J. C. *Organometallics*. **2015,** *34*, 4741-4752.

157. Miller, A. J. M.; Labinger, J. A.; Bercaw, J. E. *J. Am. Chem. Soc.* **2010,** *132*, 3301-3303.

158. Miller, A. J. M.; Labinger, J. A.; Bercaw, J. E. *Organometallics*. **2010,** *29*, 4499-4516.

159. MacMillan, S. N.; Hill Harman, W.; Peters, J. C. *Chem. Sci.* **2014,** *5*, 590-597.

160. Kuzu, I.; Krummenacher, I.; Meyer, J.; Armbruster, F.; Breher, F. *Dalton Trans.* **2008**, 5836-5865.

161. Kameo, H.; Nakazawa, H. *Organometallics*. **2012,** *31*, 7476-7484.

162. Kameo, H.; Hashimoto, Y.; Nakazawa, H. *Organometallics*. **2012,** *31*, 3155-3162.

163. Kameo, H.; Hashimoto, Y.; Nakazawa, H. *Organometallics*. **2012,** *31*, 4251-4258.

164. Figueroa, J. S.; Melnick, J. G.; Parkin, G. *Inorg. Chem.* **2006,** *45*, 7056-7058.

165. Devillard, M.; Nicolas, E.; Ehlers, A. W.; Backs, J.; Mallet-Ladeira, S.; Bouhadir, G.; Slootweg, J. C.; Uhl, W.; Bourissou, D. *Chem. - Eur. J.* **2015,** *21*, 74-79.

166. Devillard, M.; Bouhadir, G.; Bourissou, D. *Angew. Chem. Int. Ed.* **2015,** *54*, 730-732.

167. Del Castillo, T. J.; Thompson, N. B.; Suess, D. L. M.; Ung, G.; Peters, J. C. *Inorg. Chem.* **2015,** *54*, 9256-9262.

168. Crossley, I. R.; Hill, A. F.; Willis, A. C. *Organometallics*. **2008,** *27*, 312-315.

169. Cowie, B. E.; Tsao, F. A.; Emslie, D. J. H. *Angew. Chem. Int. Ed.* **2015,** *54*, 2165-2169.

170. Cowie, B. E.; Emslie, D. J. H. *Chem. - Eur. J.* **2014,** *20*, 16899-16912.

171. Conifer, C. M.; Law, D. J.; Sunley, G. J.; White, A. J. P.; Britovsek, G. J. P. *Organometallics*. **2011,** *30*, 4060-4066.

172. Boudreau, J.; Fontaine, F.-G. *Organometallics*. **2011,** *30*, 511-519.

173. Bontemps, S.; Bouhadir, G.; Miqueu, K.; Bourissou, D. *J. Am. Chem. Soc.* **2006,** *128*, 12056-12057.

174. Eisenhart, R. J.; Clouston, L. J.; Lu, C. C. *Acc. Chem. Res.* **2015,** *48*, 2885-2894.

175. Cammarota, R. C.; Clouston, L. J.; Lu, C. C. *Coord. Chem. Rev.* **2017,** *334*, 100-111.

176. Clouston, L. J.; Siedschlag, R. B.; Rudd, P. A.; Planas, N.; Hu, S.; Miller, A. D.; Gagliardi, L.; Lu, C. C. *J. Am. Chem. Soc.* **2013,** *135*, 13142-13148.

177. Eisenhart, R. J.; Rudd, P. A.; Planas, N.; Boyce, D. W.; Carlson, R. K.; Tolman, W. B.; Bill, E.; Gagliardi, L.; Lu, C. C. *Inorg. Chem.* **2015,** *54*, 7579-7592.

178. Clouston, L. J.; Bernales, V.; Cammarota, R. C.; Carlson, R. K.; Bill, E.; Gagliardi, L.; Lu, C. C. *Inorg. Chem.* **2015,** *54*, 11669-11679.

179. Siedschlag, R. B.; Bernales, V.; Vogiatzis, K. D.; Planas, N.; Clouston, L. J.; Bill, E.; Gagliardi, L.; Lu, C. C. *J. Am. Chem. Soc.* **2015,** *137*, 4638-4641.

180. Clouston, L. J.; Bernales, V.; Carlson, R. K.; Gagliardi, L.; Lu, C. C. *Inorg. Chem.* **2015,** *54*, 9263-9270.

181. Anderson, J. S.; Rittle, J.; Peters, J. C. *Nature*. **2013,** *501*, 84-7.

182. Deegan, M. M.; Peters, J. C. *J. Am. Chem. Soc.* **2017,** *139*, 2561-2564.

183. Rudd, P. A.; Liu, S.; Gagliardi, L.; Young, V. G.; Lu, C. C. *J. Am. Chem. Soc.* **2011,** *133*, 20724-20727.

184. Cammarota, R. C. Greater than the Sum of Its Parts: Tuning Nickel for Uncommon Small Molecule Reactivity and Catalysis via Dative Bonds with Group 13 Lewis Acidic Metalloligands. University of Minnesota - Twin Cities 2018.

185. Rudd, P. A.; Planas, N.; Bill, E.; Gagliardi, L.; Lu, C. C. *Eur. J. Inorg. Chem.* **2013,** *2013*, 3898-3906.

186. Albeit, the reduction potential is not as mild as originally reported. The correct electrochemical characterization is reported in: Cammarota, R. C.; Clouston, L. J.; Lu, C. C. *Coord. Chem. Rev.* **2017,** *334*, 100-111.

187. Cammarota, R. C.; Lu, C. C. *J. Am. Chem. Soc.* **2015,** *137*, 12486-12489.

188. Cammarota, R. C.; Vollmer, M. V.; Xie, J.; Ye, J.; Linehan, J. C.; Burgess, S. A.; Appel, A. M.; Gagliardi, L.; Lu, C. C. *J. Am. Chem. Soc.* **2017,** *139*, 14244-14250.

References for Chapter 2:

1. Franke, R.; Selent, D.; Börner, A. *Chem. Rev.* **2012,** *112*, 5675-5732.

2. Chirik, P. J. *Acc. Chem. Res.* **2015,** *48*, 1687-1695.

3. Dubois, M. R.; Dubois, D. L. *Acc. Chem. Res.* **2009,** *42*, 1974-1982.

4. Crabtree, R. H. *Chem. Rev.* **2016,** *116*, 8750–8769.

5. Kubas, G. J. *Metal Dihydrogen and σ-Bond Complexes*. Kluwer Academic Plenum Publishers: New York, 2001.

6. Kubas, G. J. *Chem. Rev.* **2007,** *107*, 4152-4205.

7. Fong, H.; Moret, M.-E.; Lee, Y.; Peters, J. C. *Organometallics*. **2013,** *32*, 3053-3062.

8. Harman, W. H.; Lin, T. P.; Peters, J. C. *Angew. Chem. Int. Ed.* **2013,** *53*, 1081-1086.

9. Harman, W. H.; Peters, J. C. *J. Am. Chem. Soc.* **2012,** *134*, 5080-5082.

10. Tsay, C.; Peters, J. C. *Chemical Science*. **2012,** *3*, 1313-1318.

11. Bullock, R. M. *Science*. **2013,** *342*, 1054-1055.

12. Chakraborty, S.; Dai, H.; Bhattacharya, P.; Fairweather, N. T.; Gibson, M. S.; Krause, J. A.; Guan, H. *J. Am. Chem. Soc.* **2014,** *136*, 7869-7872.

13. Zhang, G.; Scott, B. L.; Hanson, S. K. *Angew. Chem. Int. Ed.* **2012,** *51*, 12102-12106.

14. Zuo, W.; Lough, A. J.; Li, Y. F.; Morris, R. H. *Science*. **2013,** *342*, 1080-1083.

15. Gadd, G. E.; Upmacis, R. K.; Poliakoff, M.; Turner, J. J. *J. Am. Chem. Soc.* **1986,** *108*, 2547-2552.

16. Sweany, R. L.; Russell, F. N. *Organometallics*. **1988,** *7*, 719-727.

17. Bianchini, C.; Mealli, C.; Meli, A.; Peruzzini, M.; Zanobini, F. *J. Am. Chem. Soc.* **1988,** *110*, 8725-8726.

18. Bianchini, C.; Mealli, C.; Peruzzini, M.; Zanobini, F. *J. Am. Chem. Soc.* **1992,** *114*, 5905-5906.

19. Heinekey, D. M.; Lledós, A.; Lluch, J. M. *Chem. Soc. Rev.* **2004,** *33*, 175-182.

20. van Roon, M.; Heinekey, D. M. *J. Am. Chem. Soc.* **1996,** *118*, 12134-12140.

21. Hebden, T. J.; Gusev, D. G.; Kaminsky, W.; Goldberg, K. I.; Heinekey, D. M. *Angew. Chem. Int. Ed.* **2010,** *50*, 1873-1876.

22. Gunderson, W. A.; Suess, D. L. M.; Fong, H.; Wang, X.; Hoffmann, C. M.; III, G. E. C.; Peters, J. C.; Hoffman, B. M. *J. Am. Chem. Soc.* **2014,** *136*, 14988-15009.

23. Suess, D. L.; Tsay, C.; Peters, J. C. *J. Am. Chem. Soc.* **2012,** *134*, 14158-14164.

24. Tokmic, K.; Fout, A. R. *J. Am. Chem. Soc.* **2016,** *138*, 13700–13705.

25. Tokmic, K.; Markus, C. R.; Zhu, L.; Fout, A. R. *J. Am. Chem. Soc.* **2016,** *138*, 11907–11913.

26. Parkin, G. *Organometallics*. **2006,** *25*, 4744-4747.

27. Andrews, L.; Wang, X.; Alikhani, M. E.; Manceron, L. *J. Phys. Chem. A*. **2001,** *105*, 3052−3063.

28. Frohman, D. J.; Grubbs, G. S., II; Yu, Z.; Novick, S. E. *Inorg. Chem.* **2013,** *52*.

29. Grubbs, G. S., II; Obenchain, D. A.; Pickett, H. M.; Novick, S. E. *J. Chem. Phys.* **2014,** *141*.

30. Connor, B. A.; Rittle, J.; VanderVelde, D.; Peters, J. C. *Organometallics*. **2016,** *35*, 686-690.

31. Cammarota, R. C.; Lu, C. C. *J. Am. Chem. Soc.* **2015,** *137*, 12486-12489.

32. Kubas, G. J. *J. Organomet. Chem.* **2001,** *635*, 37–68.

33. Rudd, P. A.; Liu, S.; Gagliardi, L.; V. G. Young, J.; Lu, C. C. *J. Am. Chem. Soc.* **2011,** *133*, 20724-20727.

34. Rudd, P. A.; Planas, N.; Bill, E.; Gagliardi, L.; Lu, C. C. *Eur. J. Inorg. Chem.* **2013,** *2013*, 3898-3906.

35. Hammer, R.; Klein, H.-F. *Zeitschrift für Naturforschung B*. **1977,** *32*, 138-143.

36. Leach, P. A.; Geib, S. J.; II, J. A. C.; Warnock, G. F.; Cooper, N. J. *J. Am. Chem. Soc.* **1994,** *116*, 8566-8574.

37. Margulieux, G. W.; Weidemann, N.; Lacy, D. C.; Moore, C. E.; Rheingold, A. L.; Figueroa, J. S. *J. Am. Chem. Soc.* **2010,** *132*, 5033-5035.

38. Brennessel, W. W.; Ellis, J. E. *Inorg. Chem.* **2012,** *51*, 9076-9094.

39. Brennessel, W. W.; Young Jr., V. G.; Ellis, J. E. *Angew. Chem. Int. Ed.* **2002,** *41*, 1211-1215.

40. Jonas, K. *Adv. Organomet. Chem.* **1981,** *19*, 97-112.

41. Carpenter, A. E.; Margulieux, G. W.; Millard, M. D.; E., M. C.; Weidemann, N.; Rheingold, A. L.; Figueroa, J. S. *Angew. Chem. Int. Ed.* **2012,** *51*, 9412-9416.

42. Jonas, K. Method of preparing transition metal-olefin complex compounds and alkali metal-transition metal-olefin complex compounds. US4169845A, 1979.

43. Cammarota, R. C.; Clouston, L. J.; Lu, C. C. *Coord. Chem. Rev.* **2016,** *334*, 100–111.

44. Moore, J. T.; Smith, N. E.; Lu, C. C. *Dalton Trans.* **2017,** *46*, 5689-5701

45. Eisenhart, R. J.; Rudd, P. A.; Planas, N.; Boyce, D. W.; Carlson, R. K.; Tolman, W. B.; Bill, E.; Gagliardi, L.; Lu, C. C. *Inorg. Chem.* **2015,** *54*, 7579-7592.

46. Heinekey, D. M.; Mellows, H.; Pratum, T. *J. Am. Chem. Soc.* **2000** *122* 6498-6499.

47. Desrosiers, P. J.; Cai, L.; Lin, Z.; Richards, R.; Halpern, J. *J. Am. Chem. Soc.* **1991,** *113*, 4173-4184.

48. Morris, R. H. *Can. J. Chem.* **1996,** *74*, 1907-1915.

49. Morris, R. H. *Coord. Chem. Rev.* **2008,** *252*, 2381–2394.

50. Crabtree, R. H., Dihydrogen Complexes & Related Sigma Complexes. In *Encyclopedia of Inorganic Chemistry*, John Wiley & Sons, Ltd: 2006; pp 1-6.

51. Luther, T. A.; Heinekey, D. M. *Inorg. Chem.* **1998,** *37*, 127-132.

52. Maltby, P. A.; Schlaf, M.; Steinbeck, M.; Lough, A. J.; Morris, R. H.; Klooster, W. T.; Koetzle, T. F.; Srivastava, R. C. *J. Am. Chem. Soc.* **1996,** *118*, 5396-5407.

53. Holland, P. L. *Dalton Transactions*. **2010,** *39*, 5415-5424.

54. Cotton, F. A.; Murillo, C. A., *Multiple Bonds Between Metal Atoms, 3rd ed. Chapter 3.* 2007.

55. Cordero, B.; Gómez, V.; Platero-Prats, A. E.; Revés, M.; Echeverría, J.; Cremades, E.; Barragán, F.; Alvarez, S. *Dalton Trans*. **2008**, 2832-2838.

56. Morris, P. G. J. R. H. *Coord. Chem. Rev.* **1992,** *121*.

57. Rudd, P. A. Stabilizing Metal-Alanes and Metal-Metal Multiple Bonds to Effect Small Molecule Transformations. University of Minnesota 2014.

58. Pearson, R. G. *J. Am. Chem. Soc.* **1963,** *85*, 3533-3539.

59. Holland, P. L. *Dalton Trans.* **2010,** *39*, 5415-5424.

60. Kubas, G. J. *Proc. Natl. Acad. Sci. U.S.A.* **2007,** *104*, 6901-6907.

61. Corey, J. Y.; Braddock-Wilking, J. *Chem. Rev.* **1999,** *99*, 175-292.

62. Hill, R. H.; Wrighton, M. S. *Organometallics*. **1987,** *6*, 632-638.

63. Iluc, V. M.; Hillhouse, G. L. *Tetrahedron*. **2006,** *62*, 7577-7582.

64. Brookhart, M.; Grant, B. E.; Lenges, C. P.; Prosenc, M. H.; White, P. S. *Angew. Chem. Int. Ed.* **2000,** *39*, 1676-1679.

65. MacInnis, M. C.; MacLean, D. F.; Lundgren, R. J.; McDonald, R.; Turculet, L. *Organometallics*. **2007,** *26*, 6522-6525.

66. Mo, Z.; Xiao, J.; Gao, Y.; Deng, L. *J. Am. Chem. Soc.* **2014,** *136*, 17414-17417.

67. Xu, S.; Zhang, P.; Li, X.; Xue, B.; Sun, H.; Fuhr, O.; Fenske, D. *Chem. Asian J.* **2017,** *12*, 1234-1239.

68. Bart, S. C.; Lobkovsky, E.; Chirik, P. J. *J. Am. Chem. Soc.* **2004,** *126*, 13794-13807.

69. Lee, Y.; Kinney, R. A.; Hoffman, B. M.; Peters, J. C. *J. Am. Chem. Soc.* **2011,** *133*, 16366–16369.

70. Doherty, M. D.; Grant, B.; White, P. S.; Brookhart, M. *Organometallics*. **2007,** *26*, 5950-5960.

71. Denning, R. G., *Electronic Structure and Bonding in Actinyl Ions*. Springer: Berlin, 1992; Vol. 79.

72. Lam, O. P.; Franke, S. M.; Nakai, H.; Heinemann, F. W.; Hieringer, W.; Meyer, K. *Inorg. Chem.* **2012,** *51*, 6190-6199.

73. Lewis, A. J.; Carroll, P. J.; Schelter, E. J. *J. Am. Chem. Soc.* **2013,** *135*, 13185-13192.

74. Gregson, M.; Lu, E.; Mills, D. P.; Tuna, F.; McInnes, E. J. L.; Hennig, C.; Scheinost, A. C.; McMaster, J.; Lewis, W.; Blake, A. J.; Kerridge, A.; Liddle, S. T. *Nat. Commun.* **2016,** *8*, 14137-14148.

75. Pearson, R. G. *Inorg. Chem.* **2002,** *12*, 712-713.

76. Fulmer, G. R.; Miller, A. J. M.; Sherden, N. H.; Gottlieb, H. E.; Nudelman, A.; Stoltz, B. M.; Bercaw, J. E.; Goldberg, K. I. *Organometallics*. **2010,** *29*, 2176-2179.

77. Krause, L.; Herbst-Irmer, R.; Sheldrick, G. M.; Stalke, D. *J. Appl. Crystallogr.* **2015,** *48*.

78. Sheldrick, G. M. *Acta Crystallogr. Sect. A: Found. Crystallogr.* **2015,** *71*.

79. Sheldrick, G. M. *Acta Crystallogr. Sect. A: Found. Crystallogr.* **2008,** *64*, 112-122.

80. Hübcshle, C. B.; Sheldrick S. G.; Dittrich, B. *J. Appl. Crystallogr.* **2001**, 1281-1284.

81. *Persistence of Vision (TM) Raytracer.*, Persistence of Vision Pty. Ltd. : Williamstown, Victoria, Australia., 2004.

82. Frisch, M. J. T., G. W.; Schlegel, H. B.; Scuseria, G. E.; Robb, M. A.; Cheeseman, J.; R.; Scalmani, G. B., V.; Mennucci, B.; Petersson, G. A.; Nakatsuji, H.; Caricato, M.; Li,; X.; Hratchian, H. P. I., A. F.; Bloino, J.; Zheng, G.; Sonnenberg, J. L.; Hada, M.; Ehara,; M.; Toyota, K. F., R.; Hasegawa, J.; Ishida, M.; Nakajima, T.; Honda, Y.; Kitao, O.;; Nakai, H. V., T.; Montgomery, J. A., Jr.; Peralta, J. E.; Ogliaro, F.; Bearpark, M.; Heyd, J.; J.; Brothers, E. K., K. N.; Staroverov, V. N.; Kobayashi, R.; Normand, J.; Raghavachari, K.;; Rendell, A. B., J. C.; Iyengar, S. S.; Tomasi, J.; Cossi, M.; Rega, N.; Millam, M. J.; Klene,; M.; Knox, J. E. C., J. B.; Bakken, V.; Adamo, C.; Jaramillo, J.; Gomperts, R.; Stratmann, R.; E.; Yazyev, O. A., A. J.; Cammi, R.; Pomelli, C.; Ochterski, J. W.; Martin, R. L.;; Morokuma, K. Z., V. G.; Voth, G. A.; Salvador, P.; Dannenberg, J. J.; Dapprich, S.;; Daniels, A. D. F., Ö.; Foresman, J. B.; Ortiz, J. V.; Cioslowski, J.; Fox, D. J. *Gaussian 09*, Wallingford, CT, 2009.

83. Zhao, Y. T., D. G. *J. Chem. Phys.* **2006,** *125*, 194101.

84. Weigend, F. R. A., R. *Phys. Chem. Chem. Phys*. **2005**, 3297.

85. Andrae, D. H., U.; Dolg, M.; Stoll, H.; Preuß, H. *Theor. Chim. Acta*. **1990,** *77*.

86. Marenich, A. V. C., C. J.; Truhlar, D. G. *J. Phys. Chem. B*. **2009,** *13*, 6378.

References for Chapter 3:

1. Wang, W.-H.; Himeda, Y.; Muckerman, J. T.; Manbeck, G. F.; Fujita, E. *Chem. Rev.* . **2015,** *115*, 12936-12973.

2. Wang, W.; Wang, S.; Ma, X.; Gong, J. *Chem. Soc. Rev.* **2011,** *40*, 3703-3727.

3. Jessop, P. G.; Joo, F.; Tai, C.-C. *Coord. Chem. Rev.* **2004,** *248*, 2425-2442.

4. Benson, E. E.; Kubiak, C. P.; Sathrum, A. J.; Smieja, J. M. *Chem. Soc. Rev.* **2009,** *38*, 89-99.

5. Aresta, M.; Dibenedetto, A.; Angelini, A. *Chem. Rev.* **2014,** *114*, 1709-1742.

6. Olah, G. A.; Prakash, G. K. S.; Goeppert, A. *J. Am. Chem. Soc.* **2011,** *133*, 12881-12898.

7. Cokoja, M.; Bruckmeier, C.; Rieger, B.; Herrmann, W. A.; Kuehn, F. E. *Angew. Chem. Int. Ed.* **2011,** *50*, 8510-8537.

8. Leitner, W. *Angew. Chem. Int. Ed. Engl.* **1995,** *34*, 2207-21.

9. Bullock, R. M. *Catalysis without Precious Metals*. Ed.; Wiley-VCH: Weinheim, 2010.

10. Angermund, K.; Baumann, W.; Dinjus, E.; Fornika, R.; Goerls, H.; Kessler, M.; Krueger, C.; Leitner, W.; Lutz, F. *Chem. - Eur. J.* **1997,** *3*, 755-764.

11. Azua, A.; Sanz, S.; Peris, E. *Chem. - Eur. J.* **2011,** *17*, 3963-3967.

12. Federsel, C.; Jackstell, R.; Beller, M. *Angew. Chem. Int. Ed.* **2010,** *49*, 6254-6257.

13. Fujita, E.; Muckerman, J. T.; Himeda, Y. *Biochim. Biophys. Acta, Bioenerg.* **2013,** *1827*, 1031-1038.

14. Hayashi, H.; Ogo, S.; Fukuzumi, S. *Chem. Commun.* **2004**, 2714-2715.

15. Huff, C. A.; Sanford, M. S. *ACS Catal.* **2013,** *3*, 2412-2416.

16. Hull, J. F.; Himeda, Y.; Wang, W.-H.; Hashiguchi, B.; Periana, R.; Szalda, D. J.; Muckerman, J. T.; Fujita, E. *Nat. Chem.* **2012,** *4*, 383-388.

17. Inoue, Y.; Sasaki, Y.; Hasimoto, H. *J. Chem. Soc., Chem. Commun.* **1975**, 718-19.

18. Kothandaraman, J.; Goeppert, A.; Czaun, M.; Olah, G. A.; Prakash, G. K. S. *J. Am. Chem. Soc.* **2016,** *138*, 778-781.

19. Munshi, P.; Main, A. D.; Linehan, J. C.; Tai, C.-C.; Jessop, P. G. *J. Am. Chem. Soc.* **2002,** *124*, 7963-7971.

20. Ogo, S.; Kabe, R.; Hayashi, H.; Harada, R.; Fukuzumi, S. *Dalton Trans.* **2006**, 4657-4663.

21. Rezayee, N. M.; Huff, C. A.; Sanford, M. S. *J. Am. Chem. Soc.* **2015,** *137*, 1028-1031.

22. Sanz, S.; Azua, A.; Peris, E. *Dalton Trans.* **2010,** *39*, 6339-6343.

23. Schmeier, T. J.; Dobereiner, G. E.; Crabtree, R. H.; Hazari, N. *J. Am. Chem. Soc.* **2011,** *133*, 9274-9277.

24. Tanaka, R.; Yamashita, M.; Nozaki, K. *J. Am. Chem. Soc.* **2009,** *131*, 14168-14169.

25. Wesselbaum, S.; Moha, V.; Meuresch, M.; Brosinski, S.; Thenert, K. M.; Kothe, J.; Stein, T. v.; Englert, U.; Hoelscher, M.; Klankermayer, J.; Leitner, W. *Chem. Sci.* **2015,** *6*, 693-704.

26. Wesselbaum, S.; vom Stein, T.; Klankermayer, J.; Leitner, W. *Angew. Chem. Int. Ed.* **2012,** *51*, 7499-7502.

27. Badiei, Y. M.; Wang, W.-H.; Hull, J. F.; Szalda, D. J.; Muckerman, J. T.; Himeda, Y.; Fujita, E. *Inorg. Chem.* **2013,** *52*, 12576-12586.

28. Burgess, S. A.; Kendall, A. J.; Tyler, D. R.; Linehan, J. C.; Appel, A. M. *ACS Catal.* **2017,** *7*, 3089-3096.

29. Federsel, C.; Boddien, A.; Jackstell, R.; Jennerjahn, R.; Dyson, P. J.; Scopelliti, R.; Laurenczy, G.; Beller, M. *Angew. Chem. Int. Ed.* **2010,** *49*, 9777-9780.

30. Federsel, C.; Ziebart, C.; Jackstell, R.; Baumann, W.; Beller, M. *Chem. - Eur. J.* **2012,** *18*, 72-75.

31. Fong, H.; Peters, J. C. *Inorg. Chem.* **2015,** *54*, 5124-5135.

32. Jeletic, M. S.; Helm, M. L.; Hulley, E. B.; Mock, M. T.; Appel, A. M.; Linehan, J. C. *ACS Catal.* **2014,** *4*, 3755-3762.

33. Jeletic, M. S.; Mock, M. T.; Appel, A. M.; Linehan, J. C. *J. Am. Chem. Soc.* **2013,** *135*, 11533-11536.

34. Langer, R.; Diskin-Posner, Y.; Leitus, G.; Shimon, L. J. W.; Ben-David, Y.; Milstein, D. *Angew. Chem. Int. Ed.* **2011,** *50*, 9948-9952.

35. Schneidewind, J.; Adam, R.; Baumann, W.; Jackstell, R.; Beller, M. *Angew. Chem. Int. Ed.* **2017,** *56*, 1890-1893.

36. Spentzos, A. Z.; Barnes, C. L.; Bernskoetter, W. H. *Inorg. Chem.* **2016,** *55*, 8225-8233.

37. Zall, C. M.; Linehan, J. C.; Appel, A. M. *J. Am. Chem. Soc.* **2016,** *138*, 9968-9977.

38. Zhang, Y.; MacIntosh, A. D.; Wong, J. L.; Bielinski, E. A.; Williard, P. G.; Mercado, B. Q.; Hazari, N.; Bernskoetter, W. H. *Chem. Sci.* **2015,** *6*, 4291-4299.

39. Mondal, B.; Neese, F.; Ye, S. *Inorg. Chem.* **2016,** *55*, 5438-5444.

40. Wiedner, E. S.; Chambers, M. B.; Pitman, C. L.; Bullock, R. M.; Miller, A. J. M.; Appel, A. M. *Chem. Rev.* **2016,** *116*, 8655-8692.

41. Waldie, K. M.; Ostericher, A. L.; Reineke, M. H.; Sasayama, A. F.; Kubiak, C. P. *ACS Catalysis*. **2018,** *8*, 1313-1324.

42. Chakraborty, S.; Zhang, J.; Krause, J. A.; Guan, H. *J. Am. Chem. Soc.* **2010,** *132*, 8872-8873.

43. Mock, M. T.; Potter, R. G.; O'Hagan, M. J.; Camaioni, D. M.; Dougherty, W. G.; Kassel, W. S.; DuBois, D. L. *Inorg. Chem.* **2011,** *50*, 11914-11928.

44. Eberhardt, N. A.; Guan, H. *Chem. Rev.* **2016,** *116*, 8373-8426.

45. Evans, G. O.; Newell, C. J. *Inorg. Chim. Acta*. **1978,** *31*, L387-L389.

46. Ziebart, C.; Federsel, C.; Anbarasan, P.; Jackstell, R.; Baumann, W.; Spannenberg, A.; Beller, M.„*J. Am. Chem. Soc.* **2012,** *134*, 20701-20704.

47. Rivada-Wheelaghan, O.; Dauth, A.; Leitus, G.; Diskin-Posner, Y.; Milstein, D. *Inorg. Chem.* **2015,** *54*, 4526-4538.

48. Zhu, F.; Ling, Z.-G.; Yang, G.; Zhou, S. *ChemSusChem*. **2015,** *8*, 609-612.

49. Cammarota, R. C.; Vollmer, M. V.; Xie, J.; Ye, J.; Linehan, J. C.; Burgess, S. A.; Appel, A. M.; Gagliardi, L.; Lu, C. C. *J. Am. Chem. Soc.* **2017,** *139*, 14244-14250.

50. Vollmer, M. V.; Xie, J.; Lu, C. C., *J. Am. Chem. Soc.* **2017,** *139*, 6570-6573.

51. Büschelberger, P. G., Dominik; Reyes-Rodriguez, E. K., Friedrich Koszinowski, Konrad; Jacobi von Wangelin, A.; Wolf, R. *Chem. - Eur. J.* **2017,** *23*, 3139-3151.

52. Yonker, C. R.; Linehan, J. C.*Journal of Organometallic Chemistry*. **2002,** *650*, 249-257.

53. Yonker, C. R.; Linehan, J. C. *Progress in Nuclear Magnetic Resonance Spectroscopy*. **2005,** *47*, 95-109.

54. Kaljurand, I.; Kuett, A.; Soovaeli, L.; Rodima, T.; Maeemets, V.; Leito, I.; Koppel, I. A. *J. Org. Chem.* **2005,** *70*, 1019-1028.

55. Abdur-Rashid, K.; Fong, T. P.; Greaves, B.; Gusev, D. G.; Hinman, J. G.; Landau, S. E.; Lough, A. J.; Morris, R. H. *J. Am. Chem. Soc.* **2000,** *122*, 9155-9171.

56. Carpenter, A. E.; Chan, C.; Rheingold, A. L.; Figueroa, J. S. *Organometallics*. **2016,** *35*, 2319-2326.

57. Goldberg, J. M.; Goldberg, K. I.; Heinekey, D. M.; Burgess, S. A.; Lao, D. B.; Linehan, J. C. *J. Am. Chem. Soc.* **2017,** *139*, 12638-12646.

58. Nanishankar, H. V.; Dutta, S.; Nethaji, M.; Jagirdar, B. R. *Inorg. Chem.* **2005,** *44*, 6203-6210.

59. Van der Sluys, L. S.; Eckert, J.; Eisenstein, O.; Hall, J. H.; Huffman, J. C.; Jackson, S. A.; Koetzle, T. F.; Kubas, G. J.; Vergamini, P. J.; Caulton, K. G. *J. Am. Chem. Soc.* **1990,** *112*, 4831-4841.

60. Bautista, M. T.; Earl, K. A.; Maltby, P. A.; Morris, R. H.; Schweitzer, C. T.; Sella, A. *J. Am. Chem. Soc.* **1988,** *110*, 7031-6.

61. Desrosiers, P. J.; Cai, L.; Lin, Z.; Richards, R.; Halpern, J. *J. Am. Chem. Soc.* **1991,** *113*, 4173-84.

62. Tokmic, K.; Fout, A. R. *J. Am. Chem. Soc.* **2016,** *138*, 13700-13705.

63. Hebden, T. J.; St. John, A. J.; Gusev, D. G.; Kaminsky, W.; Goldberg, K. I.; Heinekey, D. M. *Angew. Chem. Int. Ed.* **2011,** *50*, 1873-1876.

64. Tokmic, K.; Markus, C. R.; Zhu, L.; Fout, A. R. *J. Am. Chem. Soc.* **2016,** *138*, 11907-11913.

65. Kubas, G. J. *J. Organomet. Chem.* **2001,** *635*, 37-68.

66. Moore, J. T.; Smith, N. E.; Lu, C. C. *Dalton Transactions*. **2017,** *46*, 5689-5701.

67. Cammarota, R. C. Greater than the Sum of Its Parts: Tuning Nickel for Uncommon Small Molecule Reactivity and Catalysis via Dative Bonds with Group 13 Lewis Acidic Metalloligands. University of Minnesota - Twin Cities 2018.

68. Vollmer, M. V.; Xie, J.; Cammarota, R. C.; Young Jr, V. G.; Bill, E.; Gagliardi, L.; Lu, C. C., *Angew. Chem. Int. Ed*. **2018,** *57*, 7815-7819.

69. Suess, D. L. M.; Tsay, C.; Peters, J. C. *J. Am. Chem. Soc.* **2012,** *134*, 14158-14164.

70. Vazdar, K.; Kunetskiy, R.; Saame, J.; Kaupmees, K.; Leito, I.; Jahn, U. *Angew. Chem. Int. Ed.* **2014,** *53*, 1435-1438.

71. DuBois, D. L.; Berning, D. E. *Appl. Organomet. Chem.* **2000,** *14*, 860-862.

72. Fulmer, G. R.; Miller, A. J. M.; Sherden, N. H.; Gottlieb, H. E.; Nudelman, A.; Stoltz, B. M.; Bercaw, J. E.; Goldberg, K. I. *Organometallics*. **2010,** *29*, 2176-2179.

73. Rudd, P. A.; Liu, S.; Gagliardi, L.; Young, V. G.; Lu, C. C. *J. Am. Chem. Soc.* **2011,** *133*, 20724-20727.

74. Cammarota, R. C.; Lu, C. C. *J. Am. Chem. Soc.* **2015,** *137*, 12486-12489.

75. Brookhart, M.; Grant, B.; Volpe, A. F. *Organometallics*. **1992,** *11*, 3920-3922.

76. Jutzi, P.; Müller, C.; Stammler, A.; Stammler, H.-G. *Organometallics*. **2000,** *19*, 1442-1444.

77. Wiedner, E. S.; Bullock, R. M. *J. Am. Chem. Soc.* **2016,** *138*, 8309-8318.

78. Krause, L.; Herbst-Irmer, R.; Sheldrick, G. M.; Stalke, D. *J. Appl. Crystallogr.* **2015,** *48*.

79. Hübcshle, C. B.; Sheldrick S. G.; Dittrich, B. *J. Appl. Crystallogr.* **2001**, 1281-1284.

80. Sheldrick, G. M. *Acta Crystallogr. Sect. A: Found. Crystallogr.* **2015,** *71*, 3-8.

81. Sheldrick, G. M. *Acta Crystallogr. Sect. A: Found. Crystallogr.* **2008,** *64*, 112-122.

82. Yonker, C. R.; Linehan, J. C., *J. Organomet. Chem.* **2002,** *650*, 249-257.

83. Frisch, M. J. T., G. W.; Schlegel, H. B.; Scuseria, G. E.;; Robb, M. A. C., J. R.; Scalmani, G.; Barone, V.; Mennucci,; B.; Petersson, G. A. N., H.; Caricato, M.; Li, X.; Hratchian, H.; P.; Izmaylov, A. F. B., J.; Zheng, G.; Sonnenberg, J. L.; Hada, M.;; Ehara, M. T., K.; Fukuda, R.; Hasegawa, J.; Ishida, M.; Nakajima,; T.; Honda, Y. K., O.; Nakai, H.; Vreven, T.; Montgomery, J. A., Jr.;; Peralta, J. E. O., F.; Bearpark, M.; Heyd, J. J.; Brothers, E.; Kudin,; K. N.; Staroverov, V. N. K., R.; Normand, J.; Raghavachari, K.;; Rendell, A. B., J. C.; Iyengar, S. S.; Tomasi, J.; Cossi, M.; Rega,; N.; Millam, J. M. K., M.; Knox, J. E.; Cross, J. B.; Bakken, V.;; Adamo, C. J., J.; Gomperts, R.; Stratmann, R. E.; Yazyev, O.;; Austin, A. J. C., R.; Pomelli, C.; Ochterski, J. W.; Martin, R. L.;; Morokuma, K. Z., V. G.; Voth, G. A.; Salvador, P.;; Dannenberg, J. J. D., S.; Daniels, A. D.; Farkas, Ö.;; Foresman, J. B. O., J. V.; Cioslowski, J.; Fox, D. J. *Gaussian 09, revision E.01*, Gaussian, Inc.: Wallingford, CT, 2009.

84. Zhao, Y.; Truhlar, D. G. *J. Chem. Phys.* **2006,** *125*, 194101/1-194101/18.

85. Weigend, F.; Ahlrichs, R. *Phys. Chem. Chem. Phys.* **2005,** *7*, 3297-3305.

86. Weigend, F. *Phys. Chem. Chem. Phys.* **2006,** *8*, 1057-1065.

87. Marenich, A. V.; Cramer, C. J.; Truhlar, D. G. *J. Phys. Chem. B*. **2009,** *113*, 6378-6396.

88. Zhao, Y.; Donald, T. G. *Theor. Chem. Acc*. **2008,** *120*, 215-241.

89. Grimme, S.; Antony, J.; Ehrlich, S.; Krieg, H. *J. Chem. Phys.* **2010,** *132*, 154104.

References for Chapter 4:

1. Büschelberger, P. G., Dominik; Reyes-Rodriguez, E. K., Friedrich Koszinowski, Konrad; Jacobi von Wangelin, A.; Wolf, R. *Chem. Eur. J.* **2017,** *23*, 3139-3151.

2. Collman, J. P. *Acc. Chem. Res.* **1975,** *8*, 342-347.

3. Ellis, J. E. *Organometallics*. **2003,** *22*, 3322-3338.

4. Ellis, J. E. *Inorg. Chem.* **2006,** *45*, 3167-3186.

5. Fout, A. R.; Basuli, F.; Fan, H.; Tomaszewski, J.; Huffman, J. C.; Baik, M. H.; Mindiola, D. J. *Angew. Chem. Int. Ed.* **2006,** *45*, 3291-3295.

6. Margulieux, G. W.; Weidemann, N.; Lacy, D. C.; Moore, C. E.; Rheingold, A. L.; Figueroa, J. S. *J. Am. Chem. Soc.* **2010,** *132*, 5033-5035.

7. Carpenter, A. E.; Margulieux, G. W.; Millard, M. D.; E., M. C.; Weidemann, N.; Rheingold, A. L.; Figueroa, J. S. *Angew. Chem. Int. Ed.* **2012,** *51*, 9412-9416.

8. Mokhtarzadeh, C. C.; Moore, C. E.; Rheingold, A. L.; Figueroa, J. S. *Angew. Chem. Int. Ed.* **2017,** *56*, 10894-10899.

9. Thompson, N. B.; Green, M. T.; Peters, J. C. *J. Am. Chem. Soc.* **2017,** *139*, 15312-15315.

10. Rudd, P. A.; Planas, N.; Bill, E.; Gagliardi, L.; Lu, C. C. *Eur. J. Inorg. Chem.* **2013,** *2013*, 3898-3906.

11. Sloane, R. H.; Press, R. *Proc. R. Soc. London, Ser. A*. **1938,** *168*, 284.

12. Burdett, J. K., *J. Chem. Soc. Chem. Commun.* **1973,** *1973*, 763-764.

13. Breeze, P. A.; Burdett, J. K.; Turner, J. J. *Inorg. Chem.* **1981,** *20*, 3369-3378.

14. Lorenz, C.; Kaas, M.; Korber, N. *Z. Anorg. Allg. Chem.* **2018,** *644*, 1678–1680.

15. Jonas, K. *Angew. Chem. Int. Ed.* **1975,** *14*, 752-753.

16. Jonas, K.; Krüger, C, *Angew. Chem. Int. Ed.* **1980,** *19*, 520-537.

17. Moret, M.-E.; Zhang, L.; Peters, J. C. *J. Am. Chem. Soc.* **2013,** *135*, 3792-3795.

18. Weinberger, D. S.; SK, N. A.; Mondal, K. C.; Melaimi, M.; Bertrand, G.; Stückl, A. C.; Roesky, H. W.; Dittrich, B.; Demeshko, S.; Schwederski, B.; Kaim, W.; Jerabek, P.; Frenking, G. *J. Am. Chem. Soc.* **2014,** *136*, 6235-6238.

19. Rudd, P. A.; Liu, S.; Gagliardi, L.; V. G. Young, J.; Lu, C. C. *J. Am. Chem. Soc.* **2011,** *133*, 20724-20727.

20. Cammarota, R. C.; Lu, C. C. *J. Am. Chem. Soc.* **2015,** *137*, 12486-12489.

21. Cammarota, R. C.; Clouston, L. J.; Lu, C. C. *Coord. Chem. Rev.* **2016,** *334*, 100–111.

22. Cotton, F. A.; Murillo, C. A., *Multiple Bonds Between Metal Atoms, 3rd ed. Chapter 3.* 2007.

23. Cordero, B.; Gómez, V.; Platero-Prats, A. E.; Revés, M.; Echeverría, J.; Cremades, E.; Barragán, F.; Alvarez, S. *Dalton Transactions*. **2008**, 2832-2838.

24. Eisenhart, R. J.; Clouston, L. J.; Lu, C. C. *Acc. Chem. Res.* **2015,** *48*, 2885-2894.

25. Berry, J. F. *Acc. Chem. Res.* **2016,** *49*, 27-34.

26. Giles, J. R. M.; Roberts, B. P. *J. Chem. Soc., Chem. Commun.* **1981,** *1981*, 1167-1168.

27. Brand, J. C.; Roberts, B. P. *J. Chem. Soc., Chem. Commun.* **1984,** *1984*, 109-110.

28. Nakamoto, M.; Yamasaki, T.; Sekiguchi, A. *J. Am. Chem. Soc.* **2005,** *127*, 6954-6955.

29. Protchenko, A. V.; Dange, D.; Harmer, J. R.; Tang, C. Y.; Schwarz, A. D.; Kelly, M. J.; Phillips, N.; Tirfoin, R.; Birjkumar, K. H.; Jones, C.; Kaltsoyannis, N.; Mountford, P.; Aldridge, S. *Nat. Chem.* **2014,** *6*, 315-319.

30. Roos, B. O.; Taylor, P. R.; Siegbahn, P. E. M. *Chem. Phys.* **1980,** *125*, 194101.

31. Zhao, Y.; Truhlar, D. G. *J. Chem. Phys.* **2006,** *125*, 194101.

32. Perdew, J. P.; Burke, K.; Ernzerhof, M. *Phys. Rev. Lett.* **1996,** *77*, 3865.

33. Perdew, J. P.; Burke, K.; Ernzerhof, M. *Phys. Rev. Lett.* **1997,** *78*, 1396.

34. Schwarz, H. A.; Dodson, R. W. *J. Phys. Chem.* **1989,** *93*, 409-414.

35. Machan, C. W.; Chabolla, S. A.; Kubiak, C. P. *Organometallics*. **2015,** *34*, 4678-4683.

36. Vollmer, M. V.; Machan, C. W.; Clark, M. L.; Antholine, W. E.; Agarwal, J.; III, H. F. S.; Kubiak, C. P.; Walensky, J. R. *Organometallics*. **2014,** *34*, 3-12.

37. Horn, B.; Limberg, C.; Herwig, C.; Braun, B. *Chem. Commun.* **2013,** *49*, 10923-10925.

38. Schmidt, A.-C.; Nizovtsev, A. V.; Scheurer, A.; Heinemann, F. W.; Meyer, K. *Chem. Commun.* **2012,** *48*, 8634-8636.

39. Ratliff, K. S.; Lentz, R. E.; Kubiak, C. P. *Organometallics*. **1992,** *11*, 1986-1988.

40. Herskovitz, T.; Guggenberger, L. J. *J. Am. Chem. Soc.* **1976,** *98*, 1615-1616.

41. Yoo, C.; Kim, Y.-E.; Lee, Y. *Acc. Chem. Res.* **2018,** *51*, 1144-1152.

42. Sahoo, D.; Yoo, C.; Lee, Y. *J. Am. Chem. Soc.* **2018,** *140*, 2179-2185.

43. Yoo, C.; Lee, Y. *Angew. Chem. Int. Ed.* **2017,** *56*, 9502-9506.

44. Cammarota, R. C.; Vollmer, M. V.; Xie, J.; Ye, J.; Linehan, J. C.; Burgess, S. A.; Appel, A. M.; Gagliardi, L.; Lu, C. C. *J. Am. Chem. Soc.* **2017,** *139*, 14244-14250.

45. Yoo, C.; Lee, Y. *Inorganic Chemistry Frontiers*. **2016,** *3*, 849-855.

46. Jeletic, M. S.; Mock, M. T.; Appel, A. M.; Linehan, J. C. *J. Am. Chem. Soc.* **2013,** *135*, 11533-11536.

47. Horn, B.; Pfirrmann, S.; Limberg, C.; Herwig, C.; Braun, B.; Mebs, S.; Metzinger, R. *Z. Anorg. Allg. Chem.* **2011,** *637*, 1169-1174.

48. Fullmer, B. C.; Fan, H.; Pink, M.; Caulton, K. G. *Inorg. Chem.* **2008,** *47*, 1865-1867.

49. Wiedner, E. S.; Linehan, J. C. *Chem. Eur. J. 24*, 16964-19671.

50. Lee, G. R.; Maher, J. M.; Cooper, N. J. *J. Am. Chem. Soc.* **1987,** *109*, 2956-2962.

51. Stricker, M.; Oelkers, B.; Rosenau, C. P.; Sundermeyer, J. *Chem. Eur. J.* **2013,** *19*, 1042 – 1057.

52. Salomon, R. G.; Kochi, J. K. *J. Am. Chem. Soc.* **1973,** *95*, 1889–1897.

53. Tsuda, T.; Yazawa, T.; Watanabe, K.; Fujii, T.; Saegusa, T. *J. Org. Chem*. **1981,** *46*, 192-194.

54. Brookhart, M.; Grant, B.; Volpe Jr., A. F. *Organometallics*. **1992,** *11*, 3920-3922.

55. Jonas, K.; Mynott, R.; Krüger, C.; Sekutowski, J. C.; Tsay, Y. *Angew. Chem. Int. Ed.* **1976,** *15*, 767-768.

56. Dierks, H.; Dietrich, H. *Zeitschrift für Kristallographie*. **1965,** *122*, 1-23.

57. Howard, J. A.; Mile, B.; Morton, J. R.; Preston, K. F.; Sutcliffe, R. *The Journal of Physical Chemistry* **1986,** *90*, 1033-1036.

58. Gunderson, W. A.; Suess, D. L. M.; Fong, H.; Wang, X.; Hoffmann, C. M.; Cutsail III, G. E.; Peters, J. C.; Hoffman, B. M. *J. Am. Chem. Soc.* **2014,** *136*, 14998-15009.

59. Luca, O. R.; Crabtree, R. H. *Chem. Soc. Rev.* **2013,** *42*, 1440-1459.

60. Cape, J. L.; Lymar, S. V.; Lightbody, T.; Hurst, J. K. *Inorg. Chem.* **2009,** *48*, 4400-4410.

61. Chaudhuri, P.; Hess, M.; Müller, J.; Hildenbrand, K.; Bill, E.; Weyhermüller, T.; Wieghardt, K. *J. Am. Chem. Soc.* **1999,** *121*, 9599-9610.

62. Wang, Y.; DuBois, J. L.; Hedman, B.; Hodgson, K. O.; Stack, T. D. P. *Science*. **1998,** *279*, 537-540.

63. Yao, S. A.; Martin-Diaconescu, V.; Infante, I.; Lancaster, K. M.; Götz, A. W.; DeBeer, S.; Berry, J. F. *J. Am. Chem. Soc.* **2015,** *137*, 4993–5011.

64. For some examples of radical bonding in the main group see: Rosenthal, A. J.; M. D. Miqueu, M. D.; Bouhadir, G.; Bourissou, D. *Angew. Chem. Int. Ed.* **2015,** *54*, 9198-9202.

65. van der Eide, E.F.; Walter, E. D.; Liu, T.; Bullock, M. R. *Angew. Chem. Int. Ed.* **2012,** *124*, 8486-8489.

66. Berry, J. F.; Bill, E.; Bothe, E.; Cotton, F. A.; Dalal, N. S.; Ibragimov, S. A.; Kaur, N.; Liu, C. Y.; Murillo, C. A.; Nellutla, S.; North, J. M.; Villagrán, D. *J. Am. Chem. Soc.* **2007,** *129*, 1393–1401.

67. Hoefelmeyer, J. D.; Gabbaï, F. P. *Acc. Chem. Res.* **2000,** *122*, 9054-9055.

68. Pauling, L. *The Nature of the Chemical Bond, Third Edition.* Cornell Universtiy Press: Ithaca, New York, 1960.

69. Clark, T. *J. Am. Chem. Soc.* **1988,** *110*, 1672-1678.

70. Maity, D. K. *J. Phys. Chem. A*. **2002,** *106*, 5716-5721.

71. Wilian Oliveira de Sousa, D.; Nascimento, M. A. C. *Acc. Chem. Res.* **2017,** *50*, 2264-2272.

72. Stoll, S.; Schweiger, A. *J. Magn. Reson.* **2006,** *178*, 42-55.

73. Fulmer, G. R.; Miller, A. J. M.; Sherden, N. H.; Gottlieb, H. E.; Nudelman, A.; Stoltz, B. M.; Bercaw, J. E.; Goldberg, K. I. *Organometallics*. **2010,** *29*, 2176-2179.

74. Krause, L.; Herbst-Irmer, R.; Sheldrick, G. M.; Stalke, D. *J. Appl. Crystallogr.* **2015,** *48*.

75. Sheldrick, G. M. *Acta Crystallogr. Sect. A: Found. Crystallogr.* **2015,** *71*, 3-8.

76. Sheldrick, G. M. *Acta Crystallogr. Sect. A: Found. Crystallogr.* **2008,** *64*, 112-122.

77. Hübschle, C. B.; Sheldrick, G. M.; Dittrich, B. *J. Appl. Crystallogr.* **2001**, 1281-1284.

78. Spek, A. L. *J. Appl. Crystallogr.* **2003,** *36*, 7-13.

79. M. J. Frisch, G. W. T., H. B. Schlegel, G. E. Scuseria, M. A. Robb, J. R. Cheeseman, G. Scalmani, V. Barone, B. Mennucci, G. A. Petersson, H. Nakatsuji, M. Caricato, X. Li, H. P. Hratchian, A. F. Izmaylov, J. Bloino, G. Zheng, J. L. Sonnenberg, M. Hada, M. Ehara, K. Toyota, R. Fukuda, J. Hasegawa, M. Ishida, T. Nakajima, Y. Honda, O. Kitao, H. Nakai, T. Vreven, J. A. Montgomery, Jr., J. E. Peralta, F. Ogliaro, M. Bearpark, J. J. Heyd, E. Brothers, K. N. Kudin, V. N. Staroverov, R. Kobayashi, J. Normand, K. Raghavachari, A. Rendell, J. C. Burant, S. S. Iyengar, J. Tomasi, M. Cossi, N. Rega, J. M. Millam, M. Klene, J. E. Knox, J. B. Cross, V. Bakken, C. Adamo, J. Jaramillo, R. Gomperts, R. E. Stratmann, O. Yazyev, A. J. Austin, R. Cammi, C. Pomelli, J. W. Ochterski, R. L. Martin, K.

Morokuma, V. G. Zakrzewski, G. A. Voth, P. Salvador, J. J. Dannenberg, S. Dapprich, A. D. Daniels, Ö. Farkas, J. B. Foresman, J. V. Ortiz, J. Cioslowski, D. J. Fox *Gaussian 09, Revision E.01*, Gaussian, Inc.: Wallingford CT, 2009. 2009.

80. Zhao, Y.; Donald, T. G. *Theor. Chem. Acc.* **2008,** *120*, 215-241.

81. Weigend, F. R. A. R. *Phys. Chem. Chem. Phys.* **2005,** *7*, 3297.

82. van Lenthe, E.; Snijders, J. G.; Baerends, E. J. *J. Chem. Phys. 105*, 6505–6516.

83. E.J. Baerends, T. Z. A.J. Atkins, J. Autschbach, O. Baseggio, D. Bashford, A. Bérces, F.M. Bickelhaupt, C. Bo, P.M. Boerrigter, L. Cavallo, C. Daul, D.P. Chong, D.V. Chulhai, L. Deng, R.M. Dickson, J.M. Dieterich, D.E. Ellis, M. van Faassen, L. Fan, T.H. Fischer, C. Fonseca Guerra, M. Franchini, A. Ghysels, A. Giammona, S.J.A. van Gisbergen, A. Goez, A.W. Götz, J.A. Groeneveld, O.V. Gritsenko, M. Grüning, S. Gusarov, F.E. Harris, P. van den Hoek, Z. Hu, C.R. Jacob, H. Jacobsen, L. Jensen, L. Joubert, J.W. Kaminski, G. van Kessel, C. König, F. Kootstra, A. Kovalenko, M.V. Krykunov, E. van Lenthe, D.A. McCormack, A. Michalak, M. Mitoraj, S.M. Morton, J. Neugebauer, V.P. Nicu, L. Noodleman, V.P. Osinga, S. Patchkovskii, M. Pavanello, C.A. Peeples, P.H.T. Philipsen, D. Post, C.C. Pye, H. Ramanantoanina, P. Ramos, W. Ravenek, J.I. Rodríguez, P. Ros, R. Rüger, P.R.T. Schipper, D. Schlüns, H. van Schoot, G. Schreckenbach, J.S. Seldenthuis, M. Seth, J.G. Snijders, M. Solà, M. Stener, M. Swart, D. Swerhone, V. Tognetti, G. te Velde, P. Vernooijs, L. Versluis, L. Visscher, O. Visser, F. Wang, T.A. Wesolowski, E.M. van Wezenbeek, G. Wiesenekker, S.K. Wolff, T.K. Woo, A.L. Yakovle *ADF2018, SCM, Theoretical Chemistry* SCM: Vrije Universiteit, Amsterdam, The Netherlands.

84. Marenich, A. V. C.; C. J.; Truhlar, D. G, *J. Phys. Chem B.* **2009,** *113*, 6378.

85. Grimme, S.; Antony, J.; Ehrlich, S.; Krieg, H. *J. Chem. Phys.* **2010,** *132*, 154104.

86. F. Aquilante, J. A.; R. K. Carlson, L. F. Chibotaru, M. G. Delcey, L. De Vico, I. Fdez Galvan, N. Ferre, L. M. Frutos, L. Gagliardi, M. Garavelli, A.; Giussani, C. E. H.; G. Li Manni, H. Lischka, D. Ma, P. A. Malmqvist, T. Muller, A. Nenov, M. Olivucci, T. B. Pedersen, D. Peng, F. Plasser, B. Pritchard,; M. Reiher, I. R.; I. Schapiro, J. Segarra-Marti, M. Stenrup, D. G. Truhlar, L. Ungur, A. Valentini, S. Vancoillie, V. Veryazov, V. P. Vysotskiy, O. Weingart,; Lindh, F. Z. a. R. *J. Comput. Chem.* **2016,** *37*, 506-541.

87. Roos, B. O.; Lindh, R.; Malmqvist, P. Å.; Veryazov, V.; Widmark, P. O., *J. Phys. Chem. A*. **2005,** *109*, 6575-6579.

References for Chapter 5:

1. Kollar, K.; Sandor, P.; Szalontai, G.; Heil, B., *J. Organomet. Chem.* **1990,** *393*, 153-8.

2. Linn, D. E. Jr.; Halpern, J. *J. Am. Chem. Soc.* **1987,** *109*, 2969-74.

3. Hou, Z.; Koizumi, T.-a.; Fujita, A.; Yamazaki, H.; Wakatsuki, Y. *J. Am. Chem. Soc.* **2001,** *123*, 5812-5813.

4. Wayner, D. D. M.; Parker, V. D. *Acc. Chem. Res.* **1993,** *26*, 287-94.

5. Ciancanelli, R.; Noll, B. C.; DuBois, D. L.; DuBois, M. R. *J. Am. Chem. Soc.* **2002,** *124*, 2984-2992.

6. Rakowski Dubois, M.; Dubois, D. L. *Acc. Chem. Res.* **2009,** *42*, 1974-1982.

7. DuBois, D. L.; Berning, D. E. *Appl. Organomet. Chem.* **2000,** *14*, 860-862.

8. Ellis, W. W.; Miedaner, A.; Curtis, C. J.; Gibson, D. H.; DuBois, D. L. *J. Am. Chem. Soc.* **2002,** *124*, 1926-1932.

9. Galan, B. R.; Schoffel, J.; Linehan, J. C.; Seu, C.; Appel, A. M.; Roberts, J. A. S.; Helm, M. L.; Kilgore, U. J.; Yang, J. Y.; DuBois, D. L.; Kubiak, C. P. *J. Am. Chem. Soc.* **2011,** *133*, 12767-12779.

10. Berning, D. E.; Miedaner, A.; Curtis, C. J.; Noll, B. C.; DuBois, M. C. R.; DuBois, D. L. *Organometallics*. **2001,** *20*, 1832-1839.

11. Jordan, A. J.; Lalic, G.; Sadighi, J. P. *Chem. Rev.* **2016,** *116*, 8318-8372.

12. Lipshutz, B. H.; Shimizu, H. *Angew. Chem. Int. Ed.* **2004,** *43*, 2228-2230.

13. Goeden, G. V.; Caulton, K. G. *J. Am. Chem. Soc.* **1981,** *103*, 7354-5.

14. Hughes, G.; Kimura, M.; Buchwald, S. L. *J. Am. Chem. Soc.* **2003,** *125*, 11253-11258.

15. Jurkauskas, V.; Sadighi, J. P.; Buchwald, S. L. *Org. Lett.* **2003,** *5*, 2417-2420.

16. Chen, J.-X.; Daeuble, J. F.; Stryker, J. M. *Tetrahedron*. **2000,** *56*, 2789-2798.

17. Daeuble, J. F.; McGettigan, C.; Stryker, J. M. *Tetrahedron Lett.* **1990,** *31*, 2397-400.

18. Cammarota, R. C.; Lu, C. C. *J. Am. Chem. Soc.* **2015,** *137*, 12486-12489.

19. Cammarota, R. C.; Vollmer, M. V.; Xie, J.; Ye, J.; Linehan, J. C.; Burgess, S. A.; Appel, A. M.; Gagliardi, L.; Lu, C. C. *J. Am. Chem. Soc.* **2017,** *139*, 14244-14250.

20. Vollmer, M. V.; Xie, J.; Lu, C. C. *J. Am. Chem. Soc.* **2017,** *139*, 6570-6573.

21. Cammarota, R. C. Greater than the Sum of Its Parts: Tuning Nickel for Uncommon Small Molecule Reactivity and Catalysis via Dative Bonds with Group 13 Lewis Acidic Metalloligands. University of Minnesota - Twin Cities 2018.

22. Kisanga; Verkade; Schwesinger, *J. Org. Chem.* **2000,** *65*, 5431-2.

23. Wroblewski, A. E.; Pinkas, J.; Verkade, J. G. *Main Group Chem.* **1995,** *1*, 69-79.

24. Burgess, S. A.; Kendall, A. J.; Tyler, D. R.; Linehan, J. C.; Appel, A. M. *ACS Catal.* **2017,** *7*, 3089-3096.

25. Lu, Z.; Williams, T. J. *ACS Catal.* **2016,** *6*, 6670-6673.

26. Enthaler, S.; Brueck, A.; Kammer, A.; Junge, H.; Irran, E.; Guelak, S. *ChemCatChem*. **2015,** *7*, 65-69.

27. Berning, D. E.; Noll, B. C.; DuBois, D. L. *J. Am. Chem. Soc.* **1999,** *121*, 11432-11447.

28. Mondal, B.; Neese, F.; Ye, S. *Inorg. Chem.* **2016,** *55*, 5438-5444.

29. Lin, T.-P.; Peters, J. C. *J. Am. Chem. Soc.* **2014,** *136*, 13672-13683.

30. Moore, J. T.; Smith, N. E.; Lu, C. C. *Dalton Transactions*. **2017,** *46*, 5689-5701.

31. Eberhardt, N. A.; Guan, H. *Chem. Rev.* **2016,** *116*, 8373-8426.

32. Rudd, P. A.; Liu, S.; Gagliardi, L.; Young, V. G.; Lu, C. C. *J. Am. Chem. Soc.* **2011,** *133*, 20724-20727.

33. Waldie, K. M.; Ostericher, A. L.; Reineke, M. H.; Sasayama, A. F.; Kubiak, C. P. *ACS Catalysis*. **2018,** *8*, 1313-1324.

34. Wiedner, E. S.; Chambers, M. B.; Pitman, C. L.; Bullock, R. M.; Miller, A. J. M.; Appel, A. M. *Chem. Rev.* **2016,** *116*, 8655-8692.

35. Kunetskiy, R. A.; Polyakova, S. M.; Vavrik, J.; Cisarova, I.; Saame, J.; Nerut, E. R.; Koppel, I.; Koppel, I. A.; Kuett, A.; Leito, I.; Lyapkalo, I. M. *Chem. - Eur. J.* **2012,** *18*, 3621-3630.

36. Saame, J.; Rodima, T.; Tshepelevitsh, S.; Kütt, A.; Kaljurand, I.; Haljasorg, T.; Koppel, I. A.; Leito, I. *J. Org. Chem.* **2016,** *81*, 7349-7361.

37. Kaljurand, I.; Kuett, A.; Soovaeli, L.; Rodima, T.; Maeemets, V.; Leito, I.; Koppel, I. A. *J. Org. Chem.* **2005,** *70*, 1019-1028.

38. DuBois, D. L.; Blake, D. M.; Miedaner, A.; Curtis, C. J.; DuBois, M. R.; Franz, J. A.; Linehan, J. C. *Organometallics*. **2006,** *25*, 4414-4419.

39. Vazdar, K.; Kunetskiy, R.; Saame, J.; Kaupmees, K.; Leito, I.; Jahn, U.; *Angew. Chem. Int. Ed.* **2014,** *53*, 1435-1438.

40. Wiedner, E. S.; Roberts, J. A. S.; Dougherty, W. G.; Kassel, W. S.; DuBois, D. L.; Bullock, R. M. *Inorg. Chem.* **2013,** *52*, 9975-9988.

41. Ciancanelli, R.; Noll, B. C.; DuBois, D. L.; DuBois, M. R. *J. Am. Chem. Soc.* **2002,** *124*, 2984-2992.

42. Curtis, C. J.; Miedaner, A.; Ellis, W. W.; DuBois, D. L. *J. Am. Chem. Soc.* **2002,** *124*, 1918-1925.

43. Wander, S. A.; Miedaner, A.; Noll, B. C.; Barkley, R. M.; DuBois, D. L. *Organometallics*. **1996,** *15*, 3360-3373.

44. Vollmer, M. V.; Xie, J.; Cammarota, R. C.; Young Jr, V. G.; Bill, E.; Gagliardi, L.; Lu, C. C. *Angew. Chem. Int. Ed*. **2018,** *57*, 7815-7819.

45. Crabtree, R. H. *Chem. Rev.* **2016,** *116*, 8750-8769.

46. Abdur-Rashid, K.; Fong, T. P.; Greaves, B.; Gusev, D. G.; Hinman, J. G.; Landau, S. E.; Lough, A. J.; Morris, R. H. *J. Am. Chem. Soc.* **2000,** *122*, 9155-9171.

47. Tsay, C.; Livesay, B. N.; Ruelas, S.; Yang, J. Y. *J. Am. Chem. Soc.* **2015,** *137*, 14114-14121.

48. Cassar, L.; Foá, M. *Inorg. Nucl. Chem. Lett.* **1970,** *6*, 291.

49. Kaschube, W.; Poerschke, K. R.; Angermund, K.; Krueger, C.; Wilke, G. *Chem. Ber.* **1988,** *121*, 1921-9.

50. Poerschke, K. R.; Jonas, K.; Wilke, G.; Benn, R.; Mynott, R.; Goddard, R.; Krueger, C. *Chem. Ber.* **1985,** *118*, 275-97.

51. Vogt, M.; Rivada-Wheelaghan, O.; Iron, M. A.; Leitus, G.; Diskin-Posner, Y.; Shimon, L. J. W.; Ben-David, Y.; Milstein, D. *Organometallics*. **2013,** *32*, 300-308.

52. Kleimann, W.; Poerschke, K. R.; Wilke, G. *Chem. Ber.* **1985,** *118*, 323-31.

53. Chakraborty, S.; Zhang, J.; Krause, J. A.; Guan, H. *J. Am. Chem. Soc.* **2010,** *132*, 8872-8873.

54. Brown, H. C.; Park, W. S.; Cha, J. S.; Cho, B. T.; Brown, C. A. *J. Org. Chem.* **1986,** *51*, 337-42.

55. Krause, L.; Herbst-Irmer, R.; Sheldrick, G. M.; Stalke, D. *J. Appl. Crystallogr.* **2015,** *48*.

56. Sheldrick, G. M. *Acta Crystallogr. Sect. A: Found. Crystallogr.* **2015,** *71*, 3-8.

57. Sheldrick, G. M. *Acta Crystallogr. Sect. A: Found. Crystallogr.* **2008,** *64*, 112-122.

58. Hübcshle, C. B.; Sheldrick S. G.; Dittrich, B. *J. Appl. Crystallogr.* **2001**, 1281-1284.

59. *Persistence of Vision Pty. Ltd.*, Williamstown, Victoria, Australia., 2004.

60. A.L.Spek, *Acta Cryst.* **2009,** *65*, 148-155.